The design and synthesis of peptides for fluorescence imaging applications

Zuzanna Konieczna

A thesis submitted to satisfy the requirements for the degree of

DOCTOR OF PHILOSOPHY

School of Chemistry

The University of Edinburgh

2024

Iwonie i Maciejowi Koniecznym - za wszechstronne wsparcie

i za ośli upór przekazany w genach

Lay summary

Fluorescence happens when a substance, such as a dye, glows after being exposed to light. It is used by researchers to look at samples under the microscope. Attaching fluorescent labels (dyes) to features-of-interest makes these stand out (bright glow) against a dark background. This project aimed at designing new fluorescent labels and developing a new kind of a fluorescence microscope to get more information from images.

Most microscopes that use fluorescence look at how bright dyes glow, so called "fluorescence intensity". While this helps researchers show a feature is present, there are other ways to use fluorescence to learn more details. Fluorescence emission wavelength describes the colour of the observed glow, which can change depending on whether the dye molecules are in solution or buried within a structure. Another useful thing to measure is the time the glow lasts for, or the "fluorescence lifetime". This time is different for different dye molecules and, more interestingly, between the same dye molecules in different surroundings. This could give researchers a chance to learn more about the density, rigidity, or acidity of the environment of the dye, and thus the feature-of-interest.

Looking at all three parameters (the brightness, colour and duration of fluorescence) together could provide more details from a single experiment. However, this is difficult to do, as current methods usually focus on only one or two of these parameters at a time. The Full Spectrum Fluorescence Lifetime Imaging Microscope (FS-FLIM), built for this project, enables 3-in-1 fluorescence imaging. It can capture fluorescence intensity and lifetime across hundreds of wavelengths. The thesis describes the construction and testing of this instrument.

Additionally, the thesis explores the use of peptides as fluorescent probes.

Proteins, which are molecular building blocks made up of long chains of amino acids, have various functions within the human body such as fighting off diseases or passing on information. Peptides are shorter chains of amino acids and can often be fragments of proteins, but they lack the complex 3D structure and shape of a full protein. Peptides are excellent at recognising proteins, making them highly specific and sensitive labels. While peptides have been modified with fluorescent dyes previously, these dye molecules are large and need to be placed away from the peptide (like a label tag placed at the end of a drawstring of a teabag). This thesis uses a new dye, SeNBD, which is small enough to be chemically placed directly at the end of the peptide or even to replace one of the native amino acids of the peptide sequence.

To show the potential of the new dye, peptides targeting two proteins-of-interest were prepared and labelled with the SeNBD dye. A peptide previously shown to bind to α-synuclein, a protein associated with Parkinson's disease, was used to label the protein in patient-derived tissue. The samples were imaged on the FS-FLIM to detect α-synuclein clumps associated with the disease. Additionally, a short peptide targeting PDZ, a protein motif present in Post Synaptic Density Protein 95 (another brain protein), was also prepared with the SeNBD dye substituting amino acids in the peptide sequence. The modified peptide was still able to interact with the protein-of-interest, allowing high-detail imaging of the structure of the protein in a brain-derived sample.

Overall, this work introduced a new class of fluorescent peptides. The new small SeNBD dye allowed for imaging with short peptide sequences. The small size of the peptides made sure the fluorescent signal was localised directly at the protein-of-interest. First experiments were conducted to observe α-synuclein on a novel microscope, the FS-FLIM, to learn more about the protein clumps formed in Parkinson's disease. It is hoped the techniques developed here could further advance research in Parkinson's disease and other areas.

Abstract

Testing new function - does this work?? Fluorescence microscopy is a tool routinely utilised to address biological questions. Direct visualisation of features of interest, confirmation of protein identity or detecting the presence of a post-translational modification enable researchers to study differences between healthy and pathological phenotypes. As the questions get more complex, more advanced imaging techniques are required to address the limit of resolution, probe specificity to target and fluorescent background. This thesis explores two advancements to the field of fluorescence microscopy: the development of a novel imaging platform and the introduction of a new imaging modality.

The study covers the design and construction of the Full Spectrum Fluorescence Lifetime Imaging Microscope (FS-FLIM): a new imaging platform. The FS-FLIM maximises the information collected in a fluorescence imaging experiment. It is capable of 3-in-1 imaging, collecting fluorescence intensity and lifetime data at 512 wavelengths simultaneously. The instrument is compatible with a wide range of samples. The spectral region observed can be matched to the emitters present in the sample. Moreover, a wide range of lifetimes (from sub-nanosecond to tens of nanoseconds) can be recorded using the FS-FLIM. The performance of the constructed instrument is validated through solution lifetime measurements of several fluorescent dyes, and its application in environment sensing is described using a model system.

Next, the thesis focuses on developing fluorescent peptides for imaging applications. Although peptides can be labelled with a range of fluorophores, this study mostly uses a selenium-derivatised nitrobenzoxadiazole dye - SeNBD, a recent exciting addition to the imaging toolbox. The fluorogenic properties of the new

dye are characterised in this study, and the incorporation of the dye on-column using standard solid state peptide synthesis methods is described. The switch-on character, as well as the small size of the dye, are leveraged throughout the work, with short peptide sequences and internally-labelled peptide sequences developed as a new generation of peptide probes.

The specificity of peptides enables their application as therapeutic agents for otherwise undruggable proteins. One such example is α-synuclein, a protein associated with Parkinson's disease (PD). It is commonly thought that aggregation of α-synuclein and formation of cytotoxic inclusions is involved in PD progression. An α-helical bacteria-derived peptide, phenol soluble modulin $\alpha 3$ (PSMα), was previously shown to bind to small oligomeric α-synuclein species. Here, the peptide sequence was derivatised with several labels to explore its applications in imaging. Pilot experiments to detect α-synuclein species *in vitro* were conducted to confirm the binding to the protein-of-interest. A biotin-labelled peptide analogue was used to perform immunohistochemistry staining on patient tissue for in situ detection. Lastly, first attempts at fluorescence lifetime imaging of α-synuclein on the FS-FLIM instrument were made.

To further illustrate the capabilities of SeNBD dye specifically, and its potential for super-resolution imaging, a range of sequences targeting the PDZ domain (a common structural motif of anchoring and signalling proteins) were then considered. The chosen sequences were only a few amino acids long, however they demonstrated retained transient binding to the protein-of-interest upon labelling with SeNBD. Moreover, an internally-labelled sequence was also synthesised and successfully used to target PDZ domains. The transient nature of the peptide-protein binding was utilised in a Point Accumulation in Nanoscale Topography (PAINT) experiment, where the on-off binding enabled precise localisation of the dye molecules and super-resolution image reconstruction. The PDZ contained in post-synaptic density proteins of a brain-derived sample was successfully imaged, and nanoclusters of the protein super-resolved, corroborating literature findings. Furthermore, an extension to the approach using a coiled-coil interacting peptide pair: 101A and 101B, was investigated as an alternative approach for protein-peptide interaction pairs for super-resolution microscopy. Whilst the delivery of the synthesised targeting sequence (101B) proved challenging, expressing 101B attached to the target protein *in cellulo*, and subsequent staining with fluorescent 101A sequence produced promising results and enabled direct visualisation and super-resolution imaging of TOM-20 and LAMP-1 in fixed HEK cells.

Overall, the work presented herein showcased a range of fluorescent peptides that could be used across versatile fluorescence imaging platforms. The small novel dye, SeNBD, enabled super-resolution imaging using peptide sequences containing less than 10 amino acids. The small size of the peptides decreased the linkage error and ensured the fluorescent signal was localised at target of interest. The environment sensing properties of the dye were explored in preliminary experiments to observe α-synuclein on a purpose-built novel microscope, the FS-FLIM. It is hoped the techniques developed here could further progress research in the field of neurodegeneration and beyond.

Acknowledgements

In many ways, this Ph.D. project has felt like a collective effort. I am grateful for the kind and supportive people I met along the way who made this work possible and cheered me on towards the finish line.

First and foremost, my sincere thanks go to my supervisors: Prof. Mathew Horrocks and Prof. Marc Vendrell. Mathew - thank you for taking a chance on me four years ago and for showing me that, despite my background and my lack of the tinkering gene, I too can build an instrument! In all seriousness, it has been a great pleasure to be a part of your growing lab. Your enthusiasm for science and dedication to the work we do have helped me keep my spirits up and find a way out of every dead-end of the project. I would not be where I am today without your support. Marc - thank you for always offering your experience, perspective, and constructive feedback in my review meetings, for your continued interest in my ideas and plans, and a boost of confidence when I needed it most.

Additionally, I would like to thank Dr Chris Mowat, whom I met on my very first day at the university and who has been in my corner ever since: first as a personal tutor and then an assistant supervisor for this project. Chris, you have been a calming presence at every annual review, and I am extremely grateful for your support throughout the years.

For a chemist with minimal experience in DIY, building a state-of-the-art microscope complete with fancy electronics certainly felt like a challenge. It was made possible by three people who all deserve my gratitude. Dr Gareth Williams was instrumental to the first year of my project; I am thankful for his time and guidance when building the FS-FLIM. I would like to thank Dr Hazel Stewart for sharing her expertise, her detailed SOPs, and for providing sanity checks when

troubleshooting issues. I also owe huge thanks to Mr George Steedman of the workshop. George has fashioned parts and holders to bring my instrument to life and was patient with my numerous requests. Most admirably, he has never shown amusement at the dramatic descriptions of bolts and threads I subjected him to when my technical vocabulary failed me.

As I transitioned from working with long chains of DNA to working with long chains of amino acids, I was lucky to have the support of the entire Vendrell group. These guys have always made me feel welcome in their lab space and were a source of chat and laughter during long purifications. I would like to especially thank Dr Lorena Mendive Tapia, who was easily the best person to learn the ropes of peptide-making from, and Dr Fabio de Moliner, who supplied me with the fluorescent amino acids and believed they could work in my hands.

Despite working across at least three buildings during my degree, the Joseph Black building has always felt like my base. Many thanks to the support staff who make the School of Chemistry run on a day-to-day basis. Thanks to the incredibly helpful and ever-patient team at the Stores, the inventive team behind the workshops, and Dr John White who supplied me with hectolitres of eGFP for "my" students to play with. A special mention to Davy Waterston, the servitor, who never failed to greet me with a smile and helped count down the days till the weekend on particularly hard weeks. My thanks also go out to the teaching laboratory support staff - Elaine Sutherland, Robert Smith, Kirsty Bain and Rory Treanor - for helping me find joy in the little things, appreciate the comedy of ill-timed, often-repeated questions, and for making time to chat whenever I stopped by!

Finally, I owe my thanks to the ESMB group who largely shaped my Ph.D. experience. They deserve my thanks not only for the direct support with the project, including - but not limited to - all the help with cell culture, tissue cutting, buffer preparation, reagent pinching, and group meeting discussions, but also for making the lab a friendly and happy environment. I would like to thank the "original" lab members - Dr Craig Leighton, Dr Owen Kantelberg and Dr Alex Chappard. You've been patient and supportive as I found my way around the

lab and fully embraced the chaos I brought into the space. I am thankful to Dr Rebecca Saleeb for leading by example and for her kind support as I struggled with Peptide PAINT, and to Dr Ji-Eun Lee for being the office coffee supplier, as well as for making time for a "museum lunch" and a catch-up whenever I would ask. I would like to thank Noelia Pelegrina-Hidalgo and Candace Adams for being great partners-in-crime in the BC2 teaching labs and a great laugh in the office. I'm grateful to Judi O'Shaughnessy for her expertise in pathology, efforts to organise our ways of working, and (most importantly!) the great tea recommendations. My thanks also go to Haresh Bhaskar and Dr Takeshi Kaizuka for their help with samples, and to Dr Dylan George for joining me on the FS-FLIM team. It was lovely to cross paths with the newer members of the group too: Augustina Salis Torres, Tianxiao Zhao, Dr Rachel James, Dr Abigail Dos Santos, April Tan.

I can safely say my Ph.D. journey would not be the same if it wasn't for Dr Zoë Gidden and Dr Katie Morris. Thank you for making me feel welcome from day one (despite the masks, the lab shift rota and the zoom group meetings), and sharing my entire rollercoaster ride of a degree, even after you had finished yours. Your help has been invaluable: I am so grateful I could lean on you in face of disappointment, turn to you for advice and support, and rally to celebrate the wins. Thank you for turning mundane tasks into adventures, and making long imaging sessions in the optics lab go by quickly. I would also like to thank Katie for proofreading this thesis - and bearing with my love of hyphens! Zoë and Katie, I am lucky to have had such fabulous lab-mates and even more fortunate to have you as my friends.

It would not be fair not to name the people outside of the university who have stuck with me through this journey. My thanks go to Gülsevim - soon to be Dr Aydin - for keeping me sane and to Asma & Nuoya for always being just a message away.

Lastly, my thanks go out to my family, my four-pawed cheerleader Tenshi, and my dear parents. You nurtured my curiosity and encouraged me to follow my dreams. When I first moved to Edinburgh, you promised me it would all work out okay. That phrase became our little mantra, a cure for every doubt and wobble I

have had since. It is because of the two of you that I can say today: look, it did work out okay!

Contents

List of Figures

List of Tables

Abbreviations

α-syn	α-synuclein
A	adenosine
AAs	amino acids
AD	Alzheimer's disease
APD	avalanche photodiode detector
BBB	blood brain barrier
Boc	tetrbutyloxycarbonyl
bp	base pairs
C	cytosine
CCD	charge-coupled device
CD	circular dichroism
CMOS	complementary metal oxide semiconductor
DAB	diaminobenzidine
DAC	digital to analogue converter
Dapa	Boc-L-diaminopropinoic acid
DCM	dichloromethane
DCR	dark counts rate
DIC	*N,N'*-diisopropylcarbodiimide
DIPEA	*N,N*-diisopropylethylamine
DLB	dementia with Lewy Bodies
DMF	dimethylformamide
DMSO	dimethyl sulfoxide
DNA	deoxyribonucleic acid
DTT	dithiothreitol
EMCCD	electron multiplying charge-coupled device

ESET	excited state electron transfer
ESI	electrospray ionisation
ESPT	excited state proton transfer
FCS	fluorescence correlation spectroscopy
FLIM	fluorescence lifetime imaging microscopy
Fmoc	fluorenylmethoxycarbonyl
FOV	field of view
FP	fluorescent protein
FPGA	field programmable gate array
FRET	Förster resonance energy transfer
FS-FLIM	full spectrum fluorescence lifetime imaging microscope
FWHM	full-width half-maximum
G	guanine
GFP	green fluorescent protein
GLP-1	glucagon-like-peptide 1
GUI	graphical user interface
HE	hematoxylin and eosin
HPLC	high-performance liquid chromatography
HRMS	high resolution mass spectrometry
HRP	horseradish peroxidase
IC	internal conversion
IDP	instrinsically disordered protein
IHC	immunohistochemistry
iPSC	induced pluripotent stem cell
IRF	Instrument Response Function
ISC	intersystem crossing
KSO	kinetically stable oligomers
LB	Lewy body
LIVE-PAINT	live cell imaging using reversible interactions points accumulation for imaging in nanoscale topography
LL	low loading

LN	Lewy neurite
MALDI	matrix-assisted laser desorption ionisation
MRI	magnetic resonance imaging
MS	mass spectrometry
MSA	multiple system atrophy
NA	numerical aperature
NAD	nicotinamide adenine dinucleotide
NBD	nitrobenzoxadiazol
OM	organometallic
OxymaPure	ethyl cyano(hydroxyimino)acetate
PACAP	pituitary adenylate cyclase activating polypeptide
PAINT	points accumulation for imaging in nanoscale topography
PALM	photoactivated localisation microscopy
PBS	phosphate buffered saline
PC	phosphatidyl choline
PCB	printed circuit board
PD	Parkinson's disease
PDP	photon detection probability
PET	positron emission tomography
PFF	pre-formed fibrils
PLL	poly-L-lysine
PPI	protein-protein interaction
PSD-95	post-synaptic density protein 95
PSF	point spread function
PSTOP	photon stop
R6G	rhodamine 6G
RAM	Rink amide
RNA	ribonucleic acid
S/B	signal-to-background
SIM	structured illumination microscopy
SiR	silicone rhodamine
SMLM	single molecule localisation microscopy

SN	*substantia nigra*
SPAD	single photon avalanche detector
SPPS	solid phase peptide synthesis
SRB	sulforhodamine B
STED	stimulated emission depletion
STORM	stochastic optical reconstruction microscopy
T	thymine
TBAF	tetra-n-butylammonium floride
TCSPC	time correlated single photon counting
TDC	time-to-digital conversion
TFA	trifluoroacetic acid
ThS	thioflavin-S
ThT	thioflavin-T
TICT	twisted intramolecular charge transfer
TIR	total internal reflection
TIRFM	total internal reflection fluorescence microscopy
TIS	triisopropyl silane
TOF	time of flight
UV-vis	ultra violet visible spectroscopy
WT	wild type
YFP	yellow fluorescent protein

Chapter 1

Introduction

1.1 Scope of the chapter

This chapter contextualises the role of optical and fluorescence microscopy in the study of Parkinson's disease. It covers physical chemistry definitions and principles that are key to the work carried out in further chapters. Current state-of-the-art techniques and imaging modalities are introduced.

1.2 Protein aggregation in neurodegeneration: a nano-scale problem with systemic consequences

There are currently over 50 million people worldwide suffering from dementia.[1] The prevalence of the disease and the significant cognitive and behavioural impairment make dementia one of the most societally impactful diseases and one of the leading causes of death. Dementia patients require medical, social and informal care around the clock and often over the span of decades. With limited treatment options[2,3] and few new drug candidates reaching the clinic, the disease cannot be stopped or reversed. Despite its high prevalence and impact, dementia remains incurable. This is partly due to the fact that the diagnosis follows the development of motor symptoms. The onset of symptoms signals neuronal loss and damage that had already occurred. The diagnostic process is slow and complicated, including but not limited to cognitive evaluation, family medical history, neuroimaging, and exclusion of other conditions.[4,5] This limits the treatment to managing symptoms and slowing down the disease progression. Early intervention could offer better patient outcomes and new therapeutic targets, however, for it to be possible, potential biomarkers need to be identified and a thorough understanding of the disease mechanisms is required.

The main symptom of dementia, cognitive impairment, is associated with neuronal damage and loss.[6,7] Due to the limited ability of neuronal cells to repair themselves or be replaced,[8] the effects of neuronal loss are irreversible: leading to a chronic, progressive disorder. Different diseases under the umbrella term of dementia, such as Alzheimer's disease (AD), dementia with Lewy Bodies (DLB) and Parkinson's disease (PD), are characterised by varying levels of neurodegeneration in different brain areas that result in the distinct symptoms across the three. AD is associated with loss of cortical neurons, leading to disrupted cognition and memory. Similar subsections of neurons are affected in DLB. PD patients show loss of neuronal cells in the *substantia nigra pars compacta* in the midbrain.[9] As these neurons play a key role in movement initiation and coordination,[10] they give rise to the motor symptoms characteristic of PD. Crucially, together with neuronal loss, the presence of intra- and extracellular inclusion bodies is considered a pathological hallmark of the diseases.[6,11,12]

The hallmark protein inclusion in PD is termed a Lewy body (LB) (Figure 1.2.1A and B). Its presence was previously used as a marker of neuronal loss.[13] In 1997, Spillantini *et al.* showed LBs are made up of the protein α-synuclein (α-syn).[14] α-syn is a small (14 kDa) protein, highly abundant in the brain, and localised primarily to pre-synaptic terminals (nerve cell junctures).[15] In its native form, α-syn is thought to be involved in synaptic trafficking (membrane-associated transport of chemicals between neurons),[16] but its specific role remains undefined.[17] In PD, increased α-syn presence is observed, alongside the formation of α-syn-containing filamentous inclusions within the cell body (LB) and along the axon - Lewy neurite (LN) (Figure 1.2.1C and D).[18]

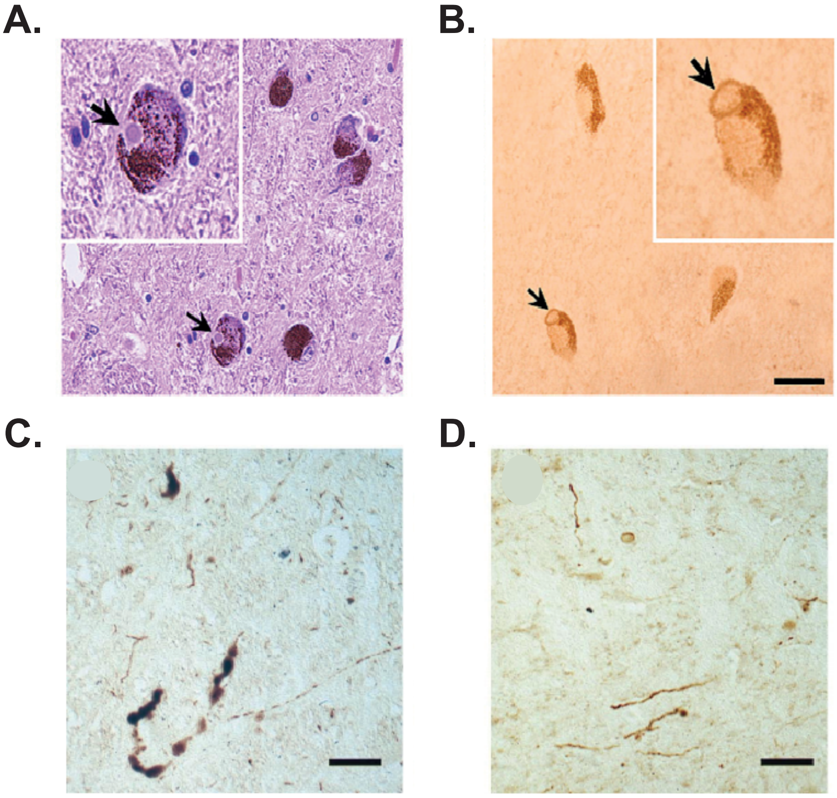

Figure 1.2.1: PD neurons from *substantia nigra* showing hallmark protein deposits. Panels A and B are images of LBs, adapted from Ryu *et al.*.[19] The arrows point to circular inclusions within cells. The two panels showcase different cell staining methods: a histological stain (pink, A) and an immunohistological stain (orange, B). Panels C and D depict Lewy neurites as observed by Spillanti *et al.*.[20] LNs are characterised by αS protein deposited along the axon. Immunohistochemistry stains were used to visualise αS and ubiquitin (C) and αS only (D), highlighting the complex makeup of LBs and LNs alike. Images from panels A and B are the same scale, scale bar is 50 μm. Scale bar for panel C is 90 μm and for panel D is 100 μm.

The mislocalisation of α-syn from the synaptic terminal to the cell body or the axon, resulting in a transient state of pale bodies and pale neurites, has also been described in the literature.[21] These structures highly resemble LBs and LNs in shape, yet are less pronounced (contain less α-syn or lack the characteristic fibrillar structure). These are thought to later mature into LBs and LNs. Despite being mostly formed of α-syn, LBs and LNs are highly heterogenous in their make-up. Over 70 proteins, as well as lipids and other macromolecules, have been observed in LBs.[22] LBs contain incorporated neurofilaments, heat shock proteins, proteosome units, ubiquitin[23] and even organelles.[24]

The observed correlation between LB presence and neuronal death,[25] the identification of insoluble α-syn within the inclusion bodies, and familial cases of PD showing mutations in the SNCA gene encoding α-syn,[26,27] resulted in the role of α-syn in PD progression being investigated. Formation of inclusions by the physiologically-relevant and otherwise soluble protein was postulated to be the result of α-syn misfolding and subsequent aggregation.

The native conformation of a protein is determined by its primary structure, the sequence of amino acids (AAs) encoded for in the genome, whereas the three dimensional structure (secondary and tertiary structure) arises as a result of the amino acid-specific interactions.[28] The folding is proposed to occur as an iterative process, starting from a random state and following geometrically similar folds to minimise the energy until the native state is reached.[29] The native conformation must be achieved for the protein to carry out its physiological function, form correct associations and establish interactions. It is therefore unsurprising that protein misfolding has been linked to biological malfunction.[30] Incorrectly folded protein monomers can often expose hydrophobic residues on their surface, making the molecule more aggregation-prone as inter-molecular interactions become favoured in the largely hydrophilic environment. The propensity to misfold depends on the primary structure of the protein. The presence of motifs in the sequence such as AAs of opposite charges that could promote electrostatic interactions,[31] or in fact the lack of secondary structure defining the fold, can encourage protein misfolding. Despite protective mechanisms, including chaperone proteins and ubiquitination (tagging proteins for clearance), factors such as mutations in the protein-coding genes or infection with prions can further facilitate protein misfolding beyond a level of clearance that can be sustainably maintained. When not cleared, the incorrectly folded proteins have a higher propensity to form inter-molecular interactions resulting in oligomers first and then larger deposits. This process is called aggregation[11,12] (Figure 1.2.2).

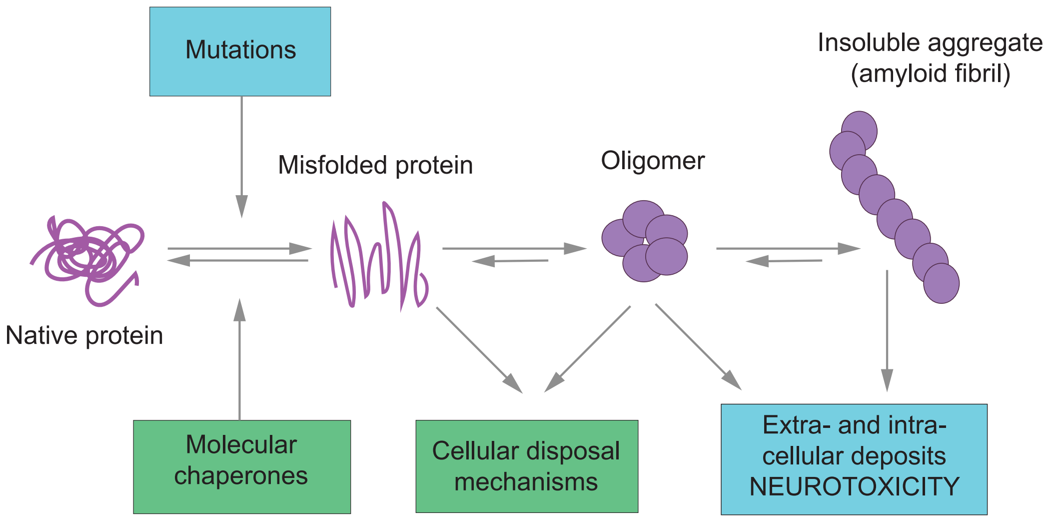

Figure 1.2.2: Schematic representation of the protein aggregation process. When proteins are misfolded and not in their native conformation, singular monomer units can associate with each other forming oligomers. Clearance mechanisms to dispose of the unwanted protein conformations and their aggregated species are in place. However these are not always effective, especially if other factors facilitating protein aggregation or misfolding, like mutations, are involved. Oligomers can further develop into mature fibrils - microscopic inclusions with characteristic β sheet structure (amyloid). The aggregation process is linked to neurotoxicity, but the role of the intermediate species and their toxicity are still under investigation.

The amino acid sequence of α-syn does not restrict the protein to any given 3D conformation under physiological conditions, making α-syn an instrinsically disordered protein (IDP). IDPs are highly flexible, biologically active proteins that can adopt various conformations depending on physiological conditions.[32] α-syn is thought to adopt a range of conformations, such an α-helix upon interaction with lipid membranes, a compact globular monomer, or an extended monomer which exposes the core of the protein and makes α-syn more aggregation-prone.[33]

Aggregation gives rise to misfolding or conformational diseases, where the process is associated with loss of function of the native protein and/or production of toxic species.[34] These are often termed "amyloid diseases", as the mature deposits exhibit β-sheet rich centres that stabilise the structures (so called "amyloid fibrils"). At this stage, the aggregates are no longer soluble within the cell matrix, and can stick to and rupture cell membranes leading to cell death.[35] The LBs and LNs observed in PD contain amyloid fibrils formed from α-syn.

The aberrant aggregation process is highly dynamic and the link between protein aggregation and cell toxicity is still under investigation. Conflicting evidence on the role of LBs in PD progression has been published. LBs were said to both be formed in a protective response (encasing the toxic species)[36] and to facilitate further aggregation through the filamentous fibres templating monomer oligomerisation and thus assisting the spread from cell to cell.[37] Their presence is associated with an advanced disease state. LBs can be observed on positron emission tomography (PET)[38] images of patients with associated cellular atrophy indicated by their magnetic resonance imaging (MRI)[39] scan. Whilst the presence of LBs can be used to classify the extent of pathology, it cannot signal early stages of disease. It is the early aggregates (oligomers) that are currently of most interest for diagnostic purposes. They are likely present years before the onset of symptoms and are thought to be highly toxic, as they facilitate calcium influx, caspase activation, and cell death.[40,41] However, they are notoriously difficult to study since due to their small size (only a few nanometers in length), highly heterogeneous structure and low abundance (low concentrations in physiological conditions).

1.3 Optical microscopy and the study of protein deposits

Optical microscopy played a crucial role in building an understanding of the basis of Parkinson's disease. When James Parkinson published his work "An Essay on the Shaking Palsy" in 1817, he described the condition in depth, naming symptoms and presenting illustrative case studies. He even hypothesised the irritation or inflammation of the medulla and thecal ligament (part of the spinal cord) caused nerve entrapment and resulted in the observed motor symptoms. Despite his theory, Parkinson highlighted it needed further validation and he called for "the attention of those who humanely employ anatomical examination in detecting the causes and nature of diseases, particularly to this malady".[42] He proposed only such "anatomical" studies could confirm the cause of the disease and thus facilitate management and treatment of the condition. At the time of his publication, optical microscopy was not routinely used to study disease.

Compound microscopes have existed since as early as 1590s, however they suffered from low magnification, chromatic and spherical aberrations. A schematic representation of an early compound microscope[43] is depicted in Figure 1.3.1.

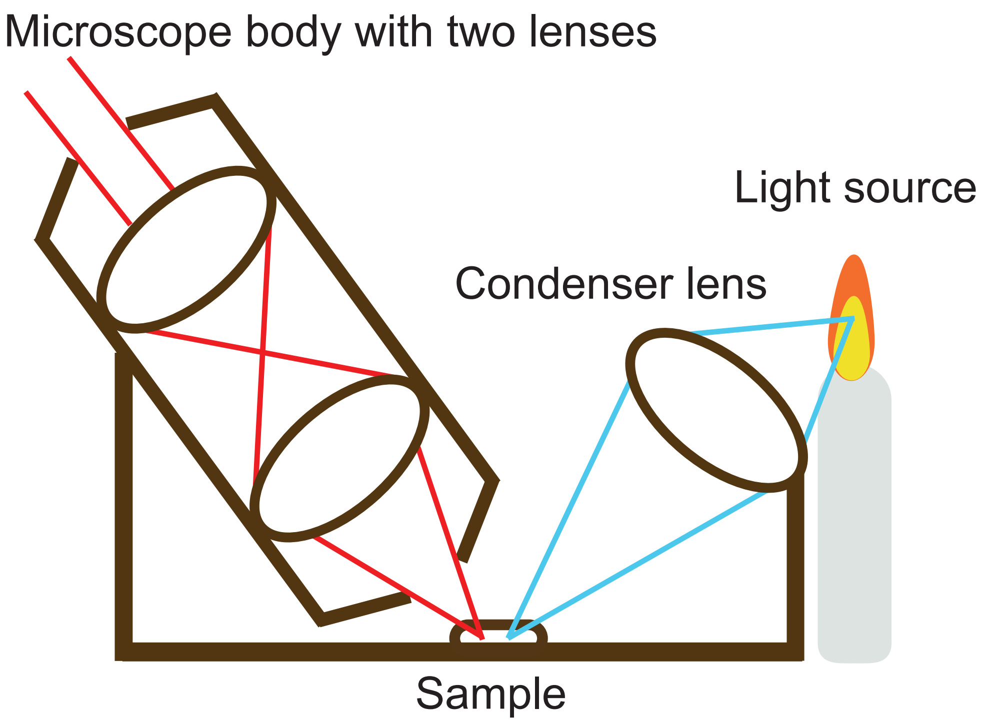

Figure 1.3.1: Schematic representation of the early compound microscope, reproduced from Wollman *et al.*.[43] The light source (a candle, later on a light bulb) was placed next to a condenser lens directed at the sample. A microscope body, containing two lenses, collected and magnified the image from the sample. This design was later modified to introduce more controls for sample positioning and focus.

The simple design used a candle as an illumination source. A condenser lens directed the illumination at a mounted sample. The reflected light was collected and magnified by the microscope body. The wooden or brass tube contained a set of two lenses, an objective and eyepiece lens, each magnifying the image. In their early years, compound microscopes were seldom used for biological samples.[44] At the turn of the centuries, Robert Hooke and Joseph Jackson Lister improved upon the state-of-the art compound microscope; their upgraded design, featuring several lenses placed a certain distance apart, resolved the issue of chromatic aberrations.[45]

Microscopy found its application in the clinic when tissue sectioning and staining became possible and dissecting rooms became part of hospitals.[46] In the second half of the 19th century, Rudolf Virchow, a German physician, suggested the need for microscopic studies of pathological tissues to understand the basis of disease.[47,48] Interestingly, it was also Virchow, the “father” of modern pathology, who first coined the term amyloid in 1845 to describe macroscopic inclusions in the brain. He used iodine and sulphuric acid, and the observed colouration of the plaques made him believe the inclusions were made of cellulose.[49]

Advancements in the optics, as well as the invention of staining agents, led to the observation of Lewy bodies. A century after the initial report of the disease, the pathology of PD was linked to lesions in the *substantia nigra* (SN) by Tretiakoff.[50,51] He reported intraneuronal inclusions in the SN of disease patients and called these Lewy bodies, after the first researcher who observed those in PD patients (albeit outside of SN) - Fritz Lewy.[52] The standard staining methods to give contrast under the microscope and stain morphological features at the time were hematoxylin and eosin (HE). Hematoxylin acts like a positively charged basic dye and has affinity for nuclei, which become blue when stained. The complementary dye, eosin, is acidic and negatively charged. It stains cytoplasm and extracellular matrix components pink.[53] These remain the gold standard in histology to this day. When Lewy first observed the inclusions, he noticed they were eosinophilic. He further subjected them to solvents (alcohol, chloroform and benzene) to determine their molecular make-up. They remained insoluble and were therefore thought to consist of proteins.[54]

Other staining methods were used to visualise the LB inclusions in later years, for instance silver staining.[55–57] The Bielschowsky staining method, first used in 1902, utilised the affinity of silver to components across tissue.[58] A colourless staining solution, containing silver ions in the form of a salt such as ammoniacal silver or silver nitrate, was applied to tissue. Ionic silver (Ag^+) bound selectively to features across the sample, including proteins containing methionine residues. These were later visualised through a reduction reaction. Metallic silver was formed across the areas where ionic silver was bound. This could either be achieved *in situ* via glutathione, adrenaline or any other native molecules of reducing capability, or externally through "chemical development" (adding an external reducing agent like hydroquinone/sodium sulfite solution). Positively stained areas (argyrophylic) appeared darker under a light microscope against the negative (non-argyrophylic) background.[59]

The next big milestone involved identifying the protein component of LBs and used immunohistochemistry (IHC). This step was possible thanks to the invention of serum therapy[60] and a drive to understand what is now known to be the antigen-antibody interaction.[61] The discovery of antibodies[62] offered unparalleled sensitivity; the staining protocols no longer relied on non-specific charge, affinity or hydrophobic interactions between the dye and feature-of-interest, but could target a specific protein. Spillantini *et al.* employed antibodies from anti-α-syn serum raised against a synthetic peptide to stain the tissue[14] (Figure 1.3.2A).

A secondary biotinylated antibody was used to target the primary. The interaction between biotin and avidin was next employed, through application of avidin functionalised with horseradish peroxidase (HRP). This created a larger complex at the protein-of-interest and enabled further staining. As a contrast agent or "chromogen", the researchers employed diaminobenzidine (DAB). This compound, which is colourless in solution, would undergo an enzymatic reaction with HRP in presence of hydrogen peroxide to form an oxidised product (insoluble brown precipitate).[63] In this manner, Spillantini et al. were able to visualise LBs and conclusively confirm the presence of α-syn in the inclusions (Figure 1.3.2B). This discovery has shaped the later years of research into the role of α-syn in PD

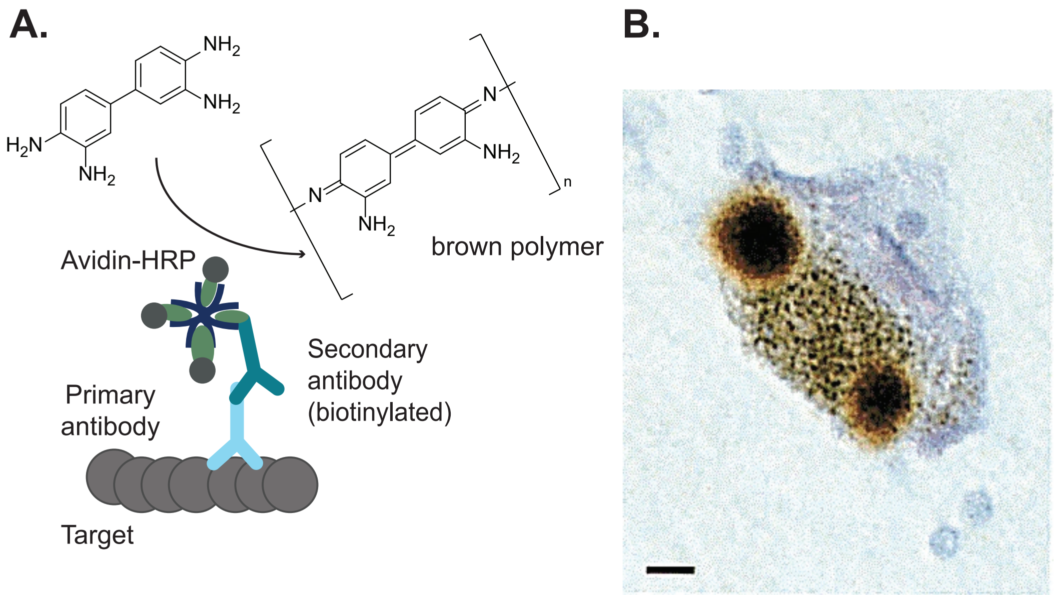

Figure 1.3.2: A. Schematic representation of the DAB staining process. Protein-of-interest is targeted with a primary antibody. A biotinylated secondary anitbody against the primary is used next. Avidin-HRP complex is applied to localise the enzyme at the protein of interest. Brown colour can be observed when DAB is oxidised, visualising the location of the primary antibody. B. An image of a nerve cell with two pigmented α-syn positive LBs. Scale bar is 8 μm. Image reproduced from Spillantini *et al.*[14]

pathology and contributed to the gold-standard disease staging method: the Braak scale.[64] Braak's method combined the available staining techniques (including IHC for α-syn and silver staining) to trace the disease progression.

With a drive for therapeutic interventions, PD research moved across from patients to animal and cellular models.[65–67] This, together with *post-mortem* tissue studies, enabled researchers to build a better understanding of the changes associated with the disease pathology. Fluorescence microscopy started being used to observe the disease phenotype and track changes more and more frequently. This fast, relatively low cost and sensitive technique is compatible across many model systems, enabling *in vitro* and *in situ* studies. The principles underlying the technique are covered in detail in the next section.

1.4 Principles of fluorescence

One of the most common contrast methods for optical microscopy uses a physical phenomenon called fluorescence. Fluorescence occurs when a molecule is able to absorb a photon and use the energy to excite an electron from its ground state energy level to a higher, excited energy level. The relaxation back to the ground state is accompanied by the emission of a photon and is described as fluorescence. The emission of light by a dye molecules gives stained features a bright appearance against the dark background. The processes resulting from photon absorption by a molecule can be schematically represented in a Jablonski diagram (Figure 1.4.1).

Molecules usually exist in their lowest energy electronic state, or ground state (S_0 on the diagram). Illumination with light of a specific wavelength (matching the energy gap between the ground state and the excited state of the molecule) can facilitate an electronic transition and a promotion of an electron to an excited electronic state (absorption, $S_0 \rightarrow S_1$). The likelihood of absorption of a photon is proportional to the square of transition dipole moment (a mathematical function describing the likelihood of an electronic transition between two energy states). Transition to higher electronic states (e.g S_2) is also possible as the vibrational

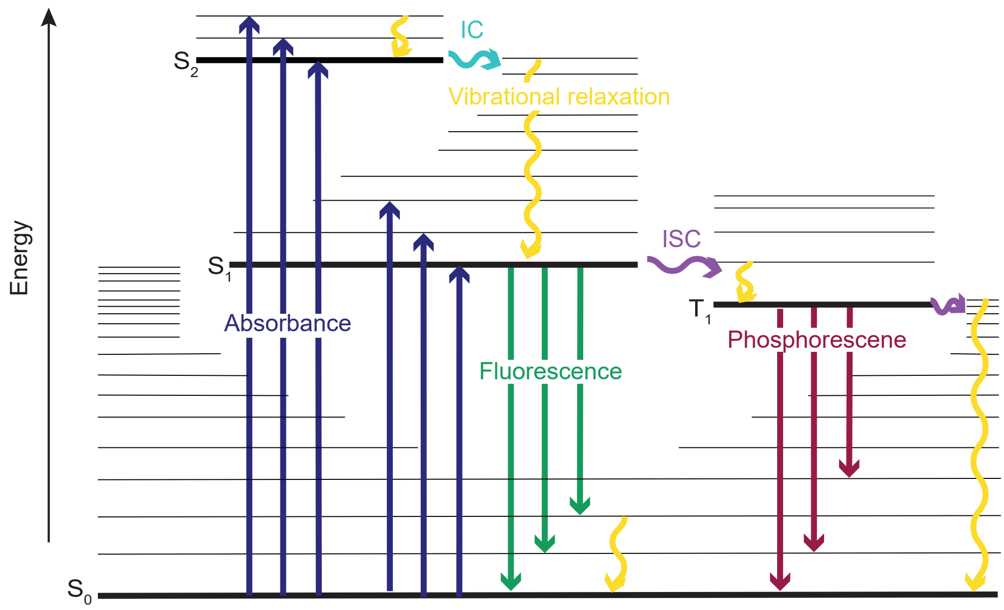

Figure 1.4.1: Jablonski diagram representing the processes occurring when a photon is absorbed by a molecule, and an electron is promoted from the ground to the excited state. Non-radiative processes (vibrational relaxation, internal conversion (IC) and intersystem crossing (ISC)) and radiative processes (fluorescence and phosphorescence) are represented.

levels of the excited state and higher excited states overlap. The transitions follow spin multiplicty rules, meaning the spin of the excited electron does not change.

Once the molecule is excited, several processes can occur concurrently to relax the molecule. Vibrational relaxation is responsible for a transition from higher vibrational states to the lowest vibrational state of S_1. This is a fast process, usually on the order of 10^{-12} s. If any electrons have reached higher excited states, they can undergo a non-radiative process called internal conversion (IC), where they transition from lowest vibrational levels of S_2 into high vibrational levels of S_1. Following the $S_2 \rightarrow S_1$ transition, vibrational relaxation occurs again with loss of heat. The IC is also a fast process lasting approximately 10^{-11} s. Fluorescence occurs when the electron releases a photon (radiative transition) as it de-excites from $S_1 \rightarrow S_0$. As per Kasha's rule, the transition originates from the lowest excited electronic state.[68] It can occur to any of the vibrational levels of the ground state. That and the fast non-radiative processes described above account for the fact that the photon emitted is of lower energy (longer wavelength) than the photon absorbed. Fluorescence is a spin-allowed transition (between singlet states) and as such is fast and occurs on the order of 10^{-8} s.

A different pathway for the electron could follow non-radiative relaxation through IC between S_1 and S_0 and further vibrational relaxation (not depicted) or loss of energy due to collisions. Equally, the electron can cross from an excited singlet state to an excited triplet state ($S_1 \rightarrow T_1$) in an intersystem crossing (ISC) event. Radiative de-excitation from $T_1 \rightarrow S_0$ is possible, and results in a long glow known as phosphorescence. The transition is spin-forbidden, and occurs with lower probability. It leads to slow emission on the order of up to 10^{-1} s. The intramolecular non-radiative processes compete with radiative decay de-excitation pathway (fluorescence). The rates of all the transitions are compared in Table 1.1.

Table 1.1: Summary of transitions related to fluorescence and their rates.

Name	**Rate, k** (s^{-1})
Absorbance	10^{15}
Fluorescence	$10^6 - 10^9$
Phosphorescence	$10^{-2} - 10^2$
Internal conversion	$10^4 - 10^{12}$
Intersystem crossing	$10^2 - 10^6$
Vibrational relaxation	10^{12}

1.4.1 Parameters describing fluorescence

The absorbance of a molecule can be expressed as a function of the incident intensity (I_0 - amount of light reaching the sample) and transmitted intensity (I - amount of light transmitted through a sample). Absorbance is proportional to the concentration of the sample (c), the length of the path the light has to travel through (l) and the intrinsic ability of the molecule to absorb light (ε: molar extinction coefficient, expressed in $M^{-1}cm^{-1}$ for a particular wavelength). The two can be related through Equation 1.1, otherwise known as the Beer-Lambert Law.

$$A = \log_{10}\left(\frac{I_0}{I}\right) = \varepsilon \times c \times l \tag{1.1}$$

Fluorescence intensity describes how much light the molecule emits (the number of photos emitted per unit of time). A useful metric to describe the probability of fluorescence is the quantum yield (Φ_f), which is the ratio of photons emitted to photons absorbed. When the number of photons emitted matches the number of photons absorbed, the ratio is equal to 1, and the fluorophore is 100% efficient. Quantum yield is usually expressed using Equation 1.2, where the rate constants for the radiative process of fluorescence, k_f, and the non-radiative processes that compete with fluorescence, k_{nr}, are included.

$$\Phi = \frac{k_f}{k_f + k_{nr}} \tag{1.2}$$

In addition to the non-radiative processes already described (all intramolecular), photobleaching (photochemical decomposition, where a change to the fluorophore structure damages its ability to absorb light) and intermolecular processes (collisions and quenching) can also compete with fluorescence. Photobleaching diminishes the intensity of observed fluorescence, as fluorophore molecules are rendered dark (unable to fluoresce). Most photobleaching is thought to occur from the triplet electronic (T_1) state. The energy can be transferred to a triplet oxygen species (molecular oxygen, $^3O_2$), generating singlet oxygen ($^1O_2$).[69] This reactive oxygen species can then undergo quenching through an irreversible chemical reaction with a fluorophore molecule.[70] Photostability is a measure of how long the fluorophore can fluoresce for under constant illumination and can describe how resistant different fluorophores are to photobleaching processes.

The wavelength (λ) relates to the colour of light that is used or observed. The wavelength of maximum absorbance, λ_{abs}, is important to know when deciding on the excitation source. The wavelength of maximum emission, λ_{em}, might dictate the choice of filters to observe the signal. Fluorescence is of longer wavelength (lower energy) than absorbance, and the difference between the two is described by the Stokes shift (Figure 1.4.2).

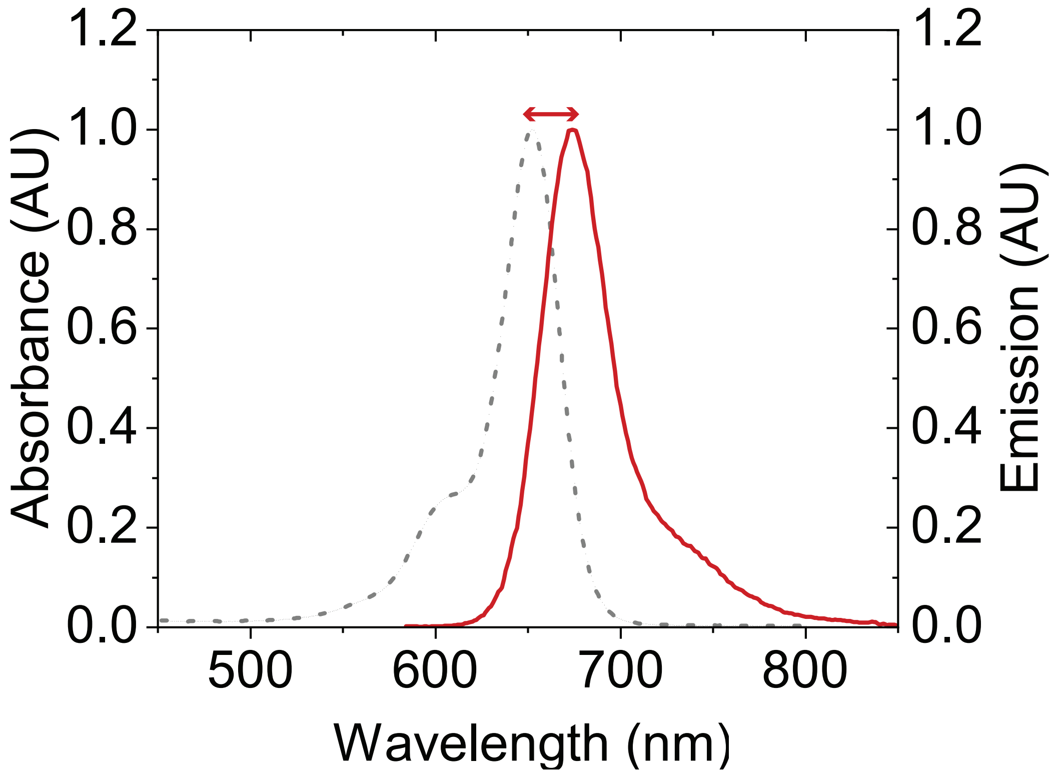

Figure 1.4.2: Absorbance (dotted line) and emission (red continuous line) of silicone rhodamine (SiR). Spectral data obtained from FPbase.[71] The red double headed arrow highlights the difference between absorbance and emission maxima - the Stokes shift.

This difference is useful in designing optical microscopes, where the emission signal can be detected selectively whilst blocking the excitation, increasing the signal-to-noise ratio of measurements.

1.4.2 Fluorescence lifetime

Another interesting parameter is the fluorescence lifetime (τ), which expresses the time a molecule spends in the excited state. It can be expressed using equation 1.3 below. The fluorescence lifetime is inversely proportional to the sum of the radiative (k_f) and non-radiative ($k_n r$) rate constants.

$$\tau = \frac{1}{k_f + k_{nr}} \tag{1.3}$$

Experimentally, it can be derived from the fluorescence intensity decay over time. Fluorescence decay usually follows first order kinetics. Lifetime can be modeled following a first order kinetic equation (Equation 1.4) where $I(t)$ is intensity at any given time t, and I_0 is the initial intensity.

$$I(t) = I_0 e^{\frac{-t}{\tau}} \tag{1.4}$$

For fluorophores with several conformational states of different lifetimes, multi-exponential decay fits are necessary. The lifetime (τ) becomes a weighted mean of the lifetimes of the different components and their fractional contributions.

The radiative decay, k_f, is a relatively long process among the energy transitions time scale (see Table 1.1), giving the high energy molecule time to undergo a variety of transitions and non-radiative de-excitation (quenching). Quenching leads to the reduction in the observed fluorescence lifetime, and it can be a direct result of internal or external processes. Thus, fluorescence lifetime can be used to report on the microenvironment of the fluorophore.

Internal quenching can be a result of bond rotation (energy expelled to twisting or photoinduced isomerisation of an alkene) or environmental factors. Temperature and viscosity can both affect the rates of non-radiative decays; as can polarity of the solvent for some dyes, not necessarily those that display emission wavelength shifts (i.e. solvatochromatic dyes). These processes all affect the stability of the excited state conformation of the dye molecule. Reversible changes to electron distribution in the excited state can also lead to internal quenching. These are enabled by structural motifs within the fluorescent molecule and can be harnessed in the design and manufacture of fluorescence-based metal sensors and long-lifetime probes. Strongly electron donating groups (like tertiary amines) or nitro groups when present in close proximity to an electron acceptor, can lead to excited state electron transfer (ESET). Upon excitation, an electron moves from the electron-rich donor to the acceptor. The resulting excited acceptor is non-fluorescent and thus can relax non-radiatively through vibrational relaxation to its ground state. ESET can explain the difference between τ of fluorescein (approx. 4 ns) and tetranitrofluorescein (2.3 ns). Equally, fast (sub-picosecond) intramolecular proton transfer can lead to excited state proton transfer (ESPT). The resulting molecule can have a distinct lifetime from the starting molecule. ESPT is exploited in applications of pH-sensing imidazole dyes. The dye structure can also increase the probability of ISC ($S_1 \rightarrow T_1$): incorporation of heavy atoms (Br, I) increases the rate of that transition and leads to increased phosphorescence.

External quenching can involve energy transfer to another molecule, as is the case in Förster resonance energy transfer (FRET). FRET occurs between two molecules in close proximity (< 10 nm), where the emission spectrum of one overlaps with the absorption spectrum of the other. Excitation of a donor leads to emission in the acceptor molecule (that was not directly excited with a laser source). Loss of fluorescence intensity of the donor is also accompanied by its lifetime shortening, the energy transfer process competes with fluorescence as a de-excitation pathway. The lifetime of the acceptor remains unchanged. FRET can occur between two molecules of the same species. The energy transfer then works both in forward and back directions (homoFRET) and this leads to general shortening of the observed lifetime. The efficiency of the energy transfer between donor and acceptor is distance-dependent, which is why FRET pairs can be used as a molecular ruler. Dynamic quenching (or collisonal quenching) is a process that involves loss of energy by an excited molecule (A^*) non-radiatively via collison with other molecules (Q) (Equation 1.5).

$$A^* + Q \xrightarrow{k_q} A + Q^* \tag{1.5}$$

This process decreases fluorescence lifetime. The effect of quencher concentration ([Q]) on fluorescence lifetime (Equation 1.6) can be derived from the Stern-Volmer equation, and explains how fluorescence lifetime can be used to monitor oxygen levels.

$$\tau = \frac{\tau_0}{1 + k_q \tau_0 [Q]} \tag{1.6}$$

To observe and study molecules using fluorescence a large toolkit of dyes and probes has been developed.

1.5 Fluorescent probes & their applications to PD

Whilst some naturally occurring molecules, such as amino acids (tryptophan, tyrosine, phenylanaline) and transmitters (for instance, nicotinamide adenine dinucleotide (NAD)), possess chromophores and are able to absorb and emit photons, most fluorescence applications rely on extrinsic fluorescent labels. This is because the intrinsic fluorescence (autofluorescence) usually requires low wavelength excitation, the efficiency of the emitters cannot be controlled or tuned, and it can only be traced back to a range of native molecules, the locations of which cannot be controlled. Most targets, including α-syn the protein of interest in PD, are non-fluorescent under native conditions and require strategies such as as the use of fluorescent protein (FP) fusions, organic dyes or organometallic complexes. These classes of fluorescent compounds are briefly described below. This list is not exhaustive, other classes of bioorthogonal probes are discussed by Cserep *et al.*,[72] and those with particular applications to live-cells by Dean *et al.*.[73]

Fluorescent proteins

The discovery of FPs can be traced back to the 1960s, when a green-light emitting protein was first isolated from *Aequorea victoria* jellyfish and aptly named green fluorescent protein (GFP).[74] FPs derived from other species, as well as genetic engineering and modification of the jellyfish-derived GFP, gave rise to an expanded FP colour pallette spanning all the way across the visible spectrum.[75–78]

FPs are characterised by a relatively large size (approximately 25 kDa), where the fluorophore is often shielded by the protein shell.[79] Their large size can impede their folding or localisation within a cell, explaining the (relatively) weak emission and short lifetime (in the range of 1-4 ns). Since FPs are produced by cells, through deoxyribonucleic acid (DNA) manipulation, the gene encoding the FPs can be built-in to a wide variety of cellular targets. The stoichiometry of the labelling can be controlled, enabling 1:1 stoichiometry for quantitiative studies,[80] although folding efficency and maturation time for FPs needs to be considered.

The genetic expression of FPs makes them compatible for the study of dynamic processes in live cell models.

Pandey *et al.* have used an α-syn GFP fusion construct to study the behaviour of wild type (WT) α-syn and point-mutated α-syn in a neuroblastoma-derived cell line SH-SY5Y. The researchers reported that the fusion to FP did not influence the aggregation properties of α-syn. After validating their constructs, they studied three familial mutations and one novel mutation of α-syn and compared their aggregation timelines. The GFP-α-syn cell lines enabled direct visualisation of the aggregates using confocal microscopy.[81]

Organic dyes

Successful synthesis of fluorescent dyes such as Magdala red (1867[82]) and the true game-changer fluorescein (1871,[83] named after its remarkable, at the time, fluorescent properties) started decades of research in organic dyes. These remain the most widely used class of fluorescent probes due to their established and scalable chemistry as well as diverse physical, chemical and biological properties. A wide variety of water-soluble functionalised dyes for microscopy applications have been developed.[84–88] They are characterised by a relatively small size of around 500 Da and favourable quantum yields and photostability. Several examples of organic dyes, with their quantum yields, are presented in Figure 1.5.1.

Although some dyes show intrinsic propensity to bind to cellular structures such as lipid-rich membranes,[93,94] usually they are conjugated to other targeting molecules (antibodies, DNA, ribonucleic acid (RNA), peptides) for specific labelling of targets of interest. Moreover, a range of self-labelling tags for proteins were developed to enable application of organic dyes in cell imaging.[95,96] The tags are often derived from enzymes. One example is HaloTag, derived from bacterial haloalkane dehalogenase. HaloTag convalently binds a ligand (containing the fluorophore) at the active site. In nature, the substrate would be released, however bioengineered HaloTag system prevents the release of the ligand from the active site. Thus, any dye can be conjugated to the reactive HaloTag ligand motif (a primary chloroalkane) for covalent capture at the HaloTagged protein.[95]

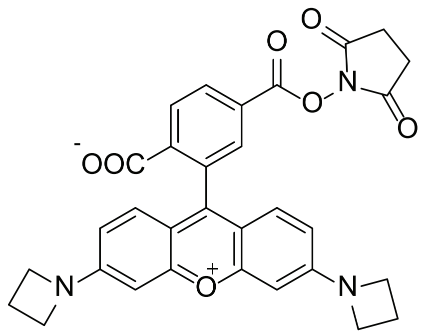

JF549
$\Phi_f = 0.88$

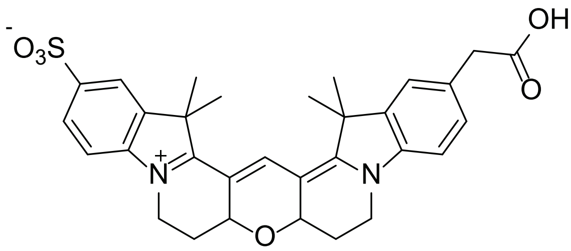

Cy3B
$\Phi_f = 0.67$

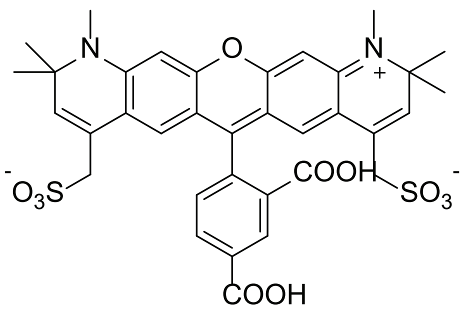

AF594
$\Phi_f = 0.66$

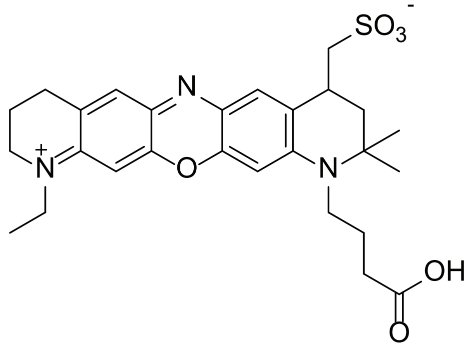

Atto655
$\Phi_f = 0.30$

Figure 1.5.1: Four examples of organic fluorophores, their chemical strucutures and quantum yields: JF549,[89] Cy3B,[90] AF594[91] and Atto655.[92] Quantum yields were obtained from aqueous solution measurements.

In the context of amyloid protein imaging, the dye most commonly used is thioflavin-T (ThT) (structure in Figure 1.5.2), a benzothiazole salt.

It contains a rotatable bond (single σ bond between two rings) and is classed as a molecular rotor.[97] The extended ring structure is responsible for its mode of action. The dye is known to bind to β-sheets within amyloid fibrils, the interaction promoted through pi-pi stacking interactions.[98] The recognition motif is specific to the secondary structure, but not a specific protein. Figure 1.5.3 shows the β-sheet organisation characteristic of an amyloid protein.[99] Anti-parallel β-strands are arranged forming a 10 Å groove.

ThT can be used to label various protein inclusions, characteristic of PD but

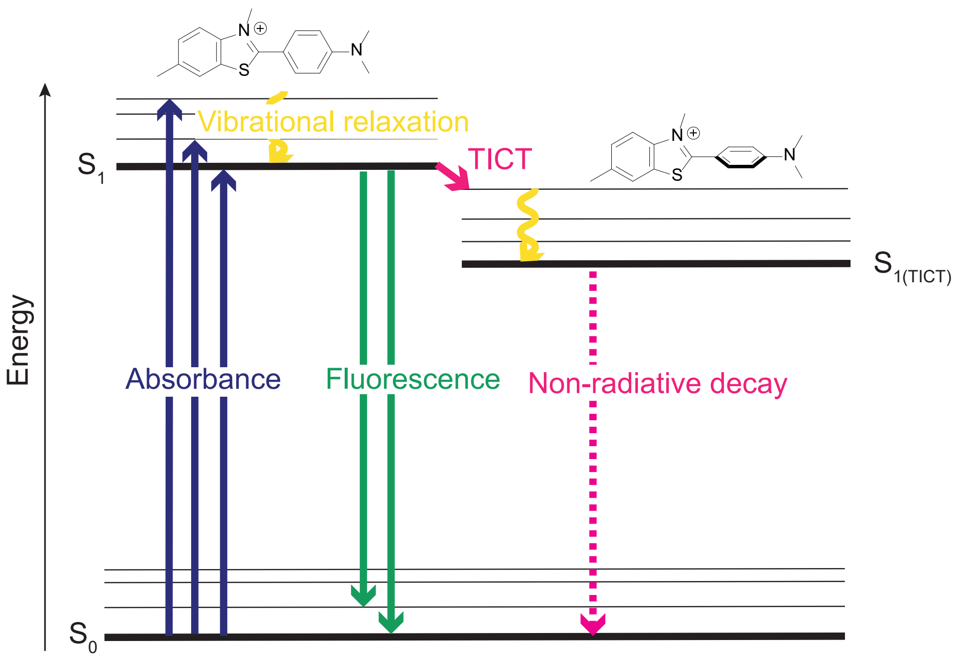

Figure 1.5.2: Jablonski diagram representing TICT and the two corresponding conformations of ThT. ThT molecules can exist in two conformations: planar and twisted. Upon excitation an electron is promoted to an excited state (S_1). This state is stabilised by ThT interactions with amyloid fibrils, leading to ThT fluorescence. TICT is a dark state, associated with the twisted conformation, where non-radiative de-excitation is favoured. TICT is the dominant de-exciation pathway for ThT in solution, where its emission is weak and its largerly non-fluorescent (molecules relaxed via non-radiative pathways). When TICT cannot be accessed (ThT edged inside a fibril), the fluorescence is the dominant relaxation pathway, explaining the difference in fluorescence lifetime and quantum yield between the unbound and bound dye.

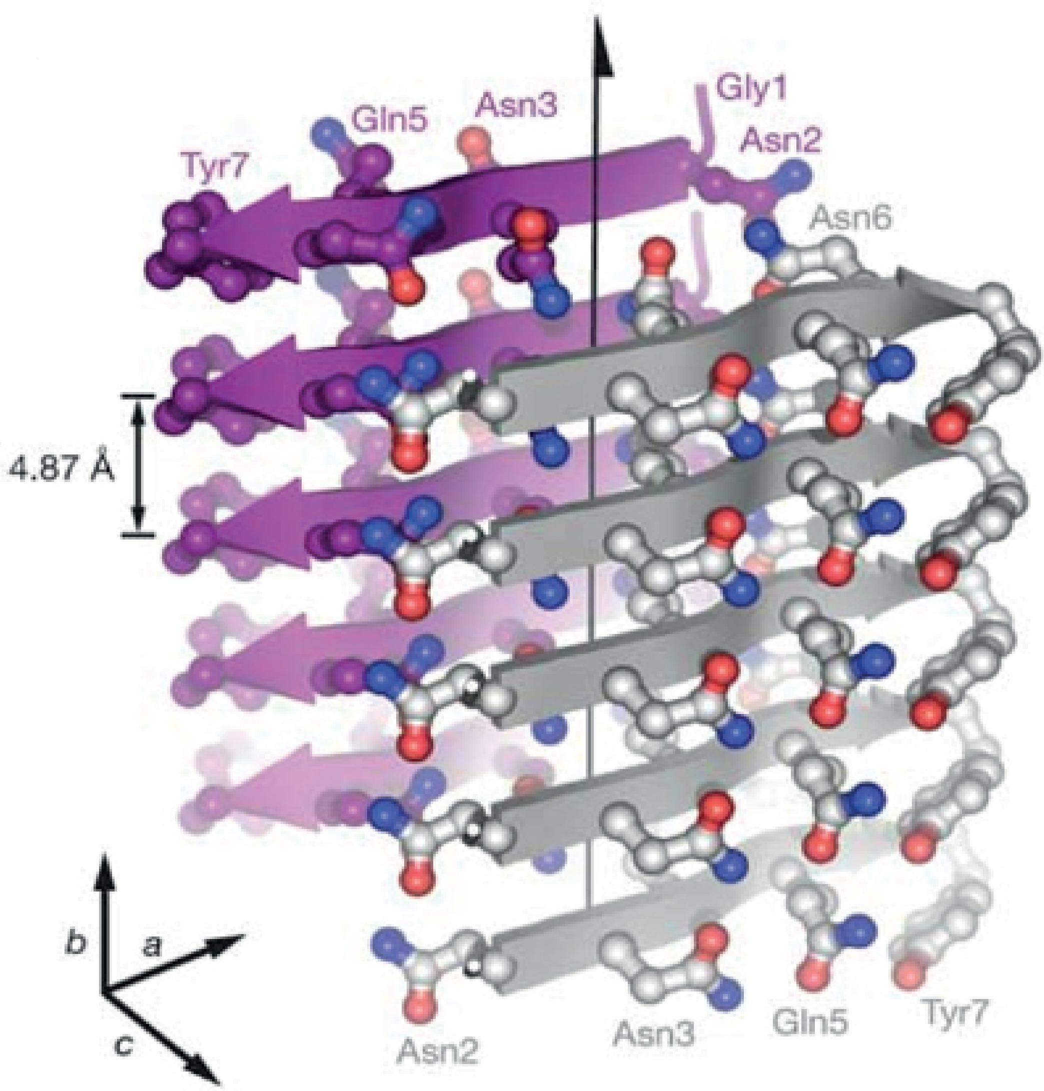

Figure 1.5.3: β-sheet structure of amyloid fibrils, image adapted from Nelson *et al.*.[99] β-strands are arranged in anti-parallel direction, with a 4 Å distance between them. A 10 Å groove is formed between two β-sheets.

also AD *etc.*, as long as they display amyloid structure. The dye molecule can enter the space between the two β-strands of a fibril, where its structure becomes locked. ThT molecules are able to interact with amino acid side chains in an orientation parallel to the long axis of the structure.[98] No rotation along the sigma bond is possible in this conformation, and the energy is expelled in the form of fluorescence. The unbound molecules rotate freely in solution, accessing a different conformation in the excited state in a process called twisted intramolecular charge transfer (TICT) as represented in Figure 1.5.2. This state is postulated to be "dark" (not fluorescent, "quenched") and the excited energy in that state is expelled through non-radiative processes. Fluorescence displayed only upon binding gives a lower fluorescence background signal (200-fold increase in quantum yield upon binding to fibrils,[100] and a ps to ns increase in lifetime of the dye[101]). ThT has been employed by Horrocks *et al.* to detect the formation of β-sheet rich oligomers and fibrils during α-syn aggregation *in vitro* and to detect amyloid species in biofluids of PD patients and healthy controls[102] at a single-molecule level.

Organometallic complexes

Some organometallic (OM) complexes, containing ruthenium,[103] rhenium[104] or iridium,[105] are characterised by long and bright emissions and thus found applications as fluorescent probes. They are highly photostable, water-soluble and exhibit large Stokes shifts. The long emissions observed are of phosphorescence origins. The excited complexes undergo energy charge transfer from metal centre to ligand (fast intersystem crossing into a stable triplet state). They are thus also characterised by long lifetimes.

Ruthenium-based complexes found an application in α-syn aggregation detection. Cook *et al.* described a switch-on dipyridophenazine ruthenium(II) complex, with good cell permeability and low cytotoxicity that binds to α-syn fibrils.[106] They observed the probe in human neuroglioma (H4) cells, where it not only co-localised with over-expressed and aggregating α-syn but also showed an 18-fold increase in fluorescence intensity, showing potential as a sensitive marker of aggregation.

All of these classes of probes offer unique advantages as well as challenges. Table 1.2 compares optical properties of several types of fluorescent compounds.

The class, excitation and emission wavelengths and lifetime value (in aqueous

Table 1.2: Fluorescent properties across the different classes of probes. The lifetimes for the organic fluorophores and the organometallic compound were measured in water.

Name	**Class**	λ_{ex} **(nm)**	λ_{em} **(nm)**	τ **(ns)**	ε $(M^{-1}cm^{-1})$	Φ_f
Tyrosine[107]	Intrinsic	275	300	2.5	1,400	0.13
NAD(P)H[108]	Intrinsic	300-380	450-500	0.3	6,300	0.02
eGFP[109]	FP	488	509	2.71	54,000	0.60
mCherry[109]	FP	587	610	1.4	72,000	0.22
BodipyFL[110]	Organic	502	511	5.87	80,000	0.93
AF647[111]	Organic	650	665	1.04	240,000	0.33
$[Ru(bpy)_3]^{2+}$[112]	OM complex	450	630	358	14,600	0.03

solvent systems) are quoted. The molar absorption coefficient (ε at λ_{abs}) and Φ_f are also presented for all the fluorophores. The two parameters are especially useful when comparing the effectivness of fluorophores in a "molecular brightness" calculation. Molecular brightness (Equation 1.7) is a product of the ε and Φ_f.

$$molecular\ brightness = \varepsilon \times \Phi_f \tag{1.7}$$

The higher the value, the brighter and thus more detectable the fluorophore. Autofluorescent molecules have very low molecular brightness values (0.18 and 0.13 for tyrosine and NAD(P)H, respectively). FPs are characterised by higher ε values, despite relatively low quantum yields. For the two examples used, the molecular brightness is in the 10,000 $M^{-1}cm^{-1}$ region. The highest molecular brightness values can be calculated for the two organic dyes, AF647 and BodipyFL.

The different classes of fluorophores also have their own niche applications. Intrinsic fluorescence of amino acids and transmitters is often exploited in fluorescence lifetime imaging microscopy (FLIM). FPs are predominantly used in cell imaging applications and disease models. Organic dyes have the most varied properties and applications, as their structures can be tuned to modulate λ_{em} or

τ. OM complexes exhibit the largest Stokes shift and the longest fluorescence lifetimes out of the probes mentioned.

1.6 Fluorescence microscopy - practical considerations

The compound microscope (first introduced in Section 1.3) was an example of a brightfield microscope. In brightfield microscopy, the sample is illuminated with white light and the image is formed based on the absorbance of light within the specimen. Contrast is achieved through staining agents, that colour features within the sample. Fluorescence can also be used as a means of introducing contrast, in a technique called fluorescence microscopy.

Imaging fluorescent samples requires a slightly different microscope set-up. An example of a basic set-up is shown in Figure 1.6.1.

The sample is illuminated by a laser source of a specific wavelength, as opposed to a white light source. An excitation filter, such as a band-pass filter, can be used to modulate the wavelength of the light. A dichroic mirror is placed at 45 °to direct the laser light towards the objective and the sample. This special type of a filter reflects light of shorter wavelengths than the cut-off wavelength and transmits light of longer wavelengths. Thus, laser light can be reflected to the sample. The objective focuses the light and illuminates the sample. The fluorophores contained within undergo excitation and emit photons (fluoresce). The light emitted from the sample is of a longer wavelength than the excitation light (Stokes shift, as introduced in Section 1.4). This means it can be transmitted through the dichroic filter towards the detector. To prevent any of the excitation light to reach the detector and block out background fluorescence, another filter is placed in front of the detector. This is an emission filter and it modulates what colour light can reach the detector, dividing light up in wavelength-based channels for data acquisition. In some fluorescence set-ups, the detector is placed at a 90 °angle to the excitation pathway, to further minimise the amount of laser light that reaches the detector. This set-up can undergo further modifications and

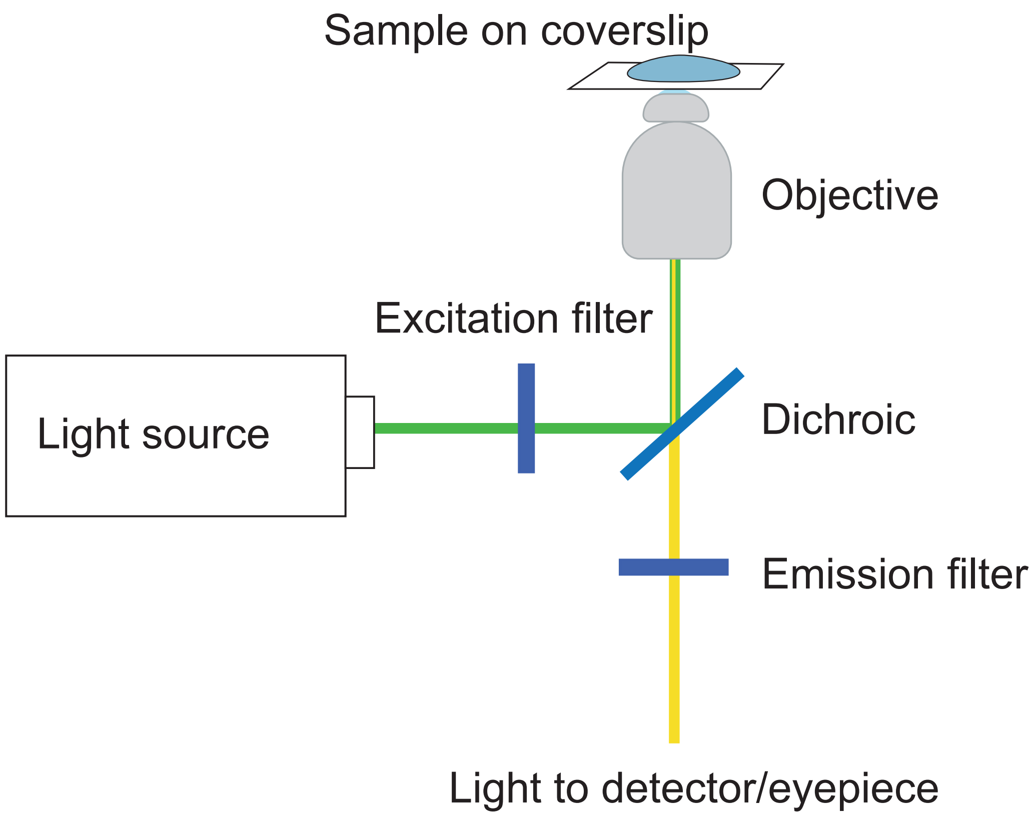

Figure 1.6.1: Basic fluorescence microscope set-up. An excitation light is passed through an excitation filter to generate light of desired wavelength. The dichroic filter reflects light up to the objective. The objective collects magnified image of the sample and passes the fluorescence back towards the dichroic mirror. The fluorescence can pass through the dichroic. An emission filter is implemented to ensure no exictation light reaches the detector.

utilise sets of filters for muliplexed imaging.

Uniform illumination of the sample is desired in light microscopy, but less favourable for fluorescence imaging. When the sample is thicker than the depth of focus of the objective lens in light microscopy, blurring of the image can occur. In such cases, the light coming from below and above the focal plane in the sample will also be detected. The problem is more prominent for fluorescence microscopy. Using widefield illumination (Figure 1.6.2A), a large area of the sample is illuminated all at once. This means all of the molecules in the illuminated volume will fluoresce at the same time. As all this fluorescence is subsequently detected, this imaging method leads to low signal-to-background (S/B) ratios. Despite wide-field illumination epifluorescence offering speed of imaging, other illumination modes, where the illuminated sample volume can be restricted, are often preferred for in-detail imaging of thick samples, such as tissue.

Confocal microscopy (Figure 1.6.2B) relies on optical sectioning to image just the focal plane. By placing a pinhole (a mechanical barrier) in the detection beam path, all out of focus light is rejected and it cannot reach the detector. The size of the pinhole restricts the confocal volume (the size of the plane imaged, usually to around 1 μm diameter). Since the confocal volume is small, the imaging speed is reduced in this approach. To build up a large field of view, the excitation beam needs to be moved across the sample. Another method of restricting the excitation volume uses light reflection from the glass-water interface. When excitation light reaches the coverslip at a steep angle, it gets reflected. This is known as total internal reflection (TIR) (Figure 1.6.2C). At the interface of the coverslip and the sample, an electromagnetic field (known as evanescent field) propagates the illumination approximately 100 nm into the sample. The level of illumination quickly drops off with distance from the coverslip, meaning the illumination is limited to surface molecules only. This greatly reduces S/B ratio, making total internal reflection fluorescence microscopy (TIRFM) a great technique for surface imaging.

Various detectors are used for different fluorescence applications from cameras to more complex time-gating and photon counting devices, including single photon

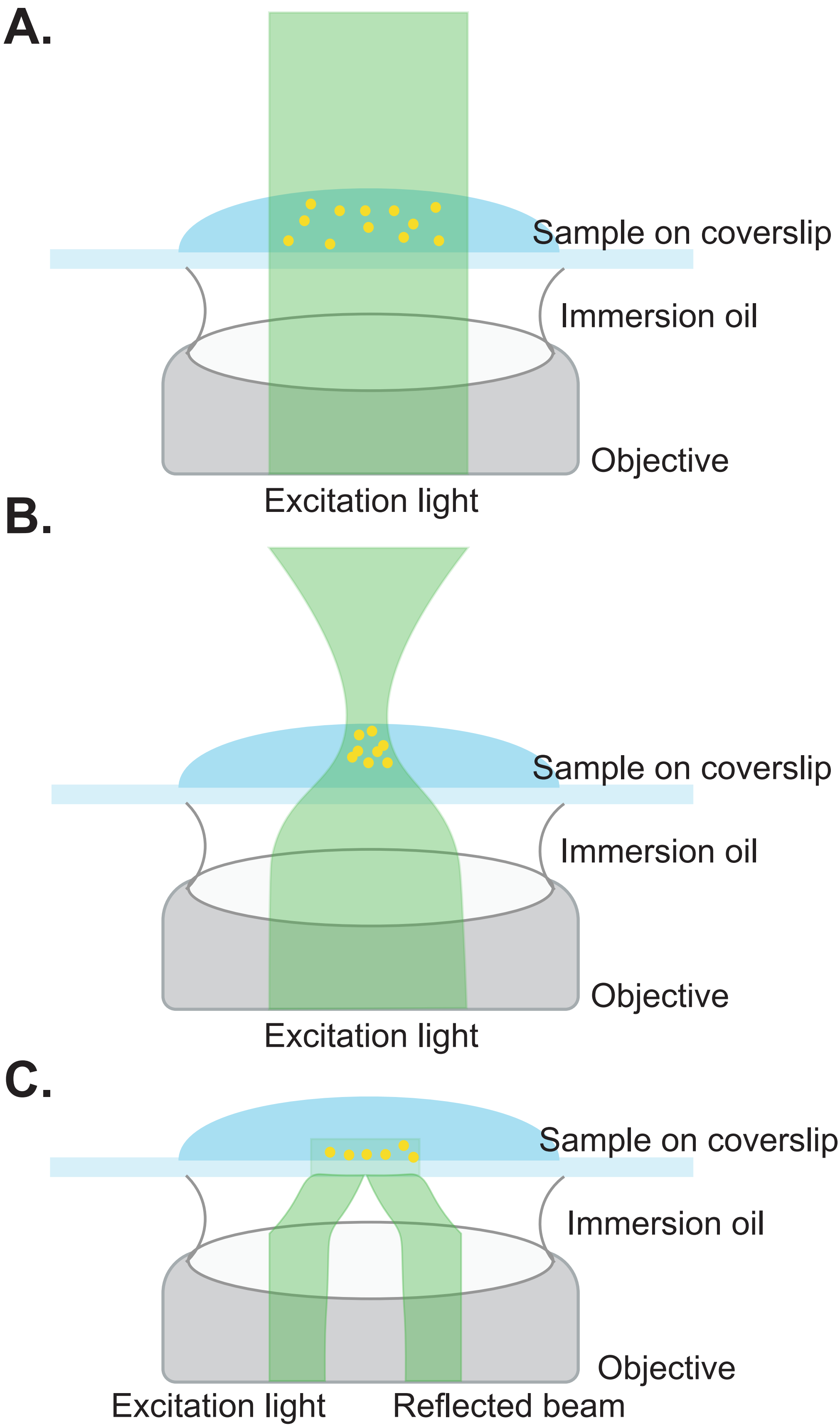
A.
Sample on coverslip
Immersion oil
Objective
Excitation light
B.
Sample on coverslip
Immersion oil
Objective
Excitation light
C.
Sample on coverslip
Immersion oil
Objective
Excitation light
Reflected beam

Figure 1.6.2: Three different illumination modes: widefield epifluorescence, confocal and TRIFM. A. Widefield illumination combined with epifluorescence detection. Excitation is directed uniformly at the sample, resulting in excitation of all fluorescent species. Emitted light is collected via the same path as excited light. B. Confocal microscopes use a pinhole in the detection beam to reject out-of-focus light and restrict the imaged volume to a small spot less than 1 μm in diameter. C. Total Internal Reflection directs the beam to the sample at an angle that creates an evanescent field at the sample-interface. The laser light does not penetrate the sample directly, and the illumination is limited to approximately 200 nm distance from the coverslip.

avalanche detector (SPAD). Most of these exploit the photoelectric effect, where photons generate electric charge. The electric charge can be translated into voltage values and read out to create an image. Most common types of cameras used in fluorescence microscopy include complementary metal oxide semiconductor (CMOS) and charge-coupled device (CCD) cameras. CMOS cameras are capable of capturing, translating and reading-out output for each pixel simultaneously, making them ideal for imaging fast events across a small number of frames. charge-coupled device (CCD) cameras, where the electrical signal for each pixel is first passed across an array of detectors and read back out to recreate the image, have design elements such as signal multiplication regions, which increase their sensitivity enable the detection of single photons.[113]

1.7 Imaging at the nanoscale

Whilst fluorescence microscopy can be applied to observe protein distribution across cells and distinguish features at sub-cellular level, in its routine applications it cannot capture fine detail of structures smaller than approximately 250 nm. Thus, the visualisation of the potentially toxic oligomeric species produced during α-syn aggregation is made difficult. These can be tracked or differentiated between using indirect approaches, but cannot be visualised in-detail until they reach mature aggregates under most fluorescence microscopes. Regardless of the optics employed, the small oligomers appear as bright “fuzzy” spots of approximately 200 nm. This is because of the physical resolution limit of any light microscope.

1.7.1 Diffraction limit of light

Light is an electromagnetic wave and it cannot be focused to an infinitely small spot. Instead it forms an Airy disk, a characteristic diffraction patter of approx. 200-250 nm wide (Figure 1.7.1A). This phenomenon is described as the diffraction limit of light. The smallest spot to which light can be focused can also be referred to as a point spread function (PSF). Its cross-section (Figure 1.7.1B) is characterised by an intense Gaussian peak surrounded by smaller concentric peaks coming from the rings of decreasing intensity. Because the PSF is not infinitely small, it means that molecules smaller than the PSF cannot be observed in detail. Moreover, the PSF affects the resolution of the microscope. The full-width half-maximum (FWHM) of the PSF is often used to compare the resolution of different microscopes (Figure 1.7.1B) and can be measured experimentally. More formally, the limit of resolution is defined as the smallest distance between two objects at which they can still be separated in space. The resolution is system-dependent and can be calculated using Abbe’s law (Equation 1.8).

$$Resolution = \frac{\lambda}{2 \times NA} \tag{1.8}$$

This equation relates the wavelength used for excitation (λ), and the numerical aperature (NA) of the system. When two molecules are far apart, their PSFs do not overlap and each molecule can be detected separately. As the distance between the two fluorophores decreases, their PSFs start to overlap. Figure 1.7.1C shows a hypothetical example of a limit-of-resolution distance where despite some overalp in PSFs, the two fluorophores can be localised as separate emitters (left-hand side). When the distance between them is smaller, their respective PSFs overlap significantly and the both molecules appear as one “blur” - making it impossible to tell them apart.

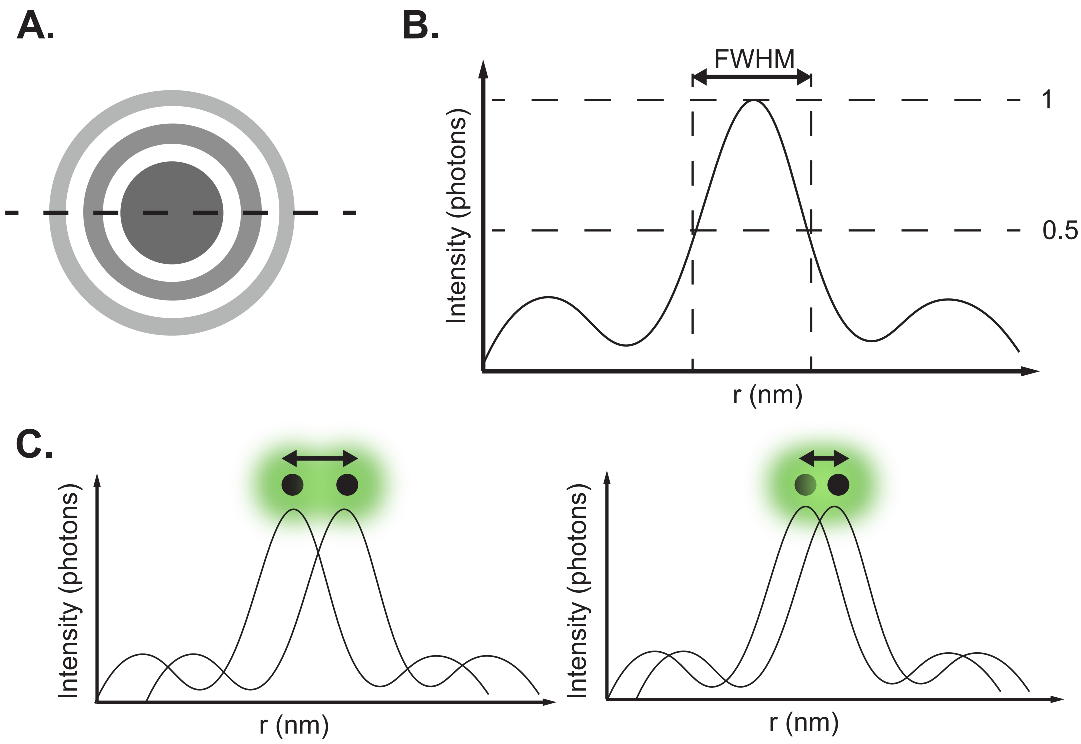

Figure 1.7.1: Diffraction limit of light. A. An airy disk pattern of a focused light beam, with a line profile through the middle. B. Intensity trace associated with the line profile - a characteristic Gaussian peak and the associated lower intensity peaks on both sides. FWHM method for resolution determination presented. C. PSFs of two emitters separated by a distance that allows for spatially resolving them (LHS) and does not allow to spatially differentiate between the two (RHS).

Since the resolution is dependent on the wavelength of incident light, using shorter wavelengths can lead to an increase in the resolution achieved. However, near UV excitation tends to cause more photodamage to the sample and introduce imaging artifacts. In addition, numerous intrinsic emitters are characterised by low λ_{abs}, increasing the likelihood of autofluorescence interfering with the desired fluorescence. The other component that can be changed is the NA, or the numerical aperture. The NA is system dependent and can be calculated using Equation 1.9,

$$NA = n \times sin(\alpha) \tag{1.9}$$

where n is the refractive index of the medium used between the objective and sample (water, immersion oil, air) and α refers to the angle of the light that can be collected by the objective lens. Chaning the objective lens can help increase resolution, however the maximum value of α is 90 °. Using a high refractive index medium like immersion oil (with an n of 1.5) can also increase the limit of resolution. There is a limit to the improvements to the resolving power of any microscope that can be introduced through these modifications, effectively capping the NA at around 1.5 and thus the achievable resolution at approximately 250 nm.

Despite these limitations, it is possible to break the diffraction limit and achieve an over 10-fold improvement in resolution using a broad range of super-resolution techniques that have been developed in recent years.

1.7.2 Super-resolution imaging

Super-resolution techniques cover a range of approaches that enable imaging with resolution higher than 250 nm. They can be broadly classified depending on the approach used.

The first group of super-resolution techniques rely on reshaping the PSF or other technical interventions that improve the overall resolution of the observed structures. These super-resolution techniques include stimulated emission depletion (STED) which introduces an additional laser source that depletes the emission of fluorescence molecules outside of the desired spot, constricting the PSF.[114,115] One of the main drawbacks of the technique is the use of laser irradiation outside of excitation, which leads to faster photobleaching. The wave-character of light is utilised by structured illumination microscopy (SIM), where a range of interference patters are placed in the illumination pathway to gain information about the sub-diffraction, high frequency, structures and reconstruct super-resolution images.[116] Expansion microscopy, on the other hand, artificially increases the size of the sample by embedding it in a gel matrix and subsequent swelling of the matrix.[117] These and other methods are discussed in detail by Huang *et al.*.[118]

Other super-resolution techniques rely on the ability to "localise" individual fluorophore molecules through temporally separating the emitters' fluorescence. These are broadly termed single molecule localisation microscopy (SMLM) techniques.[119] Instead of having all the fluorophores "on" at any given time, special buffers (stochastic optical reconstruction microscopy (STORM)) or illumination conditions (photoactivated localisation microscopy (PALM)) can result in the fluorophores going between the "on" and "dark" state and enabling single molecule detection. The centres of the PSFs can then be plotted and a super-resolution image can be re-constructed. Despite not requiring physical intervention within the imaging system, these methods require careful consideration of the fluorophores used and adjustments to be made to the imaging conditions to ensure faithful image reconstruction. A comprehensive review of these was conducted by Lelek *et al.*.[120]

One of the SMLM techniques, points accumulation for imaging in nanoscale topography (PAINT) has been used to characterise α-syn oligomers. Bongiovanni *et al.* employed Nile Red, a lipophilic dye that transiently binds to amyloid fibrils (non-specifically) to study and visualise oligomers produced in an *in vitro* aggregation reaction.[121] The transient nature of the binding allowed for separation of the emission events in time and reconstruction of super-resolution images with a high level of detail. The solvatochromatic properites of Nile Red were further exploited by them through recording the emission wavelength and thus tracking the hydrophobicity of the species throughout aggregation.[122]

1.8 Fluorescence Lifetime Imaging Microscopy in PD

Fluorescence lifetime is a highly sensitive parameter and can be used as a contrast method in Fluorescence Lifetime Imaging Microscopy (FLIM). Since the lifetime of some probes is highly dependent on their microenvironment, it can be expected to be heterogenous across the stained features. In fact, FLIM has been used to report on the pH, rigidity or viscosity of structures.[123,124] Unsurpisingly, FLIM has found applications in imaging of PD. However, the applications of FLIM to neurodegeneration are still few and far between compared to those of other fluorescence imaging techniques.

NADH autofluorescence properties and the fluorescence lifetime shift associated with the transition between free (cytosolic) and bound (protein-associated) transmitter is used to monitor mitochondrial metabolism.[125,126] Plotegher *et al.* measured the fluorescence lifetime of NADH in a HEK-cell aggregation model.[127] They used a cell line over-expressing α-syn on its own, further induced aggregation by seeding the cells with pre-formed fibrils (PFF), and used a WT HEK cell line as a control. They identified the fluorescence decays as free and bound NADH at a single pixel level and quantified the ratio of the free to bound species across the three conditions. They observed an increase in NADH lifetime upon α-syn over-expression, and hypothesised this was due to the production of toxic oligomeric species (invisible in confocal microscopy) that increased the oxidative stress and evoked mitochondrial damage.[128,129] Interestingly, the difference in the detected lifetime between the seeded cells and WT was less striking, suggesting possible sequestration of the toxic oligomers to form large fibrils (LB-like inclusions observed in confocal microscopy). Pokusa *et al.* carried on further studies and co-localised the NADH signal with α-syn aggregates[130] as detected by thioflavin-S (ThS), a variant of ThT. However, they relied on spectral un-mixing to deconvolute the ThS and NADH signal (both sharing the same excitation wavelength) and analysed the decays without determining the contributions of each of the dyes.

The lifetime of unlabelled and fluorescently-labelled α-syn has also been used to learn more about protein aggregation. Laine *et al.* demonstrated yellow fluorescent protein (YFP)-tagged α-syn could be tracked across the lifespan of a nematode species (*C. elegans*), used as a model organism for neurodegeneration. The decrease in the YFP lifetime value, corroborating the presence of highly ordered amyloid species, was only observed 10 days into adulthood when sizable inclusions were observed.[131] The method did not provide enough sensitivity to observe the formation of the oligomers, likely both due to size and their high levels of disorder. Klucken *et al.* used a tagged construct to decipher α-syn conformations, utilising a FRET interaction between the N-terminus (AF488-labelled) and the C-terminus (Cy3-labelled)[132] of the protein. They quantified the FRET based on the observed decrease in the AF488 lifetime, and postulated this corresponded to folded conformations of the protein, where the two termini are brought together close in space.

Some attempts at using FLIM for tissue imaging in PD include the reports by Klingsted, where oligothiophenes (non-specific amyloid detection) were used to image two synucleinopathies: PD and multiple system atrophy (MSA).[133] In separate experiments, they have shown the emission spectra and lifetimes of the dye differed across the two disorders, likely due to the different conformations of the aggregates formed in the two diseases. Since the change in emission was a subtle spectral shift (ratio of emission at two wavelengths rather than an extensive red-shift), it could not be monitored using the same set-up as fluorescence lifetime detection. Despite the promising trend observed, the study served as an illustrative example and would benefit from a larger sample size (n $>$ 3).

1.9 Peptides as a novel imaging modality

Most imaging modalities, except for small dyes e.g. ThT, rely on two components: a target moiety (either an antibody, or a chemical handle expressed endogenously) and an emitter (fluorophore with properties chosen for specific application). Peptides are still somewhat under-utilised as a targeting moiety, despite their desirable characteristics. This is likely due to small molecules historically dominating the therapeutic market and antibodies being the "go-to" biologic due to their high specificity.

Peptides present a number of advantages, and are a rapidly growing and promising therapeutic field. They can provide high specificity to otherwise undruggable targets, including broad protein-protein interaction (PPI) surfaces that lack pockets for traditional small molecule binding. Their natural amino acid composition means they can be easily degraded to naturally occuring components, reducing their toxicity and potential off-target effects of any metabolites. Robust technologies for manufacture and production ensure they can be prepared with high purity outside of cells. Peptides can also be easily conjugated to therapeutic agents, like radio-labelled ligands and fluorescent compounds, making them useful across many imaging techniques.[134–136]

The challenges associated with peptide applications are mostly a result of their size and include issues with cell permeability and crossing the blood brain barrier, and poor oral bioavailability. However, these are becoming increasingly well-understood and can be circumvented with appropriate structural modifications: incorporation of D-amino acids,[137] peptide staples,[138] and cyclised peptides,[139] to name a few.

In context of PD, there has been several peptides developed that are reported to interact with specific parts of the α-synuclein (α-syn) sequence.[140] Interestingly, these are explored almost exclusively as therapeutic targets, often inhibiting the early stage oligomeric species or α-syn monomer interactions.[141,142] Their simultaneous application as a diagnostic is often overlooked. This could be partly due to the potential loss of binding sensitivity upon conjugation to a fluorescent scaffold and partly due to limited techniques available for meaningful study. Between the heterogenity, small size and low abundance of α-syn aggregates, the probes could remain invisible to standard confocal microscopy approaches.

1.10 Thesis objectives

This thesis describes the development of a new imaging platform and a new imaging modality. It aims to advance FLIM as an imaging technique and its application to the field of neurodegeneration research. It is hypothesised that a novel approach to FLIM, where the intensity and lifetime are monitored across all wavelengths, could introduce further contrast in imaging and offer novel means of analysing fluorescence imaging. Moreover, the thesis proposes to introduce peptides as a versatile imaging modality and explore their potential for imaging of neurodegeneration and other super-resolution applications. Peptides offer specificity and binding dynamics that could be highly suitable for PAINT approaches. Fluorescently-labelling peptides for super-resolution imaging could provide a minimally-disruptive method for direct visualisation at the target of interest with high level of specificity and a high resolution.

1.10.1 Advancing FLIM imaging technologies

Currently FLIM instruments collect lifetime data across narrow colour-based channels and thus limit the amount of information about fluorescence available to the researchers. The first aim of this thesis is to increase the amount of information that can be extracted in a single fluorescence microscopy experiment. This is addressed through the construction and application of a novel instrument, the Full Spectrum Fluorescence Lifetime Imaging Microscope. The novel platform is effectively a 3-in-1 fluorescence lifetime microscope, capable of collecting fluorescence intensity and lifetime data across 512 discrete wavelengths, simultaneously.

The design, construction and validation of such an instrument is described in Chapter 3, together with example applications. The instrument is further employed to image patient-derived *post-mortem* tissue in Chapter 4 in a preliminary study, where the advantages of this approach are carefully considered.

1.10.2 Introducing peptides as versatile imaging modalities

Peptides have a potential to be excellent imaging agents. They are often developed as therapeutic agents for otherwise difficult-to-target proteins. Their binding to target-of-interest is specific and depends on the sequence of amino acids, making it "tunable". Rational substitutions of amino acids could lead to decreased or increased strength of interactions. Peptides can be efficiently prepared and are easily conjugated with various fluorophores, opening them up to applications across super-resolution and FLIM alike. Due to their relative ease of conjugation, peptides could address the issue of linkage error that plagues standard immunofluorescence staining methods. In most applications, a fluorophore is located on a secondary antibody, and a primary antibody is used to recognise the target. Assuming the size of a standard antibody is approximately 10 nm,[143] this places the fluorophore approximately 20 nm away from the target (10 nm for the primary antibody that detects the target and 10 nm for the secondary antibody that detects the primary and contains the fluorophore). Using a peptide that can be directly labelled decreases this distance significantly and enables researchers to observe the fluorophore directly at the molecule of interest.

To this end, the thesis firstly aims to introduce a novel dye into peptide sequences for a new generation of fluorogenic peptide probes. The properties of the fluorescent amino acid, developed by de Moliner et al.,[144] including its fluorogenic character and lifetime sensitivity are described.

The second aim is to demonstrate the potential of the new fluorogenic probes in different imaging applications. Through the incorporation of the amino acid into different peptide scaffolds, successful synthesis and purification, the peptides are further tested against their target. Potential for FLIM applications (Chapter 4) and super-resolution imaging (Chapter 5) are explored and the advantages of the new probes discussed.

Chapter 4 further focuses of an application of a therapeutic anti-α-syn sequence in a diagnostic application. The study focuses on validating the retained detection properties upon fluorescent labelling and attempts different fluorescence imaging techniques.

Chapters 5 and 6 describe a peptide-based approach to super-resolution imaging, with a focus on decreasing the size of super-resolution probes and laying groundwork for creating a versatile labelling approach.

It is hoped that the methods developed here could be further translated and applied to study neurodegeneration and characterise aggregates and disease protein conformations *in vitro* and *in situ*.

Chapter 2

Experimental

2.1 Scope of the chapter

This chapter describes general experimental methods used throughout the work and explains relevant techniques. Details of specific experiments are covered in the methods sections of each chapter.

2.2 General methods

Commercially available reagents were used where available and without further purification. For high-performance liquid chromatography (HPLC)-mass spectrometry (MS) analysis, a Waters Alliance 2695 separation module connected to a Waters PDA2996 photodiode array detector and a ZQ Micromass mass spectrometer (electrospray ionisation (ESI)-MS) with a Phenomenex column (C18, 5 μm, 4.6 $\times$ 150 mm) were used. Peptide purifications were performed in a semi-preparative Agilent HPLC consisting of a 1220 Infinity II autosampler and a 1260 Infinity II detector. Kinetex 150 $\times$ 21.2 mm (5 μm) C18 column was used, H_2O (0.1% HCOOH) and CH_3CN (0.1% HCOOH) were used as eluents and a flow rate of 8 mL/min. For MS analysis: high resolution mass spectrometry (HRMS), electrospray ionisation (ESI) positive, spectra were obtained with a Bruker ESI Micro-time of flight (TOF) mass spectrometer; and matrix-assisted laser desorption ionisation (MALDI) analysis was performed on a Bruker UltrafleXtreme MALDI

TOF-TOF mass spectrometer.

All microscopy was performed on 0.1 mm thickness 24 × 60 mm (631-0973, VWR) or 24 × 40 mm (631-0135, VWR) borosilicate glass coverslips. These were cleaned using an argon plasma cleaner (Zepto, Diener) for 30 min to remove any fluorescent residues for all super-resolution imaging applications. Frame-Seal slide chambers (9 × 9 mm^2, Biorad) were placed on the glass to create a well in which samples could be added.

The phosphate buffered saline (PBS) used throughout the work was prepared from tablets (10209252, Fischer Scientific). The buffer contained NaCl (8 g/L), KCl (0.2 g/L), Na_2HPO_4 (1.15 g/L) and KH_2HPO_4 (0.2 g/L). At 25 °C the pH of the buffer was 7.3 ± 0.2. Each tablet was reconstituted in MiliQ water to give 100 mL of buffer, as per manufacturer's instructions. The buffer was filtered through Whatman Anotop 0.02 μm filters (FIL2824, SLS) prior to use for super-resolution applications and 0.22 μm Millex syringe filters (SLGP033RS, Millipore) prior to FS-FLIM experiments.

The T50 buffer was prepared in-house and contained Tris-Cl (10 mM) and NaCl (50 mM), with the final pH of 8.0 ± 0.2. Same filtration regime was followed.

2.3 Peptide synthesis

2.3.1 Choice of resin

For the C-terminal amide-derivatised peptides, two kinds of resin were used:

- Rink Amide ProTide low loading (LL) resin (R002, CEM) - for the α-syn targeting peptides
- TentaGel R Rink amide (RAM) resin (R28902, RAPP polymere) - for 101A and 101B sequences

They both had a low loading capacity of 0.18 mmol/g, which made them suitable for synthesis of long peptide sequences.

For the unmodified free carboxylic acid peptides, 2-chlorotrityl polystyrene resin (549401, Sigma-Aldrich) was used. Its theoretical loading capacity was 0.4

- 1.0 mmol/g. The actual loading was calculated following an incorporation of the first amino acid. This was performed using 5 mL polystyrene syringes fitted with polyethylene porous discs over a suction manifold. The reaction scale was 0.05 mmol. A fluorenylmethoxycarbonyl (Fmoc) protected aa - Fmoc-aa-OH (1 eq.) and *N,N*-diisopropylethylamine (DIPEA) (10 eq.) in a minimal amount of dimethylformamide (DMF) for dissolution and resin swelling were applied to resin (0.084 g) and incubated on a shaker at r.t. for 20 minutes. Remaining active sites were capped with methanol for 10 minutes. The solution was drained and the resin was washed (4 x DMF, 4 x dichloromethane (DCM), 4 x DMF). Fmoc group was then cleaved (20% piperidine, three treatments of 1 min, 5 min and 5 min respectively). The cleavage solution was collected and its volume standardised to 25 mL. A sample for ultra violet visible spectroscopy (UV-vis) absorbance measurements was prepared (1:10 dilution of cleavage solution in DMF). The absorbance was measured on a nanodrop (Denovix) at $\lambda = 290$ nm three times. The average A value was used to calculate the actual loading following Equation 2.1:

$$f(\text{loading}) = \frac{A_{290} \times V \times DF}{\varepsilon_{290} \times l \times m} \tag{2.1}$$

where A_{290} was absorbance of sample at $\lambda = 290$ nm, V was total volume of solution collected, DF the dilution factor used in spectroscopic sample preparation, ε_{290} the extinction coefficient for Fmoc (5,700 $M^{-1}cm^{-1}$), l the path length and m the mass of resin used.

2.3.2 Peptide elongation

Automated microwave-assisted solid phase peptide synthesis (SPPS) was carried out in a Liberty Blue microwave peptide synthesizer (CEM). Manual synthesis was carried out in polystyrene syringes fitted with polyethylene porous discs over a suction manifold. Standard Fmoc/tBu based methods were used. A schematic cycle is presented in Figure 2.3.1. The cycle consists of 5 steps. The resin of choice is loaded with the first amino acid, either manually or on Liberty Blue. The Fmoc

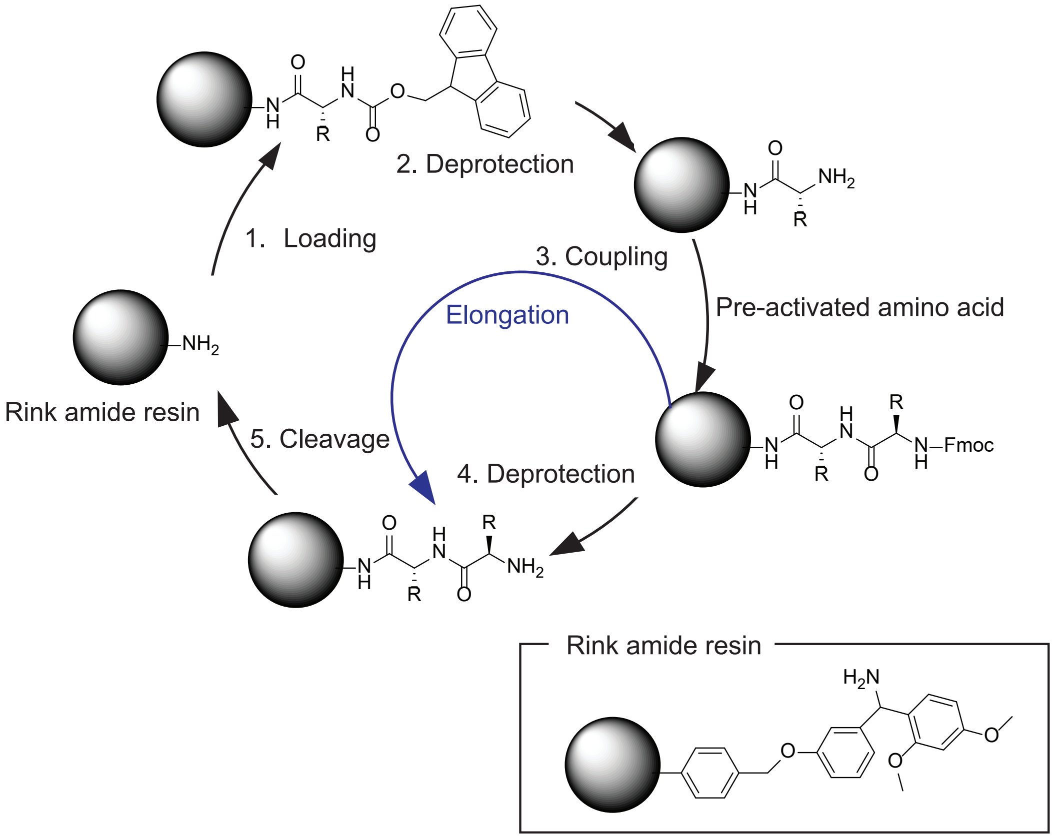

Figure 2.3.1: A schematic representation of an SPPS. Rink amide (full structure in the bottom corner, abbreviated throughout the figure) is loaded with the first amino acid, Fmoc-AA-OH. Fmoc is removed in a deprotection step to free up the reactive amine. A pre-activated amino acid is added (Fmoc-AA-O-Act) and a new peptide bond is made. Deprotection is needed to remove the Fmoc group. Peptide elongation continues in a series of couplings and deprotections until the full sequence is prepared and can be cleaved off the resin.

protecting group needs to be removed in a deprotection reaction (treatment with base) to free up the reactive amine. A pre-activated amino acid is then used in a coupling reaction. A wide range of coupling reagents is available. This amino acid (Fmoc-AA-O-Act) is set up with a leaving group in the pre-activation step and thus can readily react with the amine group. A new C-N bond is formed. The Fmoc protecting group needs to be removed before another coupling can take place. When the sequence is ready, cleavage step is performed. This cleaves the peptide off the solid support whilst removing all side chain protecting groups.

The concentrations of reagents were chosen to suit the reaction scale, following the manufacturer suggestions. For a 0.05 mmol reaction, the conditions chosen were as follows:

- Amino acid concentration: 0.2M in DMF
- Coupling using activator: 0.25M *N,N'*-diisopropylcarbodiimide (DIC) in DMF and activator base: 0.5M ethyl cyano(hydroxyimino)acetate (OxymaPure) in DMF
- Deprotection: 20% piperidine in DMF or 5% piperyzine with 0.1M OxymaPure in DMF (for R containing sequences only)

2.3.3 Microwave coupling of SeNBD amino acid to peptides

Two strategies were used to incorporate the NBD-derived amino acids into the sequences. Coupling was carried out either using Fmoc-AA-OH (1.2 eq.), Pyoxim (1.2 eq.), OxymaPure (1.2 eq.) and DIPEA (2.4 eq.) in DMF at r.t. across a course of 4 h, or using Fmoc-AA-OH (1.2 eq.), DIC (2 eq.), OxymaPure (2 eq.) and DIPEA (2.4 eq.) and a 10 min, 30 W, 90 °C microwave program on Liberty Blue.

2.3.4 Peptide capping

All peptides were capped at the N-terminus. Following complete synthesis of the full Fmoc-deprotected sequence on resin, the resin was washed (4x DMF, 4x DCM, 4x DMF) in preparation for acetylation. The peptide-containing resin was reacted with acetic anhydride (10 eq.) and DIPEA (10 eq.) in min. volume of DMF for 30 min at r.t. with shaking. The acetylation solution was then filtered off under suction.

2.3.5 Cleavage from resin & reconstitution

Cleavage was performed using trifluoroacetic acid (TFA) and scavengers - triisopropyl silane (TIS), and water (H_2O). A reducing agent, dithiothreitol (DTT), was added to methionine containing peptides to discourage oxidation under cleavage conditions. The duration of the cleavage reaction was modified according to the resin type:

- C-amide peptides were cleaved using 95% TFA, 2.5% TIS, 2.5% H_2O, 2.5% w/v DTT for 3 h
- C-carboxylic acid peptides were cleaved using 95% TFA, 2.5% TIS, 2.5% H_2O for 1 h

The filtrate was combined together with solvent used for resin washes (1x TFA, 2x DCM). The resulting solution was concentrated under reduced pressure. Peptide was reconstituted through slow addition of ice cold diethyl ether (Et_2O). The crashed out solid was further washed with diethyl ether and freeze-dried to remove any traces of solvent prior to purification.

All peptides were dissolved in dimethyl sulfoxide (DMSO) to give stock solutions that were further diluted and used for imaging applications (exceptions identified in the methods sections of respective chapters).

Where small amounts of peptide where obtained, the accurate mass for yield was back-calculated from the absorbance of the stock solution (A), and using the molar absorption coefficient (ε) for the dye, following the Beer-Lambert law (2.2).

$$A = c \times \varepsilon \times l \tag{2.2}$$

2.4 Microscopy methods

2.4.1 FS-FLIM

The FLIM optical diagram and set-up is discussed in detail in Chapter 3 (see Figures 3.4.1, 3.4.2). The microscope is a custom-built instrument, built by the author with the guidance of Dr Gareth Williams, Prof. Mathew Horrocks and Dr Hazel Stewart.

The instrument was aligned prior to every imaging session. The alignment of the FS-FLIM consisted of three parts. First, the alignment of the lasers to the fibre was checked. A power and energy meter console (Thorlabs, PM100D) was used to check the laser powers as the beam exited the collimator against recorded values. The dichroic and planar mirrors in each laser path were used to adjust the angle at which the beam entered the fibreoptic cable, until the power output was maximised. The illumination pathway was next aligned by ensuring a known sample (4 μm tetraspeck fluorescent spheres, Invitrogen, see Chapter 3 for details) was evenly illuminated. If the illumination was uneven and the beads appeared oval rather than spherical, the two mirrors of the periscope (prior to the microscope body) were used in combination to guide the beam into the objective. Lastly, the detector was also optimised using a green fluorescent slide (Thorlabs). The detector response, as observed in MatLab, was optimised using the translational stage through μm-scale movements to the board position in x, y and z. The fluorescent beads were then imaged to confirm board position and the part of the spectrum imaged (further details in Chapter 3).

2.4.2 TIRFM

The TIRF microscope used throughout the work was constructed by Dr Craig Leighton, Dr Alexandre Chappard, Dr Owen Kantelberg, Dr Katie Morris and Dr Zoe Gidden with guidance from Prof. Mathew Horrocks. It was previously described by de Moliner *et al.*[144]

The optical set-up is presented in Figure 2.4.1. Samples can be excited by the five laser sources present: 405 nm (MLD 405-250 Diode Laser System, Cobolt), 488 nm (06-MLD Diode Laser System, Cobolt), 515 nm (Fandango 300 DPSS Laser system, Cobolt), 561 nm (DPL 561-100 DPSS Laser System, Cobolt) and 638 nm (MLD 638-140 Diode Laser System, Cobolt). The laser beams were passed through excitation (band-pass) filters and attenuated by neutral density (ND) filters, before being circularly polarised to ensure uniform illumination by passing through quarter-wave plates. The beams were further expanded and collimated through a Galilean beam expander. The beams were then combined using a series of dichroic mirrors and planar mirrors. The beam was then directed through a Köhler lens to ensure even sample illumination. The beam was directed parallel to the optical axis at the edge of a 1.49 NA TIRF Objective (CFI Apochromat TIRF 60XC Oil) oil immersion lens, mounted on an inverted Nikon TI2 microscope. The microscope was fitted with a perfect focus system to auto-correct the z-stage drift during imaging. The fluorescence emitted from the sample was collected by the objective lens and separated from any stray laser light and the returning TIRF laser beam by a Di03-R405/488/561/635 dichroic mirror (Semrock) for the 405, 488, 561 and 638 nm imaging lines. A different dichroic mirror (Di02-R514-36, Semrock) was used for the 515 nm imaging line. The emitted fluorescence was then passed through an appropriate filter (488 nm: BLP01-488R, FF01-525/30; 515 nm: BPL01-561R, FF01-607/36; 561 nm: LP02-568RS, FF01-587/35; 638 nm: FF01-432/515/595/730, LP02-647RU - all Semrock) mounted on an automatic filter wheel. The fluorescence was passed through a 2.5x beam expander and recorded by an electron multiplying charge-coupled device (EMCCD) camera (Delta Evolve 512, Photometrics) operating in frame transfer mode (EMGain = 11.5 e-/ADU and 250 ADU/photon). All images were recorded using 50 ms exposure time. Each pixel was 103 nm in length. The image acquisition was automated using the open-source microscopy platform Micromanager (NIH, Bethesda).

The TIRFM was aligned prior to each imaging session and optimised using 100 nm TetraSpeck beads (Invitrogen). The beads were diluted into 0.02 μm filtered PBS at 1:100 ratio, before being placed on a glass coverslip and being placed on the microscope. The surface of the slide was then found with the help of the perfect focus system. White light imaging (no emission filters in the emission path) mode was used next and the Köhler lens was removed from the beam path. The 638 nm laser was steered using one of the mirrors immediately prior to the back aperture of the microscope, until the beam was perpendicular to the glass and the refractive ring pattern was observed on the camera. The ring pattern was used to centre the beam and adjust for even illumination. This was achieved using a combination of the two mirrors prior to the Köhler lens. Next, the remaining lasers were aligned in turn (561 nm, 488 nm, 405 nm) adjusting their refractive ring patterns through the use of dichroic and planar mirrors in the laser paths. The lasers were aligned to be on top of each other. 515 nm laser was

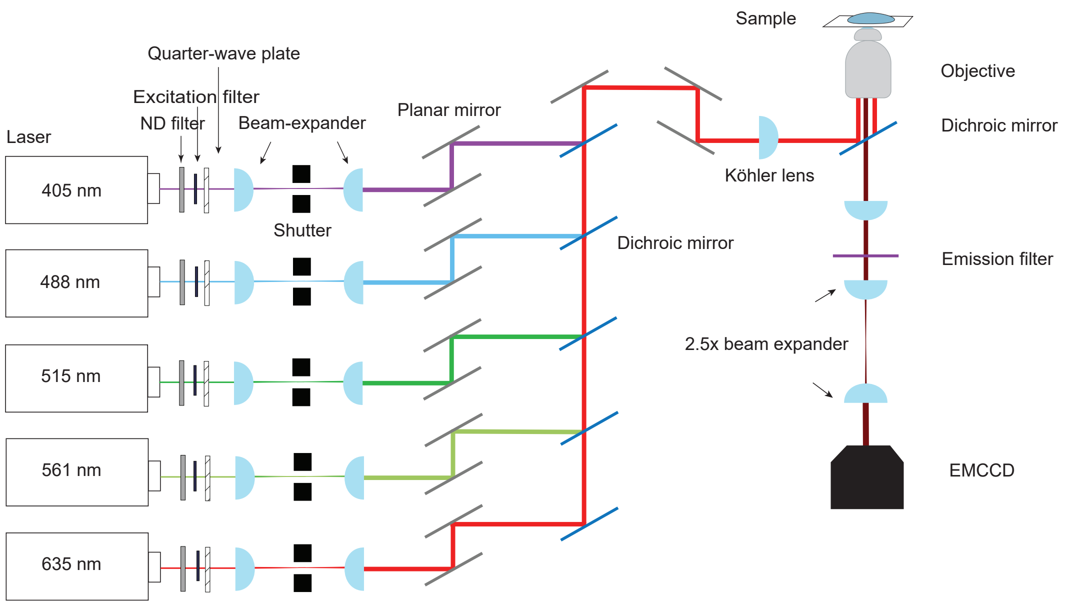

Figure 2.4.1: Diagram presenting the optical layout and light pathways of the TIRM.

always aligned last, with the microscope dichroic changed from the quad-band to the appropriate filter. The Köhler lens was then placed back into the optical path. Using the mirrors right before the lens, the 638 nm laser beam was steered through the objective and its angle adjusted until TIRF illumination was achieved. This was determined to be the point at which the signal to noise ratio within the beads image was highest, and a returning TIRF beam could be observed as a back-reflection on the mirrors. The illumination was then checked for all the channels through imaging the bead sample and adjusted using the individual laser lines, if necessary.

For cell imaging, a "dirty" TIRF angle was often used; the mirrors prior to the Köhler lens were used to adjust the illumination of the aligned microscope. This was done until the blinks in the cell were brought into focus and could be observed over the background.

2.4.3 Single-molecule confocal microscope

The single-molecule confocal microscope used in this work was a custom built instrument. It was built in-house by Dr Craig Leighton, Dr Alexandre Chappard, Dr Owen Kantelberg, Dr Katie Morris and Dr Zoe Gidden with guidance from Prof. Mathew Horrocks. It has been described previously by Chappard *et al.*.[145]

The set up is shown in Figure 2.4.2. Three laser beams 405 nm (LBX-405-100-CSB-OE, Oxxius), 488 nm (LBX-405-100-CSB-OE, Oxxius) and 638 nm (LBX-405-100-CSB-OE, Oxxius) serve as excitation sources. They were all combined using an Oxxius L6Cc laser combiner (Oxxius, France) and aligned spatially through a a 0.13 NA optical fiber (Thorlabs). The fibre output was collimated by a reflective collimator (RC08APC-P01, Thorlabs) and was directed, via two mirrors to allow for beam path adjustment, to the back port of an inverted microscope (Nikon Eclipse TE2000-U). A dichroic mirror (DI03-R405/488/561/635, Semrock) inside the microscope reflected the beam through an oil-immersion objective lens (Nikon CFI Plan Apochromat VC 100x Oil, NA 1.4, W.D 0.13 mm). Light was focused to a diffraction-limited confocal spot. The fluorescence emitted by the sample was collected by the same objective lens and passed through the same dichroic mirror. Next, it was focused through a 50 μm pinhole (Thorlabs) via a tube lens. At this point, the fluorescent light was separated using a second dichroic mirror (Omega Filters, 585DRLP). The longer wavelength passed through the dichroic to be focused by a lens (Thorlabs, Plano apoconvex, focal length 50 mm) through a filter set (long-pass LP02-647RU-25, band-pass FF01-432/515/595/730-25, Semrock) onto an avalanche photodiode detector (APD) (PerkinElmer). Shorter wavelengths were reflected from the 585DRLP dichroic and then focused through a different filter set (long-pass BLP01-488R-25, band-pass FF01-525/30-25, Semrock) onto a second APD. Output from the detectors was connected to a USB data acquisition card (Measurement Computing, USB-CTR04) which counted and combined the signals into 100 μs time bins. This was the expected residence time for molecules in the confocal volume. For the experiments presented in Chapter 6, the confocal volume was illuminated by the 488 nm laser with 1.2 mW irradiation at the backport.

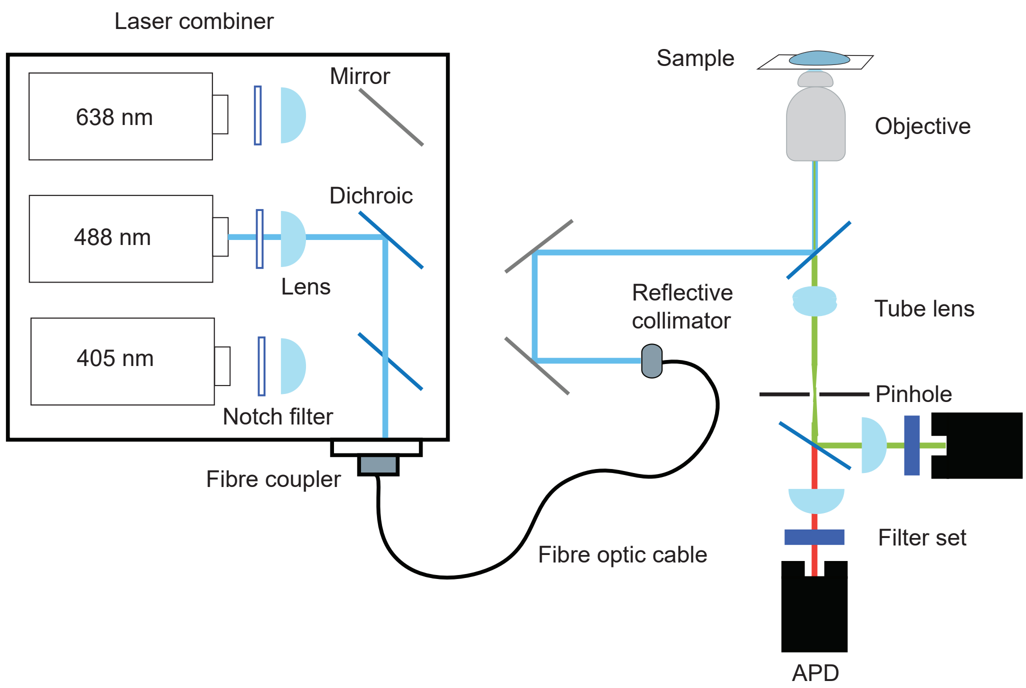

Figure 2.4.2: Set up of the SM confocal highlighting the beam path from laser source to sample, and the fluorescence emission path onto APDs.

To ensure sensitive detection of photons by the APDs, the microscope was aligned prior to every imaging session. The alignment was conducted with two laser beams (488 nm and 647 nm) at low laser powers (110 μW and 27 μW at the back-port) respectively. The alignment procedure followed two steps. Firstly, the excitation path of the lasers was adjusted using the two mirrors between the collimator and the microscope body. Even illumination at the centre of the optical axis was ensured by observing the back reflection of the laser beam off a glass slide on a CMOS camera (Thorlabs, DCC1545M). Secondly, the emission pathway was aligned to the two APDs. This was achieved using two complementary fluorescent-labelled oligonucleotides (prepared and purified by the supplier - ATDBio). The sequences (Table 2.1) were used to form a duplex through mixing of complementary strands and heat treatment (annealing performed by Dr Alexandre Chappard). A 5 nM solution of duplex DNA in 0.02 μm-filtered PBS was firstly imaged on a glass coverslip. The signal was adjusted by manual manipulation of the pinhole and APD positions to maximise fluorescent counts observed by both APDs in an iterative process. Once the signal was maximised, a 25 pM solution of duplex DNA was prepared in PBS supplemented with 0.01% Tween 20 (VWR, 437082Q). This was to minimise adsorption of the low concentration DNA onto surfaces. The sample was used to check the alignment of the two-channels and measured for 5 mins with a bin width of 0.1 ms. The output was analysed using custom-written Python code to determine the association quotient, or Q-value. This parameter compared the coincidence events to all events recorded in both channels, taking into account the chance coincidence. A Q-value > 0.180 was considered acceptable.

Table 2.1: Oligonucleotide sequences used for the alignment of the SM confocal microscope. The notation is 5' to 3' and dyes conjugated to the 5' end.

No	**Full sequence**
S1	AF488-TAGTGTAACTTAAGCCTAGGATAAGAGCCAGTAATCGGTA
S2	AF647-TACCGATTACTGGCTCTTATCCTAGGCTTAAGTTACACTA

Chapter 3

Full Spectrum Fluorescence Lifetime Microscopy

3.1 Scope of the chapter

Fluorescence lifetime imaging microscopy is an attractive technique for biomedical and diagnostic applications, however the advancements in FLIM have been dampened by technological limitations, such as the number of imaging channels available and the speed of data transfer (electronics). Williams *et al.* designed and published the details of a microscope able to collect fluorescence intensity and lifetime data at 512 different wavelengths simultaneously.[146] The capability to build lifetime histograms from binned photon data on-chip addresses the technological bottleneck of standard FLIM by diminishing the volume of data for transfer. This chapter covers the work in the design, implementation and performance optimisation of a home-built full spectrum fluorescence lifetime imaging microscope (FS-FLIM) and showcases the capabilities of the instrument.

3.2 Introduction

The scientific community has been trying to measure phosphorescence and fluorescence lifetimes since the mid-19th century. Early studies focused on phosphorescence emission (then known as "afterglow"), as fluorescence was believed to disappear immediately when the light source was removed.[147] With some phosphorescent materials emitting on the timescale of minutes and hours, the phosphorescence could be visually observed and measured with an instrument as simple as a clock. Phosphorescence emission on the order of <0.1 ns proved more challenging - stretching beyond the limit of most stop-watches, and thus requiring bespoke instrumentation.

The phosphoroscope, invented by Edmund Bacquerel in 1895, was the first piece of apparatus for phosphorescence lifetime measurements.[148] It employed two mechanically operated wheels, each with a single hole. In a dark drum a sample, such as a uranyl salt crystal used by Bacquerel, was placed between the two wheels. The wheels were positioned with the holes misaligned. The first wheel was used to deliver the light source to the sample, with the rotation of the drum creating intermittent pulses of light. The second wheel was used to view the light emitted from the sample. The speed of the rotation was varied, so that the light could be captured with each turn. When no light was visible through the emission hole, it suggested that the phosphorescence duration was shorter than a full turn (i.e. shorter than the time taken for the hole to return to its starting position). The speed of the drum limited the detection of phosphorescence emission and resulted in the phosphoroscope having a subsecond resolution (10^{-4} s). This set-up has not only further aided the discovery of radioactivity by Bacquerel's son,[149] but inspired a whole generation of commercial instruments: spectrophosphorimeters.[150] The phosphoroscope still shares similar design features with the lifetime instruments of the modern day, for instance the intermittent light source, offset emission and detection collection points, and photon timing mechanism for emitted light. However, the phosphoroscope was limited both in the detection and the generation of light pulses (with the same drum mechanism responsible for pulsing the light source). As such, the instrument was not able to record fluorescence lifetimes which were orders of magnitude shorter than the long phosophorescence. It was not until 30 years later, in 1926, when fluorescence decays were first accurately measured. The fluorescence lifetime of Rhodamine B and fluorescein salt uranine, was measured and published by Enrique Gaviola, the inventor of the first ever fluorometer.[151]

Since then, fluorescence lifetime has not only been used to characterise materials and probes *in vitro*, but has been used to provide additional contrast *in situ* through fluorescence lifetime imaging microscopy.

Today's FLIM technology relies on fast electronics and sensitive photon detectors. FLIM instruments run either in the time-domain or frequency-domain (Figure 3.2.1).[152] The time-domain FLIM uses a pulsed laser as an excitation source. It records the fluorescence decay data either directly (pulse sampling, photon gating) or with the help of time-resolved detectors, with the lifetime values generated directly from observing the decay kinetics (Figure 3.2.1A). In frequency-domain, a continuous light source can be employed. The amplitude of the sine wave of light is modulated over time and the fluorescence is recorded and compared with the original excitation wave. The fluorescence sine wave is distinct from the excitation light and exhibits changes both in the amplitude and phase value, as can be seen in Figure 3.2.1B. The phase delay and change in amplitude can be plotted against wave frequency to aid lifetime calculations. The two approaches both have their advantages. Frequency-domain FLIM is a more cost-friendly option (no need for pulsed lasers) and enables fast data acquisition, however it struggles with dim samples with low photon counts. The time-domain approaches allow for accurate lifetime estimates even with low photon count samples, and are excellent for complex systems where multiple components of a decay might need to be considered. The biggest limitation is dynamic samples. Time-domain FLIM suffers from an inherent property of the electronics called a "dead time", where most post-pulse photons cannot be captured. Thus, time-domain FLIM requires a long acquisition period to collect decay data overtime.

Since the advent of FLIM, the technique has been routinely applied to biomedical imaging. Using fluorescence lifetime, on top of the standard intensity data, enables one to distinguish spectrally similar fluorophores, allowing multiplex sample labelling. Lifetime values are broadly independent of the fluorophore concentration and the excitation source, making the measurements more robust (no need for calibration), and enabling the of study complex phenomena e.g.

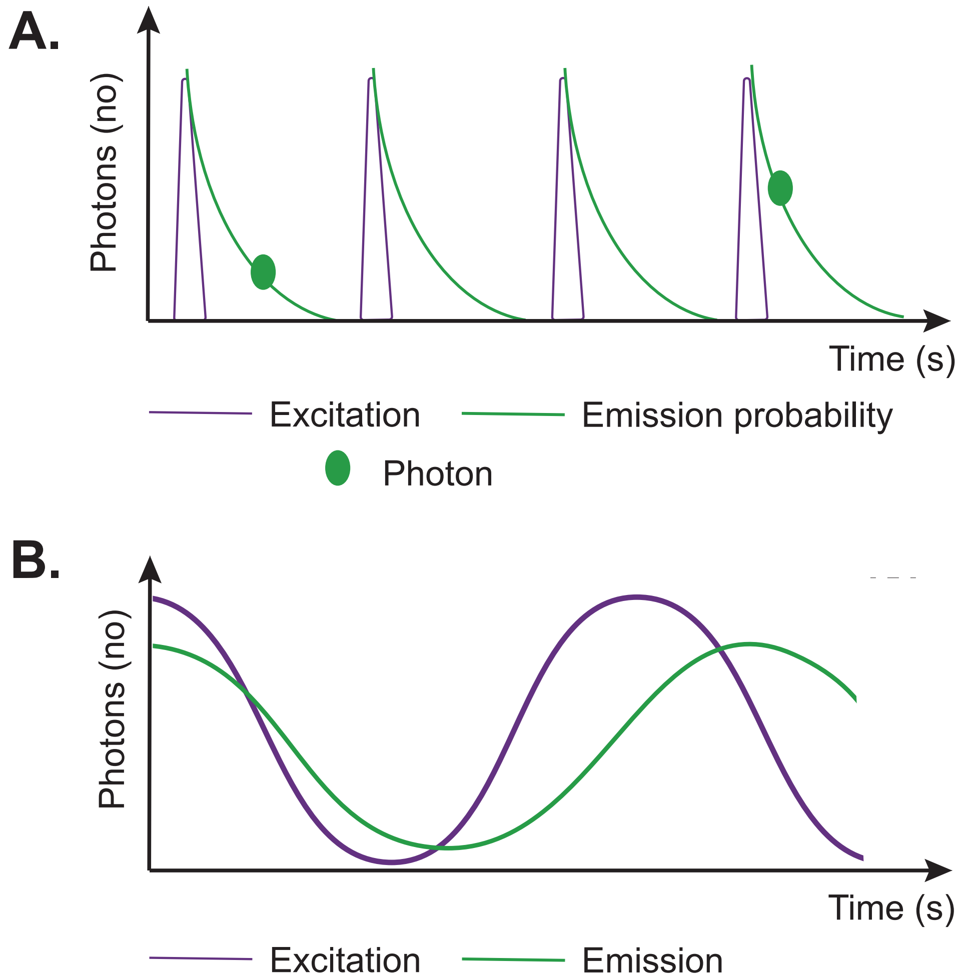

Figure 3.2.1: The two modes of FLIM. A. Time-domain FLIM. An excitation pulse is used to illuminate sample. Emission data is collected in from of fluorescence decay. Not every pulse leads to photon collection, thus multiple pulses are required to build up decay data and fit lifetime values. B. Frequency-domain FLIM. A continuous source of light is used. The excitation light is modulated to a sine function, the emitted fluorescence is also recorded as a sine function, it appears shifted from the excitation with difference in phase and amplitude.

quenching dynamics and FRET. Due to the sensitivity of fluorescence lifetime, the parameter can be used to detect the microenvironment of the emitter, thus providing extra contrast. Both endogenous and exogenous emitters have been applied to biomedical imaging. Endogenous emitters rely on autofluorescent compounds present throughout the tissue and lend themselves to clinical imaging. With applications spanning identification of infected or cancerous tissue[56] and detecting tumour margins for resection,[153] endogenous FLIM is an attractive avenue of research. Exogenous probes are also of interest since they can be designed to report on a characteristic of interest, and thus can be used to describe changes to and properties of biological systems. With the help of the right tools, FLIM can report on changes in temperature, pH or viscosity.[123,124] Exogenous FLIM has promising applications in pro-drug tracking[154] and ion trafficking visualisation[152] and reports on disease related changes to structure and homeostasis.

When looking at biological samples, complex fluorescence profiles are often expected due to autofluorescence competing with probe fluorescence or multiple environments and lifetime values for the probe across structure. Lifetime and emission shifts are even more important to understand but also more complicated to record. Subtle changes in lifetime and wavelength have been difficult to capture with the state-of-the-art technology.[155,156] Long data acquisition has limited the applications of FLIM to non-dynamic systems. Existing technology that provides spectrally-resolved data (Leica Stellaris) relies on sequential image capture (prolonging the acquisition time required further) and can only provide fluorescence lifetimes acquired and averaged across broad spectral ranges. The volume of data collected in FLIM measurements has also been a bottleneck, as electronics able to cope with gigabytes of data with fast data transfer speeds are necessary. Thus, in order to exploit FLIM to its full potential, there is a need for new technology to address the need for fast and sensitive instrumentation.

3.3 Methods

3.3.1 Optical set-up

The system is described in section 3.4.1, and shown in Figures 3.4.1, 3.4.2 in detail there.

Briefly, the system uses 5 laser lines: 405 nm, 440 nm, 470 nm, 560 nm, 635 nm (PicoQuant, Germany), with a pulse duration < 100 ps and a repetition rate of 40 MHz and an average power of ~ 2 mW, managed using Sepia II PicoQuant software. The lasers beams were combined using dichroic mirrors (Brightline, Laser2000: Di02-R405, Di02-R442, Di02-R488, Di02-R561, Di02-R635). The laser beams were all coupled to a single mode fibre (P1-460B-FC, Thorlabs) and collimated using a 2 mm collimator (RC02-FC-P01, Thorlabs). The laser beam was then guided onto the galvanometric mirror (GVS202, Thorlabs), and scanned in the x-direction. Two 50 mm diameter 300 mm radius-of-curvature mirrors (CM508-150-E02, Thorlabs) and a 25 mm diameter plane mirror (BB1-E02, Thorlabs) were used to re-image the beam onto the second scanning galvanometric mirror. Subsequently, another set of curved mirrors was used to re-image the beam: a 50.8 mm diameter 200 mm focal length spherical mirror (CM508-200-E02) and a 75 mm diameter 500 mm focal length spherical mirror (CM750-500-E02) and fold mirror. The second set of spherical mirrors introduced a magnification of 2.5 times to fill the back aperture of the objective. The objective used was a 60 x 0.5 NA water objective (Olympus). All optics used were standard silica mirrors with dielectric coating (Fused Silica Broadband Dielectric Mirrors, BB1 series, Thorlabs), for a reflective achromatic light path. The light emitted from the samples followed the same pathway and was separated from the laser light at a filter wheel, containing 5 filters (Shemrock, Laser 2000: 405 Long Pass, 480 LP, 561 LP and 635 LP as well as a 4-band dichroic Di01-R405/488/561/635) for the different laser lines and applications. The light was then passed through a 10 x 0.25 NA plan fluorite objective (Olympus), and collimated via an achromatic doublet lens (focal length 60 mm - ThorLabs AC508-075-344 A), directed onto a transmissive holographic grating with 600 lines / mm (Wasatch Photonics

WP-600/600-345 50.8), followed by focusing through a second achromatic doublet (focal length 60 mm - ThorLabs AC508-346 075-A) to produce a line on the sensor matched to the sensor pixel height of 95.12 μm. The sensor is part of a RaII board, mounted on a three-axis translation stage (PT3A/M, Thorlabs).

3.3.2 Sample preparation

Dye solutions

Phosphate buffered saline solution was made up from PBS tablets (ThermoFisher Scientific) according to manufacturer's instructions and filtered through 0.22 μm syringe filter (Millex, Millipore). Ultrapure water (MiliQ grade) was used for all experiment unless stated otherwise. Fluorescein (Sigma-Aldrich) solutions for imaging were prepared from an ethanol stock. Rhodamine 6G (Sigma-Aldrich) was diluted in methanol and sulforhodamine B (Invitrogen) directly into water. All dilutions were prepared prior to imaging. Aliquots of 50 μL of each dye solution were applied to a FluoroDish (Fluorodish 35mm, 10 mm glass well, WPI) for imaging. Glycerol (Sigma-Aldrich) was mixed with water by weight to prepare the 0, 20, 40, 60, 80 and 100 % (w/w) solutions. Sulforhodamine B was diluted into those solvent mixtures directly from the aqueous stock solution.

TetraSpeck Microspheres

TetraSpeck Microspheres (4.0 μm, ThermoFischer) were diluted 1:100 in distilled water. 20 μL of the solution was applied to a borosilicate coverslip (22 x 60 mm, thickness no. 1, VWR) equipped with a Frame-Seal sticker (9 x 9 mm, Biorad). The sample was sealed with a smaller coverslip (20 x 20 mm, thickness no. 1, VWR) and stored for repeated imaging.

Grid dish

Fluorescein (50 μL, 5 μM ethanol solution) was placed in μ-Dish 35 mm, high Glass Bottom Grid-50 (Ibidi) for the grid imaging.

3.3.3 Sample imaging

TetraSpeck Microspheres were imaged on the FS-FLIM with histogramming mode 3 (see 3.4.2) and 3000 μs exposure of the 405nm laser. The dichroic mirror used was a 405 nm long pass filter, or later on the quad-band mirror.

Fluorescein, R6G and SRB solutions were imaged on FS-FLIM, all using 470 nm excitation laser, and a 480 nm long pass filter mirror. R6G solution (1.25 μM, methanol) and fluorescein (1 μM, PBS) were imaged over 1000 μs, using hist mode 3. SRB solution (20 μM, water and water:glycerol mixtures) was imaged using 2000 μs exposure, and hist mode 2.

The grid images were acquired with the 470 nm excitation and 480 nm long pass filter, in hist mode 3, with a short exposure of 1000 μs.

3.3.4 Data processing

Initial data processing, including lifetime calculations was done in MatLab. The scripts used were developed and published by Williams *et al.* for the original iteration of the "KronoScan".[146] They were later modified to ensure compatibility with long lifetime (histogramming modes 6 & 7) and the versions used in this work can be accessed online (Dropbox folder).

- **Fitting the decay curves**

  Least-squares fitting analysis was performed to calculate lifetime values. The parameters for the decay fit were chosen using the "hyperspectral" script (DOI: 10.5281/zenodo.13858118). Once the image was loaded into MatLab, the "datapoint" tool was used to pick one of the brightest pixels in the image. A bright pixel, especially one that is a part of the feature of interest on the image, was chosen to ensure high counts and maximise the accuracy of the fit. The decay data was used to select bins for fitting and the count threshold value above which a lifetime calculation was attempted. The bins selected were always the top of the peak as bin 1, and a bin about 2/3rd down the peak as bin 2. On average the distance between bin 1 and bin 2, chosen for the decay fit, covered 4 bins.

- **Generating lifetime values from data cubes**

  The “Analysis” script (DOI: 10.5281/zenodo.13858118) was then subsequently used to generate the lifetime values. The parameters chosen were in-put into the code, and a least squares fit algorithm applied to each decay using GPUfit function in MatLab.

  The output of this analysis consists of two matrices:

  - An intensity data set - where each image pixel is associated with an intensity value (which is a sum of all intensities collected for that spectral pixel) usually forming a 256 x 256 x 512 matrix.
  - A lifetime data set - where each image pixel is associated with a lifetime value (in ns), forming a matrix of the same dimensions

  The MatLab output also allows access to images for specified wavelength (e.g. every 20 or 50 nm) both as intensity and lifetime maps and histograms of lifetime values across the whole image at those wavelengths. This, however, has not been used extensively, as custom Python scripts were developed to further handle the analytical challenges of the data.

- **Confirming sensor position**

  To determine the exact board positions TetraSpeck microscopheres were imaged (for rationale see Section 3.4.5). The TetraSpeck beads slide was imaged at the start of every imaging session, using 405 or 488 illumination with hist mode 3 and an exposure time of 2000 μs. After MatLab processing (threshold = 300, bin 1 = 13, bin 2 = 10) as described in the sections above, the images were analysed using the “find local maxima” script (DOI: 10.5281/zenodo.13858130). The workflow is presented in Figure 3.3.1.

  MatLab datacubes were read into Python, and two example images opened in a Napari GUI. The “labels” function was used to colour in the pixels containing the beads, creating an image mask. The labels were then read into MatLab, and the intensity spectrum across the chosen pixels generated. A find maxima function was then defined and used to find local maxima off

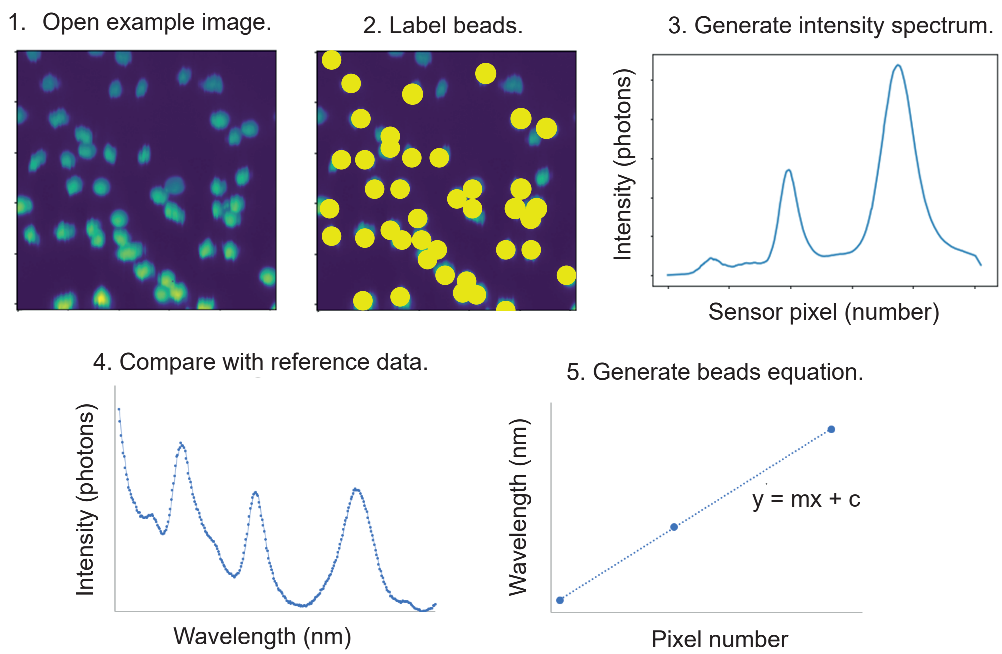

Figure 3.3.1: Determination of the sensor position and board equation calculation. A schematic representation of the workflow. An example image was generated from the data cube. The pixels corresponding to beads were labelled using Napari. Their coordinates were imported to Python and an average intensity spectrum for those pixels was generated. The peak positions were recorded. The data was compared to a pre-recorded reference bead data set. A straight line equation was fitted between the sensor pixel number and the wavelengths of the peaks observed. The equation was used in further analysis.

the graph, determining the x-coordinates of all fluorescence peaks (in sensor pixels). The extracted coordinates (usually three, at most four when the board was positioned in the blue region) were compared to the corresponding emission peaks (x-coordinates, wavelength) from the reference beads data (Table 3.1, data from Bongiovanni *et al.*[121]). The best fit linear equation was then found. The "board equation" (y = mx + c) was then used in further analysis and use to convert every sensor pixel (x) into a corresponding wavelength (y). Parameter m corresponded to the first wavelength recorded by the sensor in that position.

Table 3.1: TeatraSpeck beads and their four emission peaks as cited by the manufacturer and measured experimentally.

Fluorophore colour	**Wavelength cited (nm)**	**Wavelength measured (nm)**
Blue	430	N/A
Green	515	512
Orange	580	582
Dark red	680	675

- **Generating lifetime images**

  Further image post-processing was done in Python. The exact operations varied between data sets, but the basic workflow for measurements and imaging followed the steps outlined below.

  For solution measurements, .mat files were first read into Python. Matplotlib was used to generate all plots and numpy for basic calculations. The intensities were summed across the spectrum (to show an image, intensity summed across all wavelengths) and across image (to generate an intensity vs wavelength and identify peaks). Lifetime (averaged across image) was plotted against wavelengths and then averaged across the intensity peak to generate the average lifetime value for each of the dyes analysed. The full script can be accessed at DOI: 10.5281/zenodo.13858272.

For image processing, the workflow was similar: .mat files were read into Python, and intensities summed across the 512 channels to output a single 256 x 256 intensity image. The intensity spectrum was generated next, summed 256 x 256 image pixels across the 512 spectral channels. A threshold (manual or otherwise) was applied to help distinguish features of interest, and a thresholded image generated by applying a binary mask and multiplying the intensity image by it. Any sub-zero lifetime values (potentially due to noise in experiments or errors in fitting) were discarded, and the thresholded image was used to generate a lifetime image, 256 x 256. The intensity image was normalised and applied as an alpha mask to the lifetime image to make the lifetime images appear less flat. Histograms of lifetimes across pixels (or pixels of interest) were then plotted to observe lifetime distribution. The script used for this can be accessed at DOI: 10.5281/zenodo.13858274.

3.4 Results

3.4.1 Construction of the full spectrum fluorescence lifetime imaging microscope

The full spectrum fluorescence lifetime imaging microscope (FS-FLIM) was designed and custom-built for this project. The design followed the one described and published by Williams *et al.*.[146]

The system (as photographed and shown in Figure 3.4.1A) was based a confocal scanning microscope and employed a state-of-the-art sensor[157] for photon detection. It is capable of recording fluorescence intensity and lifetime information across 512 different wavelengths, simultaneously. The microscope was equipped with 5 lasers lines to excite and image across a wide range of biological samples. The microscope was operated using a custom-written graphical user interface (GUI) (Matlab, developed by Dr Gareth Williams and modified with his assistance). All the optics were arranged around an Olympus IX70 microscope body for ease of operation. The Olympus microscope body was also equipped with an automated stage (Tango, Märzhäuser Wetzlar), that was integrated into the GUI operable through the interface.

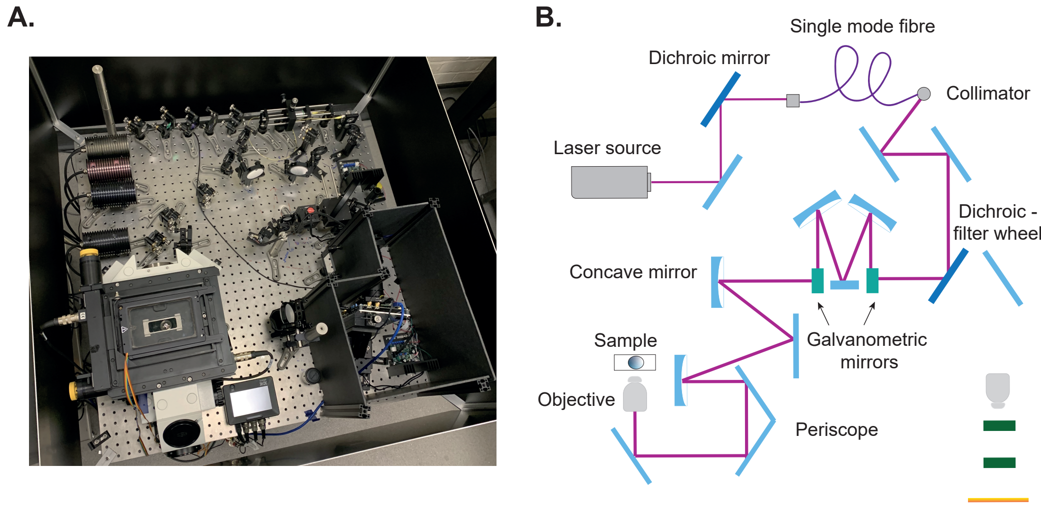

Figure 3.4.1: A. The FS-FLIM as seen from above. Light from laser is reflected by excitation optics all the way towards the sample. The mirrors guide the beam across the table, and the persicope feeds the light into the objective inside the microscope body. The black enclosure houses all detection optics. The sensor is mounted on the board, which also provides connections to the PC, laser modules and mirror drivers. Photographed in December 2021. B. A schematic representation of the excitation pathway of the microscope. Only one laser head and laser beam presented for clarity. The optics highlighted reflect light from laser source towards sample objective, and include mirrors, dichroics, concave mirrors and galvos. The galvanometric mirrors are scanning mirrors that define the confocal volume of the scan and thus the area of the sample illuminated.

Excitation pathway

5 different pulsed laser lines were implemented to excite a range of fluorophores across the spectrum. Using discrete laser lines rather than a super-continuum laser, as was done in the original version of the microscope, ensured the near-UV (405nm) region could be accessed easily for imaging a wider range of fluorophores. All the optics in the excitation pathway (and almost all the optics used in the system) are reflective mirrors. As the system was designed to enable simultaneous multi-channel imaging and collect emission data across the whole visible spectrum, it was important that light of different wavelengths was focused down to the same

point. Using transmissive optics often leads to the focus being shifted for different wavelengths, a phenomenon described as chromatic aberration. The use of mirrors with reflective dielectric coating ensured the system remained achromatic.

The excitation pathway of the microscope is presented in Figure 3.4.1B. The laser beam was reflected off a mirror before reaching a dichroic mirror. The dichroics were used to reflect and combine the beams from different laser sources. The small size of the laser beams meant that the beam needed to be expanded to fit the scanning optics. To improve system performance and ensure operational safety (avoiding an additional periscope) a single mode fibre and a 2 mm collimator, as can be seen in Figure 3.4.1B, were used. Coupling all the lasers to a single-mode fibre improved the beam shape (from diffuse ellipsoid consisting of multiple light modes to a tight circle characteristic of single-mode light) and sample illumination, as well as ensured all lasers were spatially aligned.

The laser beam was then reflected off a second dichroic mirror (this time a choice of a dichroic from a filter wheel, further discussed in the Emission Pathway section) and guided onto the first of the two galvanometric mirrors. The first galvanometric mirror scanned the beam in the x-direction. Two 50 mm diameter 300 mm radius-of-curvature mirrors (CM508-150-E02, Thorlabs) and a planar mirror (25 mm diameter plane mirror, BB1-E02, Thorlabs) were used to re-image the beam onto the second scanning galvanometric mirror. The spherical optics needed to be positioned carefully to ensure the reflected light was collimated at this point. The second galvanometric mirror scanned the beam in the y-direction. The scan area was defined by the mirror scan width. A narrower scan corresponded to an image of a smaller area of the sample, and a broader scan provided an image of a larger area of the sample. The limitation on the scan width came from the optics used. The planar mirror (between the galvanometric mirrors) had a diameter of 25 mm, and thus could only fit a beam scanning across 25 mm.

Subsequently, another set of curved mirrors was used to re-image the scanning beam: a 50.8 mm diameter 200 mm focal length spherical mirror and a 75 mm diameter 500 mm focal length spherical mirror separated by a plane mirror. This introduced an additional magnification to of 2.5 times to fill the back aperture of the objective. A periscope was then used to elevate the beam. A custom 3D printed holder houses the final mirror inside the microscope body and directly below the objective. The objective used routinely throughout this work was a 60 $\times$ 0.5 NA water objective, though other objectives could be used on the objective turret wheel.

Emission pathway

The fluorescence from the sample initially followed the same path, as can be seen in Figure 3.4.2. The light was reflected off the periscope mirror and guided towards the galvanometic mirrors. There, the beam was de-scanned. The light was passed through a dichroic mirror, where the laser light was separated from the fluorescence. The dichroic was chosen to suit each experiment out of a set of mirrors in the filter wheel, where the options included single-band dichroic mirrors and a quad-band dichroic mirror for multi-colour imaging. The laser light was reflected, whilst the fluorescence from sample was passed through and reflected off a mirror through a 10 $\times$ 0.25 NA plan fluorite objective. It was important to check for collimation of the incoming light at the mirror and the correct position of the objective to avoid beam clipping. From the objective, the fluorescence was directed through an achromatic doublet lens (focal length 60 mm), then onto a transmissive holographic grating with 600 lines / mm (the choice of the grating dictating the spectral resolution achievable), followed by focusing through a second achromatic doublet lens (focal length 60 mm). All the optics that followed the objective were considered part of the detection pathway (spectrophotometer) and boxed-in to minimise light from sources other than the sample. The detection optics had a two-fold function of changing the shape of the light beam, from circular to a thin rectangular line (thus matching the shape of the sensor), and to split the white light into its component wavelengths (thus ensuring detection of light of multiple wavelengths by the sensor). The line of light on the sensor was matched to the sensor pixel height of 95.12 μm.

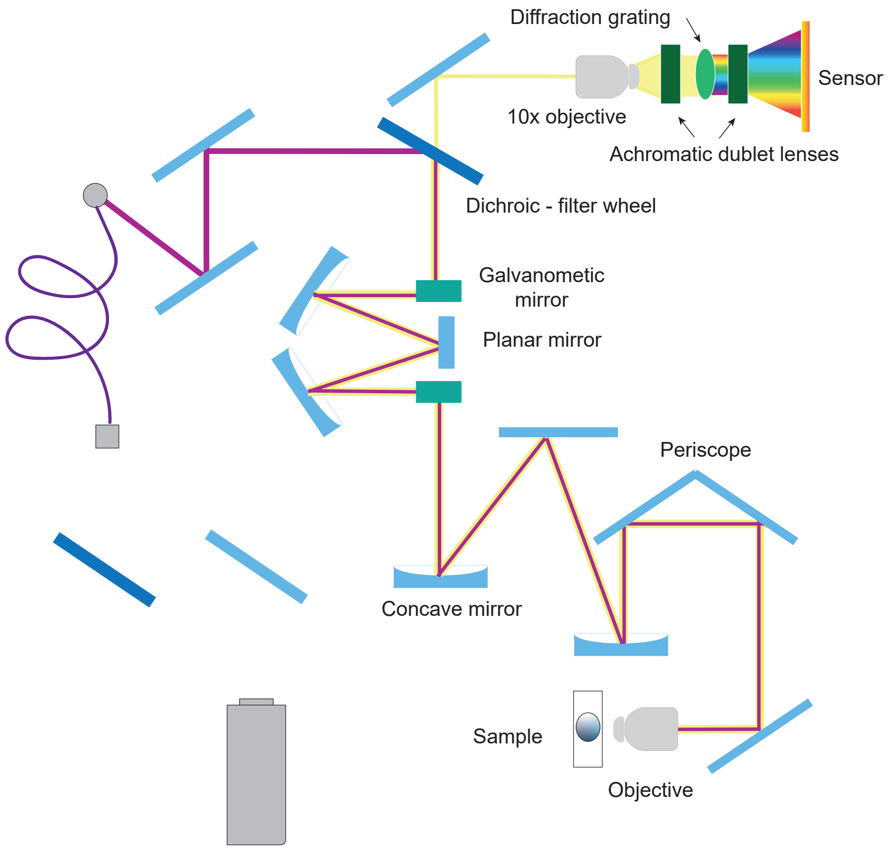

Figure 3.4.2: A schematic representation of the emission pathway of the microscope. The optics highlighted guide the fluorescence coming from the sample towards the detectors. The light was de-scanned at the galvanometric mirrors and passed through a dichroic filter. The dichroic was used to separate the laser light. The fluorescence from sample was further collimated by a 10 $\times$ objective. The beam of light was flattened by two achromatic doublet lenses and split into the component wavelengths by a diffraction grating. This was then detected by the custom sensor.

Light detection & microscope board

The sensor was mounted to an electronics board, so called Ra II, and its position is shown in Figure 3.4.3A. The sensor is a 512-channel time correlated single photon counting (TCSPC) device. TCSPCs rely on a fast-watch technology to time stamp photons arriving at the sensor. With the fluorescence split into its composite wavelengths by the diffraction grating (white arrow in Figure 3.4.3A), the time-stamping happened simultaneously across the spectrum in each of the 512 channels.

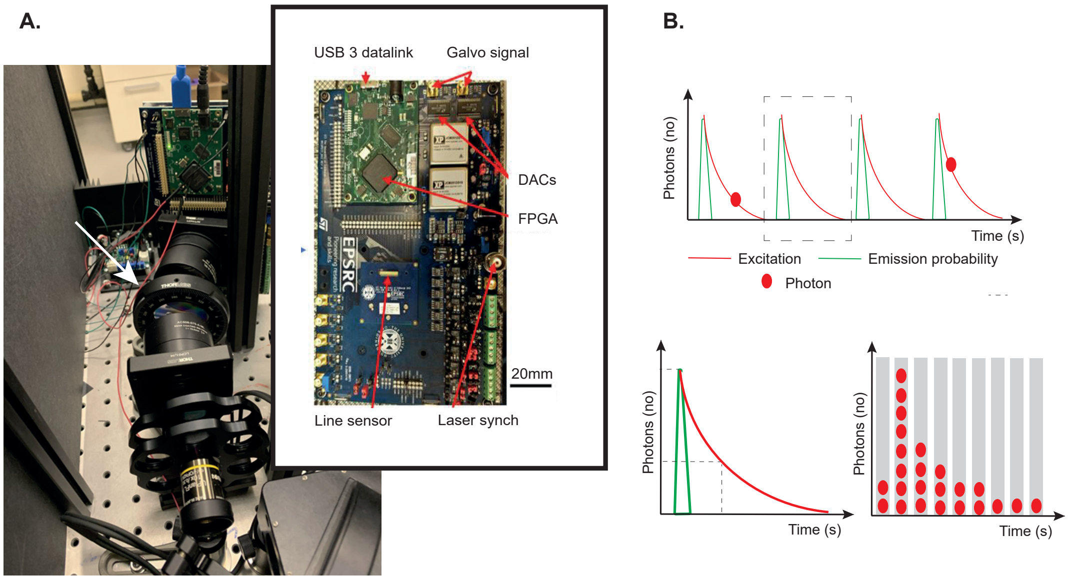

Figure 3.4.3: A. The detector optics, with the diffraction grating highlighted by the white arrow. The close-up shows the microscope board and the important electronics - the sensor, connections to PC, laser driver and galvos, DACs and FPGA. B. Principle of detection at sensor. Each laser pulse can excite a fluorophore and lead to emission of photon. Multiple pulses are necessary to build up a true picture of the fluorescence decay. The probability of emission at any given time decreases with time. The photons are detected in time bins (grey areas on the time axis), and can be fitted with an exponential function to illustrate the fluorescence intensity decay over time.

Each spectral channel consists of 16 SPAD detectors, spaced in two columns of eight (total of 16 “red” and 16“blue” SPADs with sensitivities tuned to the red or blue portion of the spectrum). The combination of SPADs used for detection was chosen in a way that minimises background counts. The SPADs are extremely sensitive to optical signal, as even a single photon causes a high and narrow voltage spike. The sensitivity and fast response make the detector capable of discerning photons arriving within tens of picoseconds of each other. The time of arrival is defined as time between the excitation photon being released (the laser pulse) and the excitation photon arriving at sensor (photon detection). This value can be converted to a voltage and thus recorded, time-to-digital conversion (TDC), by the chip. The board was connected to the laser drivers to synchronise the pulses. The chip was placed on a singular printed circuit board (PCB), instead of a more complex system, omitting the need for any delay lines and enhancing data acquisition speed. The other elements of the board included field programmable gate array (FPGA) which controls the sensor and oversees data acquisition and two sets of digital to analogue converter (DAC), which control the scanning galvanometic mirrors. A detailed description of the sensor and the associated TCSPC capabilites can be found in Erdogan *et al.*.[157]

Arriving photons were recorded after every excitation pulse (Figure 3.4.3B) in each spectral channel. The number of photons detected builds up over the exposure time, with most photons arriving right after the laser pulse and the number steadily dropping off with time. The time-stamped photon data is usually binned and further used to make a histogram. Whilst this is done post-acquisition in most cases, the new sensor technology introduced here enabled "on-chip" histogramming in each spectral channel. This reduced the volume of data usually associated with TCSPC, and enabled greater photon processing throughput, leading to an increased signal-to-noise ratio. Thus, lifetime data could be collected at lower laser powers and shorter exposure times, which is especially advantageous for applications such as live cell imaging.

The board was mounted on a translation stage enabling movement across 250 μm range in each of the three directions. The stage position was adjusted to ensure the light was fully collimated (thin line) at the sensor through Z translation. Y translation enabled fine adjustments to the height of the sensor above the breadboard. However, its most significant advantage was making the system tuneable. With the diffraction grating used here, a spectral resolution of around 0.50 nm was achieved. A different grating would lead to a different spectral resolution, with other gratings available to access and record Raman data also. The sensor is capable of detecting light between 400 - 900 nm, but the exact range of detection could be changed through adjusting the position of the board. With the help of the translation stage (X axis), the most appropriate 250 nm was imaged depending on the sample/fluorophores used.

3.4.2 Ensuring optimal performance of the microscope

Following the successful positioning of the optics and alignment of the laser light and sample fluorescence to the detector, several other parameters/properties had to be considered.

- **DCR map.**

  Each spectral pixel consists of 16 SPADs, but not all of the SPADs were used for detection during measurements. Whilst SPADs are highly sensitive detectors, able to read even single photons,[158] some of them are very prone to reading noise (so called "screamers"). This is a manufacturing feature for SPADs, where "false" events (non photon i.e. thermal or electrical field related events) cause an avalanche and generate voltage that is then read as signal. The dark counts rate (DCR), the signal produced due to noise in the absence of photons, had to be read out across the sensor first, in a dark room. The DCR map was then used by the software to select 8 or 4 SPADs for each of the spectral pixels that produced the lowest level of noise and would be activated prior to measurements. Using 8 SPADs at any given time gave a good balance of sensitive detection and high signal to noise ratio. The DCR map was updated every 8-months or so and re-acquired for any board (sensor) change.

- **Histogramming modes.**

  The sensor collects histogrammed data, and can employ 16 or 32 counters to the histogram bins. For the applications described herein, the 32 bin mode counting was used.

Upon photon detection, the counters register subsequent photon events until receiving a stop trigger. The TDCs then translate the signal and update the histogram, populating photons detected across specific time bins. With the use of a parameter called "HistMode" the detection time range and resolution of the time-window used could be changed. "HistMode" function was encoded in the Ra II firmware and could take any value from 0 to 7. With low values, a small time range was covered and each bin represented a small time slice (high time resolution). Low histogramming modes were used with fluorophores with short fluorescence lifetimes (<2 ns) with short decays. High "HistMode" values allow to observe decays on a longer time-frame, and since the detection window was split across the same number of bins, they have larger bin sizes (smaller time resolution, appropriate for long fluorescence emitters). Figure 3.4.4 represents the difference between two different histogramming modes.

When using "HistMode" = 1, the detection window is set to 3.2 ns, and every bin (grayed out area on the time axis) is 0.2 ns wide. This means that for most organic fluorophores the photons collected will not cover the whole decay period and a shallow decay profile might be observed. When a different histogramming mode is used, e.g. "HistMode" = 2, the detection window will now cover double the time span (6.4 ns), and a full exponential decay might be observed. Since the photons are always binned into the same number of time bins (32 or like in the Figure, 16), the bin width now corresponds to 0.4 ns and some of the temporal resolution is lost.

The exact detection windows and temporal resolutions for each of the seven "HistMode"s are collated in Table 5.1.

For the decays to be fitted effectively, it was important to record the whole decay as well as the levels of noise before the pulse. Thus, the positioning of the decay in the detection window was crucial. This was optimised by using a parameter called photon stop (PSTOP). PSTOP encoded a delay (each PSTOP unit corresponding to ~63 ps) before photon binning and data

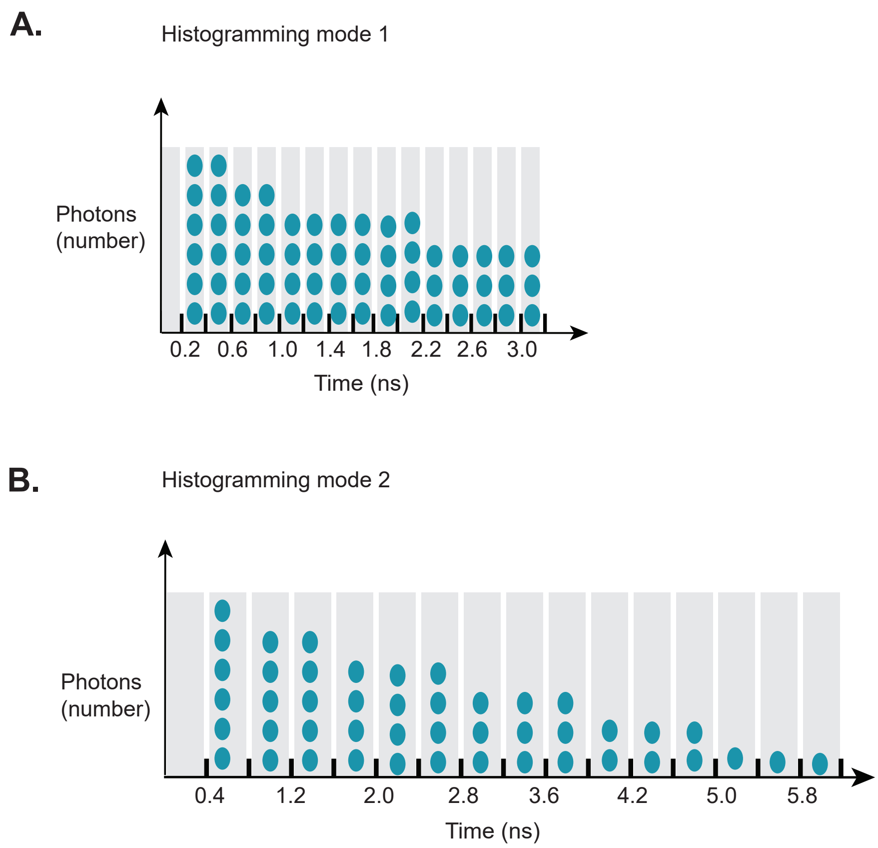

Figure 3.4.4: Cartoon representation of the detection window for "HistMode" = 1 vs "HistMode" = 2. A. The lower histogramming mode detects photons spanning across 3.2 ns, with each bin covering 0.2 ns. The bins are represented by the grey boxes on the time axis. Depending on the sample, this might not be enough to observe the whole fluorescence decay - like here, the number of photons does not drop to pre-excitation levels. B. The higher histogramming mode detects photons across 6.4 ns, and each bin is 0.4 ns wide. An exponential decay can now be observed.

Table 3.2: Time range and temporal resolution (ns) characteristic of each of the seven "HistModes", allowing for accurate detection of long and short decays.

HistMode	**Detection window (ns)**	**Bin width (ns)**
0	1.6	0.1
1	3.2	0.2
2	6.4	0.4
3	12.8	0.8
4	25.6	1.5
5	51.2	3.2
6	102.4	6.4
7	204.8	12.8

acquisition. The PSTOP was specific to each histogramming mode. The delay ensured the laser pulses were synchronised with the data acquisition, so that the photons would start arriving soon after data acquisition started, maximising the amount of data that can be obtained. As illustrated in Figure 3.4.5A, without the PSTOP some of the decays are observed ns after the acquisition began.

Fine-tuning the delay through introducing larger PSTOP values (Figure 3.4.5B) introduced a time gap before the data acquisition starts, thus shifting the relative position of the decay in the acquisition window. When PSTOP was overestimated (Figure 3.4.5C), i.e. the delay was too long, only the end tail of the decay could be observed in the acquisition window.

The PSTOP value was established using a MatLab script. A PSTOP value was input manually, starting from 0 (by-pass the delay generator) and increasing incrementally (several bins at a time for the low histogramming modes, and tens of bins at the time for high hist modes). The decay was observed and its position in the time-window noted. Through iterative testing of various PSTOP values, the values presented in Table 3.3 were

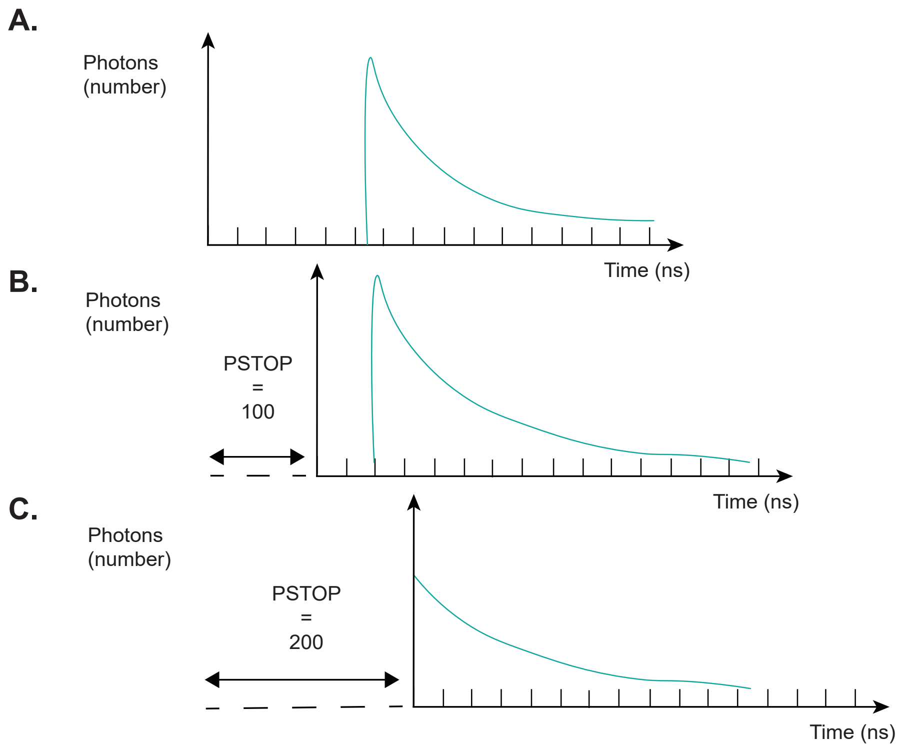

Figure 3.4.5: Cartoon representation of the effect of PSTOP value on the acquisition window. The solid line represents the time when data is acquired, the dashed line represents time before acquistion starts. A. When PSTOP is set to 0, there is no delay and the data is acquired immediately after the pulse. In this case, the decay falls in the middle of the acquisition window - for most fluorophores this would prevent accurate fitting. B. When PSTOP is set to a larger number (here PSTOP = 100), there is now a delay from when the laser pulse falls and the data acquisition starts. This means that when the data collection starts, the fluorescence decay can be observed $<$ ns after. C. When PSTOP is increased even further (here PSTOP = 200) the delay between pulse and acquisition is even longer, meaning the data acquisition starts mid-decay. If the PSTOP was even larger, the next decay from the pulse could be observed here.

chosen and used throughout the work. It is worth noting, these are specific to the system and any changes to the optical path affect the values chosen. After "upgrading" the system and fibre-coupling the lasers, the optical path was elongated. As a result the decays were shifted within the acquisition window and new PSTOP values needed to be determined.

Table 3.3: PSTOP value signifying delay generated for each of the 7 Histmodes. Modes 1-4 used most routinely throughout the work. In case of Hist 0, the PSTOP value was set so as to by-pass the delay generator altogether.

HistMode	**PSTOP (units)**
0	7
1	380
2	428
3	515
4	685
5	255
6	850
7	2100

- **Signal optimisation**

  Initially, when building the system, most samples used were excited at 470 nm and fluoresced in the green region of the spectrum (post-it notes, green slide, green ink, etc). The position of the board (Y and Z) and the angle of the diffraction grating were adjusted to maximise counts observed. This ensured an easy detection of 405/470 nm excited samples, but led to problems with detection of the further part of the spectrum (560 nm and 635 nm excitable samples), where even long acquisitions lead to few counts and noisy decay curves.

  In order to mitigate this, a white light lamp was used as a source of illumination above the objective and the signal detection maximised across the whole sensor - an even coverage across all wavelengths as opposed to peak and tail detection. This was achieved by adjusting the Y and Z positioning of the board with fine μm movements, and fine adjustment to the diffraction grating position (avoiding tilting the light beam coming out). The success of the operation was further confirmed by reflecting the 470, 560 and 635 nm lasers simultaneously off a glass slide, and observing the detector recording three sharp peaks of similar height.

This significantly improved the performance, but did not accounted for all variability in the detection across the spectrum. An inherent characteristic of SPADs is a parameter called photon detection probability (PDP), describing the sensitivity of SPADs across the spectrum. The probability of detecting a single photon varies across the spectrum. Equipping the sensor with two sets of SPADs, "blue" and "red", was one way of accounting for the variability and ensuring good performance across all sample sets. The PDP data, originally acquired by Erdogan et al,[157] is presented in Figure 3.4.6. The data were acquired in increments of 10 nm, and thus needed interpolating before correction factors could be generated.

In practice, the sensitivity of the blue SPADs was sufficient for all experiments described herein, and a PDP correction factor was introduced and applied in analysis to account for any detection discrepancies when necessary (mostly to smooth the appearance of the spectrum).

- **Instrument Response Function**

The Instrument Response Function (IRF) describes the response time of a TCSPC, and is a measure of the resolution achievable and shortest lifetime that can be measured on an instrument. For the TCSPC used, the IRF has been previously measured by Erdogan et al.,[157] for both sets of SPADs - blue and red. The red SPADs were characterised by a more diffuse, tailing, IRF with an average FWHM at 700 nm of 127 ps. The FWHM IRF for the blue SPADs, at 500 nm, was 162 ps. With both values showing only small variability across the wavelengths, and in fact shortening of FWHM at longer

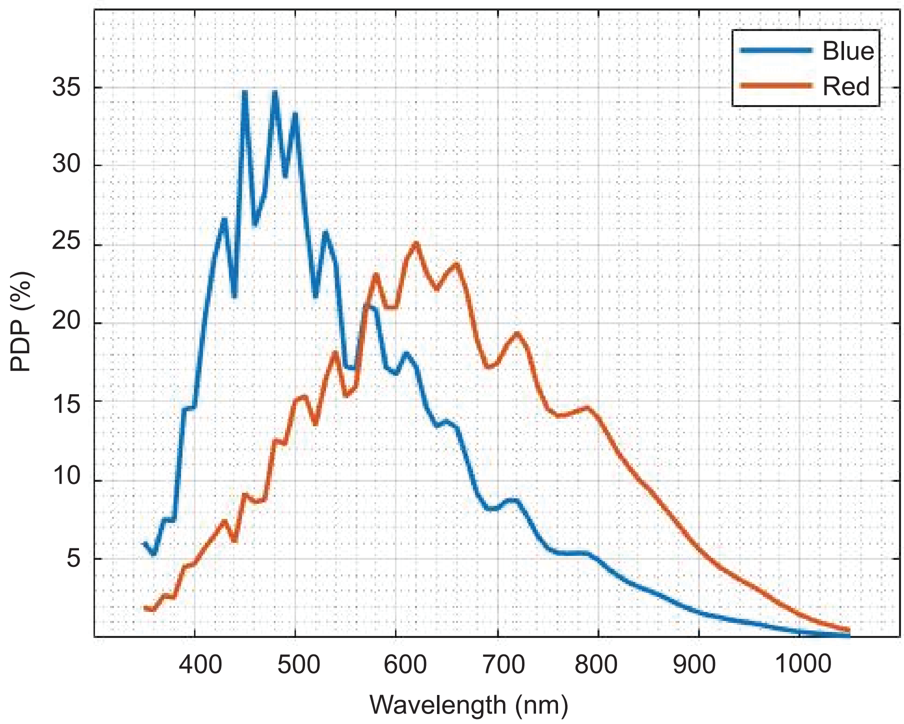

Figure 3.4.6: Photon Detection Probability as a function of wavelength. For the blue SPADs the blue region of the spectrum 450 - 550 nm is the most sensitive to incoming photons, for the red SPADs this falls around 600 - 700 nm. As the sensitivity tails off the sensor readout will showcase lower intensity. A correction factor can be introduced to mitigate this. Figure reproduced from Erdogan *et all*[157] with permission.

wavelengths, both sets of SPADs exhibit narrow IRF values. In practice, an IRF <200 ps suggests that the effect on lifetimes above 1 ns will be negligible. For measuring very short lifetimes (<1 ns), to get a true lifetime value, the IRF should be considered and an appropriate deconvolution fit applied. However, in applications where relative lifetime values are of interest, this might not be necessary.

3.4.3 Microscope output & data analysis

The lifetime data were acquired through a GUI, that recalls bespoke MatLab scripts. The GUI is an intuitive interface and gives the user a chance to define parameters including: step size (galvanometric mirror scan area, 0-70), hist mode (decay time acquisition window, 0-7), number of image pixels (usually 256), exposure times (in μs, usually set anywhere between 1000 - 100,000 μs). The software shows an intensity preview but the data needs to be further analysed to access the lifetime values.

For each single image pixel of the 256x256 2D grid (Figure 3.4.7A), the output consists of 512 intensity histograms (see Figure 3.4.7) one for each sensor (spectral) pixel. This corresponds to histograms spanning across approximately 250 nm. An emission spectrum and a lifetime value at each spectral pixel can be further extracted from this.

For the lifetimes to be calculated, a mono-exponential function needs to be fitted to every decay in the image. With the sensor collecting a decay curve for each of the 512 spectral pixels, for each image pixel, the computational load is high. A standard 256x256 image results in over 30 million decays. With various fits available, the MatLab scripts used in this work relied on the least squares fit (for details of the fitting parameters see 3.3.4). The method is easy to implement, quick for the amount of data generated, and highly accurate for data with high signal-to-noise ratios.[159] The fit determined the likelihood of detecting the specified number of photons in each of the histogram bins. The squared difference between measured photon counts and the estimated signal is minimised (least squares), with the underlying assumption that all the noise follows a Gaussian distribution. The

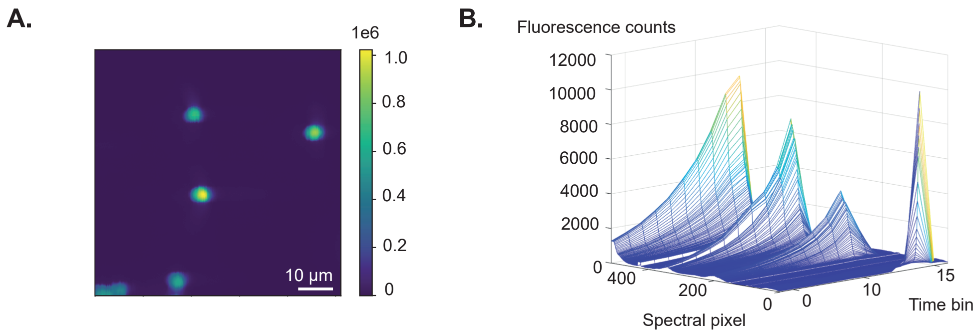

Figure 3.4.7: A. An intensity image that can be generated from the FS-FLIM data, with each of the 256x256 pixels assigned an intensity value (photon number). B. A 3D grid showing the data collected for every image pixel. The intensity is collected over time (the photons binned) for each of the 512 spectral pixels.

main drawback of using a least squares fit, is that it results in inaccurate decay fits for low SNR data. The systematic error for dim samples is approximately 5%[160] (although it will not affect relative differences between the lifetimes measured, just the absolute values). Thus, this was a consideration for both data acquisition (sufficiently long exposure times necessary) and data analysis (where bright pixels were chosen to establish fit parameters).

3.4.4 Validating FS-FLIM performance

In order to ensure that there was no systematic error, and the microscope was able to produce accurate lifetime values, conventional and well-characterised dyes were imaged on the system first and the generated lifetime values checked against literature values.

Solutions of three dyes: fluorescein in PBS, rhodamine 6G (R6G) in methanol and aqueous sulforhodamine B (SRB) (Figure 3.4.8) were imaged on the FS-FLIM. In each case, the solution was imaged above the coverslip surface to ensure no surface interactions were observed. This was undesirable as it could skew the observed lifetime values, in particular for rhodamine 6G. The intensity counts did not reveal structure, as expected, but were used to generate averaged intensity spectra and lifetime plots across all image pixels.

The fluorescent spectra of the dyes, acquired on the FS-FLIM, are shown

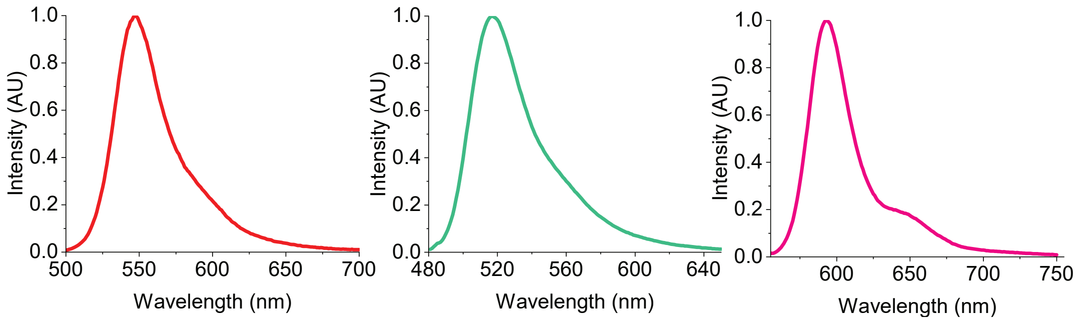

Figure 3.4.8: Fluorescence emission of rhodamine 6G (red), fluorescein (green), and sulforhodamine B (pink). Spectra plotted using data from FPbase.[71]

in Figure 3.4.9. Their emission peaks matched those observed in literature (approximately 520 nm for fluorescein,[161] 560 nm for R6G[162] and 585 for SRB[163]), see Figure 3.4.8 for literature spectra. It should be noted that the measured spectra shown were not corrected for the spectral efficiency response of the sensor (PDP correction factor not applied) and therefore the shape of the spectra deviated from the expected emission profile, especially in case of fluorescein. However, the shape of the observed emission spectrum did not impact lifetime calculations. Figure 3.4.9 also presents the lifetime values calculated for each wavelength and thus represents lifetime as a function of wavelength. The dyes did not exhibit large lifetime shifts since the lifetime value remained constant across the measured wavelengths, as would be expected. The error on the measurement (standard deviation represented as grayed out area on plots in Figure 3.4.9) increased where the emission was low. The emission peak position and lifetime across the peak were used to calculate average lifetime values.

Table 3.4 shows the averaged lifetime value for the three dyes. Fluorescein (3.7 ± 0.2 ns) and R6G (3.8 ± 0.1 ns) lifetimes are in good agreement with the quoted literature values.[161,164] SRB lifetime (1.7 ± 0.2 ns) deviated slightly from the literature value of 1.2 ns for an aqueous system.[163] SRB has been used as a temperature probe previously,[163] and a difference in temperature between the measurements could account for this deviation.

A range of concentrations of fluorescein (40 nM, 200 nM, 1 μM and 5 μM) were imaged to determine the effect of concentration on fluorescence intensity

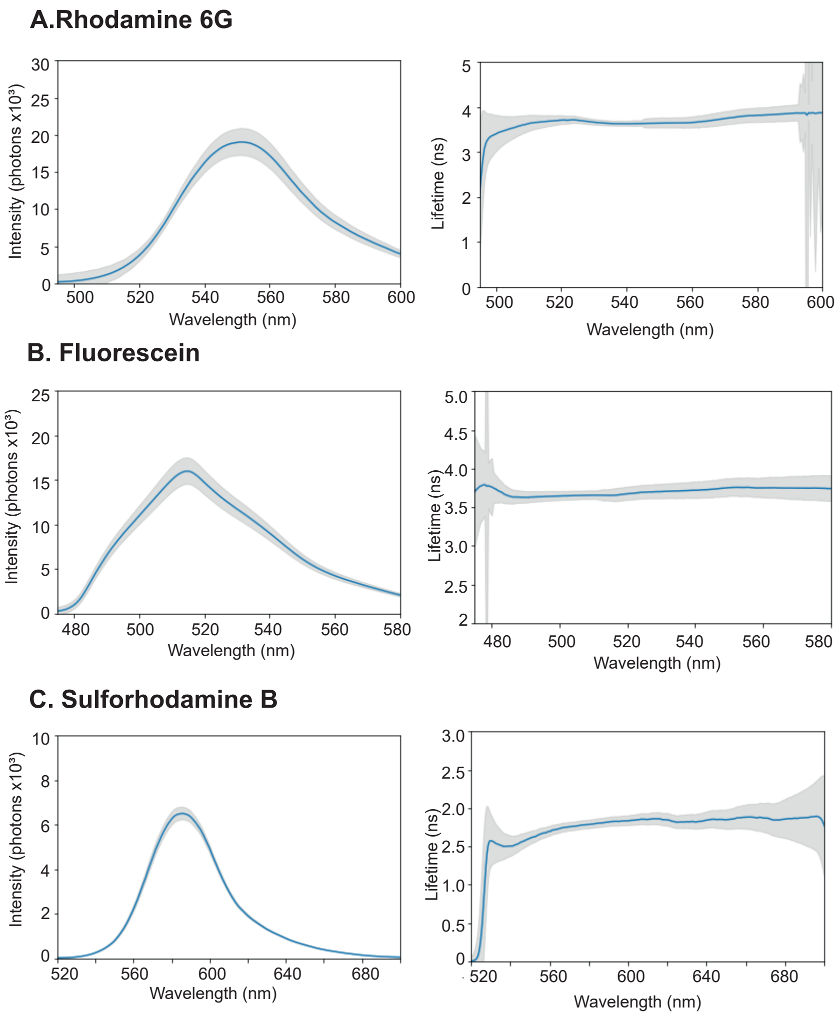

Figure 3.4.9: Fluorescence intensity (top row) and lifetime (bottom row) vs wavelength for three dyes: Fluorescein in PBS, R6G in methanol and SRB in water. Intensity spectra shown are not corrected for the spectral efficiency response of the sensor.

Table 3.4: Fluorescence lifetime values for three fluorescent dyes as measured (error is standard deviation from three separate measurements) and reported in literature.

Fluorescence standard	**Fluorescence Lifetime (ns)**	**Literature value (ns)**
Fluorescein	3.7 ± 0.2	4[161]
Rhodamine 6G	3.8 ± 0.1	3.7[164]
Sulforhodamie	1.7 ± 0.2	1.2[163]

and lifetime recorded. As the dye concentration increases, the intensity recorded should increase also. The graph in Figure 3.4.10 confirmed that trend. At higher concentrations of the dye, higher photon counts were observed. Lifetime is inherently concentration independent, and so, despite a change in concentration, the lifetime value should remain constant. This was observed between two points on the graph corresponding to fluorescein concentrations of 200 nM and 1 μM respectively. However, lower lifetime values have been recorded outside of the high nM range, outlining the limitations of the instrument and the technique. The 40 nM solution of fluorescein did not yield enough photons for a correct lifetime prediction, with the low signal-to-noise ratio leading to an underestimated lifetime in decay fits. This can be mitigated through using a longer exposure time (increasing the number of photons collected and fitted). Monitoring the total counts of an image was later introduced as a consideration for dim samples, to avoid underestimating the lifetime values measured. The 5 μM dye sample also produced a lower than expected lifetime value. At high dye concentrations, too many photons reach the sensor at the same time, causing an effect known as "pile-up". The early arriving photons are favoured, as a result of the dead time of the TCSPC (the time that need to pass between two consecutive photons for both to be detected), leading to underestimation of the fluorescence lifetime from the decay data. For bright samples, a lower laser power (to excite fewer fluorophore molecules in solution, and produce less photons) can be used to avoid pile-up. These two levels of fluorescence provided information on the potential sources

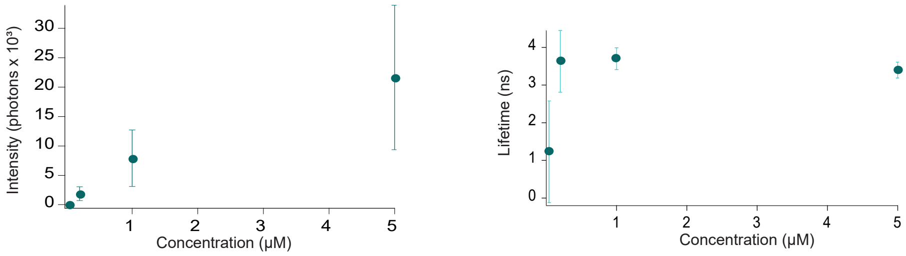

Figure 3.4.10: Fluorescence intensity (left hand side) and lifetime (right hand side) vs concentration of fluorescein solution. The intensity increases with increasing concentration. The lifetime is concentration independent, however can be underestimated if the instrument is detecting too little photons (low concentrations) or too many photons are reaching the sensor (high concentration, "pile-up" effect).

of errors during sample measurements. The sample concentrations producing pile-up/insufficient amount of photons will vary between fluorophores and systems, however the bulk number of photons observed for one pixel in a measurement produced a rough guide for these phenomena.

To illustrate the sensitivity of the system, SRB was next imaged in water-glycerol mixtures. The fluorescence emission intensity and lifetime for six conditions (0, 20, 40, 50, 60, 80 and 100% w/w glycerol) are presented in Figure 3.4.11. The intensity did not vary between water and glycerol solutions. This was unexpected, as with more decays, more photons should be observed. However, this could be partially explained by the difficulties in imaging glycerol-containing samples, varying focal planes (there is no way to ensure the samples are imaged in the same z-position) and photobleaching. The increasing viscosity did, however, produce a change in lifetime. Longer lifetimes were observed for samples with a higher glycerol percentage composition. SRB is a molecular rotor, with a "dark" Twisted Intramolecular Charge Transfer state. When the dye is rotating freely, the TICT and non-radiative processes compete with fluorescence (short lifetime of around 1.5 ns observed). When the rotation is made more difficult by the solvent, the TICT cannot be accessed, there is fewer intramolecular non-radiative processes competing with fluorescence and thus the observed lifetime is longer

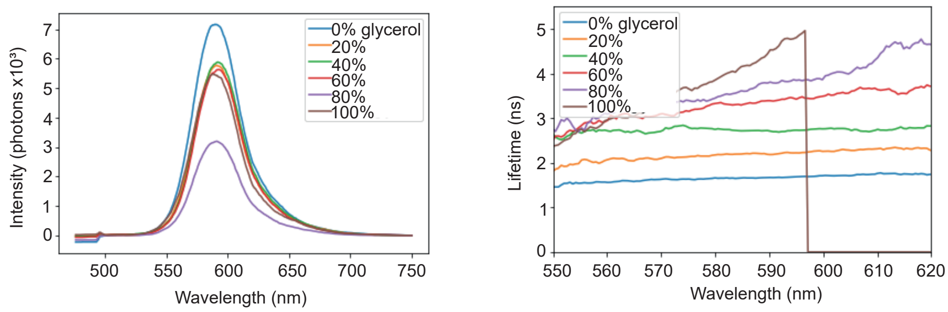

Figure 3.4.11: Fluorescence intensity (left hand side) and lifetime (right hand side) vs wavelength for six different SRB solutions. The dye concentration was kept constant in all solvent systems at 20 μM, the change relates to glycerol content and thus viscosity of the solution. The recorded intensity is very similar in all conditions. The lifetime increases in solutions with more glycerol (higher viscosity).

(over 4.5 ns). The lifetime drop off in the trace for the 100% glycerol solution can be explained by the photon counts dropping below the fitting threshold or an increase in noise that would also obscure the fits. A further repeat should have been run for the condition.

3.4.5 Imaging TetraSpeck beads & wavelength calibration

Having demonstrated the ability to measure lifetime values of solutions, it was important to evaluate the performance of the system when imaging samples with fine structure.

To that end, TetraSpeck microspheres labelled with four fluorophores were employed. With a diameter of 4 μm, these were large enough to spot easily, and the four emission peaks across the spectrum (blue, green, orange and red) ensured they were bright and easily detectable. 405 nm excitation was used with these, and caused all fluorophores to emit (either in a FRET-based landslide excitation or through off-resonance excitation).

Figure 3.4.12 presents the output from the TetraSpeck beads imaging. As expected, distinct fluorophore peaks could be observed, in Figure 3.4.12A the green, orange and red peaks can be seen. The board (and thus the sensor) was positioned to start spectral acquisition around 480 nm, with the 470 nm laser directed just off the board (and away from the sensor), explaining why only three and not four fluorophores where detected in this particular experiment. The peak shape (and the "shoulder" drop-off) can be explained by the filter set used (4-band quad dichroic). The fairly even peak height suggested good sensor calibration and a balance between green/red detection, where light of all wavelengths was well mapped onto the sensor. The spectrum was generated from all pixels representing the beads captured in the image, Figure 3.4.12B, where the 4 μm beads could be observed on the surface of the slide. The zoom-in showcases the circular structure of the beads. Due to the different fluorophores used for labelling, three distinct lifetimes could be detected. In Figure 3.4.12C, the lifetimes of the three peaks (green, orange and red from top to bottom) can be observed on the bead zoom-in picture. The change in colour is associated with longer lifetime values.

The TetraSpeck beads were further used to establish the detected wavelength range of the sensor. Since the sensor is housed on a board, that is tunable, it was important to ensure the correct spectral range was used for the measurements and in data processing. Previously, the sensor position was defined based on the position of the 470 nm laser. The translation stage was adjusted so that the 470 nm signal would peak at the first spectral pixel. Thus, the wavelength range covered by such a measurement would be 470 - 725 nm. However, this was an impractical solution for samples excited with shorter wavelength lasers and complicated when red end of the spectrum was of interest. The bead data set, as can be seen in Figure 3.4.12A, provided a useful means of "calibration". The emission maxima visible on the generated emission spectrum were compared to emission maxima measured on a standard fluorometer, and a line of best fit was chosen to describe the relationship between the two as previously described and shown in Figure 3.3.1. Thus, a "board equation" was generated and could be used to confirm the position of the sensor. This procedure was repeated prior to any measurements.

The bead data set also nicely illustrated the advantage of a"filterless" emission detection. Lifetime values can be obtained for 512-discrete wavelengths and averaged across discrete emission peaks rather than broad colour channels. The

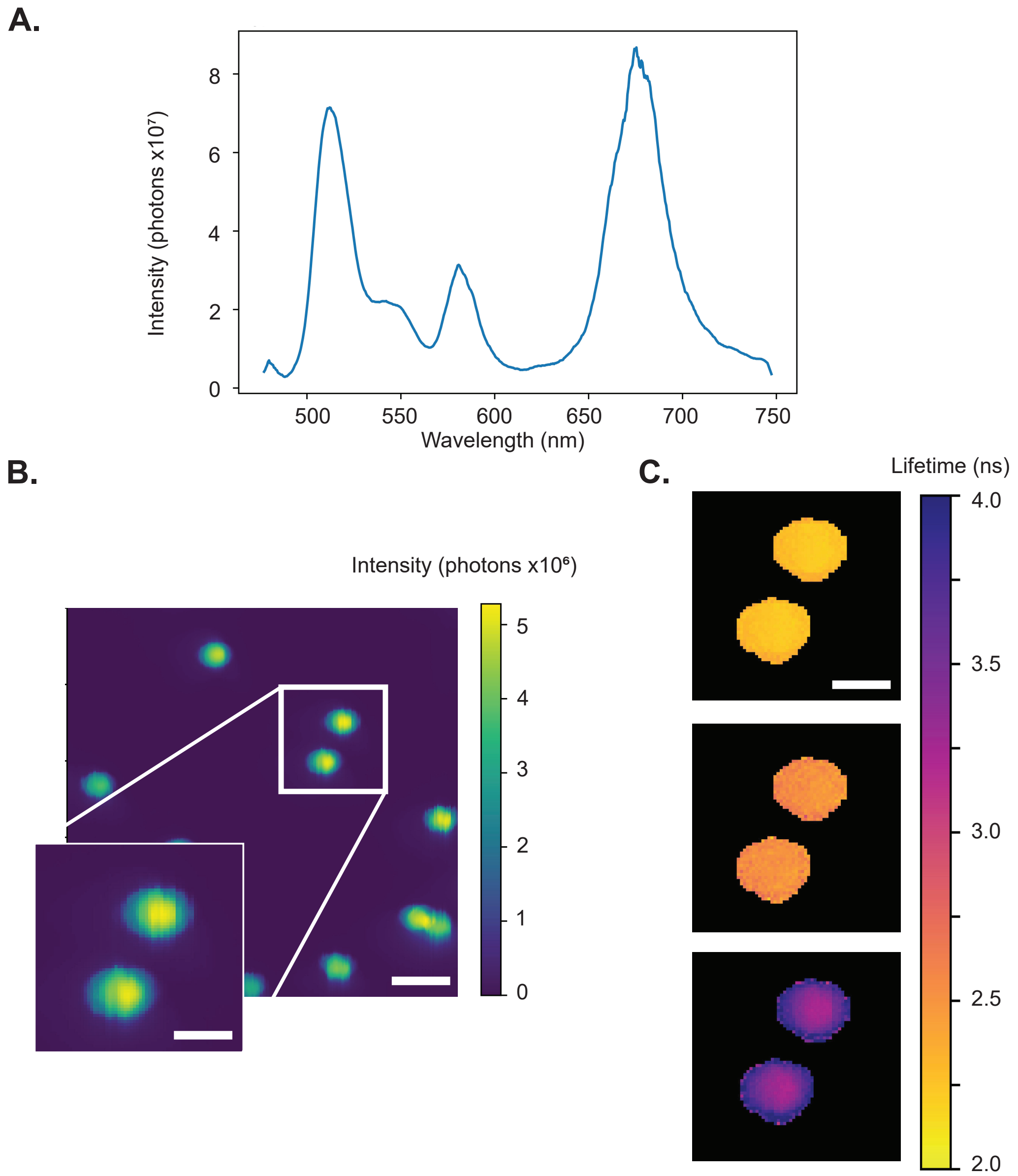

Figure 3.4.12: TetraSpeck beads, μm, as imaged on the FS-FLIM. A. The summed intensity across beads detected in image, clearly showing three peaks, from three distinct fluorophores. B. A summed intensity image showing the shape and size of the TetraSpeck beads on a glass slide. Scale bar: 10 μm, insert scale bar: 5 μm. C. Lifetime images of TetraSpeck beads, each averaged across one of the three peaks. From top to bottom: lifetime of the green fluorophore, lifetime of the orange fluorophore, lifetime of the red fluorophore. Scale bar: 5 μm.

fluorescence intensity and lifetime data can be represented in the same image, but can also be split across the detected emission peaks to enable fluorophore signal separation and feature detection (in case of multiplex labelling). The change in lifetime across wavelengths can be observed for every image pixel, not only distinguishing different fluorophores (as was done here, lifetime change due to multiple fluorophores present on the same bead) but also tracking changes in the same fluorophore across environment (diagnostics of healthy vs disease cell lines based on the lifetime values trends across the emission peak).[165]

3.4.6 Determination of the magnification

Having confirmed the microscope is able to detect and image large objects, the limit of the resolution and pixel size were studied next. The confocal system is theoretically able to achieve resolution close to the diffraction limit, however the shape of the point spread function (the shape of the beam used for imaging) and the alignment of the optical components can limit the actual resolution achievable by the microscope. At first the FS-FLIM did not rely on a fibre to filter the laser output. The beam was large and ellipsoid in shape, containing light of various modes. Implementing a single mode fibre, has helped to "tighten" the PSF, with the beam becoming more circular and only containing the fundamental Gaussian mode. Thus, the achievable resolution has improved to a near-diffraction limit.

In order to determine the size of the field of view (FOV) and the possible optical resolution, a dish with a 50 μm grating used for cell tracking was imaged. The FOV is dependent on the magnification of the objective lens used, but also the "step size" (ie the area of the sample scanned). A small step size, for example 20, leads to a "zoomed-in" image, a large step-size covers a larger area of the sample. The grating (Figure 3.4.13A) was imaged using several step sizes. The distance between the edges of the square was measured (distance in pixels) repeatedly across images to get an average length in pixels. This was then used to estimate the pixel size. The workflow, with the pre-fibre coupling data can be seen in Figure 3.4.13B. A smaller grid size (or a larger FOV) would be required to determine the optical resolution by performing a Fourier Transform of the image.

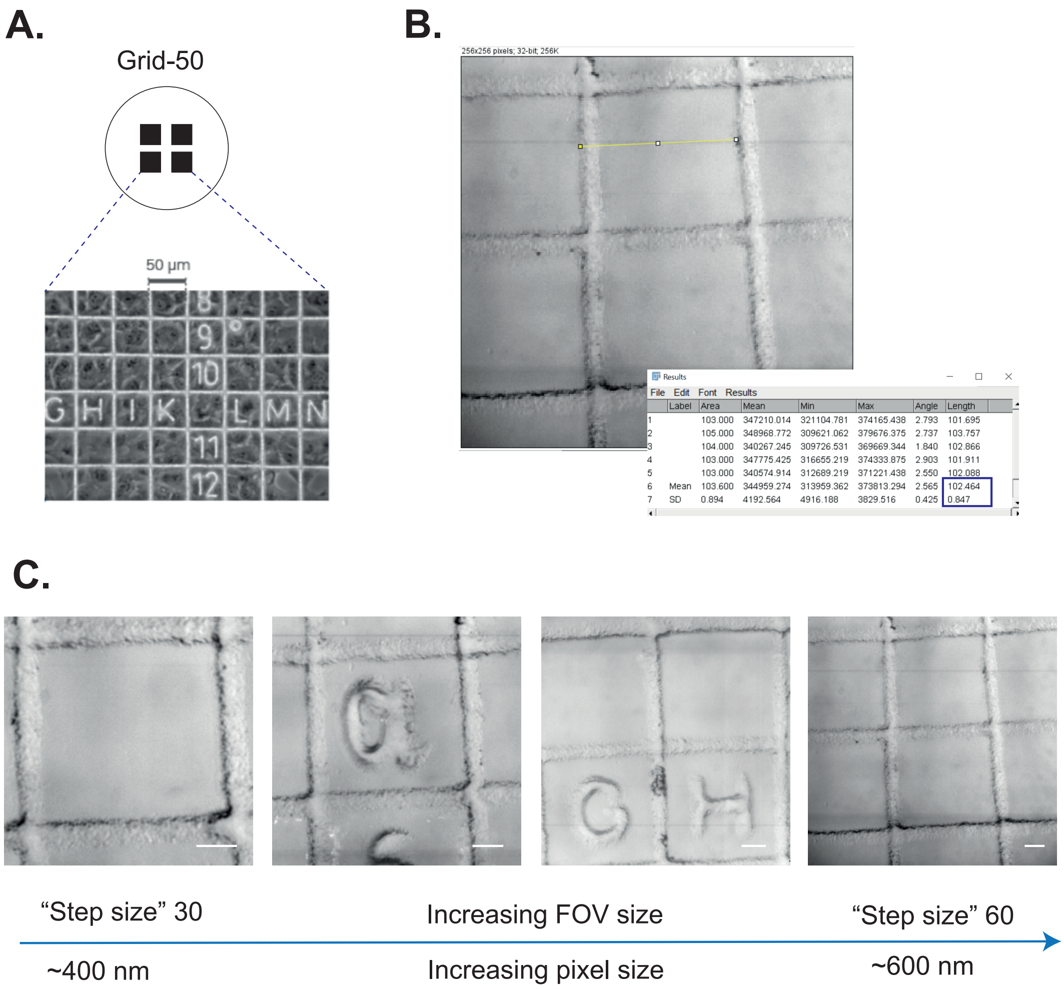

Figure 3.4.13: Imaging a 50 μm grating to determine the size of the FOV & pixel size. A. Experimental set-up. Cell tracking dish containing fluorescein was used for imaging. The layout of the grid obtained from manufacturer's info. B. The grid image from the microscope. The yellow line is representative of how the distance was measured. 5 measurements were taken across one grid square in each case, and the average distance used to determine the pixel size. C. The 50 μ grid images using various FOV settings and the pixel spacing estimated from them for the non-laser coupled system.

The images for step sizes between 30 to 60 are presented in Figure 3.4.13C. Step size 30 was the smallest FOV still containing a full square, representing the most “zoomed in” case. Decreasing the FOV size was accompanied by a decrease in pixel spacing, however this would not provide any further benefit by moving to even smaller FOVs. The resolution limit for 470 nm laser has been reached by “step size” 30, any images acquired with lower values offer limited increase in structural resolution. This value, for the smallest step size, has improved with using fibre-coupled lasers and was measured at approximately 400 nm for the 405 nm laser. Given the NA of the objective used (0.5 NA), this corresponded to the theoretical resolution of 405 nm and thus it was assumed that diffraction limited performance was achieved.

3.5 Discussion

3.5.1 Microscope performance

Since its construction, the system has undergone several rounds of optimisation to ensure satisfactory performance when imaging samples. Whilst some operations relied on the understanding of the electronics (i.e. regular DCR map updates to get rid of “screamers” visible in analysis), the alignment of the optics also played a significant role.Ensuring the detected light was well-mapped onto the sensor and could be detected with equal sensitivity at the green and red end of the visible spectrum was the main bottleneck and made the largest difference to the range of samples that could be imaged on the system. With the PDP correction technically able to overcome the problem, the PDP data set obtained in 10 nm increments required interpolation and, unless aligned perfectly, did not account for all the discrepancies in the shape of the emission spectra. Equally, the 635 nm laser used to “obscure” the signal, with most counts perceived coming from the laser reflection and not emission peaks. Only when the detection was optimised, did the red sample imaging become reliable. Equally, the fibre coupling has allowed to obtain “crisper” images containing more detail. This was especially evident when comparing first attempts at tissue imaging to images obtained post-system "upgrade", where fine structure substituted a "hazy" fluorescence outline.

The initial validation data set was important to establish whether the instrument was capable of recording true absolute fluorescence lifetime values, but also to understand the operational parameters and establish photon count ranges for further imaging sessions. Observing the concentration effect on the decay shapes, and lifetime values calculated, provided an understanding for how systematic errors in the measurements can arise and how they can be mitigated.

3.5.2 FS-FLIM vs standard FLIM microscopy

The FS-FLIM offers an opportunity to monitor lifetime across the whole spectrum instead of in defined colour-based channels. The filterless detection suggests complex systems with multiple emitters can be investigated on the FS-FLIM, where the data can be obtained simultaneously, and signal resolved to generate multiple images in post-processing. The on-chip histogramming vastly reduces the amount of time needed for the FS-FLIM measurements, with most images being recorded on the order of minutes. This provides a great advantage for live cell work, and studying dynamic systems, where objects and features could move in the time it takes to acquire an image. Moreover, FS-FLIM makes the study of lifetime across the whole emission peak of the emitter possible. Using the instrument, trends and deviations in the lifetime profile can be tracked directly, instead of comparing averaged lifetime values across features. This has been an avenue of interest in research involving nuclear protein staining across cancer cell lines and healthy cell lines, where the lifetime profile of the same probe varies across the two conditions and could potentially be used to differentiate between them.[165]

On the other hand, the large number of channels associated with the FS-FLIM can prove to be a disadvantage. In case of broad or dim emitters, the total number of photons recorded is low and divided across many SPADs. This limits the accuracy of fits and reduces the signal-to-noise ratio when compared to standard FLIM. To mitigate underestimation of lifetime, longer exposure times are needed to image dim samples. Additionally, the instrument cannot offer as high an optical resolution as a commercial FLIM systems. The FS-FLIM does not have a pinhole, which greatly improves resolution by rejecting out of focus light and is present in traditional confocal microscopes. The advantage of the additional data needs to be balanced against the need for high resolution of structures for FS-FLIM imaging.

The instrument is operated using scripts and a GUI developed in house, which are not an intuitive interface for a new user and require a good understanding of electronics and the system. The acquisition software is not fully automated (lasers controlled by user) and there is no perfect focus system on the microscope. This is different to commerical microscopes that are usually user-friendly and easy to operate. Since the development of the original instrument, the KronoScan, a fibre-coupled clinical version of the microscope, has been introduced. The KronoScan comes with bespoke software, that is more user friendly and enables even faster temporal resolution. The software is able to record decays in a rapid scanning mode, and lifetimes can be acquired on the order of μs. The caveat is that this is only possible in two spectral channels at a time, broadly defined as "red" and "green". The FS-FLIM can also be used in the "clinical" mode (that runs the clinical software, but uses the objective rather than a fibre for sample illumination), and thus is able to acquire lifetime data rapidly with a more friendly interface. However, this mode has not been used extensively throughout this work, as the output is limited (lifetime and intensity images for the two channels only) and the samples of interest were not dynamic (reduced need for speed).

The amount of data generated from each image is both the biggest advantage and drawback of the instrument. It opens up avenues for many potential applications, and invites many questions. To extract meaningful trends, a good understanding of the sample and thorough experimental planning is necessary. Whilst not attempted here, analysis methods relying on dimension reductions, including Principal Component Analysis (PCA), could be useful for identifications of features from large FS-FLIM imaging data sets.

3.6 Conclusions

A fully functioning FS-FLIM microscope has been built. The microscope is capable of imaging with a diffraction-limited resolution. Seven histogramming modes have been implemented to measure both short and long lifetimes, with hist mode 1 ideal for subnanosecond fluorophores, and hist mode 7 ideal for fluorophores with a lifetime in the range of tens of nanoseconds. These have successfully been employed to image a range of samples since.

The systems performance has been checked for systematic errors through imaging conventional dyes. The lifetime values obtained for fluorescein, rhodamine 6G and sulphorhodamine B corresponded well with literature values. Solution measurements of sulphorhodamine B in solvents of varying viscosity have revealed changes in the lifetime values recorded depending on the condition, which the instrument was able to pick up. TetraSpeck beads were also successfully imaged. The 4 μm beads are now routinely used to check for the board position and instrument alignment.

3.7 Future perspectives

The FS-FLIM is a useful imaging tool for a range of applications. To fully showcase the spectral resolution capabilities, multiplex imaging by staining the same sample using multiple fluorophores should be attempted. The system can be used as a good platform to confirm binding to target and contrast features detected with various probes (as long as they are labelled with different fluorophores). The extra contrast provided by lifetime means that conventional dyes that do not vary in intensity across features, could be used to for detection and potentially classification (assuming lifetime changes) of features of interests.

The FS-FLIM could also introduce a new way of running FRET experiments (lifetime-based readouts). The lifetime of the donor molecule changes when the donor fluorophore is placed in close proximity to the acceptor fluorophore, the drop-off in lifetime inferring about the distance between the two. Whilst nanoscopic oligomers might be difficult to detect on the FS-FLIM, larger aggregated species could be imaged once immobilised on the surface or after incorporation into cells. If the α-syn peptide was to be labelled with two different fluorophores prior to aggregation,[145] any changes in fluorescence lifetime, and thus conformation, upon permeabilisation and seeding further aggregation could be observed. Similar conformation changes could be observed upon inducing liquid-liquid separation or incorporation of α-syn into lipid droplets formed from other proteins. Equally, with an appropriate membrane counterstain, the FRET and interaction between the labelled α-syn sequence and the lipid membrane (or vesicle like lyposome inside the cell) could be measured. The FS-FLIM could be used to access new dynamic samples in the context of neurodegeneration like biocondensates or Liquid Liquid Phase Separation droplets (these are currently thought to be a potential precursor to aggregation). Initial work in this area included using Nile Red to observe and characterise liquid-liquid droplets formed by ubiquilin-2 under different environmental conditions, where the dye was used as a polarity reporter to reason about the assembly and make-up of the core and periphery of the droplets.[166]

In terms of instrument performance, its been optimised through imaging a number of samples and it provides reliable lifetime measurements and a diffraction-limited resolving power. Whilst the 512 channels offer unparalleled spectral resolution, a further version of the software where the number of channels of interest could be defined and set by the user could be useful. The 0.5 nm spectral resolution is not always necessary to study fluorescence, and the ability to sum the spectral bins together could shorten the experimental time needed to image dim samples and broad emitters. When using multiple lasers simultaneously, depending on the filter used, the laser signal can also be detected by the sensor. Whilst this can be addressed in post-processing (laser produces a sharp peak, and the decay is instantaneous with all intensity disappearing from bin to bin), the filters could be further upgraded or a band-stop filter could be added to avoid this. This has so far not been attempted, due to the limited space on the optical table.

3.8 Contributions

Dr Gareth Williams has designed the original system. The microscope described herein was constructed by the author of the thesis under his supervision and with his help. The author made active decision on the design, implemented changes to the optical lay-out and further improved the microscope following the initial construction. Mr George Steedman has produced adapters, holders and attachments that enabled construction of the microscope. He also equipped the microscope with an alternative sample stage and magnets for secure sample mounting. Dr Hazel Stewart has assisted with optimisation of the detection performance, spectrophotometer realignment, and provided DCR map software. Prof. Mathew Horrocks has initially assisted during instrument up-keep and re-alignment.

The samples were prepared, processed and measured/imaged by the author. All the data analysis was also performed by the author, the Matlab scripts used for lifetime calculations were written by Dr Gareth Williams and modified by the author. Python scripts for data/image processing and display were partially written by Prof. Mathew Horrocks and later on improved and customised by the author of this thesis.

Chapter 4

Peptide probes for FLIM imaging

4.1 Scope of the chapter

This chapter describes nitrobenzodiazole-derived dyes used to generate fluorescent peptides and presents preliminary work in the design and application of peptide probes for detection and imaging of α-synuclein.

4.2 Introduction

4.2.1 Peptide sequences targeting α-synuclein

The role of therapeutic peptides in PD has been the subject of numerous studies in recent years.[140] From endogenous sequences to sequences containing D-amino acids and other unnatural modifications, there is a drive to develop new peptide-based interventions capable of disrupting the disease-associated aggregation pathways.

Several endogenous gut-derived peptides have been found to have neuroprotective potential for PD.[167] Glucagon-like-peptide 1 (GLP-1) is a 30 aa peptide capable of crossing the blood brain barrier (BBB). Despite its main implications in diabetes, its receptors are distributed widely across the body including many residing in the brain. Exenatide, which is a peptide drug and a GLP-1 analogue, was shown to improve motor impairment in rat PD models[168,169] and showed promise in the clinic.[170] PD patients treated with exenatide showed improvement in motor and non-motor symptoms above the levels reported by the control group, an effect that persisted 12 months after initial treatement.[171] It was hypothesised this could be due to its protective function in mitochondria (which are susceptible to oxidative stress and reactive oxygen species) and promoting antioxidative enzymes.[172] Gut-derived peptides with anti-inflammatory properties, such as pituitary adenylate cyclase activating polypeptide (PACAP), have also been identified,[173] but their mechanism of action is less well-understood. Ghrelin, a peptide controlling appetite and food uptake, has been described as a neuron survival agent and might help stop apoptosis of neurons.[174] Despite the observation that ghrelin responses in PD patients are reduced in comparison to the general population,[175] thus potentially qualifying it as a peripheral biomarker for the disease, the role of these peptides in PD is still under investigation. Their therapeutic effects are thought to follow general neuroprotective pathways.

It is the peptides that were developed specifically against α-syn that are therefore of more interest, both from a therapeutic and an imaging stand-point. α-Syn is a 140 aa long (14.6 kDa) protein, and its sequence can generally be divided into three regions: the N-terminal amphipathic region (residues 1-60), a central hydrophobic region (residues 61-95) referred to as non-amyloid β-component (NAC) and implicated in amyloid formation, and the acidic C-terminal (residues 96-140). The N-terminal region is said to be the main interaction site for lipids, capable of adapting an α-helical secondary structure.[176] The relatively high content of lysines at this terminus facilitates binding to negatively charged head groups of phoshopholipid membranes, whilst the hydrophobic residues can be inserted further into the bilayer; hence its amphipathic character. This region of the protein sequence is also linked to several point mutations found in early onset PD.[140] The central hydrophobic region, especially amino acids 71-82, is thought to be the most aggregation prone sequence motif of the full-length protein, with some of the flanking amino acids involved in stabilising the misfolded species into β-sheet rich fibrils.[177] The C-term is proline rich and negatively charged, it facilitates interactions with cationic metals but also houses any post-translational modifications to the protein like the S129 phosphorylation.[178]

Table 4.1 summarises a few examples of the peptide sequences designed to target specific α-syn regions.

Meade *et al.* have used the exact N-terminal sequence of α-syn and demonstrated it is able to form α-helices in presence of lipid vesicles. When incubated with full-length α-syn, the sequence stabilised the monomeric protein and was shown to prevent aggregation in a dose-dependent manner.[179] Peptidomimetic scaffolds further stabilising the N-terminal region and preventing protein aggregation in presence of lipids were described by Bavinton *et al.*.[180] Horsley *et al.* reported success when using a rationally designed N-terminal region targetting peptide (NTR-TP), containing a recognition sequence and an aminobutyric acid (Aib) β-breaking moiety. They tested both L- and D-isoforms of the peptide, the D-isoform showed most promise both in ThT aggregation assays (reducing overall ThT fluorescence when 5-fold excess peptide was present) and cyotoxicity studies (improving cell viability following peptide treatment).[181]

Table 4.1: Examples of sequences developed to target α-syn. J stands for norleucine.

Name	**Length**	**Sequence**	**Target**
α-s_{1-25}[179]	25	MDVFMKGLSKAKEGVVAAAEKTKQG	N-term
NTR-TP-D[181]	7	GVLYVGS-Aib	N-term
CP-2[142]	6	JWHSKL	N-term/NAC
4554W[182]	10	KDGIVNGVKA	N-term/NAC
T72P-6mer[183]	6	PGVTAV	NAC
S61[184]	22	GAVVWGVTAVGRKKRRQRRRPQ	NAC
PDpep1.3[185]	12	DEEIERQLKALG	C-term
Tat-β-syn-degron[186]	25	YGRKKRRQRRRRTKSGVYLVGRRRG	monomer
p216[187]	11	WFQNRRMKWKK	oligomers
LL-37[188]	37	LLGDFFRKSKEKIGKEFKRIVQR IKDFLRNLVPRTES	oligomers

Another interesting peptide probe was developed by Jin *et al.*, its sequence mimicked residues 35-45 of β-synuclein (another protein in the synuclein family). Their design included a Tat domain (YGRKKRRQRRR; the motif ensured the peptide could be successfully delivered across the BBB and plasma membranes), the targeting region, and a "degron" domain (RRRG tag, which recruited proteosomes to the interaction site).[186] The peptide was injected into transgenic mice over-expressing α-syn and led to a reduction in general α-syn levels in 24h. A different amyloid-resembling peptide was identified by Chemerovski-Glikman *et al.*. A short cyclic peptide sequence CP-2, featuring an unnatural amino acid, was found to assemble into supramolecular structures and bind to NAC region, disrupting pre-aggregated fibrils and inhibiting fibril elongation.[142] Another short peptide sequence, 4554W was found to inhibit aggregation and toxicity in an assembled rationally-designed library screening against WT and five common point-mutations in PD.[189] 4554W binding to α-syn was studied by NMR and shown to bind to early α-syn aggregates, limiting downstream aggregation and fibril formation.[190] The peptide was shown to inhibit both the WT protein and the mutated versions, making it a good lead as a potential therapeutic. Soon-Kim *et al.* devised a library of short (6-12 residues) peptides from the NAC region, that were thought to be β-breaking (preventing fibril formation through disrupting stabilising secondary structure).[183] For one of the sequences, T72P-6mer, they reported a 90% reduction in aggregation and removal of mature fibrils upon treatment with excess peptide (1:5 molar ratio). Attempts at interrupting the seeding dynamics led Sangwan *et al.* to model peptides mimicking the NAC core to block β-strand interaction sites and prevent fibril elongation. From their hit compounds, peptide S61 demonstrated most promise in *in vitro* studies. They found the sequence was crucial to the inhibitory effect of the peptide, with scrambled sequences showing no binding to α-syn and having no impact on the aggregation kinetics.[184]

Some sequences were designed to inhibit α-syn interactions with other proteins. A C-terminal derived peptide described by Nim *et al.* restored endosomal degradation pathways for α-syn normally hampered through C-term interactions with one of the cascade proteins.[185]

Furthermore, sequences showing higher binding affinities to oligomers than other forms of α-syn have also been reported. One such example is peptide p216, which was found to inhibit oligomer toxicity in a cellular model of PD and increased cell viability by 20%.[187] Santos *et al.* studied a human antimicrobial sequence LL-37, and showed the sequence binds preferentially to oligomers and is able to reduce aggregation in *in vitro* assays. The researchers postulated the α-helical amphiphatic scaffold (rather than the exact amino acid sequence) were responsible for the mechanism of action.[188] Further examples of library-derived, rationally-designed and endogenous peptide sequences with promise of inhibiting α-syn aggregation are discussed in detail by Allen *et al.*.[140]

4.2.2 PSMα sequence

With the aim of derivatising a sequence for diagnostic applications, a lead candidate with confirmed binding properties to α-syn aggregates was of interest. Sequences that do not interact with monomer were considered to be more promising, for ease of differentiation between individuals with PD and healthy aged-matched controls (especially since increased levels of α-syn were expected in those as well). The desired criteria included tight and selective binding to α-syn (to ensure tolerance of fluorescent tag) and a known mode of action.

A sequence that met all these criteria was developed by Santos *et al.*.[188] Phenol soluble modulin α3 (PSMα3) is a bacterial extracellular peptide secreted as a defence mechanism against an immune response.[191] The naturally occuring sequence is relatively short (22 aa, sequence: MEFVAKLFKFFKDLLGKFLGNN), stable, amphipathic and cationic in character (net charge +2). It was shown to fold into an α-helix in solution. All these characteristics suggested it would make a good selective binder for oligomers and amyloid fibrils alike. Santos *et. al.* further showed the sequence does not bind monomeric protein. It did, however, show nanomolar affinity for oligomers and fibrils (K_D of 3.62 nM for oligomers). The sequence demonstrated good anti-aggregation potency, lending itself to further therapeutic applications.

Interestingly, PSMα shares a degree of structural similarity with other endogenous peptides used to inhibit α-syn aggregation including PACAP, GLP-1 and Exenatide. Their sequences give rise to amphiphatic α-helices with an overall positive charge. Santos *et al.* identified these features as crucial for interaction with the hydrophobic patches and exposed acidic C-terminus tails of α-syn.[192,193] The structural similarity of those peptide probes suggests they also share a common mode of interaction with α-syn and a similar mechanism of action. This has further enabled the creation of a peptide database, containing endogenous sequences sharing favourable physiochemical properites, which could show affinity for α-syn oligomers.[194] Additional biophysical and biochemical studies were used to elucidate the exact N-terminus residues of α-syn exposed in the oligomeric species and involved in the PSMα binding.[195]

The PSMα peptide was derivatised with a fluorescent dye in the original research paper, through cysteine incorporation at the N-term and further dye labelling using maleimide chemistry. All of these findings suggested the sequence would make a good starting point for fluorescent labelling and imaging applications.

4.2.3 Nitrobenzodiazole-derived amino acids for fluorescent peptides

Amongst the many dyes developed for use as fluorescent reporters in super-resolution imaging,[196–199] cyanines[200–204] rhodamines[205–209] and ATTO dyes[210–212] are some of the most popular. Despite their favourable optical properties, all these molecules are large (over 500 Da molecular weight) and charged species. This limits their incorporation into small binding motifs, such as peptides, and requires the use of spacers to minimise disruption to binding or changes to bioactivity. Thus, small fluorescent dyes that can be incorporated directly into the peptide sequence for super-resolution applications are needed. De Moliner *et al.* developed a library of nitrobenzoxadiazol (NBD)-derived amino acids, where atom substitutions at two positions around the ring were systematically introduced and their effect on the optical properties of the dyes observed.[144] The two positions were involved in the pull-push dipole of the fluorophore,[213,214] thus enabling tuning of the optical properties. Out of the library, the two fluorescent amino acids presented in Figure 4.2.1A, S-NBD (**Compound 3**) and Se-NBD (**Compound 4**) proved most attractive for further incorporation into peptide sequences.

A. Chemical synthesis of fluorogenic amino acids

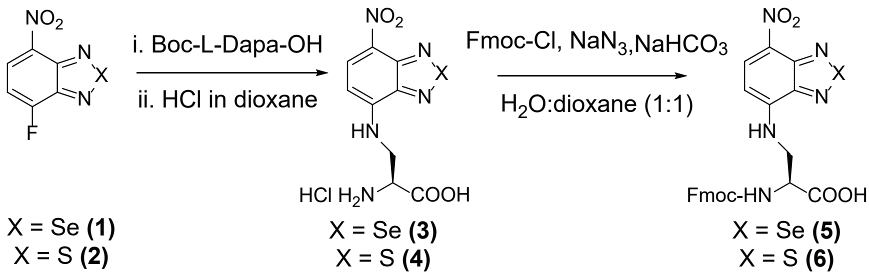

B. Optical properties of fluorogenic amino acids

Compound	λ_{abs} (nm)	λ_{em} (nm)	QY	ε (×10³ M^{-1} cm^{-1})	Polarity coefficient
3	488	601	0.19 ± 0.02	4.48 ± 0.11	3.4 ± 0.1
4	460	546	0.20 ± 0.05	9.74 ± 0.10	4.9 ± 0.1

C. Stability of fluorogenic amino acids

Compound	TFA 95%	Piperidine in DMF	TBAF	Pd^0	N_2H_4
3	>95 %	>95 %	>95 %	>95 %	>95 %
4	>95 %	84±4 %	>95 %	92±1 %	65±7 %

Figure 4.2.1: Nitrobenzodiazole-dervied fluorogenic amino acids. A. Synthesis of Se-NBD and S-NBD as building block for SPPS. B. Optical properties of Se-NBD and S-NBD, recorded in DMSO, with rhodamine B as a quantum yield reference. C. Stability of S-NBD and Se-NBD to standard SPPS conditions expressed as % purity from 254 nm HPLC traces. Reaction conditions are as follows: TFA:DCM(95:5), 1 h, r.t.; piperidine:DMF (2:8), 30 min, r.t.; TBAF 3 H_2O (3 eq.) in DCM,1 h, r.t.; $Pd(PPh_3)_4$(0.25eq.) in DCM,30 min, r.t.; 10% $N_2H_4H_2O$ in DMF,1 h, r.t.

Both of these compounds could be accessed following the same synthetic pathway from a pre-prepared fluorinated precursor molecule. A nucleophilic aromatic substitution with Boc-L-diaminopropinoic acid (Dapa) introduced an amine-based electron donating group to the heterocycle. The tetrbutyloxycarbonyl (Boc) protecting group could then be removed under mildly acidic conditions. This approach benefited from a good yield (>80 %) and good scalability (batches of approximately 100 mg). Fmoc-protected analogues could then be accessed with Fmoc-azide formed *in situ* from Fmoc-Cl and sodium azide. This transformation also proved efficient (yield of around 75 %) and scalable.

The introduction of S (**compound 3**) and Se (**compound 4**) in the nitrobenzodiazole moiety, together with the electron donating group, has affected the optical properties of the resulting dyes. The characteristics of Se-NBD and S-NBD, as determined in DMSO, are compared in Figure 4.2.1B. Both Se-NBD and S-NBD are excited by blue light (λ_{abs} = 488 nm for Se-NBD and λ_{abs} = 460 nm for S-NBD), though the maximum absorbance for S-NBD is slightly shorter than that of Se-NBD. They dyes exhibit large Stokes shifts, as the λ_{em} falls at 601 nm for Se-NBD and 546 nm for S-NBD. They are characterised by modest quantum yields (determined using rhodamine B as a reference) at approximately 0.20 for both dyes, and their ε were in the range of thousands of $M^{-1}cm^{-1}$ for both dyes with S-NBD as brigher of the two (double the ε). Despite not being the brightest fluorophores, both dyes exhibit a polarity switch that makes them interesting compounds for imaging. With low fluorescence in aqueous media, their fluorogenic response can be observed in non-polar environments as can be demonstrated by the polarity coefficients. Interestingly, both compounds are also environment-sensitive. In a range of water-dioxane mixture, of increasing polarity, the lifetime of the dyes increased in nonpolar solvent. Thus, they can be used as polarity reporters.

Moreover, the incorporation of Se in the ring structure has improved the photostability of the Se-NBD as compared to O-NBD by about 20 %.[144] This was unique to Se-NBD, as S-NBD had similar photostability as the original NBD.

Another advantage of the NBD-derived amino acids is their compatibility with SPPS methods. Both S-NBD and Se-NBD can be derivitised with an Fmoc-group, and then incorporated into peptide sequences on resin. Their stability against treatment with reagents used in SPPS was determined by HPLC, and is summarised in Figure 4.2.1C. The amino acids can withstand standard deprotection conditions (piperidine), cleavage (95 % TFA), as well as alternative deprotection conditions like tetra-n-butylammonium floride (TBAF), hydrazine, palladium without decomposition. Thus, the fluorogenic amino acids do not have to be conjugated to the ready-sequence in solution. Their stability means they can be incorporated on the peptide synthesiser and cleaved and purified without additional steps. Additionally, the amino acids do not have to be used externally, at the N-terminus, but can substitute native non-polar amino acids in the sequence. Taken together, this opens up interesting avenues for library building and high-throughput synthesis of labelled-peptides for imaging applications.

4.3 Methods

4.3.1 Peptide synthesis

Solid state peptide synthesis followed the methods described in the Methods section 2.3. The procedures and reagents used are listed there.

Briefly, the α-syn targeting library was prepared according to the scheme in Figure 4.3.1. PSMα peptide backbone was prepared using Liberty Blue microwave-assisted SPPS.

Full length sequence of PSMα was prepared. Biotin and cystein were also incorporated on Liberty Blue, under standard Fmoc/tBu-SPPS at r.t. (Figure 4.3.1).

biotin-Met-Glu-Glu-Val-Ala-Lys-Lys-Leu-Phe-Lys-Phe-Phe-Lys-Asp-Leu-Leu-Gly-Lys-Phe-Leu-Gly-Asn-Asn-NH2 (biotin-PSMα) The synthesis was performed on 55.6 mg of ProTide Rink amide resin (0.18 mmol g^{-1}). After cleavage, the crude peptide was precipitated by adding cold Et_2O (dropwise) and the resulting precipitate was decanted and dried (4 $\times$). Purification was conducted by semi-preparative HPLC with detection at 254 and 280 nm. Pure

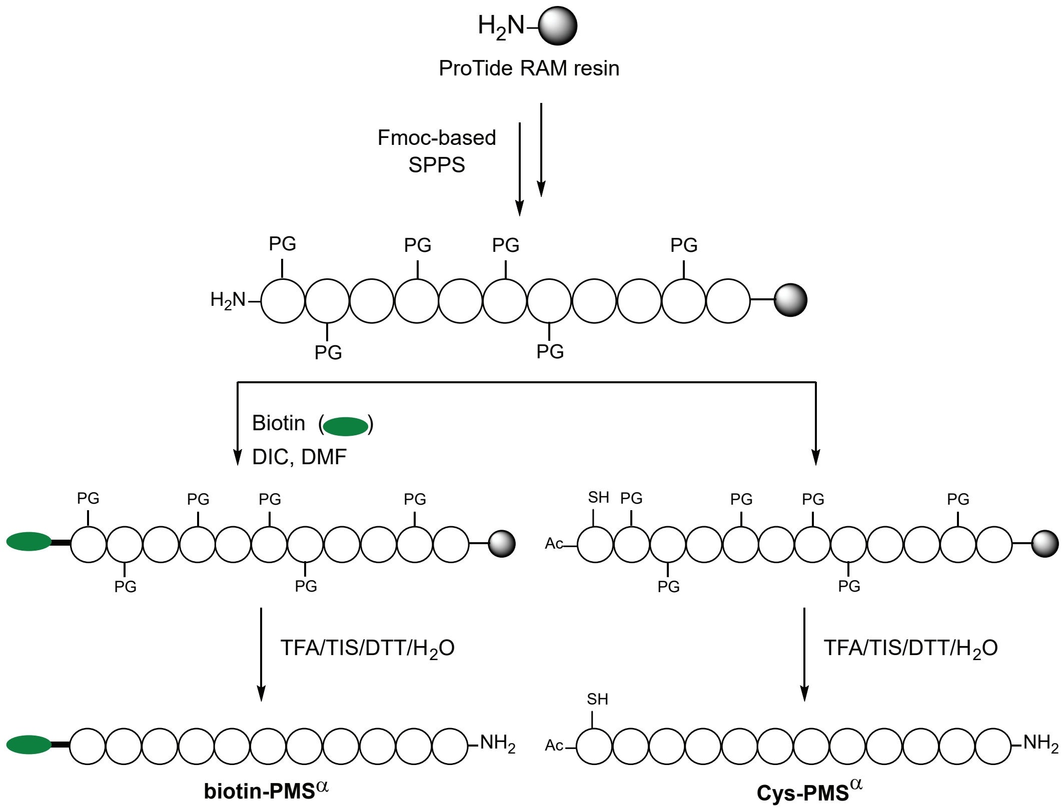

Figure 4.3.1: Synthesis of PSMα peptides for maleimide labelling and biotin conjugation - reaction scheme.

fractions were collected and lyophilized to afford pure peptide as a white solid (1.8 mg, 6%). HPLC-MS: tR: 4.41 min, 98% purity. HRMS (ESI+) (m/z) for $C_{142}H_{222}N_{34}O_{34}S_3$, [M+H]$^+$: 3044.58 predicted. [M+4H]$^{4+}$: 761.92, [M+5H]$^{5+}$: 609.81, [M+6H]$^{6+}$: 508.30 observed.

Ac-Cys-Met-Glu-Glu-Val-Ala-Lys-Lys-Leu-Phe-Lys-Phe-Phe-Lys-Asp-Leu-Leu-Gly-Lys-Phe-Leu-Gly-Asn-Asn-NH2 (Cys-PSMα) The synthesis was performed on 140 mg of ProTide Rink amide resin (0.18 mmol g^{-1}). Double couplings were performed for all amino acids from Ala onwards. After cleavage, the crude peptide was precipitated by adding cold Et_2O (dropwise) and the resulting precipitate was decanted and dried (4 $\times$). Purification was conducted by preparative HPLC with detection at 220 and 280 nm. Pure fractions were collected and lyophilized to afford pure as a white solid (14.2 mg, 20%). HPLC-MS: tR: 4.37 min, 98% purity. (m/z) for$C_{134}H_{210}N_{32}O_{33}S_2$, 2859.52 predicted. [M+3H]$^{3+}$: 1014.71, [M+4H]$^{4+}$: 761.23, [M+5H]$^{5+}$: 609.24 observed.

Ac-Cys(JF646)-Met-Glu-Glu-Val-Ala-Lys-Lys-Leu-Phe-Lys-Phe-Phe-Lys-Asp-Leu-Leu-Gly-Lys-Phe-Leu-Gly-Asn-Asn-NH2 (JF646-PSMα) The synthesis was performed at 1.7 μM scale. Cys-PSMα (5 mg, 0.0017 mmol) was dissolved in PBS (300 μL, pH = 7.4). JF-646 maleimide (1.2 mg, 1.2 eq; Tocris) was dissolved in DMSO (100 μL) and added portion-wise to the peptide solution. The reaction was left in the dark, at r.t. with shaking for 2h. The freeze-dried crude was purified by semi-preparative HPLC with detection at 220 and 646 nm. Pure fractions were collected and lyophilized to afford pure peptide as a blue solid (2.3 mg, 72.3%). HPLC-MS: tR: 4.89 min, 97% purity. (m/z) for $C_{169}H_{244}N_{36}O_{38}S_2Si$, [M+H]$^+$: 3478.75 predicted. [M+4H]$^{4+}$: 870.91, [M+5H]$^{5+}$: 696.75, [M+6H]$^{6+}$: 580.79 observed.

For the synthesis of SeNBD-labelled analogues the backbones were prepared on Liberty Blue at a 0.05 mmol scale. The reaction was scaled down (0.015 mmol) and SeNBD incorporations were performed in the microwave vessel using Fmoc-AA-OH Fmoc-AA-OH (1.2 eq.), DIC (2.4 eq.), OxymaPure (2.4 eq.) and DIPEA (2.4 eq.) and a 10 min, 30 W, 90 °C microwave program. All subsequent amino acids were incorporated following the same protocol, with Fmoc-AA-OH Fmoc-AA-OH (4 eq.), DIC (8 eq.), OxymaPure (8 eq.) and DIPEA (8 eq.) and a 10 min, 30 W, 90 °C microwave program.

Ac-Met-Glu-Glu-Val-Ala-Lys-Lys-Leu-SeNBD-Lys-Phe-Phe-Lys-Asp-Leu-Leu-Gly-Lys-Phe-Leu-Gly-Asn-Asn-NH2 (F9SeNBD PSMα) The synthesis was performed on 84.2 mg of ProTide Rink amide resin (0.18 mmol g^{-1}). After cleavage, the crude peptide was precipitated by adding cold Et$_2$O (dropwise) and the resulting precipitate was decanted and dried (x4). Purification was conducted by preparative HPLC with detection at 254 and 485 nm. Pure fractions were collected and lyophilized to afford pure peptide as a deep orange solid (mg, 6%). HPLC-MS: tR: 4.43 min, 96% purity. HRMS (ESI+) (m/z) for $C_{131}H_{203}N_{33}O_{38}SSe$, [M+H]$^+$: 2879.41 predicted. [M+3H]$^{3+}$: 960.47, [M+4H]$^{4+}$: 720.60, [M+5H]$^{5+}$: 576.69 observed.

Ac-Met-Glu-Glu-SeNBD-Ala-Lys-Lys-Leu-Phe-Lys-Phe-Phe-Lys-Asp-Leu-Leu-Gly-Lys-Phe-Leu-Gly-Asn-Asn-NH2 (V4SeNBD PSMα) The synthesis was performed on 84.2 mg of ProTide Rink amide resin (0.18 mmol g^{-1}). After cleavage, the crude peptide was precipitated by adding cold Et_2O (dropwise) and the resulting precipitate was decanted and dried (4 ×). Purification was conducted by preparative HPLC with detection at 254 and 485 nm. Pure fractions were collected and lyophilized to afford pure peptide as a deep orange solid (0.5 mg, 1%). HPLC-MS: tR: 4.47 min, 96% purity. (m/z) for $C_{137}H_{205}N_{33}O_{34}SSe$, $[M+H]^+$: 2969.42 predicted. [M+4H]4+: 743.10, [M+5H]5+: 594.68 observed.

For the SeNBD-variants of the peptide, the masses of peptide obtained were calculated from prepared stock solutions to minimise the measurement error with small amounts of the material obtained.

4.3.2 Optical characterisation of NBD dyes

Optical properties were measured in a Synergy H1 BioTek spectrophotometer as previously described.[215] For liposome experiments, phosphatidylcholine (PC)-based liposomes were purchased from Liposoma, diluted in PBS and transferred into a black flat-bottom 96-well plates (ThermoFisher) for optical measurements. All experiments were performed in triplicate, unless otherwise indicated.

4.3.3 Aggregate immobilisation and staining

Human α-syn was obtained from StressMarq:

- monomer (Type 1, catalogue number SPR-321)
- kinetically stable oligomers (SPR-484)
- preformed fibrils (Type 1, SPR-322)
- preformed fibrils (Type 1, SPR-317)

Sample preparation followed the previously published protocol.[216] Briefly, coverslips were cleaned using argon plasma for 45 min to remove autofluorescent organic contaminants. Ibidi 18-well sticky chambers were affixed to the glass. 50 μL of PLL (Sigma-Aldrich, P4707-50ML) was incubated in the chamber for 15 min. Excess PLL was removed by washing three times with 0.02 μm–filtered PBS. Protein (500 nM, each type) was incubated on the surface for 1 hour and replaced with imaging solution before imaging. Imaging solution contained ThT (5 μM) and imaging peptide (JF646-PSMα) at either of the three concentrations 0, 0.5 nM, 10 nM, 100 nM. V4SeNBD PSMα or F9SeNBD PSMα were used at either of the three concentrations 0, 10 nM, 100 nM, 500 nM.

4.3.4 TIRF imaging

Single-molecule and super-resolution imaging was performed on a Total Internal Reflection Fluorescence microscope (TIRFM) described in Methods section 2.4.2. The laser lines and mirrors are described therein.

Liposomes

50 μL of poly-L-lysine (PLL) (70,000-150,000 Da, Sigma-Aldrich) was added to a coverslip and incubated for 30 minutes, before being washed with PBS three times. Liposomes (Liposoma) were diluted 100-fold to a concentration of 0.04 mg/mL and incubated on the coverslip for at least 10 min. Three PBS washes were then performed to remove excess sample. BODIPY-FL or compound 7 were added at either 10 nM or 1 μM and imaged with 515 nm excitation for 50 frames. To determine the photobleaching lifetimes, the liposomes imaged with 1 μM compound 7 μM or BODIPY-FL were segmented and their intensity profiles over the frame stack were fit to an exponential decay. Only fits with an $R^2 > 0.70$ were considered (Python code available at: https://doi.org/10.5281/zenodo.7275931).

Aggregate imaging

The ThT was excited using 405 nM laser (100 W cm^{-2}) and the JF-646 peptide using 638 nm illumination (50 W cm^{-2}). 50 frames were recorded in each channel. 9 regions of interests were imaged for each condition. Maximum projection z-stacks were created in Fiji. Number of spots was determined using the Find Maxima function with Fiji with prominence set to 350.

4.3.5 Brain sample preparation and staining

Paraffin-embeded brain sections were mounted on coverslips to accomodate 8 2-mm biopsy punch-out of tissue per slide. Both PD and healthy controls were stained and image. The brains were part of the PINE cohort, the cases and numbers imaged were as follows: 130/17 for an individual with PD with dementia, and 15/19 for a healthy individual. In both cases the tissue section came from putamen.

The staining for α-syn included the following staining agents:

- JF-646 PSMα
- Phospho S129 antibody (ab209422, Abcam) - primary antibody
- AF-586 labelled secondary (ab175695,Abcam)
- Hoescht (1:800 dilution, mg/mL)

The staining process was split across two days and involved:

- **Tissue deparaffinisation:** 4 washes by submering slides in xylene (5min), xylene (5min), 100% EtOH (5min), 70% EtOH (5min), followed by a wash in running tap water.
- **Antigen retrival:** The coverslips were placed in citric buffer (10 mM citric acid, pH = 6.0) and pressure cooked for 5 min (browning meat setting).
- **Ibidi chamber mounting:** The slides were air dried and argon dried to remove residual water. The tissue was aligned to ibidi chambers and the sticky wells were applied to the coverslip.
- **Permeabilisation:** The slides were washed with PBS (2 $\times$, 5 mins) and incubated in permeabilisation buffer (PBS, 0.3% v/v Triton-X, 15 min). The slides were thorouhgly washed (3 $\times$ PBS, 5 min). Following this step the sections were kept hydrated at all times.
- **Autofluorescence quenching (when carried out):** Sections were washed in 70% ethanol (2 min). True Black was placed over each section (1:20

dilution in 70% EtOH, as per manufacturers recommendation) and incubated for 20 mins (in the dark). PBS wash was performed (5 min). TrueView was prepared as per manufacturers recommendation and incubated over the sections for 5 mins in the dark. 3 × PBS washes were performed next.

- **Blocking:** Sections were incubated for 1hr in blocking buffer (PBS, 1% Bovine Serum Albumin, salmon sperm DNA 1:100 dilution).

- **Staining - overnight:** Staining buffer was prepared in blocking buffer and included primary antibody at 1:1,000 dilution (1.02 μg/mL) and the peptide (variety of concentrations). The sections were left in the fridge (4 °C) for anywhere between 14-18h, covered from light.

- **Staining - following morning:** The sections were washed 3 × PBS, before the secondary anitbody (1:1,000, 1.0 μg/mL) and Hoescht (1:800) were applied for 2h at r.t. in the dark.

- **Curing:** The sections were washed 2 × final times with PBS, before air-drying for 5 minutes and curing in Prolong Gold (antifade mountant, ThermoFisher) to preserve the tissue until imaging.

4.3.6 Brain sample imaging

Pre-prepared brain samples were imaged either on a spinning disk confocal set-up (Opera Pheonix Plus) by Dr Justyna Cholewa-Waclaw or on the FS-FLIM by the author. QuPath and ImageJ were used for image generation and data processing. The FS-FLIM measurements used 470 nM illumination. Histogramming mode used was hist 2, and the exposure time ranged from 3,000-8,000 ms. Images processed as before.

4.4 Results

4.4.1 Fluorogenic properties of SeNBD-labelled probes

To demonstrate the fluorogenic properties of SeNBD and its potential for fluorescence imaging, the dye was first conjugated to form a lipid-analogue compound. The carboxylic acid moiety of SeNBD was activated and conjugated to a long chain alkyl amine, following the reaction shown in Figure 4.4.1A. Two compounds of different length (n = 12 and n = 18) were initially prepared. The compounds were isolated and purified, before testing their fluorescent properties.

Phosphatidyl choline (PC) liposomes were chosen as a good model system for hydrophobic environments. These artificial vesicles mimic cell membranes and are composed of a lipid bilayer encapsulating an aqueous core. Thus, alkyl chains of the prepared carbohydrates can insert themselves into the hydrophobic tails of the lipid bilayer. This brings the dye moiety, SeNBD, into a hydrophobic environment and enables the quantification of the observed fluorescence. As the amino acids showed fluorogenic character, it was expected the prepared probes to be significantly brighter when incorporated into the membrane of the liposomes (hydrophobic) than when in solution (hydrophilic).

The fluorescence emission was measured for both lipid-analogues in PBS and in a PBS solution containing PC liposomes. The shorter chain (n = 12, shown in Figure 4.4.1A as **compound 7**) showed better propensity to insert into liposomes, with similar trends observed in literature.[217] As expected, the lipid analogues showed low fluorescence counts in PBS. Upon addition of liposomes, the fluorescence signal for **compound 7** increased 44-fold, showing hydrophobicity-mediated switch-on of the Se-NBD fluorophore, as demonstrated in Figure 4.4.1B. This was a promising result for fluorescence microscopy, as it indicated the dye might allow to significantly reduce the fluorescent background in the buffer and achieve a high signal-to-background (S/B) ratio.

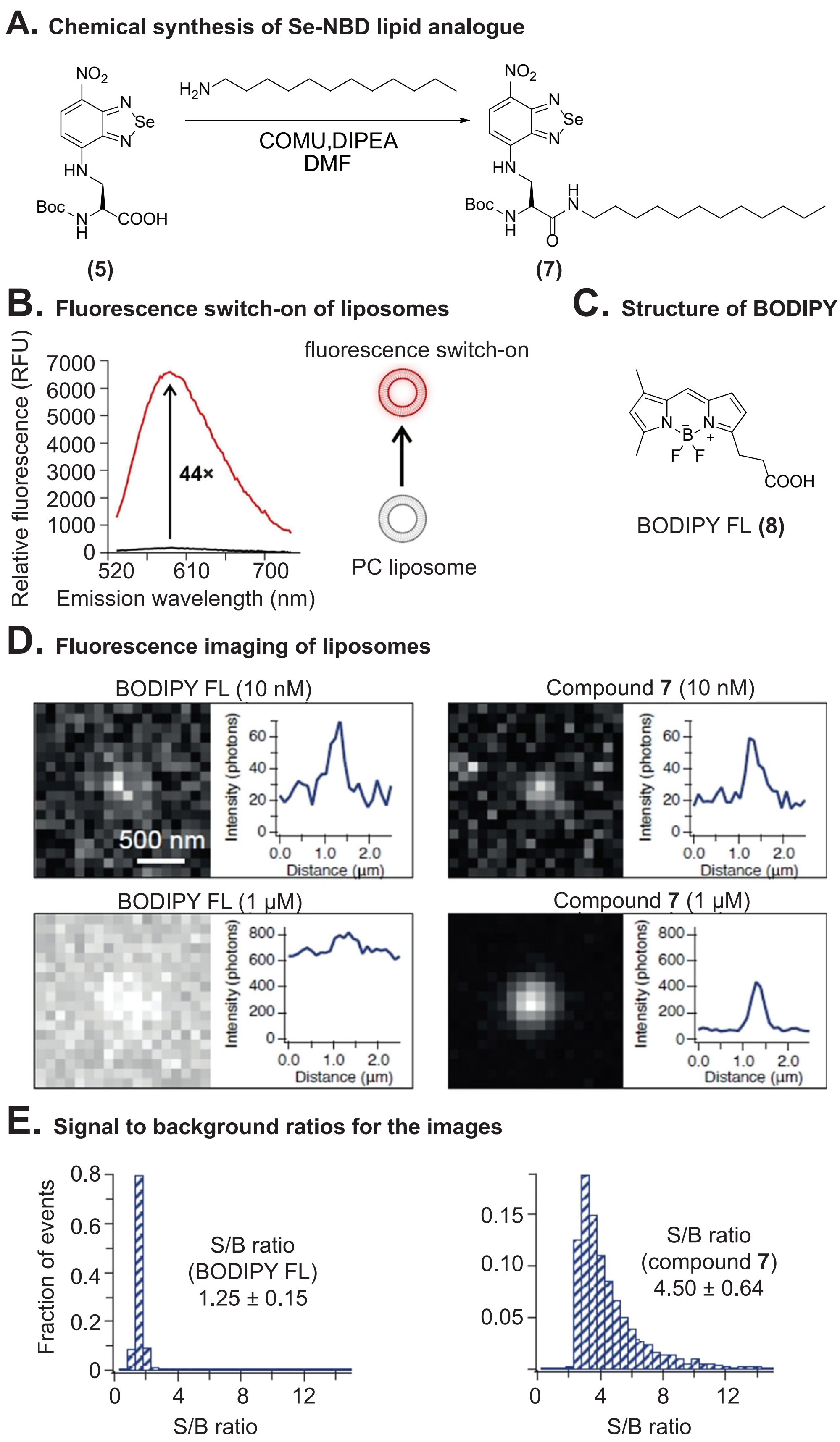
A. Chemical synthesis of Se-NBD lipid analogue
COMU,DIPEA
DMF
(5)
(7)
B. Fluorescence switch-on of liposomes
Relative fluorescence (RFU)
Emission wavelength (nm)
44×
fluorescence switch-on
PC liposome
C. Structure of BODIPY
BODIPY FL (8)
D. Fluorescence imaging of liposomes
BODIPY FL (10 nM)
Compound 7 (10 nM)
BODIPY FL (1 μM)
Compound 7 (1 μM)
500 nm
Intensity (photons)
Distance (μm)
E. Signal to background ratios for the images
Fraction of events
S/B ratio
S/B ratio (BODIPY FL) 1.25 ± 0.15
S/B ratio (compound 7) 4.50 ± 0.64

Figure 4.4.1: Visualising PC liposomes with a SeNBD-labelled lipid analogue A. Synthesis of Se-NBD containing lipid-analogue for insertions into liposomes. B. Fluorescence of the compound at 10 μ in PBS (black) vs in presence of PC liposomes, showing the fluorescence switch-on. C. Structure of BODIPY FL, lipid labelling dye. D. Fluorescence imaging of liposomes stained with compound 7 and BODIPY FL, without any washing steps. Line profiles showcase intensity across the image - the presence of a peak suggests liposomes appear brigher above background. D. Quantification of S/B for the 1 μM lipsome images for BOPIPY FL and compound 7. S/B presented as mean $\pm$SD, from n=8.

To illustrate the advantage of the fluorogenic dye, its performance was tested against a commercial lipid-dye, BODIPY FL (structure shown in Figure 4.4.1C). The PC liposmes were incubated with two concentrations of **compound 7**: one low (10 nM) and one high (1 μM), and the same experiment was repeated with BODIPY-FL. The samples prepared this way, with no washes, were imaged using TIRFM. At low dye concentration, Se-NBD and BODIPY FL showed similar performance when visualising liposomes (Figure 4.4.1D). Increasing the dye concentration allowed for the visualisation of SeNBD-labelled lipsomes clearly above background. The BODIPY FL-labelled liposomes were not detectable due to the increased background fluoresence of the dye, as can be observed both in the images and intensity traces across the image pixels in Figure 4.4.1D. To successfully use BODIPY at micromolar concentrations and detect individual liposomes, a wash step was needed. SeNBD-labelling was compatible with wash-free imaging of the prepared sample.

To further illustrate this point, the S/B ratio was quantified for liposome images taken with 1 μM of each of the two dyes (Figure 4.4.1E). The BODIPY FL had a S/B ratio of 1.5, whereas the S/B ratio was higher for Se-NBD at 4.50.

Further applications of the fluorogenic Se-NBD dye focused on incorporation of the amino acid variant of the dye (**compound 5**, Fmoc-SeNBD-OH) into peptide sequences. Specifically, it was hypothesised that the PSMα peptide could be derivatised with the dye, whilst retaining its α-syn binding properties, and used to image pathological protein aggregation *in situ*. It was hoped that the small size of the dye and its incorporation directly into the sequence would enhance the fluorescence upon binding to target whilst allowing the peptide to retain its native binding.

4.4.2 DAB staining for α-syn pathology with biotin-PSMα

With the goal of visualising pathological α-syn *in situ*, the first technique investigated was immunohistochemistry. IHC experiments are routinely performed to examine *post-mortem* tissue and used to visualise pathological protein inclusions in patient tissue. The IHC staining could confirm if the prepared peptide can penetrate tissue efficiently and stain pathological features above background. To this end, a biotin-labelled PSMα peptide was first prepared. The full PSMα sequence was prepared using SPPS methods and an N-terminal biotin moiety was introduced. The peptide was purified following derivatisation and supplied to a collaborator to conduct a pilot IHC staining.

Dr Jenna Gregory at the University of Aberdeen performed the staining experiment using the supplied peptide to visualise α-syn. A 500 nM peptide solution was used to incubate pre-processed tissue sections overnight. The biotin was used to visualise the stained locations, through DAB staining in presence of strepatvidin-HRP. Example images from this staining are presented in Figure 4.4.2.

The peptide signal corresponds to the brown-stained areas (due to presence of DAB) and the blue is a counter-stain to visualise the nuclei. The pathological features in the images were also assigned by Dr Jenna Gregory. In these images, PSMα successfully identified aggregated α-syn in form of mature LBs (white arrows), smaller intracellular LBs (orange arrows), and even smaller aggregates (blue arrow). As could be seen on the staining pattern of the larger LBs (white arrows), the peptide did not penetrate all the way through the structure of the LBs. Optimisation of the staining protocol (longer incubation time, varying the peptide concentration) could help mitigate this issue.

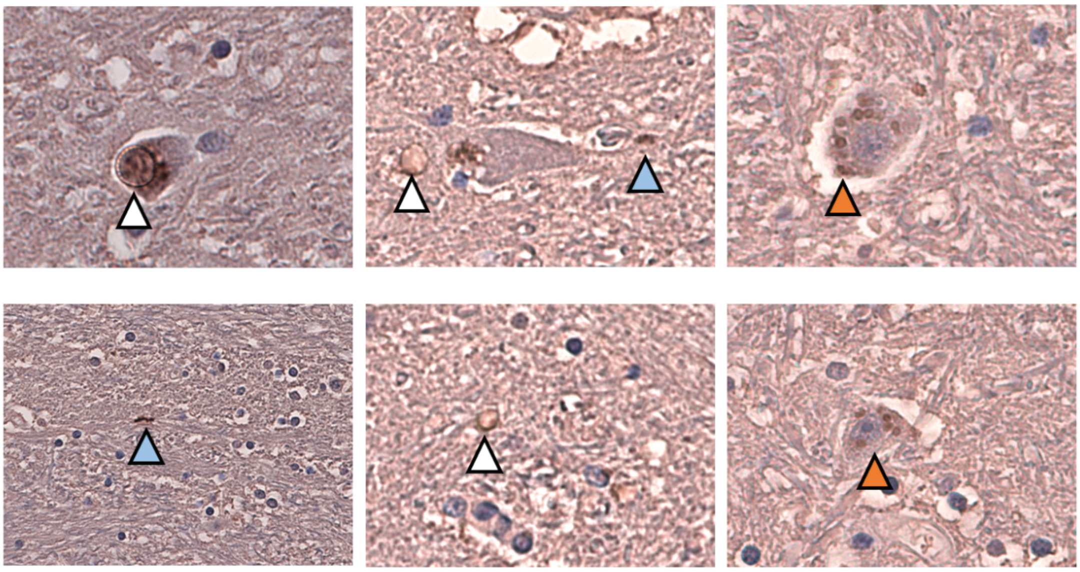

Figure 4.4.2: DAB-staining for α-syn pathology with biotin-PSMα. 6 panels showing brain tissue of an individual with PD stained for α-syn pathology using the peptide. Brown signal corresponds to peptide and blue to nuclear stain. Blue arrows: aggregates, white: Lewy Bodies, orange: small intracellular LBs. Experiment and pathological assignment performed by Dr Jenna Gregory.

This data set provided encouragement that the peptide could be a good staining agent for tissue. The peptide was able to penetrate tissue and stain features-of-interest when following standard tissue staining protocols. The peptide signal in the tissue corresponded to pathological α-syn inclusions as identified by a pathologist, further suggesting the probe was suitable for *in situ* studies. Further IHC experiments, including the staining of aged-matched healthy control tissue and comparing the peptide signal to a gold-standard α-syn antibody, are needed to explore the feasibility of using biotin-PSMα to classify disease state and stage.. The lack of expertise in describing pathological inclusions and short tissue supply, meant that further efforts did not focus on IHC staining. IHC provides a standardised approach to tissue staining and is compatible with high-throughput tissue processing, however the technique has its drawbacks. The DAB staining limits the contrast that can be achieved and is not compatible with multiplexing (one probe needs to be tested at the time). Moreover, the resolution that can be achieved is limited, and the smaller aggregate species are not easily visualised. Thus, a fluorescence label for the PSMα peptide was considered next. Fluorescence is characterised by high contrast and could provide definitive identification of α-syn through multiplex staining with the peptide and an antibody at the same time.

4.4.3 Fluorescence imaging with the PSMα peptide

Fluorescence microscopy offered several key advantages over the IHC approach. The high sensitivity of fluorescence detection set-ups and the low background in most fluorescently-labelled samples increase the contrast that can be achieved. Multiplexed imaging, where several probes with different fluorophores can be imaged simultaneously, is possible and lends itself to co-localisation studies between a known-binder and a newly-developed probe. Quantitative analysis is also possible with fluorescence microscopy, increasing the amount of data that can be extracted from every experiment.

Thus, a fluorescent label was introduced to the PSMα peptide. The first attempt at fluorescent functionalisation focused on incorporating a bright, "always on", commercially-available dye. The method for its incorporation followed the protocol previously described by Santos *et al.*. To generate a fluorescent version of the PSMα peptide, the full sequence was first prepared using SPPS methods. An additional cystein residue was installed at the N-terminus. The cystein incorporation enabled a Click chemistry coupling to a JF646-maleimide. A far-red dye was chosen for its compatibility with multiplexing and an excitation away from the UV-region of the spectrum reserved for autofluorescence, nuclear stains, and the gold-standard amyloid dye ThT. Whilst the conjugation itself was relatively easy, the peptide sequence needed to be purified prior to the Click reaction and following the Click reaction. Thus, two rounds of semi-preparative purifications were conducted, which did not only prolong the process, but likely led to loss of yield (the fluorescent peptide was prepared at 1.7 μM scale). However, JF646-PSMα was delivered successfully.

To test whether the labelled peptide would be able to detect α-syn *in vitro*, an assay was conducted. Various forms of pre-aggregated α-syn were obtained from StressMarq, including monomer, oligomers and fibrils. The oligomers were kinetically stable oligomers (KSO), oligomeric species associated with pre-fibrillar secondary structure.[218] The fibrils came in two types: Type 1 (more rigid, a polymorph associated with PD) and Type 2 (more flexible, twisted polymorph associated with MSA).[219] All protein samples were incubated on a coverslip. JF646-PSMα and ThT containing imaging buffer was then applied over the proteins and the coverslips imaged on the TIRFM. 50-frame stacks were acquired and the maximum intensity projections of these generated and compared. Figure 4.4.3 shows representative images of KSO and the two types of fibrils imaged with 10 nM peptide (red) and ThT (blue). The oligomeric species images showed few small spots co-localising in both channels, indicating most KSO were non-ThT active. However, more events were detected in the red (peptide) channel with no corresponding ThT signal. It is possible that these early oligomers do not exhibit extensive β-sheet structures for ThT incorporation, and the peptide is a better suited probe for the detection of those species. The images of the fibrils showed more dense peptide events (presumably corresponding to larger protein species). Type 1 fibrils showed some co-localisation with ThT, whilst examples of signal co-localisation with type 2 fibrils were hard to come-by. The amyloid fibrils are characterised by their β-sheet structure and thus they were expected to be ThT active. The lack of perceived ThT staining was therefore somewhat surprising. However, it is possible the peptide and ThT compete for the same binding sites in case of the mature fibrils or inadvertently block the mode of interaction of the other imaging agent through introducing steric hindrance across the surface. A FRET interaction between the two dyes is also not impossible. This would require further investigation to determine with certainty. Staining the fibrils with the two probes separately and testing out the sequential staining, through addition of a peptide solution first and then ThT could confirm whether this reflected a low content of β-sheet-rich fibrils in the imaged samples or revealed the incompatibility of PSMα with ThT. Super-resolution imaging was not attempted at this stage.

Next, the performance of 10 nM peptide was compared across the different protein species. The number of spots (as determined with the same prominence threshold) was detected across the different wells (Figure 4.4.4A). The trends

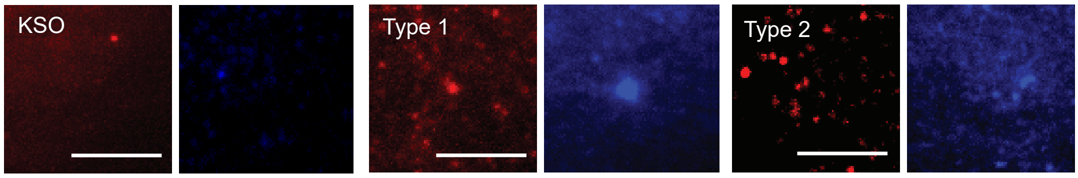

Figure 4.4.3: Imaging α-syn oligomers and fibrils with 10 nM JF646-PSMα and 5 μM ThT to visualise oligomeric and fibrillar species immobilised on a surface. Scale bar 5 μm.

observed were encouraging. The control slide used 1% BSA solution in place of α-syn. Application of the imaging peptide directly to a PLL-coated slide was avoided, due to previously observed peptide aggregation on the coated surface. Whilst some events were detected even without the α-syn present, the number of spots detected in presence of protein was notably higher. KSO sample and both types of fibrils (Type 1: Fibril 1 and Type 2: Fibril 2) all produced hundreds of events. The signal detected in the monomer sample was increased with respect to the control, but less so than with KSO and fibrils. Since the monomer was not pre-processed prior to the experiment, it was hypothesised some aggregation could have occured during the handling of the protein. Thus, the detected events were not suggestive of the peptide binding to the monomer.

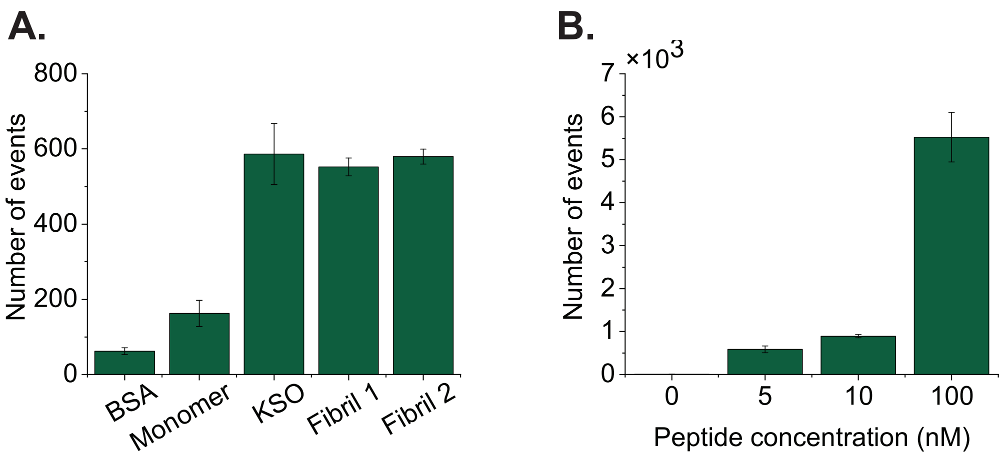

Figure 4.4.4: Investigating the binding of JF646-PSMα to α-syn. A. The number of localisations (defined as number or events detected in 50 frames of an image, mean $\pm$ SD, n = 3) detected when imaging different forms of α-syn (500 nM) and BSA control. B. The number of events (defined as in A) as a function of peptide concentration, when imaging KSOs (500 nM).

In case of the KSOs and fibrils, many events were detected. A further experiment investigating the effect of protein concentration on the number of spots detected could be performed in the future. Perhaps an incubation with a lower concentration protein (here 500 nM protein was used in all cases) could be considered for further applications. Equally, decreasing the peptide concentration in future imaging experiments could be used to further optimise the imaging conditions, especially given the high numbers of events detected in the concentration regime investigated. Figure 4.4.4B presents the difference in the number of events detected for KSO at 0, 5, 10 and 100 nM respectively. It is important to note the same prominence threshold was used for all these. The prominence threshold became less meaningful in the 100 nM peptide case, where the background was higher. Encouragingly, few events were observed at the 0 nM peptide condition, with a steady increase in spots observed with the increase in peptide concentration.

Driven by the encouraging results observed in the *in vitro* experiments, further attempts focused on using the red-labelled JF646-PSMα for tissue staining. To this end, patient-derived tissue sections were processed. The wax embedding medium was removed, antigens retrieved through incubation in hot citric acid, the tissue was permeabilised and non-specific binding blocked through application of BSA solution. The staining agents used included the PSMα peptide (excited by the 635 nm laser and detected in the red channel) and a gold-standard anti-α-syn antibody phospho S129 (imaged in the 580 nm channel). The antibody detects α-syn with a post-translational modification (phosphorylation of serine at position 129) present in LBs and associated with pathological aggregation.[220] The stained sections were imaged on a spinning disk confocal microscope, chosen for this purpose due to its high throughput capabilities.

First, unstained sections were imaged as a control. Representative images of unstained tissue are presented in Figure 4.4.5, where the PSMα channel is shown in red and the antibody channel (590 nm excitation).

Despite the lack of staining, the images reveal autofluorescence pattern of small granular puncta, in both channels. When the red and green images were overlayed,

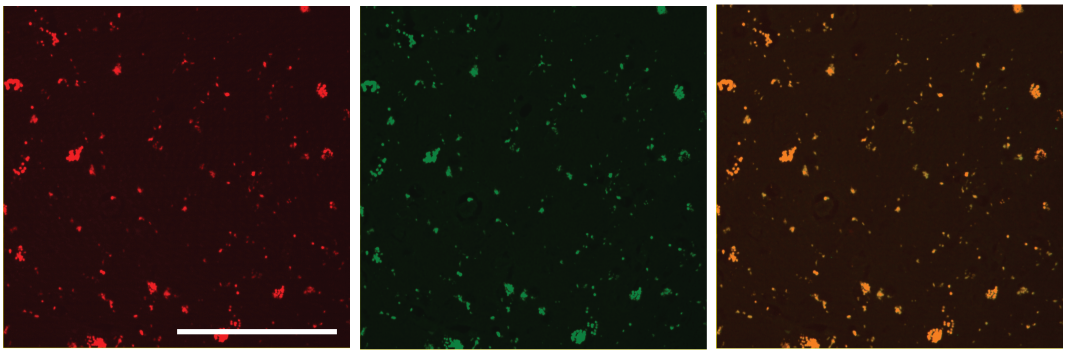

Figure 4.4.5: Autofluorescence of PD-patient derived brain tissue recorded in two channels: 580 nm (presented in green) and 650 nm (presented in red). The third image is an overlay of the two channels. Scale bar is 100 μm.

the fluorescence signal showed perfect co-localisation with all features in yellow. These were identified as lipofuscin, an “aging pigment” formed from degradation by-products of mitochondria, present throughout neurons in aging cells.[221] It is characterised by broad fluorescence emission, and thus can be detected across both emission channels. Lipofuscin can be segmented out of images, where the structural features of the target of interest are different to those of lipofuscin. Unfortunately, α-syn aggregates in neuronal cells form a similar pattern of puncta and granules distributed around the cell making the distinction between the two challenging.

Next, the tissue was stained with 200 nM PSMα peptide and the Phosho S129 antibody and imaged to check if the staining could be observed above the autofluorescence levels. Representative images are presented in Figure 4.4.6.

The peptide channel showed the desired aggregate structures. However, when compared to the antibody channel (green, on the left hand side image), an almost complete overlap between the two was observed. This was deceptively similar to the non-stained tissue case. Therefore, it was reasoned the puncta were in fact not a result of the peptide staining, but autofluorescence of lipofuscin. It was suggested the autofluorescence signal was stronger than the peptide staining, obscuring any real α-syn structures. Alternatively, it is also possible that PSMα has some propensity to bind to lipofuscin, given the make-up of the granules (lipids) and the hydrophobic character of the peptide. This interaction could explain the overlap

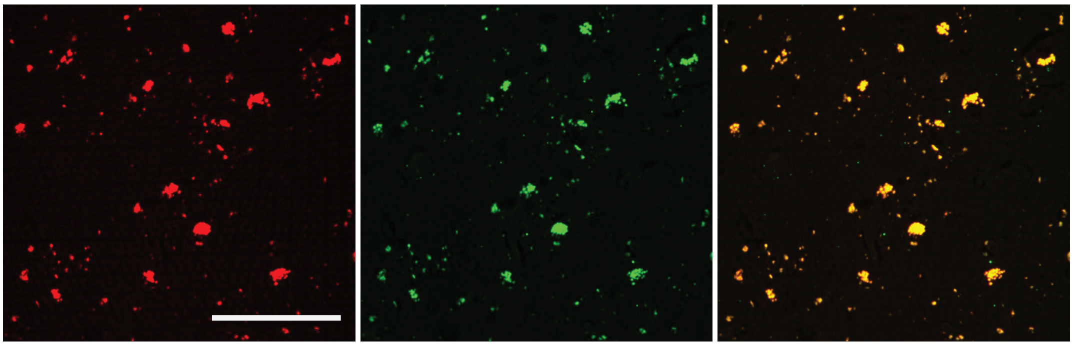

Figure 4.4.6: Immunoflorescence staining for α-syn pathology with JF646-PSMα (PD-patient derived brain tissue). Representative ROIs showing peptide staining (200 nM, red colour), antibody staining (Phospho S129 anti-α-syn antibody, green colour), and a merged image of the two channels. Scale bar is 100 μm.

between the channels, but would not be distinguishable from autofluorescence on the red image. Moreover, due to the deceptively similar appearance of lipofuscin to the protein aggregate structures, it would be impossible to segment it out of the image. Other methods, such as spectral unmixing[222] could be employed to remove lipofuscin signal. The dye emission spectrum should provide a sharp peak at emission maximum as opposed to the broad emission of lipofuscin. Spectral unmixing could differentiate between the fluorophore and autofluorescence signals, based on the emission profile. A lipofuscin imaging channel (excitation 488 nm, emission 647 nm) was even devised by another group member, however since the un-mixing matrix was prepared with a different emitter in mind, it could not be readily applied to the above case. Further optimisation of the method would be necessary to fully address the problem and observe the actual peptide staining.

Thus, quenching steps were introduced to the staining protocol to mask the autofluorescence signal and reveal peptide staining. Two quenchers: TrueBlack and TrueView were used. The two agents block endogenous emitters through chemical reaction modifying the emitter and disrupting fluorescence and physical blocking of autofluorescent lipids. The quenching steps were introduced before the blocking step and the application of imaging agents (as before: a S129 α-syn antibody and various concentrations of the peptide). The sections were then imaged on a spinning-disk confocal microscope (Figure 4.4.7).

All peptide concentrations used (10 - 200 nM) in the experiment led to low

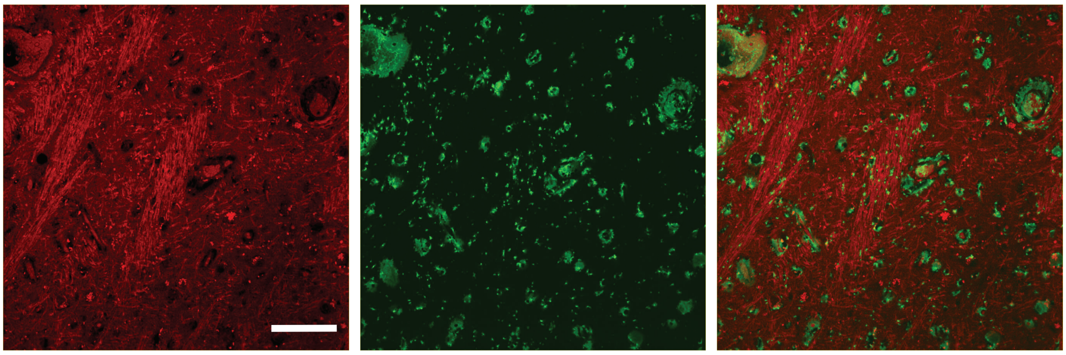

Figure 4.4.7: Immunoflorescence staining for α-syn pathology with JF646-PSMα (autofluorescence-quenched tissue, disease case). A representative ROI showing peptide staining (200 nM, red colour), and peptide staining merged with α-syn antibody (green). Scale bar is 100 μm.

levels of red fluorescence. Despite the fluorescence quenching steps, the far-red dye should remain able to absorb and emit photons under the experimental conditions. Additionally, the staining pattern recorded in the red channel did not resemble the expected "punctate" appearance expected of α-syn. The green (antibody) channel showed an expected pattern of fluorescent puncta and aggregate-like structures, similarly stained features were expected in the red channel also. The peptide signal seemed more likely a result of remaining autofluorescence or off-target interactions with lipid membranes. It was reasoned that the application of the autofluorescence quenchers potentially interfered with the peptide fluorescence or its ability to recognise the target. Thus, a different technique was considered to try to visualise the peptide signal in tissue.

4.4.4 FLIM imaging with SeNBD-labelled PSMα

With the lipofuscin interfering with fluorescence intensity images, the attentions were turned to FLIM next. It was hypothesised that the autofluorescence and peptide fluorescence would differ in lifetime. Thus, lipofuscin could be separated out of the image through applying a lifetime-mask to the intensity image. The FS-FLIM system was used for this round of experiments, as the additional spectral and lifetime information could make the deconvolution of the autofluorescence from sample fluorescence easier.

To that end, the nitrobenzodiazole derived amino acid, Fmoc-SeNBD-OH **(compound 5)**, was next incorporated into the PSMα sequence. The SeNBD amino acid was used for this purpose due to its polarity-dependent switch-on and lifetime sensitivity. The fluorescence labelling was achieved using SPPS methods and did not require extra steps or purifications. Due to the small size of the dye, the fluorescent amino acid was used to replace native PSMα residues, rather than to decorate the N-terminal. Two amino acids, V4 and F9 were chosen to be substituted by SeNBD. It was hoped that the small size of the dye would enable substitutions without disrupting the secondary structure or the binding. Given the length of the sequences, and some previous success with internally-labeling shorter sequences (discussed in further chapters), the peptides seemed likely to tolerate the substitution. This would have to be confirmed through biophysical characterisation of the probes to know for certain. Assuming the mode of recognition relies on non-specific hydrophobic interaction, two hydrophobic amino acids were chosen to be swapped out for SeNBD. Both valine and phenylalanine are hydrophobic amino acids, and phenylalanine is structurally most similar to the SeNBD core. In both cases, the Fmoc-SeNBD-OH was used in microwave-assisted synthesis, was incorporated on resin and remained stable throughout the following deprotection, coupling and cleavage steps. A purification step yielded V4SeNBD-PSMα and F9SeNBD-PSMα. No capping steps throughout the synthesis were used in this instance, though they could perhaps be implemented in the future to ease the purification. The gradient of the eluent system used needed to be adjusted iteratively to ensure a good resolution of the peptide from n-1 impurities.

Fmoc-SeNBD-OH (**compound 5**) was first characterised using the instrument (Figure 4.4.8).

5 μM solutions of the fluorescent amino acid was prepared in water/glycerol mixtures, with an increasing glycerol percentage. It was hypothesised that the more viscous environment would cause both the fluorescence switch-on of they dye (more emission observed in glycerol vs water) and show lifetime variability (longer lifetimes expected in high viscosity solutions). The desired increase in intensity at the λ_{em} was observed (Figure 4.4.8A). The lifetime also did increase

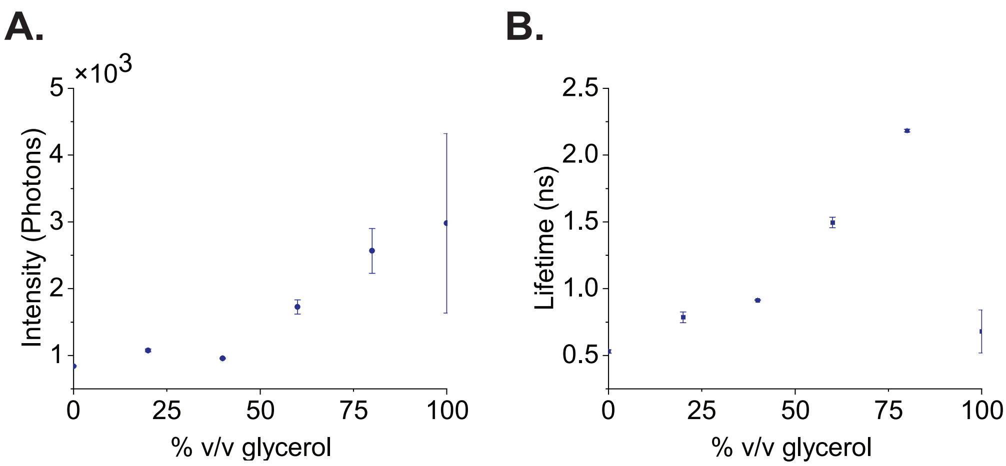

Figure 4.4.8: Intensity and lifetime of Fmoc-SeNBD-OH in solutions of increasing glycerol content. 5 μM amino acid was prepared in solutions of increasing glycerol concentration (from 0 - 100% v/v). The intensity recorded at maximum emission wavelength (n = 3 ± SD) (A) and lifetime at maximum emission wavelength (n = 3 ± SD) (B) were observed.

(Figure 4.4.8B) as expected averaging 0.53 ns in water and 2.18 ns in 80% glycerol. The lifetime measured in 100% glycerol was lower than expected. The measured fluorescence lifetime increased with the increasing glycerol content. However in neat glycerol solution, both the intensity and lifetime measurement showed more variability (higher standard deviation). Given previous difficulties when working with glycerol samples, this was not surprising.

Next, tissue sections were stained with F9SSeNBD-PSMα at varying concentrations. No quenchers were used in the staining protocol. The tissue was excited with a 470 nm laser. A FLIM image obtained using 500 nM F9SSeNBD-PSMα is presented in Figure 4.4.9A.i. Some features with punctate morphology where observed. An intensity threshold was used to pick up these features, and the average lifetime across the spectrum was calculated for these. Low lifetimes of approximately 1 ns were observed. When a histogram of these was plotted (Figure 4.4.9A.ii.) a broad distribution, potentially indicative of many populations of emitters, was observed.

When compared to unstained tissue (Figure 4.4.9B.i.), by eye the structures highlighted in both images did not vary much in appearance nor lifetime. However, the lifetime histogram (Figure 4.4.9B.ii.) showed a Gaussian-like population with

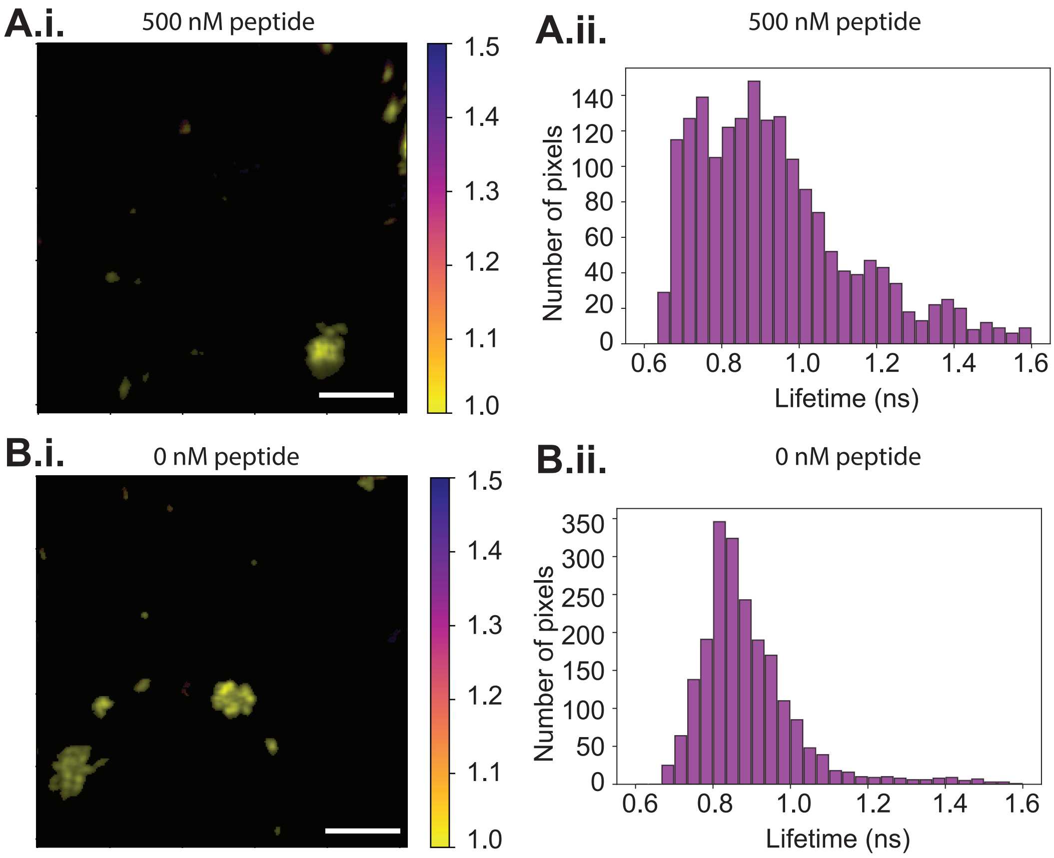

Figure 4.4.9: F9SeNBD-PSMα stained tissue observed using FS-FLIM. 500 nM peptide staining: A.i. FLIM image and A.ii. Corresponding lifetime histogram (average lifetime between 470-720 nm). 0 nM peptide staining: B.i. FLIM image and B.ii. corresponding lifetime histogram. Scale bar is 1 μm.

a narrower distribution pattern. This was indicative that FLIM could perhaps help separate the tissue autofluorescence from the peptide signal.

Thus, an attempt at thresholding out the longer lifetime pixels was attempted. Ideally, this would also involve spectral information but at this moment in time, this improvement has not been introduced due to the large overlap between the two spectra observed. Figure 4.4.10 shows emission spectra of the features observed on images in Figure 4.4.9. The two emission profiles in presence (500 nM peptide) and absence (0 nM peptide) of the peptide staining are very broad, without clearly identifiable features.

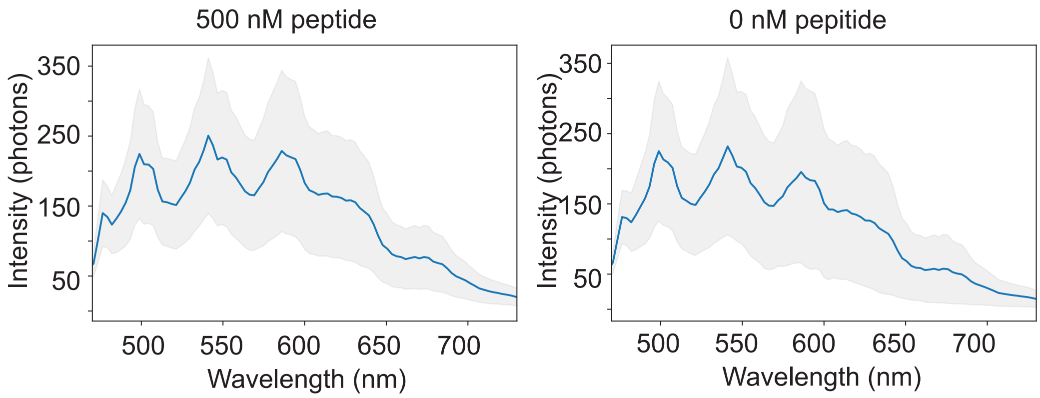

Figure 4.4.10: FS-FLIM analysis to compare peptide emission and autofluorescence in tissue. Fluorescence emission spectra generated from features of interest on previously shown images. 500 nM peptide and 0 nM peptide (lipofuscin autofluorescence) show similar emission profile as recorded by the FS-FLIM.

The results of the lifetime thrsholding are shown in Figure 4.4.11.

Figure 4.4.11A shows a summed intensity image, with zoomed-in structures presented in Figure 4.4.11B. The left hand side images are a result of zoom-in on panel A, right hand side inserts show the same ROIs with the lifetime mask applied. The highlighted pixels are associated with lifetimes longer than 1 ns (based on the expected lifetime of the probe). It can be noticed that these pixels highlight smaller structures, that appear dimmer in the main image (likely emitting fewer photons than the autofluorescent lipofuscin), often of a very pixelated pattern. This would be consistent with small aggregate-like inclusions, which would prove challenging to image with diffraction-limited techniques. However, this result is

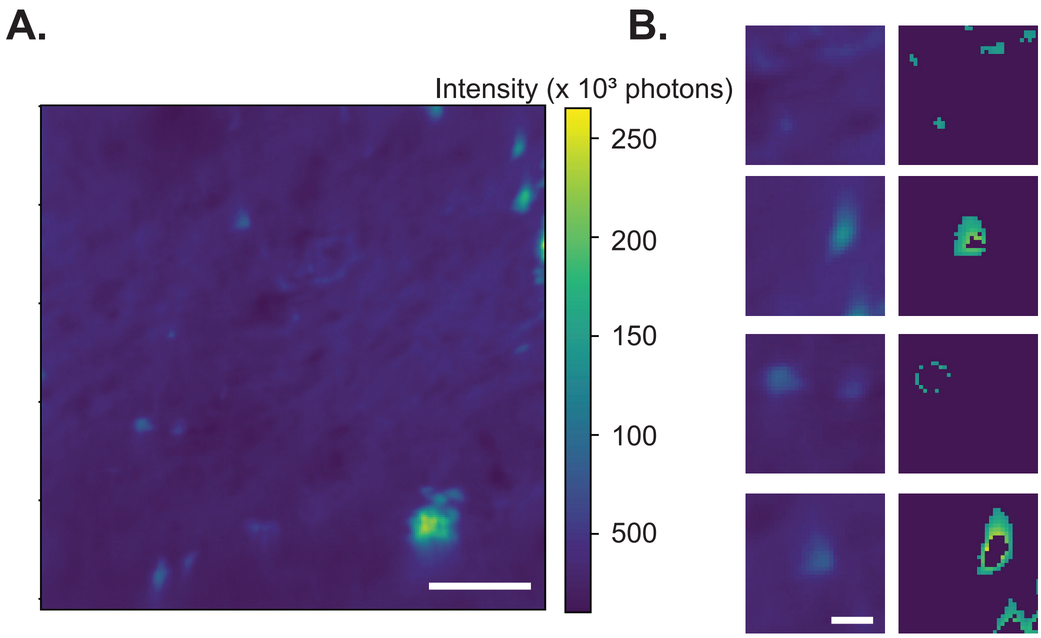

Figure 4.4.11: Removing autofluorescence based on lifetime. A. Intensity image of a representative ROI. Scale bar is 1 μm. B. Zoom-ins showing the intensity (LHS) and the pixels of lifetime above 1 nm. Scale bar is 200 nM.

by no means conclusive. Further work on using the lifetime (especially including the spectral component to unmix the two) is necessary, and a counter-stain should be used to confirm the signal is in fact coming from α-syn.

4.5 Discussion

Imaging of patient-derived brain tissue with PSMα proved to be a challenging task. The initial attempts included an IHC experiment conducted by a collaborator. The pattern of staining seemed consistent with α-syn inclusions within neuronal cells, however the peptide did not penetrate some of those features fully. The α-syn staining appeared with low contrast over the background. The protocol would require further optimisation for applications in tissue classification and disease staining. The fluorescent staining with JF646-labelled peptide was inconclusive and did not reveal the same kind of structures. Despite some success with the peptide in detecting α-syn oligomers and fibrils *in vitro* over monomer and BSA control, these structures could not be visualised *in situ*. High prevalence of lipofuscin in the imaged tissue and limited success using autofluorescence quenchers were thought to be two main reasons for this.

Interestingly, an N-terminally labelled PSMα variant was used previously to detect α-syn in tissue sections by Sim *et al.*.[223] The researchers reported the importance of using a far-red dye, BODIPY 630/650, as the use of a cyanine dye led to non-specific binding. Thus, they highlighted the fluorescent label can have implications on the probe beyond disrupting the binding to target. Their BODPIY-labelled PSMα was successfully used to visualise α-syn in PFF-injected rodent brain tissue. Sim *et al.* mentioned that a green variant of the peptide (labelled with the more common BODIPY-FL) was difficult to detect above the endogenous autofluorescence. This could explain difficulties in visualising SeNBD-labelled PSMα, especially given the broad emission of both lipofuscin and the dye, however should not impact the JF646-PSMα experiments.

The biggest difference in the experimental approaches was the tissue model used. Sim *et al.* opted to use wild-type mice injected with PFFs before culling. This treatment results in PFFs seeding aggregation and recruiting endogenous α-syn into PD-like inclusions.[224] The model can be used to track the spread of the pathology through following the α-syn spread from the injection site. With limited reports in literature on the subject, it is reasonable to assume this model leads to less lipofuscin accumulation than what would be observed in patient-derived tissue, where age and compounding factors including oxidative stress and disease-states increase the lipofuscin load.[225–227] In fact, even the age-matched control brain tissue used for this study (derived from non-PD individuals) was characterised by high lipofuscin load. Sim *et al.* did not discuss the potential propensity of the peptide towards lipofuscin, but they did choose intestinal tissue as the main sample in their study. Whilst some lipofuscin is still expected in the intestine, the levels are less. It might also be easier to differentiate between lipofuscin signal and fibrilar deposits of α-syn in the muscle cells. Although the detection of α-syn above the background in the brain was possible with the BODIPY-labelled PSMα, perhaps for these reasons Sim *et al.* focused on detection of α-syn in the intestine in their research.

With the lack of success in fluorescent staining of patient-derived brain tissue, potential issues in the used protocol where identified. One of the concerns around the experimental design was the possible competition, or epitope incompatibility, between the chosen antibody (phoshpo S129) and the peptide. Sim *et al.* successfully employed both for counter-staining and identification of α-syn. However, their protocol included incubation with the antibody as the first overnight staining agent and a much shorter (30 min) peptide staining. In the protocol used throughout this chapter, the peptide staining was performed overnight at the same time as the primary antibody incubation. It would be interesting to see if the modified protocol could produce more fluorescent signal from the peptide at the desired target.

Further differences in the protocols included no permeabilisation step (no Triton-X used), but addition of Tween-20 to blocking and wash buffer by Sim *et al.*. Tween-20 is a detergent, which can be used to block non-specific interactions, but could also help to retain a favourable conformation of the peptide probe. Addition of Tween-20 to the buffer could also reduce off-target staining and non-specific interactions. This small change to buffer composition could be easily implemented in the next staining attempt.

The fixation method and subsequent de-waxing protocol were similar between the methods described by Sim *et al.* and the protocol described here. The fixation protocol together with the antigen retrieval step could impact the availability of different epitopes for interactions with the staining agent, and thus the signal detection. However, seeing as these protocols were remarkably similar and followed standard tissue processing methods, this was unlikely to be the reason for the unsuccessful staining. Moreover alternative fixation methods could not be explored, given the fact that the tissue was fixed at the point of harvest from donor by the brain bank.

α-syn-like structures were imaged on the FS-FLIM. The advantage of the instrument could not be fully leveraged, due to the short lifetime of the SeNBD fluorophore incorporated into the peptide sequence. In addition, the broad emission of SeNBD did not produce a distinct peak over the broad lipofuscin fluorescence.

Distinguishing between the two would require PCA-type analysis. Using a different fluorophore, with longer lifetime and a sharp emission peak (ideally in the red region of the spectrum) would simplify the data analysis and potentially showcase the advantages of the FS-FLIM approach better. Another advantage of FS-FLIM was providing extra contrast by combining the technique with an environment-sensitive fluorophore (SeNBD). A probe with longer fluorescence lifetime would make this approach more promising. While the fixation could affect the absolute lifetime values measured in FLIM experiments, the relative differences between environments should reflect true differences in rigidity or polarity of the structures and thus could be used for additional analysis.

Another study successfully employing PSMα for α-syn detection was published by Giarola *et al.*.[228] The study covered the design and validation of a surface plasmon resonance based biosensor. The device surface utilised PSMα as a capture peptide to selectively immobilise oligomers. A linear relationship was observed between the oligomer concentration and the perceived sensor response, with a limit of detection estimated to be in the low nanomolar range. The oligomers were successfully detected in artificial cerebrospinal fluid (CSF) and patient-derived CSF of healthy individuals, with some modifications to the method. The study highlighted several interesting observations relevant to PSMα applications. The peptide performance was highly dependent on its conformation and ability to fold. In cases where folding was disrupted through mutation of native amino acids or tight packing on the sensor surface, less peptide-oligomer interactions were observed. The peptide was shown to bind to monomer more in those cases too, although likely just through non-specific binding mechanisms rather than sequence recognition. The introduction of SeNBD in the PSMα sequence, although closer to the N-terminus than the known fold-disrupting mutations (K9P-F11P), could influence the secondary structure in solution. The SeNBD amino acid is believed to be more favourable than a proline substitution (known to introduce kinks and disrupt α-helices), but the true effect of these mutations in the buffer conditions should be assessed in a circular dichroism experiment. Furthermore, the complex matrix of CSF led to a higher limit of detection for the sensor, suggesting detection varies in different media. The researchers found the addition of Tween-20 particularly useful in inhibiting non-specific interactions. This was the second report of Tween-20 supplemented buffer for work with PSMα and such buffer should be tested in the experimental protocols used for tissue staining here also. Overall, the study aligns with the observations made in the TIRFM *in vitro* experiment and suggests the need to further adjust the protocol when moving from solution to immobilised surface detection (or solution to tissue) particularly with regards to peptide conformation.

4.6 Conclusions

In summary, the fluorogenic properites of SeNBD were investigated. The dye showed an increased fluorescence upon incorporation into liposomes and an improved S/B ratios when compared to a conventional dye. The small size of the dye was further exploited through its incorporation into peptide sequences.

Four derivatised versions of PSMα peptide, a known α-syn binder were prepared. Firstly, a biotin-variant was made and tested in an IHC experiment. The peptide labelled α-syn species (LBs and smaller aggregates), but did not penetrate all the way through tissue. A full study (including staining of aged-matched controls) could further validate the success of IHC staining with PSMα. A JF646-PSMα peptide was used in preliminary studies to detect *in vitro* α-syn aggregates and to stain patient-derived brain tissue. Whilst the *in vitro* study gave promising results, the tissue staining proved difficult due to the endogenous lipofuscin fluorescence. The peptide signal was covered up by tissue autofluorescence and the peptide staining did not work in presence of quenchers. Thus, a FLIM-compatibile version of the peptide was prepared. The Fmoc-SeNBD-OH amino acid was used to replace an internal residue in the PSMα sequence giving two internally-labelled peptides for fluorescence lifetime imaging applications. FS-FLIM was able to reveal some differences in lifetime between the 0 and 500 nM peptide conditions. An attempt at separating out α-syn signal using lifetime was made, however the nature of the highlighted features should be confirmed with an antibody counter-stain.

4.7 Future perspectives

Whilst the initial attempts suggest with further work the PSMα peptide with a SeNBD dye could be used to image PD-patient derived tissue, there is several things of interest that should be investigated next.

The performance of the SeNBD-labelled peptides should be compared to that of JF646-PSMα. Given the smaller size of SeNBD, the effect of the dye in the peptide scaffold on the dissociation constant, K_D, would be interesting to measure. JF646-PSMα, at low nM or even pM concentrations, should be tested for potential applications in super-resolution microscopy.

The lifetime-sensing properties of SeNBD-labelled peptides could be further tested on an more relevant *in vitro* system. StressMarq proteins were not imaged on the FS-FLIM, due to their small size, but they could be incubated with peptide and the fluorescence lifetime measured using a fluorometer. It would be interesting to see if the lifetime varies from oligomers to fibrils, and whether it remains similar irrespective of fibril type. Equally, the switch-on of the peptides could be quantified with α-syn oligomers or fibrils in a plate reader assay. The effect of the position of the SeNBD could be better understood, if that data was to be collected.

Should the biotin-PSMα to be used in IHC staining further, a validation study comparing the peptide to the current gold-standard staining method would be necessary. Such a study could help evaluate the performance of the peptide and understand its potential advantages over the use of antibodies.

Lastly, optimisation of all imaging conditions might be necessary before further studies: a different quenching protocols could be investigated for the use of JF646-PSMα in tissue, or robust lipofuscin detection and removal pipelines could be developed in image post-processing and data analysis.

4.8 Contributions

Dr Fabio de Moliner prepared the Fmoc-SeNBD-OH used in the experiments and the liposome probes. The author synthesised all peptide probes. Prof. Marc Vendrell carried out the plate reader experiments characterising liposomes. Dr Rachel James performed the incubation of α-syn on the pre-prepared ibidi plates for staining and imaging. The author designed the experiment, prepared the surface and the staining reagents and provided instructions for the incubation step. The author imaged the ibidi plates and processed the acquired data. The tissue was fixed by the brain bank. Judi O'Shaugnessy and Bev Notman performed the tissue coring, block preparation and sectioning. The brain staining was initially performed with Judi O'Shaugnessy's help and expert supervision. The author designed all experiments, decided on staining conditions and prepared the tissue independently for the experiments described. Dr Jenna Gregory performed and analyzed the IHC staining using the biotin-PSMα. Dr Justyna Cholewa-Waclaw imaged the brain samples on a Spinning Disk confocal set-up. All other imaging was done by the author as was all the image processing and analysis.

Chapter 5

Fluorogenic peptides for super-resolution imaging

5.1 Scope of the chapter

This chapter covers work in the design and application of peptide probes for super-resolution microscopy. A short peptide sequence with specific target-binding properties was modified with a fluorogenic amino acid and used to image Post Synaptic Density 95 protein (PSD-95) *in situ* to illustrate the nanostructure of the protein complex.

Parts of the work covered in this chapter have been published in the following journals, following peer review:

- **Imaging proteins sensitive to direct fusion using transient peptide-peptide interactions.** Z. Gidden, C. Oi, E. J. Johnston, Z. Konieczna, H. Bhaskar, L. Mendive-Tapia, F. de Molinier, S. J. Rosser, S. G. J. Mochrie, M. Vendrell, M. H. Horrocks, L. Regan, *Nano Lett.* 2023, **23**, 22, 10633-10641

- **Small fluorogenic amino acids for peptide-guided background-free imaging.** F. de Molinier*, Z. Konieczna*, L. Mendive-Tapia, R. S. Saleeb, K. Morris, J. A. Gonzalez-Vera, T. Kaizuka, S. G. N. Grant, M. H. Horrocks, M. Vendrell. *Angew. Chem. Int. Ed*, 2023, **60**, e202216231

  * these authors contributed equally

5.2 Introduction

5.2.1 PAINT techniques for super-resolution imaging

A range of different Single Molecule Localisation Microscopy (SMLM) techniques have been developed in the last two decades[120,229,230] to allow for high-detail imaging of structures with a nano-scale resolution. These methods break the diffraction limit of light through separating the fluorescence signal in time. Instead of visualising all fluorophores within the sample, SMLM relies on visualising only a subset of fluorophores at any given time. Thus, the exact position of single emitters can be estimated and the signal from all fluorophores collected over the course of an image acquisition. The detected single molecule localisations are used to reconstruct a super-resolution image. SMLM requires the molecules to go between a fluorescent "on" state and a dark "off" state to temporally separate fluorophores in the sample. This "blinking" behaviour can be induced using photoactivation[231] or photoswitching and chemical intervention.[232] This approach places a limitation on the fluorophores that can be used to image a sample, as this is only possible for a small selection of dye molecules. Alternatively, proxy-molecules can be used to temporarily localise the fluorophore at the target in approaches called points accumulation for imaging in nanoscale topography (PAINT). PAINT techniques are compatible with a wider variety of dye molecules, as the fluorophores can now remain "on" at all times, opening up the dye tool box for biologists and microscopists alike.

The classic PAINT imaging approach employs oligonucleotides (short strands of DNA, several nucleobases long) to bring the fluorophore molecule and target molecule together.[233] As illustrated by Figure 5.2.1A, the "imager" strand (oligonucleotide decorated with the fluorophore at the 3' end) and "docker" strand (localised to target) are complementary DNA sequences and thus capable of hybridising *in situ*.

The nucleotide bases have one preferred binding partner (adenosine (A) and thymine (T), cytosine (C) and guanine (G); top and bottom pair respectively in Figure 5.2.1B), based on the hydrogen bonding interactions between the two bases

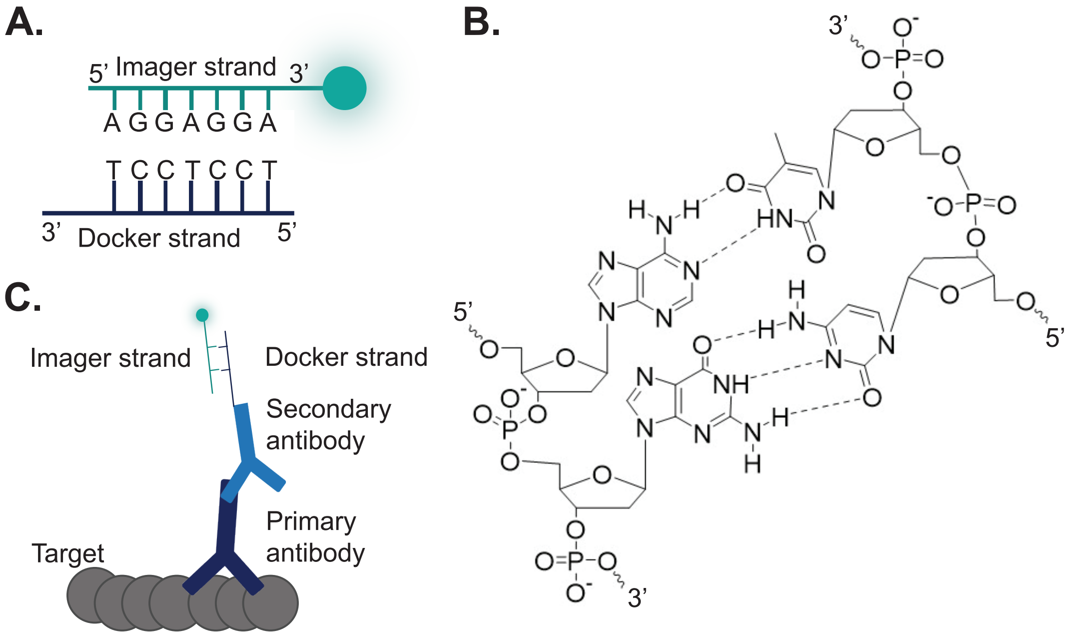

Figure 5.2.1: Principle of DNA-PAINT. A. Two short oligonucleotide strands with complementary sequences are used to bring together the fluorophore (here represented as a circle on the imager strand) and target of interest (conjugated to docker strand). B. Hydrogen bonding between the base pairs: top pair is A and T, bottom pair is G and C. The curly lines signify further nucleobases in the chain. C. Cartoon representation of a DNA-PAINT experiment where immunohistochemistry is used. Primary antibody binds to the target, secondary antibody conjugated with the docker strand is used to label the primary antibody. Imager strand diffuses freely in solution.

forming the base pairs (bp). The number of hydrogen bond donor and acceptor atoms on the ring structures determines the binding partner, two hydrogen bonds are formed between A and T, and three between the G and C pair. When the imager strand diffuses in solution, the fluorophore cannot be accurately localised. It appears as a "smear" on camera and contributes to general background fluorescence (this is an "off" state). When the imager strand hybridises with the docking strand, the fluorophore is held in place at the target of interest. The fluorescence can be localised, and appears as a bright punctum on the camera ("on" state). The binding is specific to the complementary DNA strand only and is transient in nature, meaning repeated "on" events can be observed over time. The stability of the duplex formed by imager and docker strands can alter the binding kinetics (duplex dissociation rate), so tuning the oligonucleotide length and base pairs used can facilitate longer bound times or quicker dissociation and imager exchange.[233,234] Jungmann *et. al.* quote the dissociation rate to be very sensitive to the oligonucleotide length with a $k_{off} = 1.6\,\mathrm{s}^{-1}$ for a 9 bp duplex and $k_{off} = 0.2\,\mathrm{s}^{-1}$ for a 10 bp duplex.[235] DNA-PAINT experiments require the signal to be localised to the target of interest, and thus functionalising the target with the docker strand. The most common approach for this involves immunolabelling,[233,236] where the target is labelled with a primary antibody and a secondary antibody previously conjugated to the docker strand (Figure 5.2.1C). The two antibodies introduce a linkage error, where the dye is in fact tens of nanometers away from the target. Other labelling methods, including the use of conjugated nanobodies[236–238] and aptamers,[239] are under development to decrease the distance between the fluorophore and the target.

Interestingly, application of protein-peptide interactions in place of the standard imager-docker interactions have been explored for the peptide-iteration of DNA-PAINT, called Peptide-PAINT. The technique employs endogenous interactions of a peptide sequence with a protein target, reducing the need for step-wise functionalisation of target with the docker and enabling researchers to use shorter imager strands. Following the same principle as DNA-PAINT, the transient binding between the peptide and its protein partner generates fluorescent localisations under the microscope and enables super-resolution imaging. For instance, a short protein fragment known to interact with an adhesion protein, talin, was exploited by Fischer *et al.* PIPKIγ peptide was able to detect isoforms of talin *in vivo* and allowed the study of the elusive protein at nanometer scale.[240] Harnessing an endogenous interaction, Bhaskar *et al.* co-expressed a short Lifeact peptide with enhanced Green Fluorescent Protein that transiently bound to actin filaments in live mammalian cells. They used this system to visualise the actin network and track its movement in time.[241] Tas *et al.* explored using an even shorter peptide sequence (a four amino acid peptide DTWV) and its interaction partner, a protein domain (PDZ domain) construct. The peptide was employed as a tag for the protein-of-interest, whereas PDZ-fluorescent protein was the "imager" counterpart. The technique proved effective in fixed cells and was used to visualise vimentin and mitochondria.[242]

The success of these approaches relies on fluorescently labelling the "imager" peptide. Methods compatible with live cells have to utilise fluorescent proteins. Delivering the imager peptide post fixation opens the dye tool box up to organic dyes that can be used to synthetically label the imager peptide. Even then, careful consideration is needed. Since the blinking is a result of transient binding, the dye remains always "on" in solution. This could lead to high signal-to-background ratios and "noise" detection throughout measurements. What is more, the available fluorescent dyes are usually charged hydrophobic scaffolds and can induce non-specific binding.[243] The folding of the peptide must also be retained post-labelling. Whilst this is not a primary concern for longer peptides, it raises concern for the short protein-interaction partners. If Tas *et al.* were to fluorescently label their 4 aa long peptide instead of the PDZ domain, it would likely lose its ability to interact with the protein domain if labelled with a fluorescent protein or even a conventional fluorophore.

In this chapter, a novel synthetic dye SeNBD was incorporated into a short peptide sequence creating short fluorogenic peptides that could super-resolve a native protein *in situ*. It was hoped that the dye could help generate a new generation of probes that minimise linkage error and further explore its suitabilty for native amino acid substitution.

5.2.2 Peptide-PAINT - choosing the target protein

The fluorogenic character and high signal-to-noise ratio make SeNBD (first introduced in Section 4.2.3) an ideal dye for super-resolution microscopy and Peptide-PAINT. The dye is capable of producing bright emission when close to target (hydrophobic environment such as tissue, organic matter) and the concentration regime is not limited as the dye is significantly less bright in solution. Thus, high concentrations can be used to ensure quick signal replenishment and ample localisations without compromising localisation precision. Moreover, SeNBD benefits from an amino acid core. This makes the dye easily incorporated into any peptide sequence and allows to target indigenous proteins *in vitro* and in complex *in situ* environments.

For the first proof-of-concept Peptide-PAINT experiments, a synaptic protein was chosen as the target of interest. The protein, post-synaptic density protein 95 (PSD-95), is present throughout the human brain and is localised to post synaptic membrane of neuronal excitatory synapses. PSD-95 is one of the most abundant post-synaptic proteins and is often used in imaging as a marker of the post-synapse. It is considered a scaffolding protein and has many known interaction partners, playing a part in synaptic plasticity and signal transduction.[244–247] The organisation of PSD-95 into small nanodomains and its implications for neurotransmission is a topic that has gained interest in recent years.[248–251] Tools to study the protein complexes and their structure in a high level of detail are necessary.

PSD-95 is a modular protein and consists of 5 defined sub-domains, crystal structures of which have been previously obtained.[252–255] These include an src homology 3 (SH3) domain, a guanylate kinase-like (GK) domain and three PDZ domains, all presented in Figure 5.2.2A. The domains are linked via flexible loop regions, and are thought to be able to exist in various conformations to facilitate binding to proteins and ligands.

The PDZ domain (**P**SD-95, **d**isc large tumor suppressor, **z**ona occludens

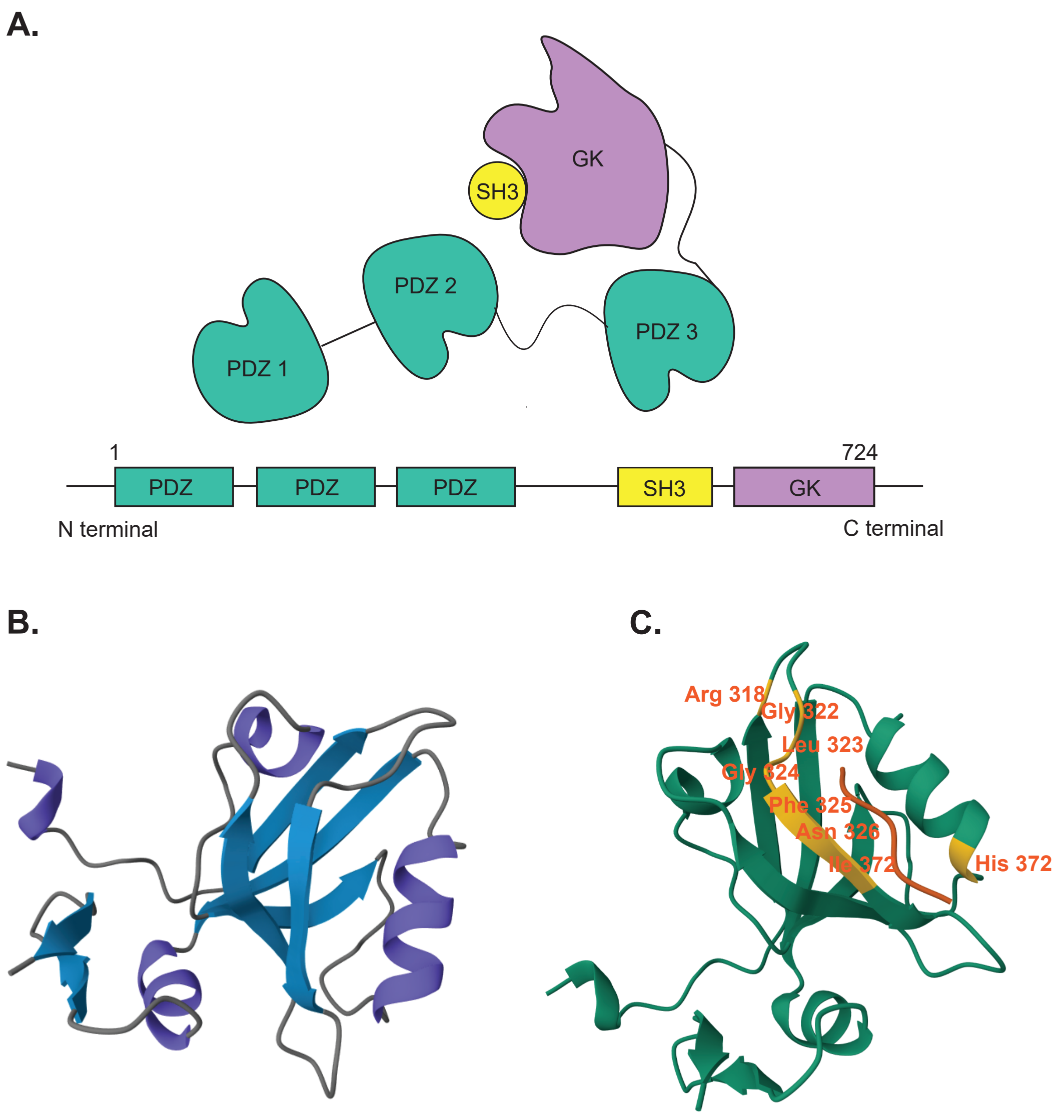

Figure 5.2.2: Structure of PSD-95 A. Genetic construct and a cartoon representation of PSD-95 protein, highlighting the 5 domains: three PDZ domains, an SH3 and GK domain. B. A crystal structure of the third PDZ domain with the various components highlighted: β-strands in blue, α-helices in purple. C. A binding groove between an antiparallel β-strand and an α-helix, here occupied by a cartoon representation of a ligand. All the residues forming hydrogen bonds to ligand (directly or via water coordination) are highlighted in yellow and named. PDB access code for PDZ structure: 1BE9

1, named after three proteins where it was first identified) is a sequence motif responsible for peptide binding. It mediates protein-protein interaction, and in the human synapse organises glutamete receptor complexes and larger signalling receptor assemblies.[256] From the target perspective, the third PDZ domain (PDZ3) is of most interest. It consists of approximately 90 amino acids, several β-strands and α-helices arranged in an overall globular structure.[257] Figure 5.2.2B highlights this 3D structure, with β-strands represented in blue and α-helices in purple. Between the α-helix on the right hand side and the downward pointing anti-parallel β-strand lies an elongated groove. This has been determined as the ligand binding site, based on several solved PDZ domain structures.[257–259] The amino acids directly exposed in the binding pocket are highlighted and named in Figure 5.2.2C. These are also most crucial for the ligand coordination. For the PSD-95 PDZ domains, the tightest binding ligands are those resembling the C-terminal motifs of proteins such as NMDA (N-methyl-D-aspartate) receptors and Shanker-type ion channels or CRIPT (Cysteine-Rich Interactor of PDZ Three).[260–262] It is from those interactions that binding information and the crucial amino acids are identified.

The PDZ3 domain of PSD-95 is known to bind CRIPT protein.[263] The C-terminal sequence of CRIPT protein is known, and a crystal structure of a CRIPT derived peptide (KQTSV) and PDZ3 complexed together was obtained and solved.[257] This binding is illustrated in Figure 5.2.2C. The three C-terminal residues are most important for the binding. It is the C-term of the peptide that inserts itself into the binding groove between the α-helix and β-strand. The free carboxylate group of the peptide binds to the loop between the two β-strands (GLGF on the diagram). The carboxylate of the C-terminal amino acid (valine) forms hydrogen bonds to the amide in the loop (G322 L323 G324 F325 residues) and makes further contact with the parallel β-strand on the other side of the binding pocket through a water molecule coordinated to the arginine (R318). The hydrophobic valine (position 0, first amino acid of the peptide) side chain points into a pocket of hydrophobic residues. The threonine (position -2) lies in a pocket containing a histidine (hydrogen bonding between the N of histidine and the hydroxyl group on a side chain). Thus the universal binding sequence for the domain was determined to be - S/T X V, where X can be any amino acid. For PDZ3, valine in position 0 is critical, and the amino acid at -2 needs to be a threonine or serine to take part in hydrogen bonding. However, different classess of PDZ domains exist, some have additional binding pockets that facilitate further ligand-protein interactions[264] and thus might require or prefer different amino acids in further positions.

The known binding interactions of PDZ and C-terminal peptides of various proteins made it possible to identify several hit sequences for fluorescent labelling. The two chosen for fluorescent labelling were the CRIPT peptide, KQTSV[257] targeting PDZ3 of PSD-95, and SSIESDV (7 residues of GluN2B subunit) binding to PDZ2 of PSD-95.[265] The second sequence has been used as an affinity tag for protein purification, where addition of the short peptide tag to a protein of interest allowed for a selective interaction with a PDZ-modified resin. Elution from the column was further achieved by washing the resin with a different peptide (a tighter binder).[265] Despite the interactions of the peptides with their respective domains being well-known and characterised, no attempts at fluorescent labelling of these have been reported.

5.3 Methods

5.3.1 Peptide synthesis

Solid state peptide synthesis followed the methods described in section 2.3. The procedures and reagents used are listed there.

Briefly, the PSD-95 targeting library was prepared according to the scheme in Figure 5.3.1. Peptide 10 was prepared using Liberty Blue microwave-assisted SPPS. Peptide 9, 11 and 12 were prepared manually using 5-mL polystyrene syringes fitted with porous discs, under standard Fmoc/tBu-SPPS at r.t. Amino acid 5 was coupled using Fmoc-SeNBD-OH (1.2 eq), Pyoxim (1.2 eq.), OxymaPure (1.2 eq.) and DIPEA (2.4 eq.) in DMF. Solvents, excess reagents and soluble byproducts were removed by suction.

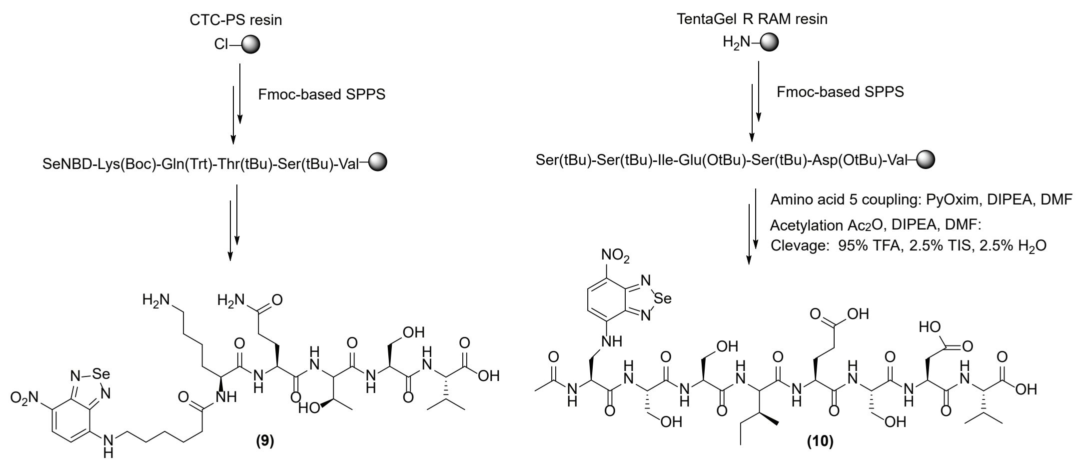

Figure 5.3.1: Synthesis of PDZ targetting peptides - reaction scheme to compound 9 and 10.

SeNBD-Lys-Gln-Thr-Ser-Val-OH (9)

The synthesis was performed on 62.5 mg of 2-chlorotrityl polystyrene resin (0.4 mmol g^{-1}). After cleavage, the crude peptide was precipitated by adding cold Et_2O (dropwise) and the resulting precipitate was decanted and dried (×2). Purification was conducted by semi-preparative HPLC with detection at 220 and 500 nm. Pure fractions were collected and lyophilized to afford pure peptide 9 as an intense orange solid (3.3 mg, 16%). HPLC-MS: t_R: 4.52 min, 98% purity. HRMS (ESI+) (m/z) for $C_{35}H_{55}N_{11}O_{12}Se$, $[M+H]^+$: 902.3270, found, 902.3306. MALDI (m/z): $[M+H]^+$: 902.3270.

Ac-SeNBD-Ser-Ser-Ile-Glu-Ser-Asp-Val-NH_2 (10)

The synthesis was performed on 28 mg of Tentagel R RAM resin (0.18 mmol g^{-1}). The resin containing the peptide sequence (0.005 mmol) was coupled to amino acid 5 (Fmoc-SeNBD-OH). After acetylation and cleavage, the crude peptide was precipitated by adding cold Et_2O (dropwise) and the resulting precipitate was decanted and dried (×3). Purification was conducted by semi-preparative HPLC with detection at 220 and 480 nm. Pure fractions were collected and lyophilized to afford pure peptide 10 as an intense orange solid (1.1 mg, 20%). *HPLC-MS: t_R: 3.22 min, 98% purity.*

Compounds 11 and 12 were prepared from the same backbone, as is highlighted in Figure 5.3.2.

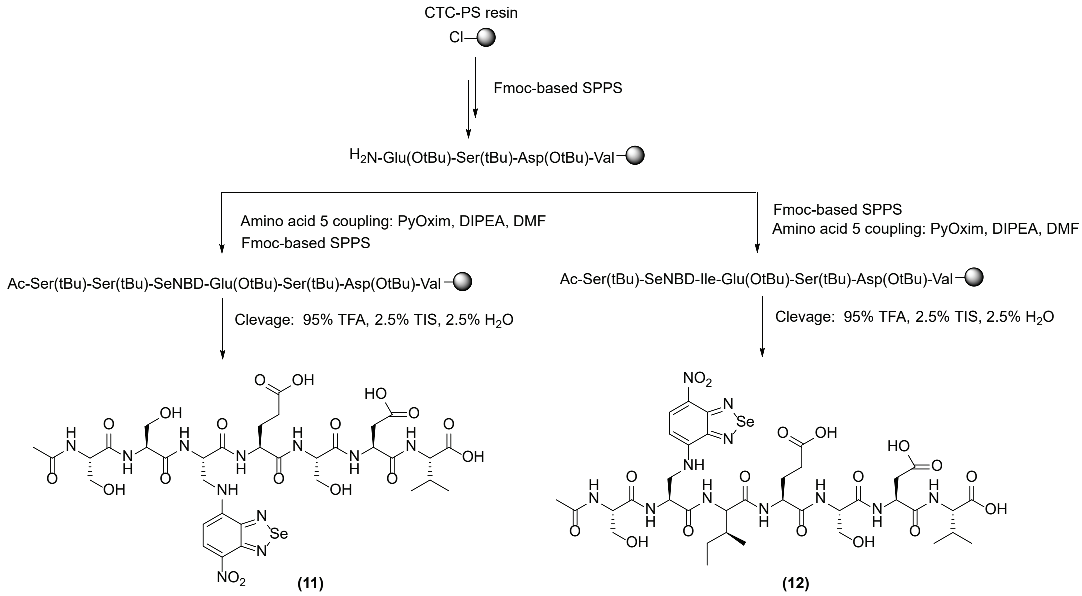

Figure 5.3.2: Synthesis of PDZ targetting peptides. Reaction scheme to compound 11 and 12 from the same backbone.

Ac-Ser-Ser-SeNBD-Glu-Ser-Asp-Val-OH (11)

The synthesis was performed on 28.2 mg of 2-chlorotirtyl polystyrene resin (0.6 mmol g^{-1}). After cleavage, the crude peptide was precipitated by adding cold Et_2O (dropwise) and the resulting precipitate was decanted and dried (×2). Purification was conducted by preparative HPLC with detection at 220 and 480 nm. Pure fractions were collected and lyophilized to afford pure peptide 11 as an intense orange solid (0.9 mg, 5.5% yield). HPLC-MS: t_R: 2.84 min, 98% purity. HRMS (ESI+) (m/z) for $C_{34}H_{47}N_{11}O_{18}Se$, [M-H]$^-$: 976.2193, found, 976.2098. MALDI (m/z): [M+Na]$^+$: 1000.2161.

Ac-Ser-SeNBD-Ile-Glu-Ser-Asp-Val-OH (12)

The synthesis was performed on 28.2 mg of 2-chlorotirtyl polystyrene resin (0.6 mmol g^{-1}). After cleavage, the crude peptide was precipitated by adding cold Et_2O (dropwise) and the resulting precipitate was decanted and dried (×2). Purification was conducted by preparative HPLC with detection at 220 and 480 nm. Pure fractions were collected and lyophilized to afford pure peptide 12 as an intense orange solid (1.3 mg, 7.66% yield). HPLC-MS: t_R: 3.18 min, 98% purity.

5.3.2 Synaptosome preparation

The synaptosome extraction was performed according to published procedures with minor modifications.[266] The experiment was performed at 4 °C, using the homogenization buffer (0.32 M sucrose, 1 mM HEPES at pH 7.4, cOmplete EDTA-free protease inhibitor cocktail). Briefly, heterozygous PSD-95$^{\mathrm{HaloTag}}$ mouse forebrain[267] (approx. 300 mg wet weight) was suspended in the homogenization buffer (3 mL) and the homogenization was performed by 12 strokes with a teflon-glass homogenizer. A pellet was obtained by centrifugation (1,400 g, 10 min, 4 °C) and resuspended in homogenization buffer (1.5 mL) with 3 strokes of the teflon-glass homogenizer. After centrifugation (700 g, 10 min, 4°C), the supernatants from both spins were pooled. Another centrifugation (14,000 g, 10 min, 4 °C) was carried out and the pellet containing synaptosomes was collected. The pellet was resuspended in homogenization buffer (0.6 mL) and underwent a final sucrose gradient centrifugation (0.85M/1.0M/1.2M sucrose, 2 mL each, 83,000 g, 2 h, 4 °C). The purified synaptosomes were collected from the band between 1 M and 1.2 M sucrose. The same preparation method was used for the brain tissue of a homozygous PSD-95$^{\mathrm{HaloTag}}$ mouse and a heterozygous PSD-95$^{\mathrm{HaloTag}}$ mouse pre-injected with a JFX-650 dye.

5.3.3 FCS measurements

In order to quantify the binding of PDZ peptide to its target, fluorescence correlation spectroscopy (FCS) was used together with an *ex vivo* system: a chemically synthesised and fluorescent-labelled KQTSV peptide and PDZ domain protein (1×PDZ domain-biotin, purified from E.Coli). The difference in masses between the two is presented in Table 5.1. The full sequence of the PDZ peptide is shown below, the last six histidines were a purification tag.

The peptide was incubated with a range of protein concentrations (for 1×PDZ: 0, 0.5, 4, 8, 12, 16 μM). All solutions were prepared in triplicates. The final peptide concentration was kept constant at 100 nM.

The diffusion through a confocal volume was observed using a home-built

Table 5.1: Mass difference between PDZ protein and the binding peptide.

Name (Sequence)	**Mass (gmol^{-1})**
PDZ peptide (SeNBDlinker-KQTSV)	901
1×PDZ (MGLNDIFEAQKIEWHEGSGEEDIPREPRRI VIHRGSTGLGFNIVGGEDGEGIFISFILAGGPADLSGE LRKGDQILSVNGDLRNASHEQAAIALKNAGQTVTII AQYKPEEYSRFEAGSHHHHHH*)	13,800

single molecule confocal instrument, described in detail in the Methods section. The confocal volume was illuminated by a 488 nm laser (LBX-405-100-CSB-OE, Oxxius; 1.2 mW irradiation at the back-port), and 5 × 30 second traces were recorded for each sample. The bursts of fluorescence as the peptide/peptide-protein passed the confocal volume were recorded on an Avalanche Photodiode (APD) detector (PerkinElmer).

The variation in intensity over time was calculated according to equation 5.1:

$$G(\tau) = \frac{\langle \delta F(t) \delta F(t+\tau) \rangle}{\langle F(t) \rangle^2} \tag{5.1}$$

where τ: lag time, $F(t)$: fluorescence at time t, and $\langle\rangle$ is an average in a time range.

The data were then fit to the 3D diffusion curve (equation 5.2) and thus the diffusion time lag could be obtained from fit parameters for that particular experiment.

$$G(\tau) = \frac{1}{\langle N \rangle} \left(1 + \frac{\tau}{\tau_D}\right)^{-1} \left(1 + \frac{\tau}{S^2 \tau_D}\right)^{-1/2} \tag{5.2}$$

where τ: lag time, N: number of particles observed in the diffusion volume, τ_D: diffusion time, S: structure factor accounting for the dimensions of the confocal volume.

A custom-written Python script was used to transform the burst data into autocorrelation curves and calculate diffusion lag times and diffusion coefficients (code available at: DOI: 10.5281/zenodo.13829074).

Further analysis was performed in GraphPad (Prism). The red channel diffusion lag time data were averaged for each condition (N=3, or N=2 for one case where the residual value for a repeat exceeded the other residuals by an order of magnitude), and the standard deviation between repeat measurements was calculated. The resulting plots were fitted using a non-linear regression function (binding kinetics, one site specific binding) to the following function:

$$y = \frac{B_{max} \times x}{K_D + x} \tag{5.3}$$

where B_{max} is the max diffusion lag time (plateau), K_D is the equilibrium dissociation constant.

Three fits were performed to obtain the average K_D, using the mean from the three measurement and the values obtained on either extreme (+/- standard deviation).

5.3.4 TIRFM sample preparation, image acquisition and analysis

Single-molecule and super-resolution imaging was performed on a TRIFM described in Methods section 2.4.2. The laser lines and mirrors are described therein.

The synaptosome preparation (heterozygous PSD-95$^{\mathrm{HaloTag}}$) was incubated with SiR HaloTag ligand (40 μM) for 10 min on ice. The solution was diluted in PBS (1:10 ratio) and incubated for 3 mins on a plasma-cleaned coverslip. The prepared slides were then washed with PBS (three times) to remove excess sample and HaloTag-ligand. Next, 50 μL of one of the imaging peptides (compounds 9 or 11; 500 nM) was added. SiR was excited using the 638 nm laser light and 500 frames were collected. Peptide 9 was excited with the 561 nm and peptide 11 with the 515 nm laser. Images were acquired for 5000 frames and 10,000 frames, respectively. Laser illumination used was approximately 500 W cm^{-2}. Peptide-PAINT images were analysed using Fiji (Java 8 2017 release).

Single localisations were detected with the Peak Fit function (Fiji GDSC-SMLM plugin), using a signal strength threshold of 20, and a precision threshold of 50 nm. Using a previously published approach,[248] clusters of PSD-95 localisation events indicative of whole synaptosomes were defined using DBSCAN,[268] compiled in Python 3.8 (sklearn v0.24.2). An epsilon value of 1 pixels and a minimum points threshold of 100 were used to cluster the data and remove unclustered localisations. For each localisation within its respective cluster, the distance to the nearest neighbouring localisation (defined as the nearest neighbour distance) was determined. From this, the mean nearest neighbour distance (ND_{ave}) for each cluster was calculated. The number of neighbours (NN) for each localisation was then determined by counting localisations within 5 $\times$ ND_{ave} for each cluster. Nearest neighbourhood images were generated by plotting each localization as a circle, the color of which was weighted on the NN coefficient. The resolution of each synaptosome was calculated as a function of the localisation fitting precision and the average nearest neighbor distance in accordance with previously published methods[269] (Python code available at: https://doi.org/10.5281/zenodo.7275947). The overall resolution of the images was calculated using Fourier Ring Correlation analysis (Python code available at: https://doi.org/10.5281/zenodo.7275952).

To compare the effect of synaptosome preparation on the number of localisations, the homozygous and heterozygous PSD-95$^{\mathrm{HaloTag}}$ was prepared as above and stained using peptide 9 (50 μL, 500 nM). The SiR labelling step was omitted for PSD-95$^{\mathrm{HaloTag}}$-JFX-650 sample. All conditions were imaged using 561 nm illumination for 3,000 frames. Super-resolution images were reconstructed using the same GDSC SMLM plugin and settings as above. The number of localisations for each condition (from 3 FOVs) was compared and plotted using Origin (Origin 2023b release).

To compare all PDZ-binding peptides, the same protocol was followed. The synaptosome was labelled with SiR-HaloTag, before dilution and deposition on a coverslip. Each coverslip was stained with one of the peptides (9, 10, 11, or 12, 50 μL, 500 nM). 515 nm laser was used to excite all of these, and the super-resolution images were acquired from 10,000 frames. The GDSC SMLM and NN analysis was performed as above. The number of localisations for each condition (from 4 FOVs) was compared and plotted using Origin (Origin 2023b release).

5.4 Results

5.4.1 Peptide-PAINT - designing a target library

The two PDZ-targeting sequences, KQTSV and SSIESDV, were chosen for fluorescent labelling for three reasons: the binding of the peptides to target domains was well documented in the literature, the binding affinities for these were estimated in the μM range,[263,270–276] and both probes are short sequences. The knowledge of binding to target and its affinity was helpful in choosing labelling approaches and sites. The μM affinities to the protein domain suggested compatibility with super-resolution techniques. The short sequences presented a labelling challenge. 5 or 7 amino acid sequences make for probes of a relatively small molecular weight. The molecular weight of commercially available dyes, such as Alexa Fluors, is comparable to the molecular weight of the whole sequence. If these were to be used to label the peptides, it would add substantial bulk to the probe. Moreover, Alexa Fluors are charged dye molecules, which could further disrupt the binding affinity of such labelled peptides. Thus, the usual labelling approach would involve implementing a carbohydrate linker chain. This would also increase the total size of the probe and, in turn, could impede the probe's permeability and also offset the localisation of the fluorophore with respect to the target molecule for imaging. As such, SeNBD dye provided a unique opportunity to retain the small size of the probe despite functionalisation for super-resolution imaging. It was hypothesised that with the use of SeNBD dye, the binding properties of the peptide would be retained, and it would be possible to localise the fluorophore directly at target (minimising offset and linkage error) in super-resolution imaging.

Thus, four sequences to target PSD-95 were designed and prepared as shown in Figure 5.4.1.

For the CRIPT peptide, the N-terminal labelling approach was utilised and

A.

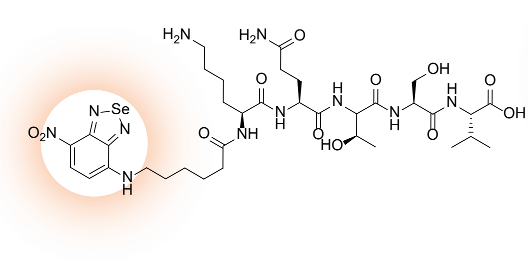

(9)

B.

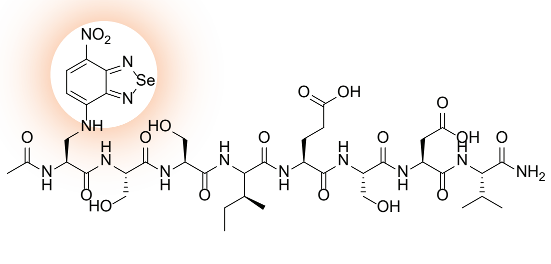

(10)

B.

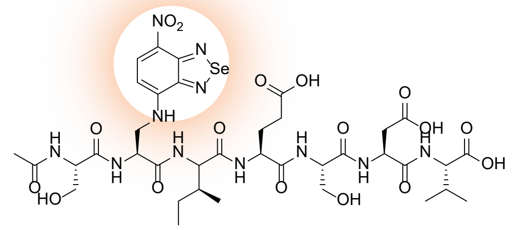

(11)

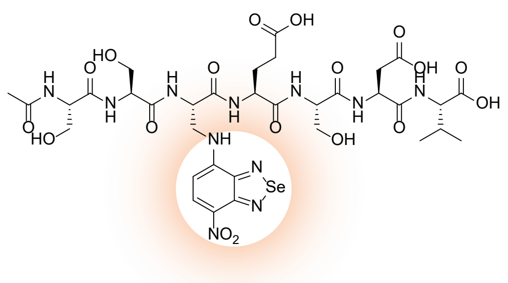

(12)

Figure 5.4.1: PSD-95 protein binding peptides. A. CRIPT derived peptide sequence KQTSV, with SeNBD placed at the N-terminal. Compound 9 and 10 vary in the C-terminal modification. The free carboxylic acid (compound 9) is the binding peptide, amide (compound 10) is the control peptide. B. Affinity chromatography derived peptide sequences. The fluorescent label, SeNBD, was placed internally substituting the native isoluecine (compound 11) and serine (compound 12). SeNBD amino acid highlighted by orange glow.

a short linker implemented leading to **compound 9** as the lead molecule, as shown in Figure 5.4.1A. This followed the more "conventional" way of fluorescently tagging molecules, placing the fluorophore away from the binding groove. For the affinity tag peptide, a different approach was taken. The peptide was prepared on two different resins: Rink amide and 2-chlorotrityl polystyrene resin, leading to an amide modification and a free carboxylic acid on the C-term, respecitvely. **Compound 10** was prepared as an amide, and the labelling strategy followed the "conventional" route with SeNBD placed as the last amino acid on the N-terminal. This peptide was to serve as a control to compare binding. The inability of **compound 10** to partake in hydrogen bonding within the binding groove of PDZ2 in the same way as the carboxylate versions (**compound 11 & 12**) was hypothesised to lead to a less potent binder. The sequence was then labelled internally, by substituting native amino acids: isoleucine (I for SeNBD, **compound 11** in Figure 5.4.1B) and serine (S for SeNBD, **compound 12** in Figure 5.4.1B). Isoleucine was chosen for this as a non-polar amino acid, and the serine as a non-binding amino acid. Both positions were proposed to tolerate the substitution. This incorporation was made possible by the stability of SeNBD dye, since the fluorescent amino acid could be incorporated on resin, and further coupling and deprotection cycles to complete the sequence left the benzoselenodiazole core undisturbed. The peptides were synthesised, purified and lyophilised to give red powder. The peptides were reconstituted in DMSO for all the biological applications work presented below.

5.4.2 Binding affinity as determined by FCS

After identifying and preparing candidate peptides that bind to target, it was important to understand how the fluorescent label influenced their ability to bind to PDZ domains and confirm the affinity of the binding would be compatible with super-resolution microscopy. The small size of SeNBD, especially in comparison to other fluorescent dyes, allowed to add less bulk to the targeting peptide and thus suggested the necessary binding interactions might still be retained. A recombinantly expressed PDZ protein construct (see Methods for sequence) was obtained from a collaborator, and fluorescence correlation spectroscopy (FCS) was employed to quantify binding between the protein construct and **compound 9**.

The protein and the fluorescently labelled peptide (SeNBD-KQTSV-COOH) were incubated together, before being imaged on a single-molecule confocal microscope (Figure 5.4.2). The laser excitation created a small observation volume (confocal volume) which the molecules could freely defuse in and out of. The protein construct remained undetected (non-fluorescent) whereas the peptide and peptide bound to protein appeared as bursts of fluorescence in the confocal volume (Figure 5.4.2A). The time spent in the confocal volume by both of these species differed based on their size. The peptide moved across the confocal volume faster on its own than when bound to a protein molecule.

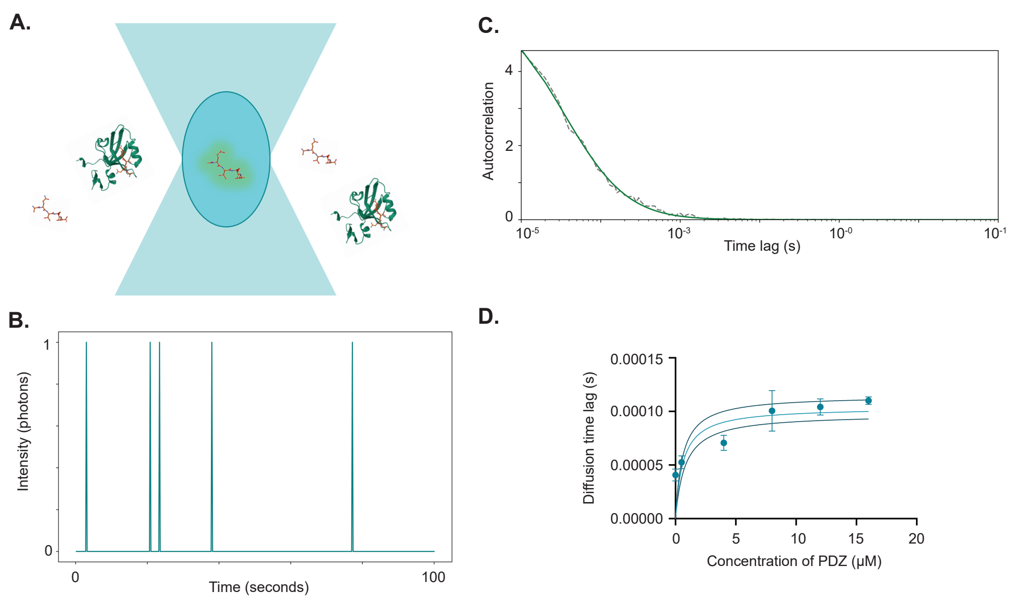

Figure 5.4.2: Studying the binding between PDZ peptide and an *in vitro* PDZ construct. A. A cartoon representation of the experimental principle: protein, protein with PDZ peptide and PDZ peptide on its own diffusing through a confocal volume. When the molecules are within the confocal volume they are illuminated by the laser and detected as fluorescence bursts. B. Example data recorded on the single-molecule confocal, fluorescent intensity seen as tall "bursts" across time. The change in fluorescence intensity over time can be further expressed as auto-correlation function. C. Auto-correlation function vs time-lag: experimental data were fitted to a non-linear regression curve to extract a diffusion time lag. D. Diffusion time lag was calculated for a range of PDZ protein concentrations in three separate experiments. The K_D was estimated at 670±110 nM (mean±SD

.

Thus, fluorescence intensity traces were recorded for 2.5 minutes (Figure 5.4.2B) for each sample preparation and the variation in intensity over time was calculated and plotted (Figure 5.4.2C). The data were then fit to the 3D diffusion curve and thus the diffusion time lag could be obtained from fit parameters for that particular experiment.

The diffusion time lag was analysed across a series of protein concentrations (0-20 μM), with each experiment was performed in triplicate. The diffusion lag time was plotted as a function of peptide concentration. Through fitting equation **??** to the experimental data points (mean diffusion lag time for each peptide concentration), the dissociation constant, K_D was calculated.

The K_D was estimated to be 670±110 nM (mean±SD) for this peptide. The low μM dissociation constant suggested a suitable binding tightness for super-resolution microscopy applications. The moderate K_D value for this system could be the result of the fluorescent label incorporation or the buffer make-up. Perhaps the peptide-PDZ interaction is tighter *in situ*, given the crowding effects of a complex solution matrix or even the higher temperature used to keep live samples. Potential avidity effects, where several PDZ are close together could make the apparent K_D lower too. The dye moiety itself could also influence the binding dynamics. The K_D value measured here is true for the **compound 9** and PDZ domain, but will likely vary when different dyes or dye positions within the peptide are considered.

5.4.3 Imaging synaptosome samples

Having tested the peptide on an *in vitro* protein construct and concluding the binding affinity could be favourable for super-resolution applications, the peptide was next used for fluorescence microscopy *in situ*.

The sample that provided a true complex environment to look at was a synaptosome preparation. Synaptosomes are extracted from a homogenised and processed mouse brain tissue, and conserve the synaptic structures, whilst removing other structural proteins highly abundant in tissue.[277] Synaptosomes can be deposited onto a glass slide and subsequently imaged without the need for permeabilisation and blocking (as is the case with tissue), or specific pull down techniques (charged species stick to the argon-treated surfaces easily). The mouse model used in these experiments contained PSD-95 with a HaloTag,[278,279] enabling efficient counterstaining through incubating the synaptosome with a silicon rhodamine (SiR)-HaloTag ligand. Such labelled sample was then incubated on a glass slide, excess sample washed off, and imaging solution containing the PDZ-binding peptide (**compound 9**) was applied. It was hypothesised discernible "blinking" would be observed (burst of fluorescence coming from the peptide localising to PSD-95). Furthermore, the events detected by the probe could be compared to the PSD-95 HaloTag signal (a control stain) to reason about specificity.

The experimental principle is illustrated in Figure 5.4.3 A, where the two probes binding to PSD-95 can be observed.

The HaloTag is covalently bound to a HaloTag ligand (in this case, SiR) giving off constant fluorescence. The peptide (**compound 9**) binds transiently to PSD-95 and, due to its fluorophore, it switches on when bound. Representative fluorescence microscopy images are presented in Figure 5.4.3B. The SiR can be visualised with limited detail (top panel, diffraction-limited imaging) whilst the super-resolution reconstruction (bottom panel, **compound 9**) allowed for observation of the structure of PSD-95 in high detail. The signal from the two probes is highly co-localised across images. The blinking, used to reconstruct the super-resolution image, can be seen in Figure 5.4.3C. Each frame in the montage is 1 second apart, the fluorescence signal appears and disappears as time passes (from top right to bottom left). Thus, PSD-95 molecules can be localised one at a time across the image acquisiton. This is further iterated in Figure 5.4.3D, where a line profile shows the variation in fluorescence intensity over time. The peaks (ON events) characterise the peptide binding to PSD-95, whilst the troughs (OFF events) are background counts where the peptide diffuses in solution. Thus, it was demonstrated that **compound 9** can be successfully used for super-resolution imaging of PSD-95.

Furthermore, the peptide-PAINT imaging highlighted the nano-structure of

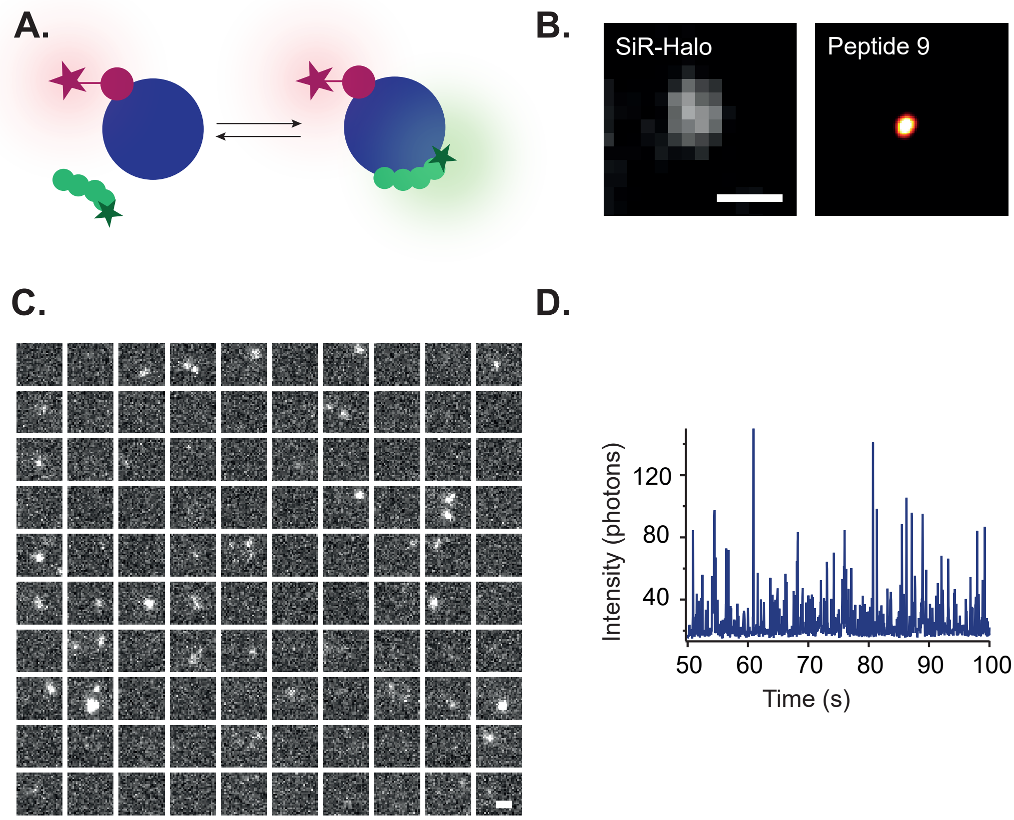

Figure 5.4.3: Super-resolution imaging of synaptosome. A. A cartoon representation of the experimental principle - PSD-95 protein (blue sphere) is labelled with a halo tag (crimson sphere) and a Halo ligand (SiR-Halo, crimson star). The peptide (chain of green spheres) is labelled with SeNBD (green star). The peptide binding is transient and its fluorescence switches on in the bound state. B. Representative fluorescence microscopy images of PSD95-HaloTag within a synaptosome labeled with SiR-HaloTag ligand (40 μM, right:diffraction limited image) and peptide (500 nM, left: peptide-PAINT image). Scale bar: 500 nm. C. Montage of frames, starting from the top left frame and going from left to right and top to bottom with 1 second separation between frames, from time-lapse fluorescence microscopy of a single synaptosome after incubation with peptide 9. Scale bar: 500 nm. D. Longitudinal plot of fluorescence emission (intensity profile at a defined location as a function of time) of peptide 9 within the synaptosome shown in c. The peaks "ON" indicate the binding of peptide to the PDZ domain and the troughs "OFF" indicate the dissociation of peptide 16 from the PDZ domain.

the protein in the sample. The images obtained revealed hotspots with high density of localisations, similar to those previously observed by Broadhead and *et al.* using PALM microscopy.[251] These hotspots correspond to several PSD-95 molecules concentrated closely in space forming "aggregates" or nanoclusters of approximately 50-250 nm in diameter. These PSD-95 nanoclusters were observed in synaptosome preparations derived from mouse brain tissue previously,[251] with the nanoclusters thought to form post-synaptic building blocks and useful in estimating synapse size. This nano-distribution of PSD-95 inspired further analysis of the spatial distribution of PSD-95 in nearest neighbour (NN) analysis. To that end, the local density of the fluorescence signal was first quantified (based on the number of neighbouring events). The density revealed hot-spots (coordinates with many localisations) and showed the distribution of individual PSD-95 molecules within the synaptosome (Figure 5.4.4A). The NN analysis confirmed clustering of PSD-95 within individual synaptosomes and allowed to estimate the size and number of cluster within the synaptosome also. Thus, various types of synaptosomes could be distinguished based on the number of PSD-95 clusters present. Synaptosomes containing one, two and more than three PSD-95 nanoclusters could be observed in super-resolution images and their identity was further confirmed by the nearest neighbour density map plots (Figure 5.4.4). Thus, the distribution of the image precision and resolution could be plotted and mean number of neighbours and distance between neighbour events could also be observed (Figure 5.4.4B). The overall image resolution achieved was quantified using the Fourier Ring Correlation[280] method, and estimated at 63.2±5.7 nm.[281]

To exclude the possibility that the peptide is in fact interacting with the HaloTag ligand or HaloTag rather than the PDZ domain of PSD-95 as expected, the peptide was tested across three synaptosome preparations available: one from a PSD-95$^{\mathrm{HaloTag}}$ heterozygous mouse, one from PSD-95$^{\mathrm{HaloTag}}$ homozygous mouse, and one from a PSD-95$^{\mathrm{HaloTag}}$-JFX650 homozygous mouse where the labelling was performed prior to synaptosome extraction. Through using these three conditions the dependence between the number of events observed and the degree of labelling of PSD-95 within the synaptosome could be determined.

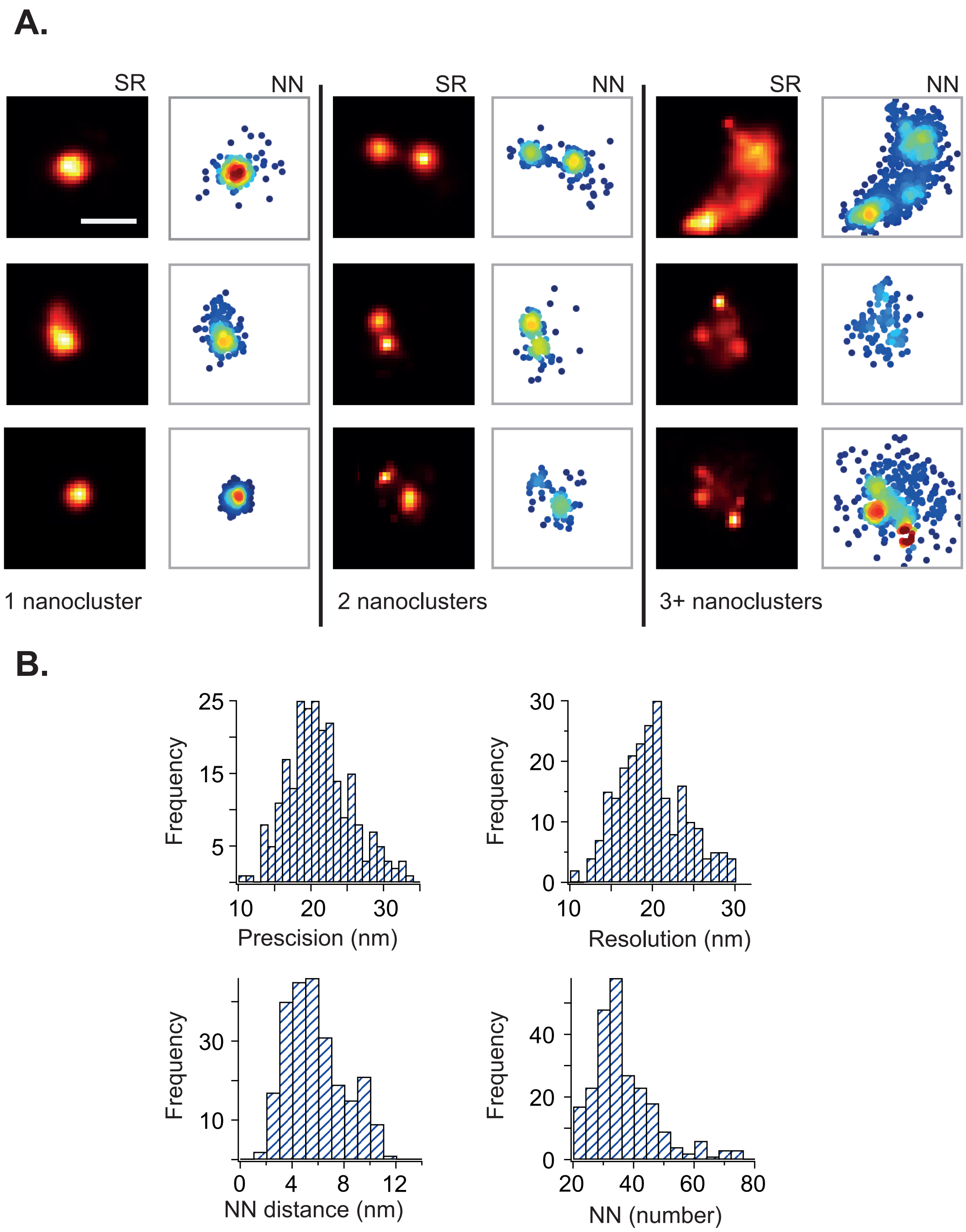

Figure 5.4.4: Imaging and classifying PSD-95 nanoclusters using peptide-PAINT. A. Representative fluorescence microscopy images from different synapse subtypes as defined by the number of PSD95 nanoclusters per postsynaptic density (PSD). The left panels display peptide-PAINT SR microscopy images of PSD95 in synaptosomes, and the right panels display the same images after nearest neighbor (NN) analyses, which feature high local density in the protein nanoclusters. Scale bar: 200 nm. B. Representative histograms of the mean local density (top, determined by counting the number of neighbors within a radius of each molecule scaled to the mean density in its synaptosome) and the effective map resolution for each synaptosome (bottom).

Homozygous mice had all copies of the protein carrying the HaloTag modification and heterozygous animals had half the copies modified with HaloTag. Equally, this experiment was used to check whether the dye made any difference to the number of binding events detected. As can be seen in Figure 5.4.5A the obtained images looked similar in all three cases, showcasing PSD-95 nanoclusters in individual synaptosomes as confirmed by white light imaging (not shown). Density map analysis was not attempted here, as the images were collected in fewer frames (3,000 as opposed to 10,000 used for the high-detail imaging in Figure 5.4.3). 3,000 frames proved sufficient to compare the conditions, but the super-resolution images would benefit from higher precision and detail. More localisations should be collected (either through increasing the concentration of the peptide or increasing the acquisition time). Moreover, a different laser illumination (561 nm) was used for this experiment. It was later decided that 515 nm is most suitable for exciting SeNBD in a non-polar environment. This explains the overall low numbers of localisations detected, but since it is consistent across the three conditions it does not void the comparison.

The number of events detected per 1,000 frames was compared in Figure 5.4.5B for all three conditions. It is relatively consistent across the three synpatosome preparations, with the lowest number of spots detected in the homo SiR sample at an average of 2,500 localisations detected per 1,000 frames. The heterozygous SiR sample produced an average of 4,600 localisations and the homozygous JFX650 - 4,100. Some variation here was expected, due to the sample preparation introducing variability to the number and concentration of synaptosomes. This is difficult to quantify, and normalise for, across the three different biological conditions. The experiment would further benefit from carrying out repeats to account for variation between each preparation. The standard deviation here expresses variation across three different regions of interests, and not three different sample preparations. Electrostatic interactions of the dyes (SiR vs JFX650) might influence how well the samples stick to the glass slide surface. On the whole, the peptides performance seems consistent across the samples and independent of the counter-staining dye.

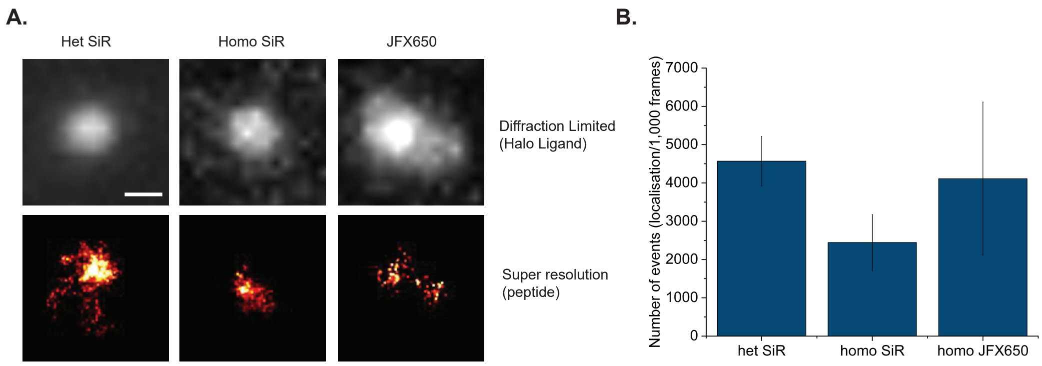

Figure 5.4.5: Comparing the peptide performance across three different synaptosome preparations. A. Representative fluorescence microscopy images of PSD-95 contained in three different synaptosome preparations: heterozygous PSD-95^{HaloTag}, homozygous PSD-95^{HaloTag} - both labelled with SiR-HaloTag and homozygous PSD-95^{HaloTag}JFX650. Top row presents diffraction limited images from the signal of the Halo Tag ligands, bottom is super-resolution reconstructions imaged using 500 nM of peptide 9. Scale bar: 400 nm. B. Bar chart quantifying the localisation (peptide blinks) detected on average per 1,000 frames from three consecutive images. The error represents the standard deviation.

5.4.4 Internal amino acid substitution for a new generation of PSD-95 peptides

Peptide 9 showcased that the small size of SeNBD dye and its switch-on character make it amenable for super-resolution imaging. However, the labelling approach used still followed the standard approach to fluorescent labelling of probes and placed the dye at the N-terminal. Another advantage of choosing SeNBD as the dye was the ability to prepare internally labelled fluorogenic peptides for Peptide-PAINT applications. **Peptides 11** and **12** were designed and prepared with the dye introduced in place of a natural amino acid within the peptide sequence. The substitution of the native amino acids for the dye amino acid could disrupt sequence-specific binding. The positions chosen for the substitutions were towards the N-term of the peptide, away from the C-term sites responsible for peptide insertion into the protein. Even still, given the short sequence of the probe, these substitutions could decrease the probe specificity or cause off-target events. To this end, an experiment comparing the performance of the internally-labelled peptides to the known binders was designed. The performance of the internally labelled peptides was tested against the N-terminally labelled **peptide 9**.

First, it was important to ensure that the label incorporation did not disrupt the ability of the peptide to insert itself into the PDZ domain of PSD-95. To this end, the number of localisations obtained when imaging synaptosomes was compared with the original peptide (**compound 9**) and the longer derivatised sequences (**peptides 11 and 12**). As a control for these experiments, **compound 10** was also employed. This peptide contained the fluorescent dye, SeNBD, at the N-terminal and more importantly was capped at the C-terminal. The presence of an amide instead of a free carboxylic acid was to disrupt some of the crucial binding interactions and confirm that sequence specificity is at the source of binding.

With this in mind, the synaptosome samples were incubated with 500 nM of each of the peptides: **peptide 9** (KQTSV-analogue used in sections above), **peptide 10** (SSIESDV control) and **peptide 11** & **12** (both internally labelled SSIESDV sequences). From 10,000 frame acquisitions, an average number of localisations per 1,000 frames per FOV was calculated for each of these and presented in Figure 5.4.6A.

Peptide 9 produced on average 17,600 localisations. The performance of SSIESDV analogues was slightly better: **peptide 11** averaged around 20,100 localisations, and **peptide 12** produced even more localisations (average of 25,000 localisations per 1,000 frames per FOV). However many of the localisations detected by **peptide 12** were revealed to be single localisations rather than repeat localisations. Whilst they could be easily removed by clustering alogorithms and a “synaptosome localisations” threshold, this analogue was potentially more promiscuous than **peptide 11**, especially given the largest variability in localisations from FOV to FOV. Encouragingly, the amide version of the SSIESDV (**compound 10**) produced the least number of localisations averaging at 6,500 per 1,000 frames. When further analysis was performed, most of these were removed giving the smallest number of synaptosome-like clusters detected out of all 4 probes. A similar trend was observed when the number of localisations per cluster were compared for the four peptide (Figure 5.4.6B). The smallest

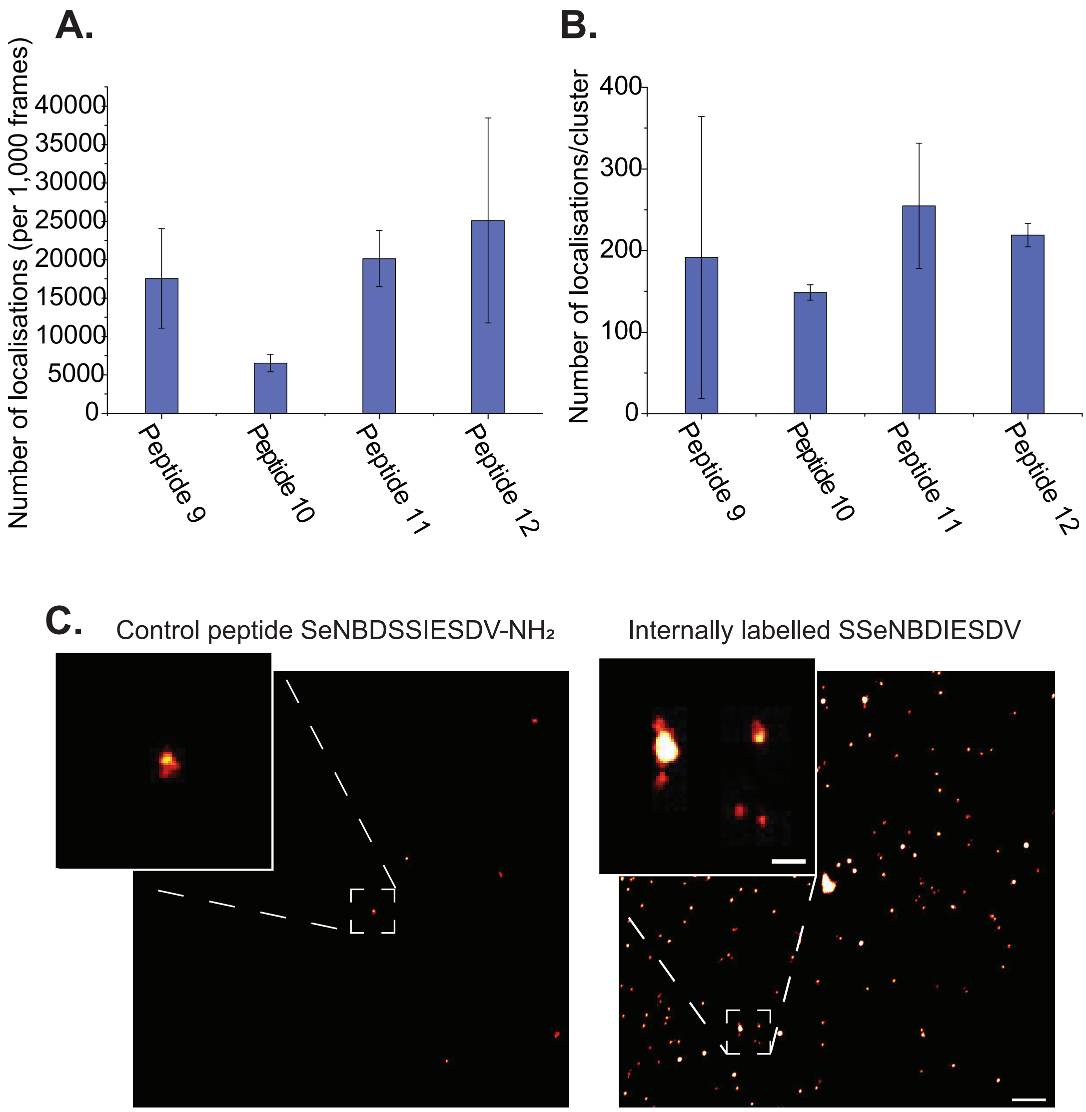

Figure 5.4.6: Detecting synaptosomes with a library of PDZ peptides. A. Average number of localisations detected per 1,000 frames for each of the 4 PDZ binding peptides when imaging the synaptosomes. Error bars are standard deviation from 4 different acquisitions. B. Average number of localisations detected per cluster for the PDZ binding peptides. Error bars are standard deviation from 4 different acquistions. C. Representative super-resolution images of two FOVs acquired using peptide 10 (left hand side) and peptide 12 (right hand side). Scale bar: 1 μm. Zoomed in images showing synaptosome-like clusters. Insert scale bar: 200 nm.

number of localisations per cluster was exhibited by **peptide 10** (the control), and the internally labelled peptides showed most localisations per cluster. **Peptide 12** showed slightly fewer localisations than **peptide 11** per cluster. Processed super-resolution images of synaptosome using **compound 10** and **compound 12** can be seen in Figure 5.4.6C. The images are representative 12 μm x 12 μm FOVs, showcasing the number of clusters (synaptosomes) detected with both peptides.

Thus, it could be concluded that the internally labelled SSIESDV peptide can perform on par with the N-terminally labelled KQTSV one. Whilst no biophysical characterisation of its binding was performed, the performance of the probe in the imaging experiment suggests the peptide tolerated the internal label well without compromising the number of events detected. The signal from this peptide co-localised with the counterstain (SiR) still. There was a potential preference in positioning of the fluorescent amino acid for optimal binding properties retention, as **compound 12** showed more localisations than **compound 11**, however fewer localisations per cluster. The C-terminal interactions were crucial for correct insertion into the binding pocket of the PDZ domains of PSD-95, as **peptide 10** performed worse than its two analogues: **peptide 11** and **12**, and also showed less localisations than **peptide 9**.

The performance of **peptide 11** was further compared to **sequence 9** in a repeat of synaptosome imaging and nearest neighbour analysis. As before, synaptosome families containing one, two or several PSD-95 clusters could be observed both in super-resolution and as localisation densities maps (Figure 5.4.7A), with a high level of detail. Comparing the performance metrics between the two experiments, **peptide 10** benefits from a marginally higher precision averaging at 20.7$\pm$0.1 nm (as illustrated in Figure 5.4.7B), resolution as calculated using the Fourier Ring Correlation method (60.8 $\pm$4.8 nm), and S/B ratio of 14.8$\pm$1.3 (ccounted for in the histograms in Figure 5.4.7).

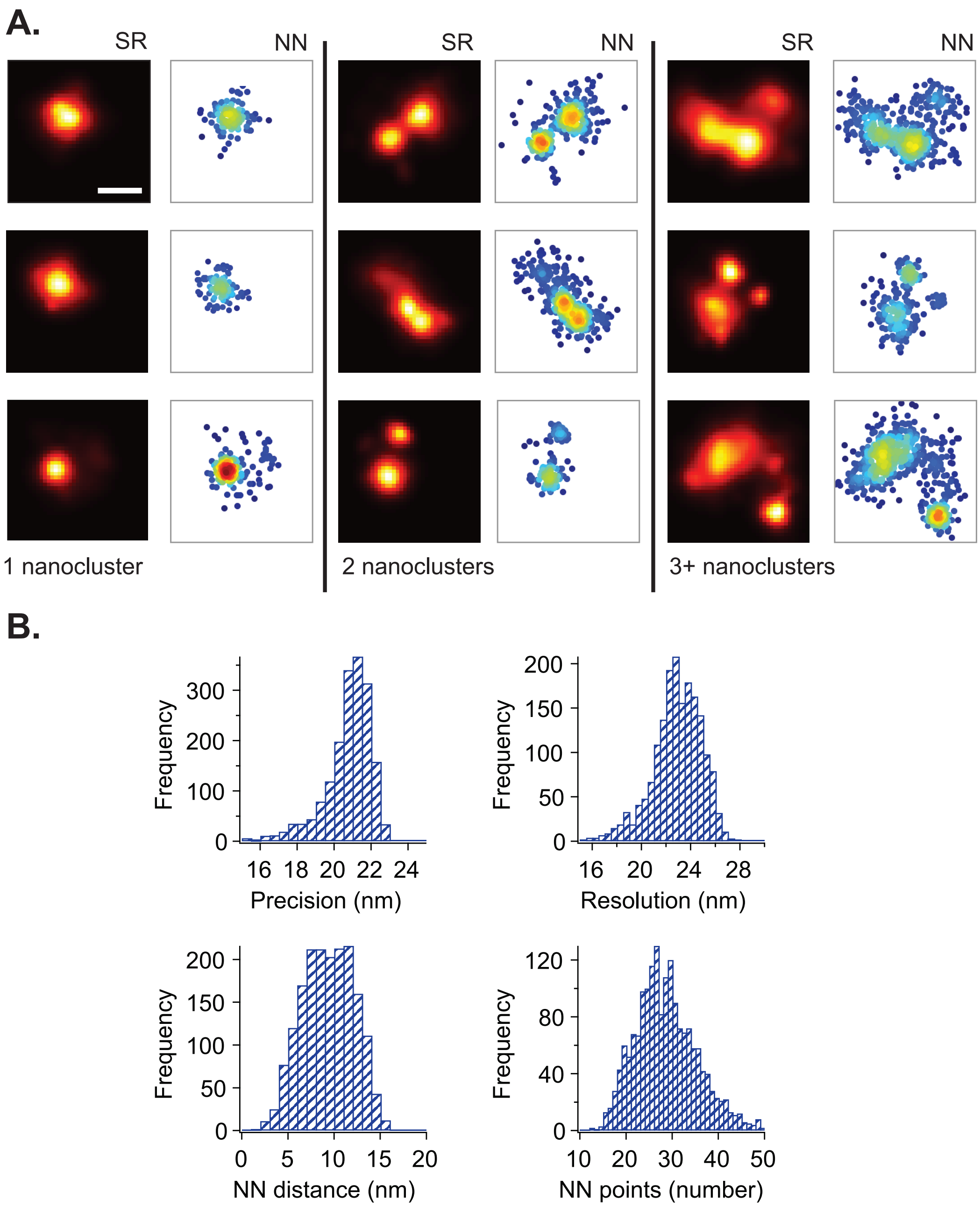

Figure 5.4.7: Imaging and classifying PSD-95 nanoclusters using peptide 10 for peptide-PAINT. A. Representative fluorescence microscopy images from different synapse subtypes as defined by the number of PSD95 nanoclusters per postsynaptic density (PSD). The left panels display peptide-PAINT SR microscopy images of PSD95 in synaptosomes, and the right panels display the same images after nearest neighbor (NN) analyses, which feature high local density in the protein nanoclusters. Scale bar: 200 nm. B. Representative histograms of the mean local density (top, determined by counting the number of neighbors within a radius of each molecule scaled to the mean density in its synaptosome) and the effective map resolution for each synaptosome (bottom).

.

5.5 Discussion

SeNBD was developed as a small fluorogenic amino acid and its switch-on character showed promise for super-resolution imaging. To showcase the potential of this small fluorescent reporter, a PDZ-peptide targeting library was rationally designed. By substituting non-interacting amino acids for SeNBD, a short sensitive probe was obtained. The switch-on character of the dye was demonstrated with a plate reader experiment, where the fluorescence intensity of SeNBD-labelled carbohydrate in the presence and absence of liposomes was measured. A similar experiment, titrating the N-labelled and internally labelled PDZ peptides against recombinantly expressed PDZ in bulk could be attempted. This would provide more insight in how the positioning of the fluorophore could affect the switch-on and thus signal to noise ratio. The data set could also be used to confirm the binding kinetics observed by FCS. This was not attempted, due to limited amount of PDZ protein available.

The experiments performed showed that the fluorescent amino acid incorporation did not affect the binding affinity of the peptide sequence. The binding affinity was optimal for super-resolution imaging, where blinks were observed under the microscope and used to reconstruct PSD-95 clusters with a high level of detail. When comparing the performance of the peptides, it was observed that the C-terminal modification led to reduced number of localisations. The specificity of the peptide was confirmed based on co-localisation with a genetically encoded label expressed with PSD-95. It would be interesting to observe what binding looks like in the absence of PSD-95, especially in a sample likely to contain PDZ domains across various proteins. Whilst the crystal structures show which features enable and facilitate binding, no tests on the promiscuity of the probe were conducted. This should be kept in mind when the peptides are used as a primary probe (without a co-localisation signal).

FCS facilitated the observation of the interactions between PDZ and its binding peptide and quantify the dissociation constant K_D for the pair. However, k_{off} and k_{on} rates could not be determined using this method. An alternative assay, with immobilisation of PDZ on a coverslip surface and an in-depth study of the blinking dynamic, would have to be designed.

5.6 Conclusions

The above body of work showcases the development and application of peptides for super-resolution microscopy.

Small peptides targeting the native PDZ protein were successfully decorated with the SeNBD-amino acid and used to super-resolve the nano-structure of PSD-95 in mouse-derived synaptosomes. Two sequences, previously shown to bind to PDZ domains of PSD-95, were successfully modified with a fluorescent probe and in both cases the binding was unaffected by the presence of SeNBD. The switch-on character of the benzoselenadiazole dye allowed for imaging with high signal to noise ratio. A resolution of 60.8 ± 4.8 nm was achieved as determined by Fourier Ring correlation. The small fluorogenic peptides developed here could enable new super-resolution imaging studies of protein localisation and turnover within the synapse and are a promising lead for rapid detection of proteins levels in complex samples.

5.7 Future perspectives

The PDZ binding peptides have worked well in the complex *in vitro* sample of synaptosomes. A step forward would be to use these probes within tissue. This has not been attempted before and could come with its own challenges. Tissue is highly fluorescent, so it is possible quenching methods would need to be employed to visualise the probe above background fluorescence. Another potential difficulty would be PDZ domains present outside of the PSD-95 clusters, as the specificity of the probe has not been studied, and PDZ domains are present throughout many proteins. A co-localisation stain for diffraction limited imaging could help with localising signal belonging to PSD-95 even in the event of some cross-staining. The nanocluster classification attempted within the synaptosomes could provide very useful insight, if it could be replicated in tissue. The spectral properties of SeNBD make it compatible with co-staining experiments, and its relatively broad emission could make it a good donor for dual labelling for FRET experiments.

5.8 Contributions

The fluorescent dyes (SeNBD and SNBD) used in this chapter were synthesised by Dr Fabio de Moliner. The original PDZ targetting peptide, compound 9, and amide control, compound 10, were synthesised by Dr Lorena Mendive Tapia. The author synthesised all other peptides and performed repeat syntheses where the stocks were low. Dr Louise Holyoake supplied recombinant PDZ protein. The author designed, planned and performed all experiments and analysed the data. Dr Takeshi Kaizuka prepared the synaptosome samples used and Dr Katie Morris assisted with synaptosome labelling for the co-staining experiments and super-resolution imaging.

The CD measurements were performed at the University of Glasgow, thanks to Dr Andrew Jamieson's hospitality, and with the expert guidance of Dr Danielle Morgan.

Prof. Mathew Horrocks authored several of the Python scripts used throughout this chapter (FCS, GDSC-SMLM, nearest neighbour analysis, liposome analysis). Some of these were further modified by the author. Analysis was performed by the author and the author created the graphics and figures from the analysis outputs.

The TIRF microscope and SM confocal microscope used in this chapter are home-built instruments. They were built by Dr Craig Leighton, Dr Alexandre Chappard, Dr Owen Kantelberg, Dr Katie Morris and Dr Zoë Gidden with guidance from Prof. Mathew Horrocks.

Chapter 6

Coiled-coil peptide interaction in super-resolution imaging

6.1 Scope of the chapter

This chapter covers work in the design and application of a universal labelling approach utilising peptide-peptide interactions for super-resolution microscopy. The feasibility of using a coiled-coil interaction using synthetic peptides was tested, and proof-of-concept images of cellular organelles in fixed HEK cells were obtained.

6.2 Introduction

6.2.1 Peptide-PAINT techniques for super-resolution imaging

An alternative approach to DNA-PAINT introduced peptides in place of the imager and docker oligonucleotides for PAINT. For this purpose, α-helical peptides are most likely to be employed. Two α-helical peptides can twist around each other and form a so called coiled-coil structure.[282] This is a common folding motif across a variety of proteins, responsible for association and interactions of protein subunits. The α-helices are characterised by a periodic structure (a heptad: seven amino acid repeat in the form of $(abcdef)_x$).[283] Out of the seven amino acids two, ones in positions *a* and *d*, are often apolar. This allows the helix to form a hydrophobic side (core). The hydrophobic cores of two helices facilitate "knobs-into-holes" packing, where apolar side chains of one peptide can insert themselves into the hydrophobic core of the other peptide.[284] This is a non-specific interaction and it is often stabilised further by attractive electrostatic interactions formed between other polar residues between the two peptides. Various peptide pairs that are able to form coiled-coils were reported in recent years. "Versatile Interacting Peptide" tags were developed by Doh *et. al* as a genetically encodable CoilE tag for a target protein and a CoilR reporter peptide. Their tag system had dual applications in electron microscopy and diffraction-limited fluorescence microscopy of sub-cellular structures without good immunohistochemistry labels.[285] Chen *et al.* developed several orthogonal peptide pairs based on leucine-zipper structures for phenotype monitoring in yeast cells.[286] Charged coil pair (E/K peptides, named after their repeat heptatds containing several glutamic acid residues and lysine residues respectively) were successfully employed as a capture-detection system for bio-sensing and affinity chromatography[287] and, more recently, for fluorescence imaging. The E/K interaction was used to visualise membrane proteins[288,289] and observe internalisation of receptors in real-time.[290] However, until 2020, the applications focused on diffraction limited imaging with no reported attempts at super-resolution imaging due to the tight binding between the peptides. Eklund *et al.* revisited the kinetic studies of the E/K peptides,[291,292] paying attention to the peptide length and its effect on dissociation in non-denaturing conditions,[293] and thus have rationally redesigned the sequences to allow for transient binding. Following the E/K heptad repeat (Figure 6.2.1A) pattern, and introducing a length mismatch between the K and E helices, they have confirmed E19 and K22 coils display the desired transient binding (K_D = 81 nM as opposed to K_D = 20 nM for 21 aa long peptides[294]).

Not only did they image two cellular targets: vimentin and tubulin in super resolution (experimental principle shown in Figure 6.2.1B), showing their structures with a high degree of detail, but they also designed a platform to quantitatively assess the technique. The kinetics of the associations were compared to DNA-

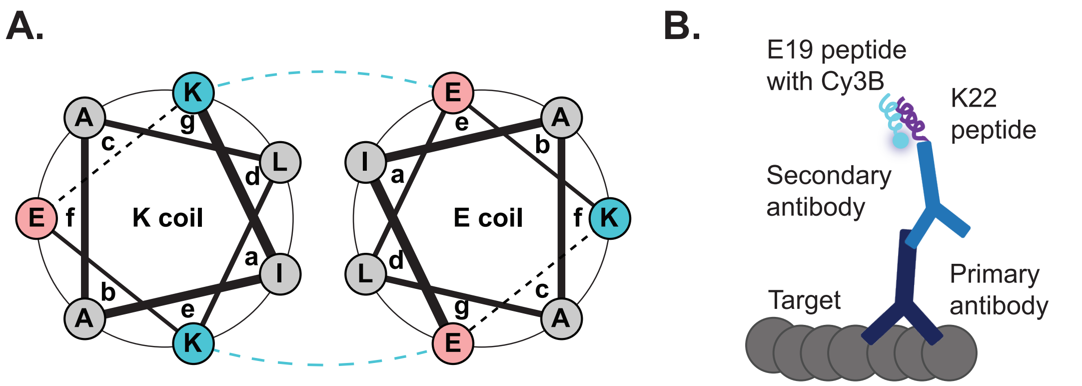

Figure 6.2.1: Principle of Peptide-PAINT. A. A helical wheel diagram presenting the fold of E and K α-helical peptides. The two helices interact via hydrophobic interactions stabilised through favourable electrostatics between postively charged lysine residues and negatively charged glutamic acid residues. The colour of the amino acids indicates its properties: grey - hydrophobic, blue - negatively charged, red - positively charged. B. Peptide-PAINT as performed by Eklund *et al.*.[294] The set-up follows standard DNA-PAINT practice, with a primary antibody for target of interest and a secondary antibody conjugated to the docker strand (here K22 peptide). Imaging peptide, E19, diffuses freely in solution.

PAINT in a direct assay, where the K22 peptide was conjugated to a DNA-strand that provided means of immobilisation and an alternative detection with the complementary oligonucleotide sequence. 86% of the signal detected with the E19 peptide labelled with Cy3B was co-localised to the DNA-PAINT signal,[294] suggesting the two techniques are comparable in performance. What is more, the localisation precision was similar across the two acquisition methods (3.6 nm for DNA-PAINT and 4 nm for Peptide-PAINT). An advantage of Peptide-PAINT over DNA-PAINT was also revealed, with more frequent binding events observed in Peptide-PAINT than DNA-PAINT at the same imager concentration. Eklund *et al.* qualified the association rate of the peptides to be twice that of oligonucleotides, quoting the average dark time as $30.0 \pm 0.9s$ for Peptide-PAINT and $71.2 \pm 5.5s$ for DNA-PAINT. The efficiency of hybridisation of oligonucleotide strands is affected by the charge repulsion forces between the negatively charged phosphate backbones of DNA strands. Thus, using Peptide-PAINT (and replacing oligonucleotides with peptides) could address one of the bottlenecks of DNA-PAINT: long image acquisition times.

Following the initial reports, coiled-coil interactions were further utilised in super-resolution imaging of cellular targets. Maity *et al.* successfully used the E22/K19 pair for imaging of membrane proteins, organelles, histones and receptors in mammalian cells and neurons. Their modified protocol involved co-expressing the E22 docker with the target of interest, further delivering the imager peptide to fixed or live cells prior to imaging.[295] In search of an orthogonal coiled-coil pair that could facilitate multiplexed imaging, Eklund *et al.* followed similar protocol with a P3/P4 pair. They showed co-expression of P3 to Her2 receptors and used a P4 binding partner for its detection in cells post-fixation.[296] Co-expression of a similar coiled-coil pair named SYNZIP, with one peptide attached to the target of interest and the other peptide attached to a fluorescent protein, gave rise to the live cell imaging using reversible interactions points accumulation for imaging in nanoscale topography (LIVE-PAINT) approach.[297] Oi *et al.* pioneered this technique in *S. cerevisiae*, imaging proteins in the yeast bud neck. Co-expression of both interaction partners removed the need for cell fixation and permeabilisation and allowed for an approach fully compatibile with live organisms. Gidden *et al.* later proved this technique is particularly attractive for proteins that do not tolerate direct fusion of fluorescent proteins and can be used to image otherwise difficult targets.[298] The work was further extended into mammalian cell lines.[299]

6.2.2 Peptide-PAINT using coiled coil interactions

Whilst the peptide-protein interaction approach presented in the last chapter proved peptide probes can be excellent tools for super-resolution microscopy, it lacked translational capacities. The two peptide sequences derivatised in this work have already been shown to bind to PSD-95. Several other proteins have known peptide-binders as peptides make interesting targets for otherwise undruggable proteins or interaction sites, with several high throughput lead sequence identification methods available for lead sequence generation.[300] To identify therapeutic peptide sequences, methods such as integrated venomics and display technologies are commonly used. Integrated venomics relies on identifying peptide sequences from the venom of animals such as snails, insects or centipedes. These venom peptides often contain a disulphide-rich scaffold that can be further engineered and mutated to enhance the number of hits in screenings against therapeutic targets.[301–303] Display technologies such as phage or mRNA display can be used to create large ($10^{10} - 10^{15}$) and diverse peptide libraries, that can be screened based on affinity to desired target.[304,305] Alternative *in silico* approaches, including using complementary-determining regions (CDRs: short peptide sequences rationally designed for target proteins), have enabled the identification of binding peptides to specific proteins of interest and their further functionalisation in antibody-constructs.[306] Excitingly, *de novo* peptide libraries can also be generated using RaPID (RAndom nonstandard Peptides Integrated Discovery) platform that can incorporate nonstandard amino acids into the hit sequences through flexible *in vitro* translation. RaPID combines mRNA display technology with affinity-based selection of *in vitro* macrocyclic peptide libraries.[307] Despite these advances, the timeline from initial library building to confirming specificity and affinity of the lead sequence, produces a significant bottleneck when it comes to fluorescent peptide development.

With that in mind, the simplest approach to extend the range of applications of Peptide-PAINT outside of a few set targets, was to look at a protein independent approach. Following the footsteps of Gidden *et. al.*, and Eklund *et al.*, a transient interaction between two α-helical peptides[294,299] was harnessed to generate blinking for SMLM. Figure 6.2.2 shows a cartoon representation of the principles of Peptide-PAINT in SMLM. One α-helical peptide is conjugated to the target molecule (anchor peptide), whilst the other peptide (imager peptide) diffuses freely in solution. As was the case with peptide-protein version of the technique described above, the imager peptide cannot be localised when moving in solution. When the imager encounters the anchor peptide, the transient binding holds the imager peptide in place ensuring localisation of the fluorophore molecule (imager and anchor peptide complex in Figure 6.2.2A). The interaction is transient, the complex dissociates and another imager peptide can interact with the anchor. The intensity profile that would be associated with these events is presented in Figure 6.2.2B.

The asterisk (*) signifies binding events above the general background, repeated

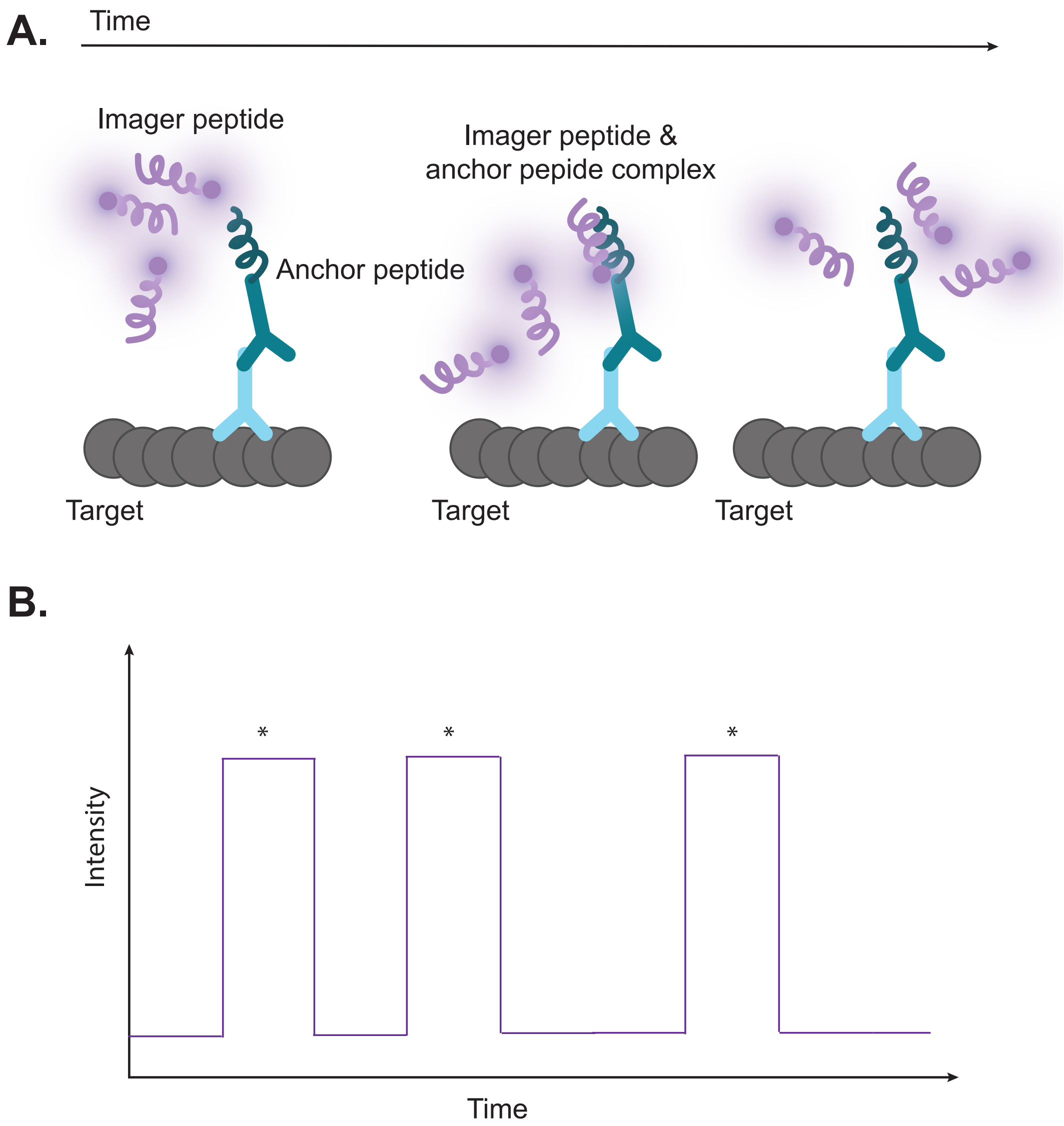

Figure 6.2.2: Peptide-PAINT using transient coiled-coil interactions. A. A cartoon representation of the target functionalised with an anchor peptide (here through a pair of antibodies). The imager peptide diffuses freely in solution, forming transient imager-anchor complex over the course of imaging. B. Schematic representation of an intensity profile over time associated with a Peptide-PAINT experiment. Asterisk (*) denotes high intensity associated with imager-anchor interaction, which would be observed as “blinks” on a camera.

across the imaging time. Mimicking the LIVE-PAINT approach,[297] the synthetic approach to Peptide PAINT employed a 101A and 101B peptide pair. The 101A peptide was chosen as the imager, following fluorescent labelling at the N-terminal, and 101B peptide as the anchor peptide for functionalisation of a target protein.

The chosen interaction pair was a set of heterodimeric coils - 101A and 101B, the structures of which were first reported by Chen et. al[286] as a modification to the original SYNZIP leucine zipper pair. The amino acid sequence of these are based on the bZIP - basic lecuine-zipper transcription protein.[308,309] The crystal structures of the two interacting peptides,[309] 101A (grey) and 101B (blue) are presented in Figure 6.2.3. The full sequences are denoted in Figure 6.2.3B. Both coils are 42 aa long, and their sequences follow the classic heptad repeat patter characteristic for coiled-coil pairs.[310] The first amino acid in the sequence is in position *f*, the next 7 follow the *abcdef* labelling convention. The helix wheel diagram is presented in Figure 6.2.3C, where the specific interactions between the two peptides can be better observed. The two interacting grooves are hydrophobic and made up of (mainly) leucine residues in positions *d*, with some more variability in the hydrophobic amino acids in positions *a*. The interaction is further stabilised by the attractive electrostatics of residues in positions *g* and *e*. Negatively charged amino acids are presented in blue, and positively charged amino acids in red. The green spheres represent a few polar non-charged amino acids present throughout the sequence.

The feasibility of using synthetic 101A and 101B peptides for super-resolution imaging was tested *in vitro* and *in situ* using a cellular model.

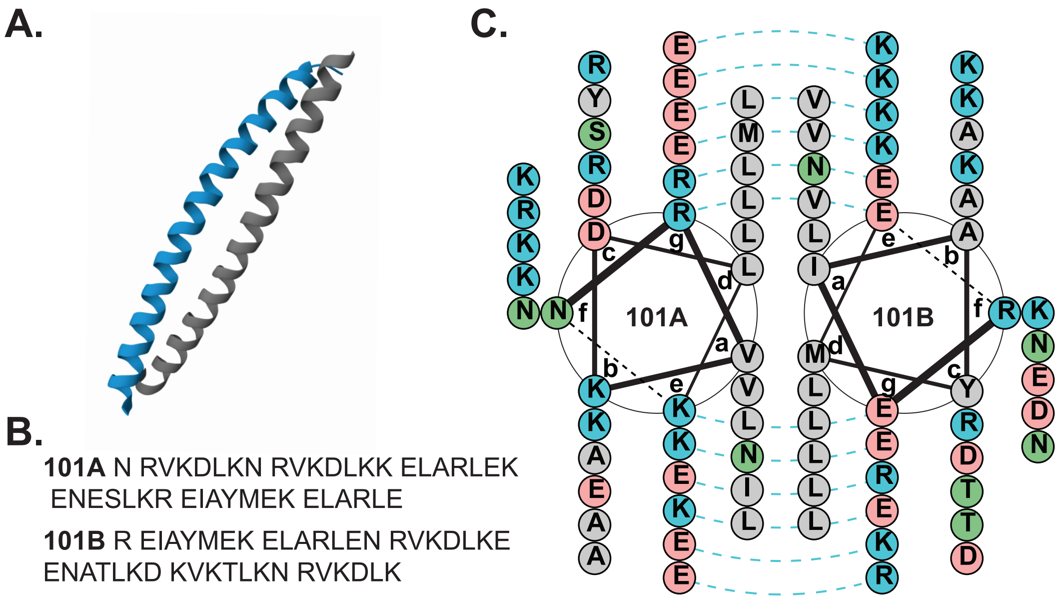

Figure 6.2.3: 101A and 101B peptide structures. A. A cartoon representation of the crystal structures of 101A (grey) and 101B (blue) forming a coiled-coil. PDB access code: 3HE5. B. Amino acid sequences of both peptides. Notation follows the *abcdef* heptad repeat pattern, the first amino acid is in position **f**. C. A helix wheel diagram showcasing the interactions between 101A and 101B. Grey amino acids are non-polar, green polar uncharged, red negatively charged and blue positively charged.

.

6.3 Methods

6.3.1 Peptide synthesis

101A peptide library was generated following the scheme presented in Figure 6.3.1.

Ac-Asn-Arg-Val-Lys-Asp-Leu-Lys-Asn-Arg-Val-Lys-Asp-Leu-Lys-Lys-Glu-Leu-Ala-Arg-Leu-Glu-Lys-Glu-Asn-Glu-Ser-Leu-Lys-Arg-Glu-Ile-Ala-Tyr-Met-Glu-Lys-Glu-Leu-Ala-Arg-Leu-Glu-NH2 (Ac-101A)

The synthesis was performed on 28 mg of Tentagel R RAM resin (0.18 mmol g^{-1}). After cleavage, the crude peptide was precipitated by adding cold Et_2O (dropwise) and the resulting precipitate was decanted and dried (×3). Purification was conducted by semi-preparative HPLC with detection at 220 nm. Pure fractions were collected and lyophilized to afford pure peptide Ac-101A as a white solid (4.8 mg, 18%). HPLC-MS: t_R: 4.82 min, 99% purity. HRMS (ESI+) (m/z) for $C_{224}H_{389}N_{69}O_{68}S$, $[M+H]^+$: 5169.000.

Ac-SeNBD-Asn-Arg-Val-Lys-Asp-Leu-Lys-Asn-Arg-Val-Lys-Asp-Leu-Lys-Lys-Glu-Leu-Ala-Arg-Leu-Glu-Lys-Glu-Asn-Glu-Ser-Leu-Lys-Arg-Glu-Ile-Ala-Tyr-Met-Glu-Lys-Glu-Leu-Ala-Arg-Leu-Glu-NH2 (SeNBD-101A)

The synthesis was performed on 28 mg of Tentagel R RAM resin (0.18 mmol g^{-1}). After cleavage, the crude peptide was precipitated by adding cold Et_2O (dropwise) and the resulting precipitate was decanted and dried (×3). Purification was conducted by analytical HPLC with detection at 340 and 486 nm. Pure fractions were collected and lyophilized to afford the pure peptide SeNBD-101A as a pale-yellow solid (3.1 mg, 11%). HPLC-MS: t_R: 4.70 min, 98% purity. HRMS (ESI+) (m/z) for $C_{233}H + 396N_{74}O_{71}SSe$, $[M+5H]^{5+}$: 1097.3790, $[M+6H]^{6+}$: 914.4846, $[M+7H]^{7+}$: 783.9881, $[M+8H]^{8+}$: 686.2394. MALDI (m/z): [M+H]+: 5482.9403

Cy3B-Asn-Arg-Val-Lys-Asp-Leu-Lys-Asn-Arg-Val-Lys-Asp-Leu-Lys-Lys-Glu-Leu-Ala-Arg-Leu-Glu-Lys-Glu-Asn-Glu-Ser-Leu-Lys-Arg-Glu-Ile-Ala-Tyr-Met-Glu-Lys-Glu-Leu-Ala-Arg-Leu-Glu-NH2 (5-101A)

The synthesis was performed on 7 mg of Tentagel R RAM resin (0.18 mmol g−1). The resin was reacted with Cy3B-NHS ester (2 eq.), DIPEA (2.eq) for

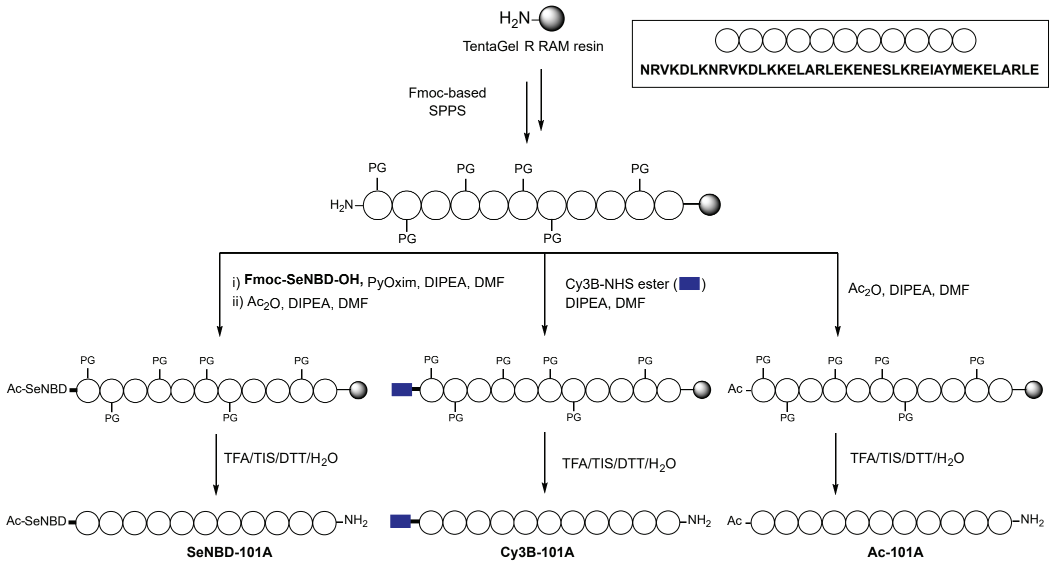

Figure 6.3.1: Synthesis of 101A and analogues using Fmoc-based SPPS.

4h at r.t. The excess reagent was washed off with MeOH. After cleavage, the crude peptide was precipitated by adding cold Et_2O (dropwise) and the resulting precipitate was decanted and dried ($\times 3$). Purification was conducted by semi-preparative HPLC with detection at 220 nm and 560 nm. Pure fractions were collected and lyophilized to afford the pure peptide Cy3B-101A as a bright pink solid (0.7 mg, 9.6%). HPLC-MS: t_R: 4.93 min, 98% purity. (m/z) for formula 5666.06 predicted, $[M{+}6H]^{6+}$: 944.93, $[M{+}7H]^{7+}$: 809.71 observed.

The 101B peptides were prepared according to the scheme in Figure 6.3.2.

biotin-Arg-Glu-Ile-Ala-Tyr-Met-Glu-Lys-Glu-Leu-Ala-Arg-Leu-Glu-Asn-Arg-Val-Lys-Asp-Leu-Lys-Glu-Glu-Asn-Ala-Thr-Leu-Lys-Asp-Lys-Val-Lys-Thr-Leu-Lys-Asn-Arg-Val-Lys-Asp-Leu-Lys-NH2 (biotin-101B)

The synthesis was performed on 28 mg of Tentagel R RAM resin (0.18 mmol g-1). After cleavage as described above, the crude peptide was precipitated by adding cold Et2O (dropwise) and the resulting precipitate was decanted and dried ($\times 3$). Purification was conducted by semi-preparative HPLC with detection at 220 and 280 nm. Pure fractions were collected and lyophilized to afford pure peptide biotin-101B as a pale-yellow solid (9.9 mg, 38%). HPLC-MS: t_R: 4.53 min, 95% purity. HRMS (ESI+) (m/z) for $C_{230}H_{399}N_{69}O_{68}S_2$, $[M{+}5H]^{5+}$: 1057.5960, $[M{+}6H]^{6+}$:881.4974, $[M{+}7H]^{7+}$: 755.7128, $[M{+}8H]^{8+}$: 661.2490. MALDI (m/z):

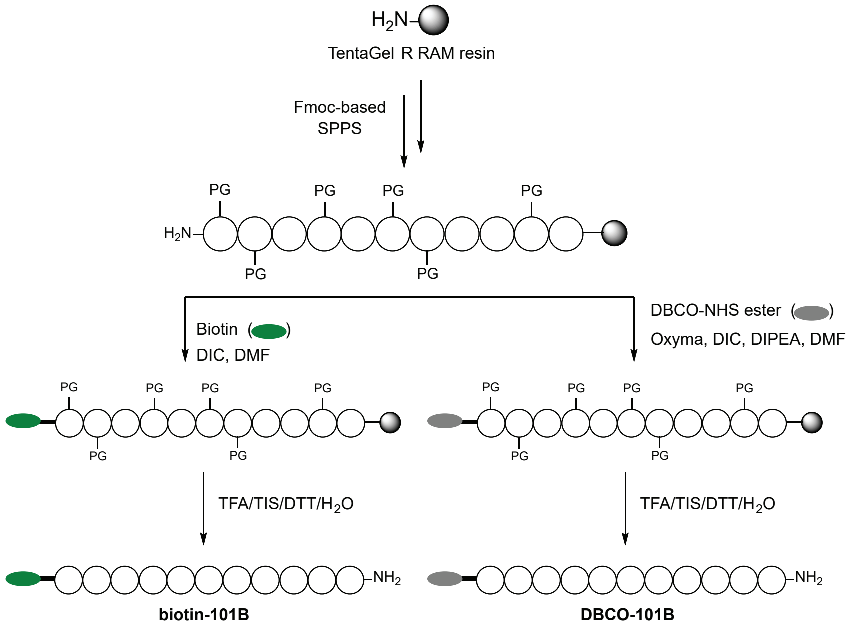

Figure 6.3.2: Synthesis of 101B and analogues using Fmoc-based SPPS.

$[M+H]^{+}$:5283.8171.

DBCO-Arg-Glu-Ile-Ala-Tyr-Met-Glu-Lys-Glu-Leu-Ala-Arg-Leu-Glu-Asn-Arg-Val-Lys-Asp-Leu-Lys-Glu-Glu-Asn-Ala-Thr-Leu-Lys-Asp-Lys-Val-Lys-Thr-Leu-Lys-Asn-Arg-Val-Lys-Asp-Leu-Lys-NH2 (DBCO-101B)

The synthesis was performed on 28 mg of Tentagel R RAM resin (0.18 mmol g−1). The resin was reacted with DBCO-NHS ester (4 eq.), DIPEA (4 eq.) in presence of DIC (4 eq.) and Oxyma (4 eq.) in DMF, at 60 °C, 30 W for 10 mins. for After cleavage as described above, the crude peptide was precipitated by adding cold Et2O (dropwise) and the resulting precipitate was decanted and dried (×2). Purification was conducted by semi-preparative HPLC with detection at 220 and 310 nm. Pure fractions were collected and lyophilized to afford pure peptide DBCO-101B as a pale-yellow solid (1.3 mg, 4.8%). HPLC-MS: t_R: 4.92 min, 96% purity. (m/z) for formula, $[M+5H]^{5+}$: 1068.99, $[M+6H]^{6+}$: 891.11, $[M+7H]^{7+}$: 763.23.

6.3.2 CD measurements

CD spectra were obtained at r.t. using a JASCO J-810 CD spectrometer. A range of 190-260 nm was scanned at a speed of 50 nm min^{-1}, with 1 nm data pitch, 1 nm bandwidth and 8 s response time. The presented spectra are averaged across 8 accumulations taken. Samples were prepared in phosphate buffered saline (PBS, pH 7.4). CD spectra were measured in 0.2 mm quartz cuvettes at two indicated concentrations in each case. Raw data (observed ellipticity - θ; mdeg) were converted to mean residue ellipticity (MRE; deg cm^2 dmol^{-1} res^{-1}) by normalizing for path length (l), peptide concentration (c), and number of amide bonds (N) using the formula in Equation 6.1 below.

$$MRE = \frac{\theta}{10 \times l \times c \times N} \tag{6.1}$$

6.3.3 FCS measurements

For measuring the association between 101A and 101B, SNBD-101A peptide, biotin-101B and streptavidin (SA101, Sigma Aldrich, 0.2 mg/mL stocks) were used. First, biotin-101B and SNBD-101B were prepared from DMSO stock. All solutions were prepared in duplicates. 400 nM biotin-101B solution and 400 nM and 100 nM SNBD-101A solutions were prepared in eppendorfs and heated on a heating block (Eppendorf) at 60 °C for 10 minutes. The diffusion of 100 nM SNBD-101A solution was then measured on the confocal microscope under 488 nm laser illumination. 400 nM biotin-101B and 400 nM SNBD-101A were incubated for half an hour at a 1:1 ratio. Following the incubation, the peptides were further incubated with strepatividn for 30 minutes. The streptavidin was used at two concentrations of approx. 3.8 μM (0.2 mg/mL stock) and 1 μM. This resulted in final concentrations of 1.9 μM and 500 nM streptavidin. FCS of all solutions was acquired. The same analysis as above was performed to obtain diffusion lag times. The data were plotted in GraphPad (Prism).

6.3.4 TIRFM sample preparation, image acquisition and analysis

Single-molecule and super-resolution imaging was performed on a TRIFM described in Methods section 2.4.2. The laser lines and mirrors are described therein.

101A-101B peptides

The plasma-cleaned coverslips were incubated with BSA-biotin (1 mg/mL, 50 μL) for 10 min. Slides were washed three times with PBS and incubated with streptavidin (0.2 mg/mL, 50 μL) for 10 min. Following three PBS washes, the anchor peptide biotin-101B (experiment dependent: 0 nM, 1 nM, 100 nM) was incubated for 10 min. Finally, after three PBS washes, the imaging peptide (experiment dependent: 1 nM Cy3B-101A or 100 nM SeNBD-101A) was applied to the surface. Samples were imaged using 515 nm excitation (for SeNBD-101A), 561 nm excitation (for Cy3B-101A) and 638 nm excitation (for AF647) under wash-free conditions. Fluorescence images were acquired for 500 frames with 50 ms exposure and approximately 500 W cm^{-2} in both channels.

Heat-treated peptides were prepared (through dilution into PBS) to the concentration required by the experiment and heated on an Eppendorf heating block to 60 °C for 10 minutes. Such prepared peptides were used immediately in the experiments and used up within 12h of heat treatment.

500 frame stacks were used to compare the "mobility" of the peptide when prepared cold or heated. A single particle tracking script was used for this purpose. A threshold was used to identify localisations within a single frame. These were then tracked across the image (with the assumption that the molecule could move up to 5 px between frames and be missing for 5 frames to qualify as the same event). A tracks image representing the movement of each of the detected spots was generated. The total displacement within the stack (MSD) was recorded for each molecule to generate histograms. The code used to track molecules and plot histograms can be access at DOI: 10.5281/zenodo.13829155.

For the surface optimisation experiment all coverslips were plasma cleaned for 30 minutes. The different surfaces were prepared as following:

- **Plasma cleaned** - no further preparation;
- **PLL** - 50 μL of poly-L-lysine (70,000-150,000 Da, Sigma-Aldrich) was added to a coverslip and incubated for 30 minutes, before being washed with PBS three times;
- **BSA** - BSA-biotin (1 mg/mL, 50 muL) was applied to a coverslip for 10 min. The coverslips were washed three times with PBS and incubated with streptavidin (0.2 mg/mL, 50 muL) for 10 min. Another three washes were performed;
- **Tween** - the slides were dipped in 5% v/v solution of Tween-20 in T50, and washed thoroughly (3×) with PBS;
- **PEG** - surface modified with PEG-silane according to SimPull methods,[216] incubated with streptavidin (0.2 mg/mL, 50 μL) for 10 min, and washed with MiliQ water (3×);
- **PEG+** - surface modified with PEG-silane according to STAPull methods,[216] incubated with streptavidin (0.2 mg/mL, 50 μL) for 10 min, and washed with MiliQ water (3×); 1% v/v Tween-20 solution was applied for another 10 minutes. Slide was washed with MiliQ water for final three times;
- **DT20** - surface preparation followed published protocol.[311] BSA-biotin (1 mg/mL, 50 μL) was applied to a coverslip for 10 min. The coverslip was washed three times with T50 and incubated with 0.2% Tween-20 in T50 buffer for 10 minutes. Following three more washes, streptavidin (0.2 mg/mL, 50 μL) was incubated for 10 min. Another three washes were performed.

Such prepared surfaces were treated with 100 nM heated SeNBD-101A solution. 9 FOVs were imaged for each condition using 561 nM excitation, taking 500 frames in each image. For each of the images, a standard deviation based projection was created. The spots were localised using the "find maxima" function in Fiji - the prominence used for this was 50. The number of spots detected for all conditions was visualised in Origin.

For the co-localisation experiments the plasma-cleaned coverslips were incubated with BSA-biotin (1 mg/mL, 50 μL) for 10 min. Slides were washed three times with PBS and incubated with AF647-labelled streptavidin (16.6 nM, 50 μL) for 10 min. Following three PBS washes, the anchor peptide biotin-101B (100 nM) was incubated for 10 min. Finally, after three PBS washes, the imaging peptide (100 nM SeNBD-101A) was applied to the surface. Samples were imaged using 515 nm excitation (for SeNBD-101A) and 638 nm excitation (for AF647) under wash-free conditions. Fluorescence images were acquired for 500 or 50 frames with 50 ms exposure on both channels. Merge images were created in Fiji.

6.3.5 Cell fixation and staining - biotin-101B

All cell were seeded in ibidi 18-well plates with glass bottom for super-resolution microscopy. The seeding was conducted at approx. 5,000 cells per well to achieve 30% confluency on the day of imaging. The cells were kept in the incubator until fixation. Post fixation cells were processed immediately and after fixation stored at 4 °C up to 1 week before further processing.

The initial cell handling protocol followed the procedure devised by Eklund *et. al* for Peptide-PAINT.[294] The buffers outlined below were prepared on the day of imaging. Stock PBS was filtered through 0.02 μm filter (Whatman, Anotop) and used to prepare the following:

- **fixation buffer** - 3% glutaraldehyde (prepared from 25% w/v solution) in PBS;
- **pre-extraction buffer**: 0.3% glutaraldehyde, 0.25% v/v Triton X-100 in PBS;
- **blocking buffer**: 1mM EDTA, 3% (wt/volume) BSA, 0.02% Tween-20, 1% (wt/vol) dextran sulfate in PBS;

- **blocking buffer + TX**: 1mM EDTA, 3% (wt/volume) BSA, 0.02% Tween-20, 1% (wt/vol) dextran sulfate, 0.25% Triton X-100 in PBS;
- **reduction buffer** - 0.1% (wt/v) $NaBH_4$ in PBS - prepared during the fixation step.

The PBS and fixatives were warmed to 37 °C. Cells were rinsed with PBS (1x) and treated with the pre-extraction buffer for 90s. The pre-extraction buffer was removed and substituted with the fixation buffer for 10 minutes. The cells were then rinsed with PBS twice. The remaining fixative was reduced by a freshly prepared sodium borohydrate buffer - the reduction buffer was applied over the cells for 7 minutes. Subsequently, a series of PBS washes was performed (1 min, 3 min, 5 min, 10 min). The blocking buffer supplemented with TX was applied for 2.5h and cells kept at room temperature.

Following primary antibodies were prepared in the blocking buffer (without TX):

- α tubulin - Rabbit anti-tubulin antibody (ab52866, Abcam), at 1:500 dilution
- TOMM20 - Rabbit anti-TOMM20 antibody (ab78547, Abcam), at 1:500 dilution

The incubation time ranged from 16-19h (overnight) at 4 °C. The cells were washed with PBS (3×) the next morning before treatment with a secondary antibody (1-1.5h at room temperature). The secondaries used included:

- Donkey anti-Rabbit biotinylated antibody (ab7082, Abcam) at 1:200 dilution, amounting to 0.0005 mg/mL);
- Donkey anti-Rabbit Cy5 antibody (711-175-152, JacksonImmuno) at 1:200 dilution.

The cells were washed 3 times after the incubation period had passed.

The biotin-101B peptide was diluted in PBS to a range of concentrations (0.2 nM, 200 nM, 400 nM, 1 μM and 2 μM) and heated as before. A range of streptavidin concentrations was prepared (0.05 nM, 50 nM, 100 nM, 250 nM and 500 nM). The solutions were mixed in 1:1 ratios to yield solution of the total concentrations of: 0.1 nM biotin-101B & 0.025 nM streptavidin, 100 nM biotin-101B & 25 nM streptavidin, 200 nM biotin-101B & 50 nM streptavidin, 500 nM biotin-101B & 125 nM streptavidin, 1 μM biotin-101B & 205 nM streptavidin. These were designed to follow a 4:1 ratio biotin and streptavidin and for streptavidin concentration to exceed the biotin concentration in the antibody. These solutions were incubated at 36 °C with 250 rev/min shaking for 30 minutes and applied to the stained cells for another 30 minutes. 3x PBS washes were performed to wash excess reagents.

The imaging peptides (10 nM Cy3B-101A and 1 μ SeNBD-101A) were applied prior to imaging on TIRFM. Cy3B-101A was excited with 561 nM illumination ($\sim$ 25 W cm^{-2}) and SeNBD-101A was excited with 515 nm laser ($\sim$ 40 W cm^{-2}). 10,000 frames were recorded. White light images (50 frames) were recorded for each cell. The GDSC SMLM plugin was used to find single localisations (precision = 50 nm, signal strength = 0, fail limit = 10).

6.3.6 Cell fixation and staining - genetically encoded 101B

All cells were seeded in ibidi 18-well sticky plates for super-resolution microscopy. Coverslips were argon plasma cleaned for 45 minutes, before attaching the wells. The slides were then incubated for 1 hour in poly-D-lysine (PDL) (50 μg/mL, Gibco) and thoroughly washed with deionised water. The wells were seeded as before. The cells were kept in the incubator until desired confluency of 30% was achieved. Post fixation cells were processed immediately and after fixation stored at 4 °C up 1 week before further processing.

The fixing protocol was simplified slightly. The buffers outlined below were prepared on the day of imaging. Stock PBS was filtered through 0.02 μm filter (Whatman, Anotop) and used to prepare the following:

- **fixation buffer** - 3% glutaraldehyde (prepared from 25% w/v solution) in PBS;
- **blocking buffer**: 3% (wt/volume) BSA in PBS;

- **blocking buffer + TX**: 3% (wt/volume) BSA, 0.25% Triton X-100 in PBS;
- **reduction buffer** - 0.1% (wt/v) $NaBH_4$ in PBS - prepared during the fixation step.

The PBS and fixatives were warmed to 37 °C. Cells were rinsed with PBS (1×) and treated with fixation buffer for 10 minutes. The cells were then rinsed with PBS twice. The remaining fixative was reduced by a freshly prepared sodium borohydrate buffer - the reduction buffer was applied over the cells for 5 minutes. Subsequently, three PBS washes were performed. The blocking buffer supplemented with TX was applied for 2.5h and cells kept at room temperature.

For the co-localisation experiments, the primary antibodies were prepared in the blocking buffer (without TX):

- TOMM20 - mouse monoclonal anti-TOMM20 antibody (ab56783, Abcam), at 1:200 dilution
- LAMP1 - mouse monoclonal anti-LAMP1 antibody (ab25630, Abcam), at 1:100 dilution

The incubation time ranged from 16-19h (overnight) at 4 °C. The cells were washed with PBS (3×) the next morning before treatment with a secondary antibody (1-1.5h at room temperature) also prepared in the blocking buffer. The secondary used was an AF647-labelled donkey anti-mouse antibody (131571, ThermoFisher) at 1:1,000 dilution in blocking buffer. The cells were washed 3 times after the incubation period had passed.

The imaging peptides (Cy3B-101A and SeNBD-101A) were applied directly prior to imaging on TIRFM. Cy3B-101A was excited with 561 nM illumination ($\sim$ 25 W cm^{-2}) and SeNBD-101A was excited with 515 nm laser ($\sim$ 40 W cm^{-2}), AF647 was excited with 635 nm illumination ($\sim$ 20 W cm^{-2}). 10,000 frames were recorded for the peptide signal and 50 frames for the antibody signal. White light images (50 frames) were recorded for each cell also. GDSC SMLM plugin was used to find single localisations (precision = 50 nm, signal strength = 0, fail limit

= 10) and create the Peptide-PAINT images. Z-projections and merge images were created in Fiji.

6.4 Results

6.4.1 Characterisation of 101A and 101B *in vitro*

The α-helical peptides were synthesised using standard SPPS methods on a Rink amide resin. Fluorescent amino acids and a conventional dye (for a control peptide) were placed at the N-terminal of the 101A sequence. Two types of linker molecules for further derivatisation of antibodies to 101B sequence were considered: DBCO to perform a Click reaction with azide-tagged antibodies, and biotin for binding to streptavidin-tagged antibodies. The 101A sequence was built on resin and the final Fmoc group removed. Functionalisation with **amino acids 5** and **6** (SeNBD and SNBD) was performed on resin, using the same coupling conditions as for all other amino acids, with a small excess of the fluorescent amino acid. Subsequent Fmoc deprotection, cleavage from resin, and HPLC purification yielded the desired peptides: SeNBD-101A and SNBD-101A at 95% purity. A similar route was followed to prepare a biotinylated version of the 101B anchor peptide, where biotin was treated as an "unnatural" amino acid and coupled to the peptide chain on resin (a large excess of biotin was used in this case at approximately 4 equivalents). The same approach as for biotin was followed for DBCO-NHS. The decision to perform the conjugation on resin was dictated by the reports of DBCO resistance to long term TFA treatement.[312,313] For the conventional fluorophore, despite the pre-activated dye (Cy3B-NHS ester), microwave conditions were needed to push the reaction towards completion. Thus, three fluorescent imager peptides: SeNBD-101A, SNBD-101A, and Cy3B-101A, a control Ac-101A peptide and two anchor peptides: biotin-101B and DBCO-101B were prepared.

Circular dichroism analysis

Next, the secondary characteristics of the α-helical peptides were studied to confirm correct folding of peptides in solution. To this end, circular dichroism (CD) was used. CD is a spectroscopic technique that measures the difference of absorbance between left-handed (LH) and right-handed (RH) circularly polarised light. Chiral molecules, such as α-helical peptides, interact differently with RH and LH circularly polarised light, giving rise to characteristic peaks in the spectrum. The difference in absorbance (mdeg) is observed across wavelengths (range around 190 nm - 260 nm). The mdeg can be further converted to mean residue ellipticity (MRE; $degcm^2mol^{-1}res^{-1}$) to account for path length, peptide concentration and number of amide bonds and make meaningful comparisons across measurements possible. For α-helical peptides, three features are needed for identification: a positive peak at around 193 nm and two negative peaks (dips) near 208 nm and 222 nm. The CD traces recorded for 4 peptides: Ac-101A, SeNBD-101A, Cy3B-101A and DBCO-101B were compared. The acetylated version of 101A, containing no dye, was treated as a positive control, where α-helical folding could be observed. It was hoped the small size of the SeNBD was unlikely to disrupt the coil structure, and in fact even with Cy3B a level of tolerance was expected due to the size of the peptide (41 aa) and the positioning of the fluorescent dye (position g, which is not involved in the hydrophobic interactions of two coiled-coils). The CD spectra obtained for the peptides are presented in Figure 6.4.1. These were measured in PBS buffer (no traces of organic solvent) at two concentrations: 25μM and 50μM. The limiting factor in choosing these was the solubility of the peptides in purely aqueous buffer. The solutions needed to be homogeneous for accurate absorbance measurements at concentrations high enough to detect signal. At concentrations of 100μM, the DBCO-101B peptide was observed to crash out of the solution. When measured at 5μM, the difference in absorbance was indiscernible from the buffer (blank) signal. The traces were compared across two concentrations to account for any concentration effects on secondary structure. Figure 6.4.1A compares the secondary strucutre of SeNBD-101A and Ac-101A.

The three peaks characteristic of an α-helix were observed, with a positive

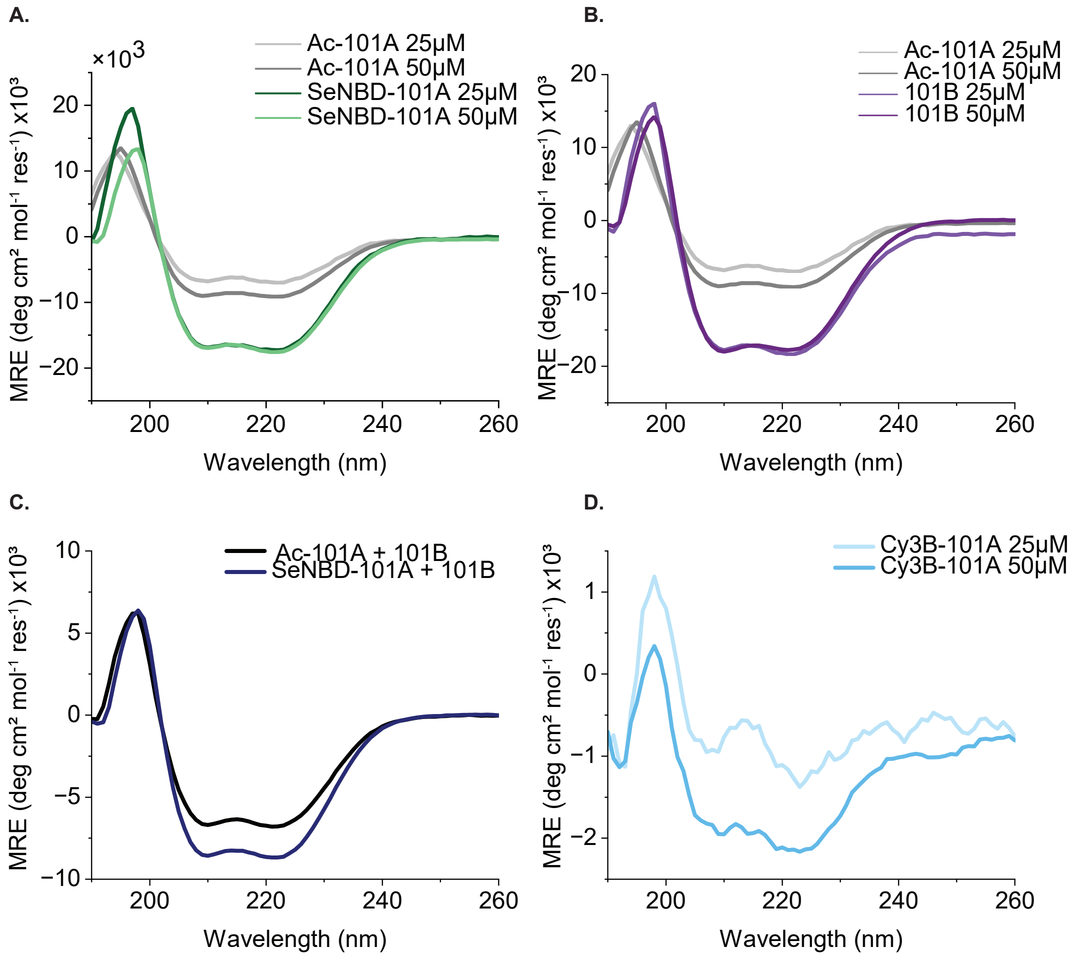

Figure 6.4.1: CD spectra of 101A and 101B analogues. All spectra averaged across 8 accumulations, acquired at two different concentrations 25μM and 50μM except for mixtures where both peptides are incubated in equal volumes (1:1) to the total concentration of 25μM. A. Ac-101A spectrum compared to SeNBD spectrum - the addition of the fluorophore does not disrupt the secondary structure observed. B. Ac-101A and DBCO-101B display α-helical structure *in vitro* C. CD spectra of 101A-101B mixtures: Ac-101A and DBCO-101B and SeNBD-101A and DBCO-101B, no change observed between the two. D. Cy3B-101A CD spectrum: a lot of noise observed due to solubility issues and subsequent concentration overestimation.

peak around 193nm, and two double dips roughly at 208 and 220 nm. The SeNBD trace showed a larger dip (more negative MRE measured) in the α-helix region, suggesting the dye potentially promotes dimerisation. The shape of the spectrum was consistent between the two conditions. The remaining spectra obtained followed the same shape. Ac-101A and DBCO-101B are compared in Figure 6.4.1B. Mixtures of 101A and 101B, to a total concentration of 25 μM for each peptide, were prepared and their CD spectra acquired. No change in the spectral shape was observed. This posed some concern and suggested homo-interactions between the peptides and dimerisation inhibit binding with the partner in the experimental conditions. The fluorescent 101A and Ac-101A gave similar spectra in terms of magnitude of the absorbance difference (Figure 6.4.1C). Interestingly, both traces spanned a lower range of MRE. This could be accounted for in the calculations, as now there was double the number of peptide bonds in the mixture. The Cy3B-101A measurements (Figure 6.4.1D) were inconclusive. It was hypothesised that the dye did not affect the secondary structure of the peptide, as the trace roughly followed the shape of all other spectra. The main reason for the noise and low MRE observed in the case of Cy3B-101A was its solubility, the peptide was observed crashing out of solution throughout the measurement. This not only interfered with data acquisition, but also made the concentration value used for mdeg to MRE calculation inaccurate. Thus, this particular spectrum had to be interpreted with caution.

Based on the observed spectral shape, indicating helical structure, further analysis was attempted. The helical fraction of the peptide was calculated to determine how much of the peptide (%) adopted the α-helix structure under the measurements conditions (PBS buffer). This was achieved by comparing the ellipticity value at 222nm to a theoretical value of a fully-helical peptide, following the Equation 6.2, where θ_{222} is the ellipticity value measured at 222nm and $\theta_{222,predicted}$ is the theoretical value.

$$\%helicity = \frac{\theta_{222} - \theta_{(c)}}{\theta_{222,predicted} - \theta_c} x100 \tag{6.2}$$

For θ_{222}, an average of the ellipticity measured at 222nm at the two distinct concentrations was used. θ_c is a term accounting for the temperature of the measurements, and was calculated using equation 6.3, where T is temperature expressed in degrees Celsius. The CD measurements were performed at 22°C.

$$\theta_c = 2220 - 53T \tag{6.3}$$

$\theta_{222,predicted}$ accounted for both the temperature and peptide size, through incorporating N_p - number of peptide bonds, T (temperature in Celsius, as above) and k - a scaling factor equal to 3, in equation 6.4.

$$\theta_{222,predicted} = (-44000 + (250 \times T)) \times (1 - \frac{k}{N_p}) \tag{6.4}$$

$\theta_{222,predicted}$ was calculated for the peptides and mixes separately (again accounting for the larger number of peptide bonds N_p present in the mixes). Unsurprisingly, in both cases, the value was estimated at around -36,000 $degcm^2dmol^{-1}res^{-1}$, which was consistent with literature reports.

As a result the helical fraction for each of the four peptides and the two mixes was calculated and presented in Table 6.1.

Table 6.1: Calculated helical fraction of peptides based on the CD measurements. Average value measured for two conditions presented for all samples (bar mixes). Error bars represent standard deviation.

Peptide	**Fraction helical (%)**
Ac-101A	25±3
SeNBD-101A	50±1
Cy3B-101A	8±1
DBCO-101B	52±1
Ac-101A + DBCO-101B	38
SeNBD-101A + DBCO-101B	48

The lowest % helicity observed was for the Cy3B-101A peptide. However, this could not be assigned to the fluorophore disrupting the folding, and rather accounted for by the solubility issues and likely incorrect concentration. All other values align with those observed for α-helical peptides in literature.[314,315] Ac-101A showed a slightly lower % helical fraction than SeNBD-101A (25% for the former and 50% for the latter). This could either be explained by the SeNBD having a favourable effect on the helix in comparison to an acetyl group, the dye promoting dimerisation of the peptide *in vitro*, or an inaccurate concentration estimate for the Ac-101A solution. The helical fraction was similar across SeNBD-101A and DBCO-101B. Interestingly, the % helicity has not increased for both mixes, indicating the coiled-coil interactions were not observed under the experimental conditions. Whilst Ac-101A became more helical on addition of 101B (25% to 38%), SeNBD-101A and SeNBD-101A + DBCO-101B remained basically constant (50% and 48% respectively). This was interesting, since % helicity is often used to monitor folding (or unfolding) under different conditions.[315] Thus, another parameter was used to try to measure the structure. θ_{222}:θ_{208} ratio was previously used to suggest the presence of coiled coils. Calculating the ratio of elliptcy at the two specific wavelengths, coiled coils were reported to exhibit a ratio around and higher than 1, whereas a ratio of less than 0.9 was characteristic of isolated helices.[315] With that in mind, the ratio for the peptides and the mixes was calculated from the CD data. Where measurements at two concentrations were acquired, these were calculated separately and then averaged for presentation in Table 6.2. Data for Cy3B-101A was not presented, due to the amount of noise in the spectrum (however, the ratio exceeded 1 in line with all the other peptides).

The ratios averaged at around 1 for all the peptides under investigation. With no difference in the ratio observed between solutions containing single peptides and mixes of peptides, it was proposed quaternary structure and coiled-coil interactions could be present across all experimental conditions. This suggested formation of homo dimers in solutions of Ac-101A, SeNBD-101A and DBCO-101B in abscence of an interaction partner. This somewhat surprising finding was in fact in line with the observations of Chen *et. al*, who found homo interactions between coils, whilst 100-fold weaker, are in fact present. They suggested 101A, in particular, can form homo dimers in an anti-parallel orientation with itself in absence of 101B.[286]

Table 6.2: θ_{222}:θ_{208} ratio as an indication of quaternary structure. Values of and above 1 are stipulated to be coiled-coils, values of less than 0.9 are isolated helices.

Peptide	**θ_{222}:θ_{208} ratio**
Ac-101A	1.05
SeNBD-101A	1.07
DBCO-101B	1.06
Ac-101A + DBCO-101B	1.06
SeNBD-101A + DBCO-101B	1.05

Whilst the affinity for these interactions is smaller, at high μM concentrations (exacerbated by the freeze drying process used to prepare the samples) these could result in formation of coiled coils.

Imaging immobilised 101B peptide

This unexpected finding explained the initially unsuccessful attempts at observing 101A-101B interactions under a microscope. To confirm the ability of the prepared peptide probes to interact *in vitro* and produce blinks under the microscope, an experiment - as shown in Figure 6.4.2A was attempted. A surface of a coverslip was incubated with biotin-BSA, and streptavidin prior to biotin-101B immobilisation. The surface was subsequently treated with an imager peptide solution and imaged on a TIRF microscope. In the first run, 500 frames of 100ms exposure were compared for three conditions: 1nM biotin-101B only, 1nM Cy3B-101A only, and 1nM biotin-101B with 1nM Cy3B-101A (Figure 6.4.2B). As predicted, the standard deviation projections of the z-stacks revealed no significant blinks (4 maxima on the image from the figure) for the biotin-101B peptide, confirming no fluorescence contamination or autofluorescence of the surface. However, the difference in the amount of events detected for the Cy3B fluorescence, in presence of stoichiometric 101B and in its absence, was negligible at best, with approx. 330 events detected in both cases. The images showcase representative ROIs.

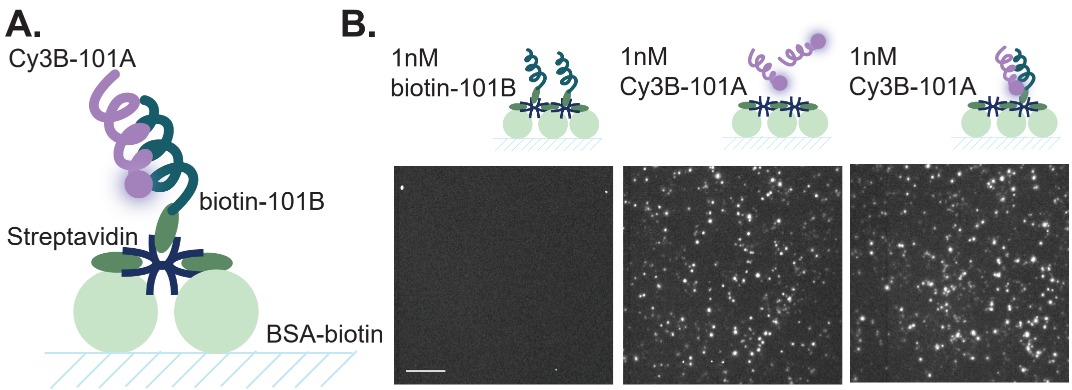

Figure 6.4.2: 101A-101B binding events as detected on TIRFM. A. Experimental set up: BSA-biotin used to treat coverslip surface, streptavidin incubation and subsequent biotin-101B immobilisation. Cy3B-101A in solution, forming coiled-coil with 101B transiently leading to observable blinks. B. Standard deviation z-projections of a 500 frame stacks for 1nM 101B, 1nM Cy3B-101A in abscence and presence of 101B. Similar number of events is observed from Cy3B-101A in presence and abscence of the binding partner, suggesting the observed events are due to the presence of Cy3B-101A dimers. Scale bar is 5μm.

Initially, the lack of difference between Cy3B-101A in the presence and absence of 101B was attributed to the experimental set-up. There was no optimisation of the surface, and spurious binding was to be expected with a bright dye such as Cy3B. 101A and 101B peptides were assumed to be present at 1:1 stoichiometric ratio through using the same concentrations on the surface, however the immobilisation process could result in a sparsely labelled surface with few interaction sites for 101A. Thus, the next attempts looked at using excess 101B on the surface. However, no difference was observed regardless of the 101B concentration. It was therefore reasoned that, as seen in the CD experiments, the Cy3B-101A peptide forms dimeric coils with itself. These interactions are likely formed during the freeze-drying process, where the solvent is removed. Despite further dilutions (lower concentrations needed for TIRFM than CD), the homo-dimeric coiled-coils bind tightly. The spots observed on the TIRFM are in fact signal from just Cy3B-101A dimers, not from Cy3B-101A and 101B interactions.

This, together with the CD data, confirmed the presence of homo dimeric coiled-coils could be at the root cause of the imaging problems. It was hypothesised, that unless these peptide homo-dimers could be disrupted, interactions between

101A and 101B leading to actual localisation will be highly unlikely. The theory was tested through another TIRFM experiment. The 101A imager (this time 100 nM SeNBD-101A) was imaged in presence and absence of the anchor peptide (biotin-101B), and the relative mobility of the peptides was assessed through particle tracking. One of the issues encountered during imaging thus far was that the blinks observed fell within the first frames of the image and disappeared quickly with poor signal replenishment observed over time. Some "always on" events were also observed. With that in mind, 500 frames of 100 nM SeNBD-101A were imaged on a surface (a montage of 9 of these is shown in Figure 6.4.3A). It can be seen that one of the blinks disappears within the first 50 frames, and the other bright event remains on across the 500 frames. The particles from that image where identified in each frame and their movements tracked across the entire image stack. Particles within a 5 pixel distance from the initial localisation and absent for less than 5 frames were classed as the same localisation. The movements of the particles were presented as traces on an image, with each colour representing one molecule (Figure 6.4.3B, top panel). Moreover, the movement in time was analysed as Mean Square Displacement (MSD). The maximal MSD of each particle was then plotted on a histogram to show how much the molecules moved across the imaging session (Figure 6.4.3B, bottom histogram). The same analysis was performed for SeNBD-101A in the presence of 101B on the surface. It was quickly discovered that the tracks for both these conditions showed little movement and sparse localisations, and the MSD histograms binned most MSD as 0-0.03nm (Figure 6.4.3C). This suggested that the hypothesised homo dimeric scenario (Figure 6.4.3D) was in fact taking place. It was hypothesised that the homo dimeric interactions take place in the highly concentrated stock solutions (for instance 650μM), and cannot be effectively replaced by hetero dimer formation on the timescales of the experiment (where relatively low, nM at most, concentrations are used). Thus, an intervention was deemed necessary to un-coil the homo dimers and enable successful Peptide-PAINT.

Whilst changing the peptide interaction pair, or investigating point mutations in the peptide sequence that would inhibit the propensity of 101A and 101B to self-

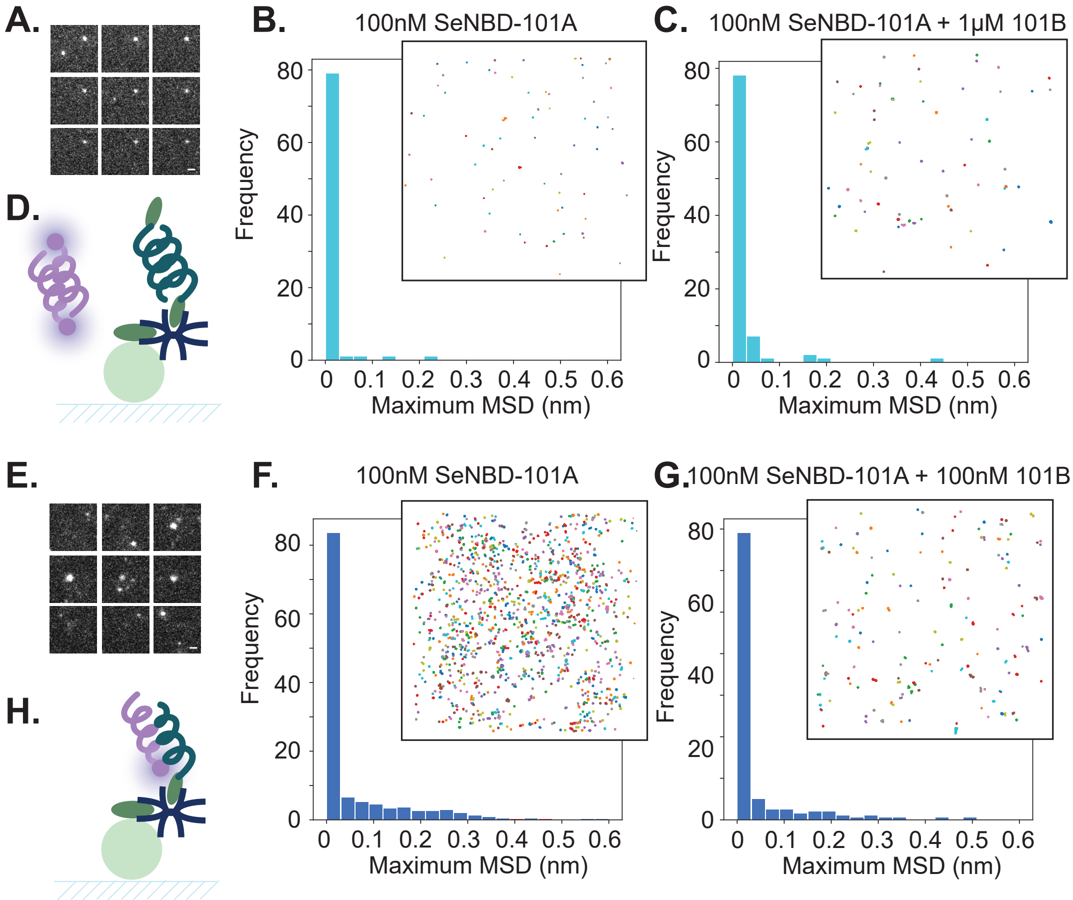

Figure 6.4.3: 101A-101B binding events as detected on TIRFM. A. A montage of 9 frames from a 500-frame stack of 100nM SeNBD-101A imaging. Left to right frames 1, 50, 100, 150, 200, 250, 300, 400, 500. Scale bar is 1μm. B. Histogram showcasing max MSD for each particle detected from an image of 100nM SeNBD-101A on a surface. The insert showing the tracks (each molecules is a different colour - the molecules are not too scale). C. Same data set displayed for 100nM SeNBD-101A in presence of 1μM 101B. D. Cartoon representation of the homo-dimers between the imaging partners. E. A montage, as in A, for heated solution of 100nM 101A. The tracks for heated 100nM 101A solution in absence and presence of (heated before immobilisation) 101B, and the MSD histograms, shown respectively in F and H. G. Cartoon representation of the interactions observed.

assemble, would provide a complete solution to the problem, the efforts focused on finding a work-around and enabling imaging with the chosen system. To this end, heat was chosen as the least intrusive intervention and most compatible treatment for further applications to biological systems. Dilutions from stock solutions into PBS were performed, and the resulting solutions were heated to 60°C for approx. 10 minutes. Solutions prepared in this manner were used in a repeat of the above experiment, with the results presented in Figure 6.4.3E-G. A higher number of blinks was observed, with new localisations and repeat localisations observed across the whole 500 frames (montage of 9 in Figure 6.4.3F). Figures 6.4.3G and 6.4.3H show the tracks in the presence and absence of 101B. It can be noticed that whilst many tracks are still of low MSD values, the distribution is broader than before. The tracks in presence of 101B are characterised by more "clustered" localisations, where it is possible that the same molecule of 101A transiently interacts with several 101B strands localised on the surface. Whilst further quantification was not attempted, it was concluded that the heat treatment was necessary to observe Peptide-PAINT interactions between 101A and 101B (Figure 6.4.3H) and it was a crucial step to avoid homo dimeric coiled-coil formation in the stock solutions.

101A-101B affinity

Having confirmed the secondary structure of the probes, the affinity of the interaction was investigated next. First attempts involved using FCS. However, the relatively small size of both peptides did not introduce enough of a diffusion coefficient shift to measure K_D that way.

Thus, an alternative approach was used. Bio-layer interferometry assay (BLI)[316] was conducted. In this experiment, streptavidin coated biosensor surface was incubated with biotin-101B peptide at a known concentration. This lead to the immobilisation of the peptide on the biosenor surface. The sensor was then "dipped" in solutions of SeNBD-101A of varying concentrations. The interference pattern of white light reflecting off the sensor was compared in the absence and presence of the binding partner, and the different responses were used to estimate the K_D. The *in vitro* measurements conducted suggested a K_D of approximately

10 nM. This was about 10-fold less than expected, as the K_D for the unlabelled peptide pair *in situ* (i.e. expressed in yeast cells) was previously reported at approximately 200 nM.[286] Since the experiment was conducted as a one-off, it would be worth investigating the method further and compare the interaction to the Ac-101A & 101B pair. It is likely that the assay conditions do not reflect the binding kinetics observed by Chen *et al.*, nor those observed in yeast LIVE-PAINT,[298] given the use of PBS buffer as opposed to dense cellular cytoplasm (no crowding effects) and the small fluorophore tag present in place of a large fluorescent protein. The dye introduced could also potentially effect the measured affinities, with the larger dyes potentially leading to less tight binding. Further quantification of the interaction was not pursued at the time.

6.4.2 Transient interaction between 101A and immobilised 101B

The 101A and 101B interactions were studied on the surface next. Having successfully observed a difference in the number of localisations between SeNBD-101A in presence and absence of biotin-101B immobilised on the surface, it was important to ensure the signal was coming from peptide-peptide binding events and was not a result of non-specific interactions with the functionalised surface. Firstly, different surface coatings were tested for the amount of noise they produced. With charged amino acids present throughout the 101A structure, a surface that did not attract the peptide was needed. The protocol used previously (functionalisation with 5% biotin-BSA solution, followed by streptavidin incubation) was compared against 6 other protocols. Argon plasma cleaned slides, PLL-coated slides, and slides dipped in Tween-20 solution were prepared using simple one-step functionalisation protocols. They were compared against two pegylated surfaces (where PEG-silane was incubated with streptavidin, and where this process followed an additional 1% Tween-20 incubation), and a DT20 preparation (biotin-BSA, followed by 0.2% Tween-20, then streptavidin). 100 nM SeNBD-101A was imaged on all surfaces, and an average number of localisations detected via

GDSC-SMLM in 9 $\times$ 20-frame images was plotted for all conditions with the SD between FOVs represented as error bars (Figure 6.4.4A). The Tween-20 produced the highest number of localisations (average of approximately 13,500$\pm$800/20 frames), the surfactant coating attracting SeNBD-101A molecules to deposit on the slide surface. Perhaps the concentration of Tween-20 in the dip should be further investigated, as the wash process has produced "streaks" across the slide surface. With the number of localisation approximately 10-fold higher than in other cases, it could be hypothesised that the signal detected is not only due to the peptide but also fluorescent contaminants. With only a few frames collected, it was impossible to tell whether these could be bleached down to uncover just peptide signal. Alternatively, the surfactant could further promote the monomeric form of 101A, discouraging homo- and hetero-dimer formation and more spurious monomer localisations. Either way, the Tween-20 dip was not effective at minimising background localisations. Plasma cleaned slides produced the second highest number of localisations (approximately 4,300$\pm$1,100/20 frames). Both PEG-based surface blocking protocols and the PLL-coating produced similar level of localisations (approximately 3,400$\pm$1,500/20 frames for PEG + Tween-20, 3,100$\pm$1,500/20 frames for PEG without the Tween-20 wash, and approximately 3,200$\pm$1,100/20 frames for PLL). Both surfaces using biotin-BSA in the blocking step have performed well, with slightly less localisations produced by DT20 (2,200$\pm$1,200 localisations/20 frames) than the in-house BSA protocol (2,600$\pm$000 localisations/20 frames). This was reassuring and suggested that the protocol followed so far for surface blocking and 101B immobilisation would produce the most reliable results.

With that in mind, the streptavidin in the protocol was substituted for AF-647 labelled streptavidin to try to observe colocalisation between the red dye on the surface and the blinks generated by SeNBD. The schematic representation of the experiment is shown in Figure 6.4.4B, where BSA-biotin is bound to AF-647 streptavidin. Biotin-101B can be functionalised to the same streptavidin molecule, and when the peptide imager partner - SeNBD-101A is in proximity, the fluorescent signal of the two co-localises (this can be observed as a yellow

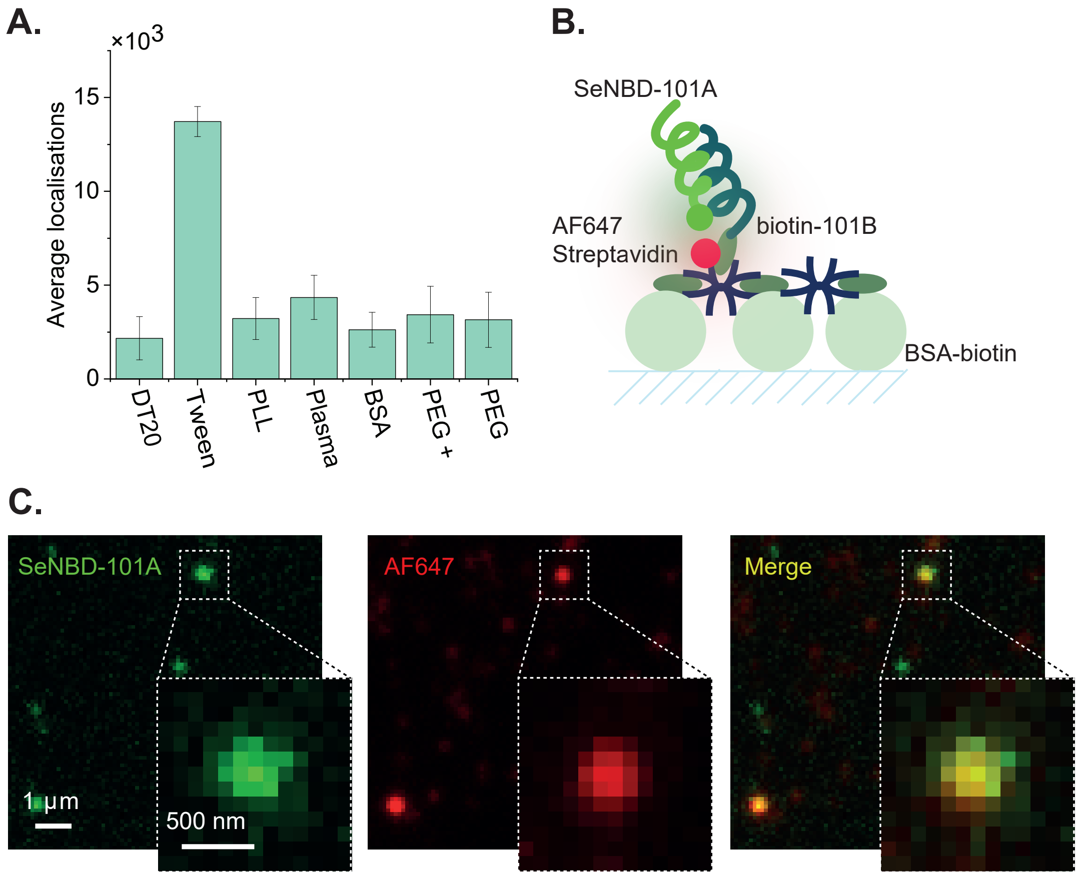

Figure 6.4.4: Showing co-localisation between red-labelled streptavidin and SeNBD-101A to confirm 101A-101B interaction is specific. A. Surface optimisation experiment, testing the number of localisations detected from 20 frames by the GDSCLM Fiji analysis for different surface preparations. PEG + is PEG and Tween-20 wash. Average from 9 FOVs, with the error bars representing SD. B. Cartoon representation of the co-localisation experiment set-up. C. Representative fluorescence microscopy images showing the binding between SeNBD-101A (100 nM, green) and biotin-101B (100 nM) in the presence of AlexaFluor647 (AF647)-streptavidin (17 nM, red). Merge fluorescence signals displayed in yellow.

glow). The concentration of red-labelled streptavidin was tested first, to ensure sufficient yet not dense coverage of the surface. Out of three dilutions (final concentrations 8.5 nM, 13.6 nM and 17 nM), 1:1000 dilution of the original stock (final concentration of 17 nM AF647) gave an optimal number of spots. Such prepared surface was then incubated with SeNBD-101A and imaged, first using 647 nm excitation, then 515 nm, to localise streptavidin and SeNBD-101A molecules respectively (Figure 6.4.4C). Co-localisation could be observed by the presence of yellow spots on the merged images, confirming interaction between 101A-101B.

6.4.3 Imaging cellular targets using 101A and 101B system

To test the feasibility of performing Peptide-PAINT experiment with the 101A-101B coiled-coil system in fixed cells, the Eklund *et al.* protocol was first employed.[294] First attempts at the experiment required functionalisation of a secondary antibody with an azido-group, followed by a Click-reaction with the DBCO-101B peptide. Such prepared constructs were then used in the immunofluorescence staining protocol, in place of a regular secondary antibody incubation. This simple approach had two disadvantages: no control over the density of antibody labelling and, more pressingly, the possibility of homo dimeric coiled-coils forming during the antibody-construct preparation. The DBCO-101B peptide could be heated prior to the Click reaction, however the conjugation was performed at low volume and thus high concentration substrate. Furthermore, the purification involved passing the reaction mixture through a spin-filter column and thus further concentration of the reaction mixture. Once the DBCO-101B was conjugated to the antibody, the sample could not be subjected to heat due to protein denaturation. Staining performed with the obtained antibody-101B construct was inconclusive, with many “off-target” localisation and thus an alternative staining approach was needed.

To that end, biotin-101B was employed as the alternative anchor peptide. Biotin-101B was prepared at the desired concentration, heated and incubated with streptavidin first. The target protein was treated with primary and biotinylated secondary antibodies, before an extra (2h long) incubation with streptavidin-biotin-101B. Next, the imager peptide was applied. The schematic representation of this targeting set-up is shown in Figure 6.4.5A.

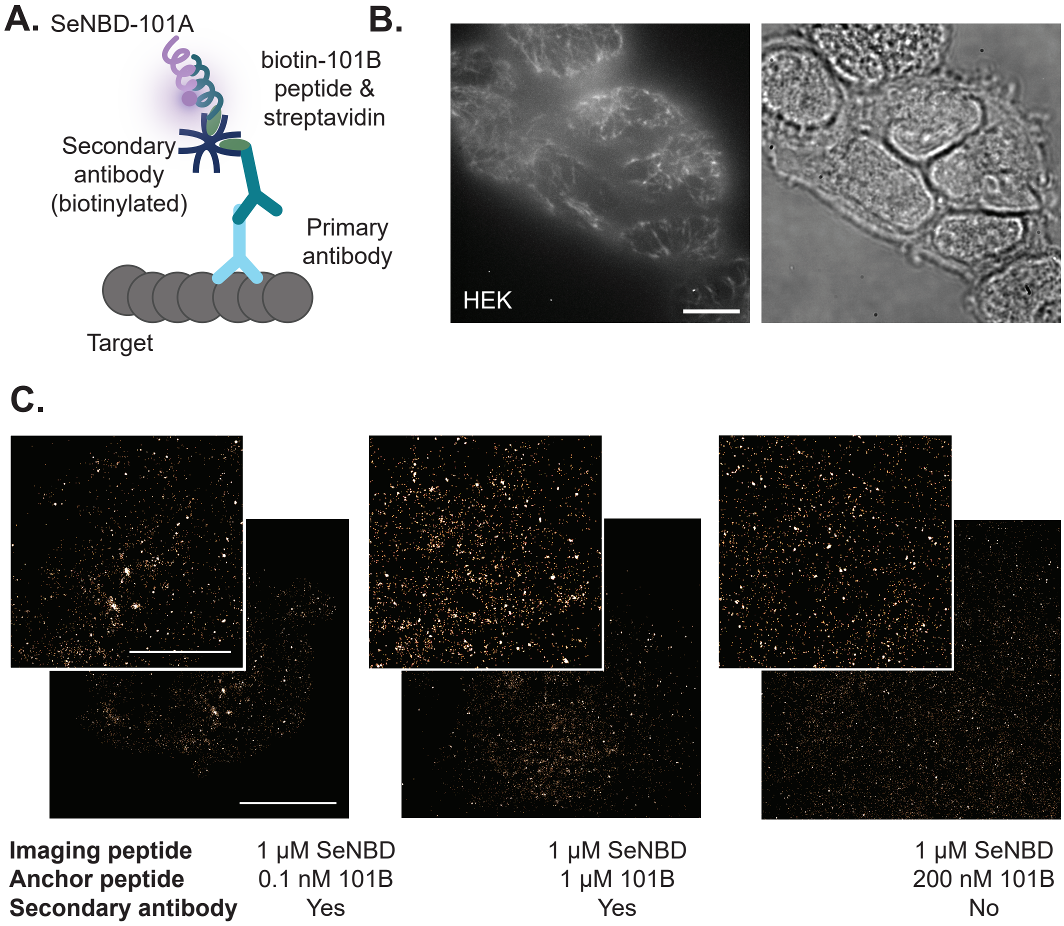

Figure 6.4.5: Peptide PAINT - biotin-101B and SeNBD-101A in HEK cells. A. Cartoon representation of the staining steps undertaken to localise SeNBD-101A to target. B. Primary antibody against TOMM-20 used in this experiment, stained with a red-labelled secondary to confirm TOM-20 networks. WL image of the cell. C. super-resolution images using 1 μM SeNBD-101A and three different 101B concentration (in presence and absence of the secondary biotinylated antibody). Legend underneath the images. Scale bars are 10 μm, except for inserts where they represent 5 μm.

Whilst this extended the staining protocol, the extra step guaranteed the peptide could be heat-treated prior to use, to “unzip” any preformed homo dimeric coiled-coils. In this approach, the concentration of the anchor, 101B, could be controlled independently of the secondary antibody concentration. In theory, this could lead to a better control of the number of blinking events. With the three step staining protocol devised, it was next tested on wild type cells (HEKs) that were fixed, permeabilised and blocked prior to the experiment (details in the Methods section). The primary antibody staining was tested through using a red-labelled secondary antibody in place of the biotinylated secondary (Figure 6.4.5B) and provided the example TOM-20 distribution along mitochondrial networks in HEKs and SHY5 cells (left hand side image). White light (right hand side image) was used to find cellular signal. A relatively high (1 μM) imager concentration was used, to ensure enough peptide to replenish signal and encourage repeat localisations. At lower concentrations, most localisations were observed within the first 50 frames. 10,000 frames were acquired for each cell. The localisations were detected and processed using the GDSC-SMLM plugin. The resulting super-resolution images are shown in Figure 6.4.5C. None of the super-resolution images have displayed the mitochondrial structures observed with secondary antibody. Moreover, the concentration of 101B did not introduce a difference to the observed number, nor the perceived distribution, of localisations: 0.1 nM and 1000 nM 101B-biotin produced similarly disappointing images. When the biotinylated secondary antibody was omitted from the staining procedure, non-specific 101A-101B interactions were observed across the cell and resulted in a visually similar image to when the biotinylated antibody was present.

When the staining was repeated with a different cell line, the results were equally discouraging. Figure 6.4.6 summarises one of the experiments conducted with an SH-S5Y5 cell line. As previously, the primary antibody staining was checked with a red-labelled secondary (Figure 6.4.6) revealing extensive mitochondrial networks.

In this rendition of the experiment, Cy3B-101A peptide was used. Two concentrations of biotin-101B were incubated with streptavidin, prior to targeting the secondary biotinylated antibody. 0.1 nM 101B (Figure 6.4.6B) and 100 nM 101B (Figure 6.4.6C) produced similar images. It could be argued that some of the localisations here are more clustered, however there is a high number of spurious events present still. Additionally, the cells themselves appeared bright and fluorescent under the microscope. Some autofluorescence was expected here, however the high background was likely exacerbated by the appearance of the

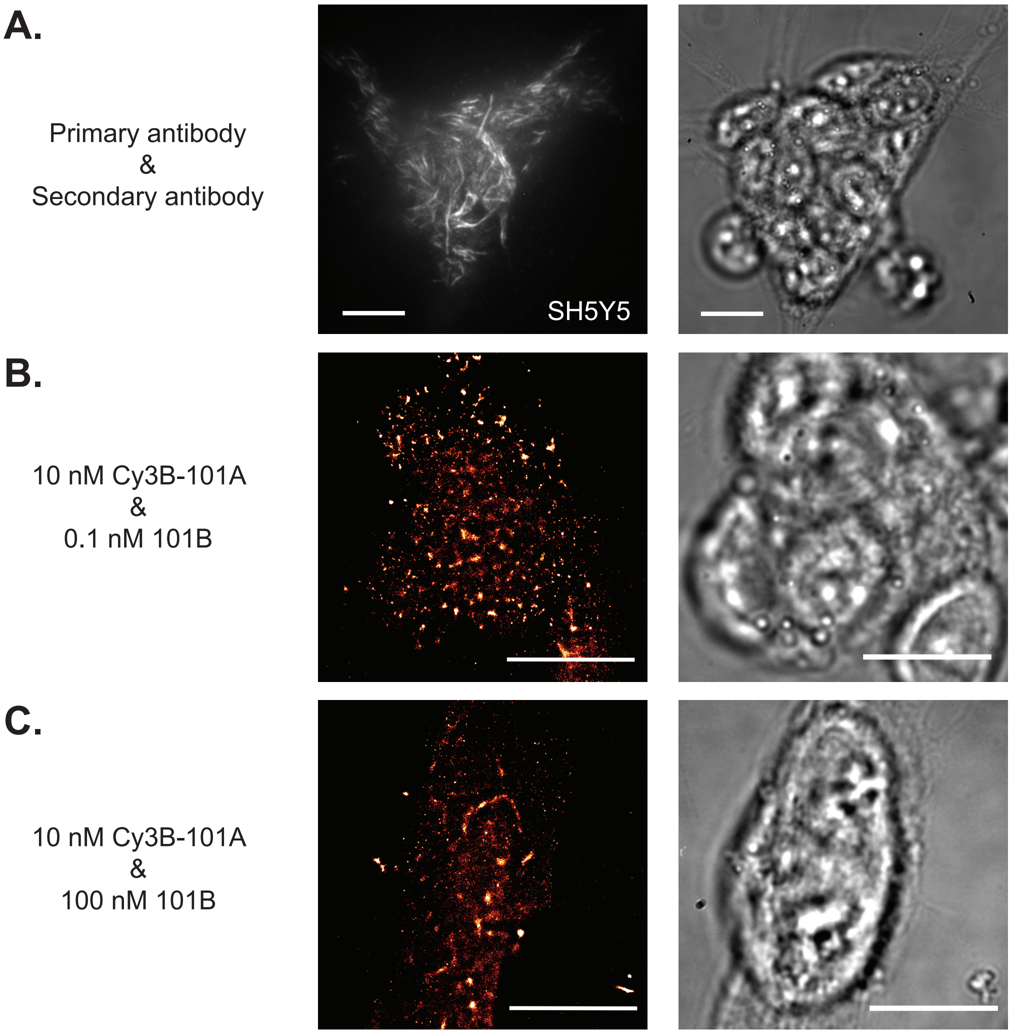

Figure 6.4.6: Peptide PAINT - biotin-101B and SeNBD-101A in SH-SY5Y cells. A. Primary antibody against TOMM-20 used in this experiment, stained with a red-labelled secondary to confirm TOMM-20 networks. WL image of the cell. B&C. super-resolution images using 10 nM Cy3B-101A and two different 101B concentration. Scale bars are 10 μm. WL images presented on right hand side.

imaged cells. After the extensive staining protocol, the fixed cells were prone to lifting off the slide, clumping and "blebbing". The shape and protrusions suggest cell death and increased autofluorescence.

Similar attempts were made to visualise a different target (α-tubulin), with no evident success. The imaging buffer composition was further investigated, with additions of Ficoll and dextran to induce "crowding" and increase the perceived concentration of imaging strand on target whilst working in the nM regime still. Various incubation times for both the preparation of biotin-101B, streptavidin construct and secondary antibody were tested. None of the efforts have produced well-resolved molecular target structures, in super-resolution or diffraction limited imaging. Despite the efforts, the number of off-target localisation remained high. Thus, the biggest issue seemed the anchor peptide delivery.

One of the advantages of working with a peptide system (as opposed to oligonucleotides) was that the amino acid sequences could be genetically encoded and expressed by a cell. Gidden *et al.* made use of that by producing HEK cell lines expressing 101B-TOM-20 and 101B-LAMP-1. The cells could be further induced to express fluorescently tagged 101A under a promoter.[299] It was those cells (under no promoter induced expression, i.e. without 101A) that were used in the next set of experiments. Since the cell model and the expression levels were already validated, the cells were used to test if, with the 101B peptide already at target, the 101A could find and localise it within a fixed cell. The fixation protocol was further shortened (see methods) and the synthetic 101A peptide was delivered to permeabilised cells (Figure 6.4.7A).

The shorter handling protocol meant that the cells appeared "healthier" than before on the white light images, with a representative cell in Figure 6.4.7B. Two types of cells - HEK 101B-TOM-20 and wild type HEK cells (no 101B anchor) were stained with 1 nM Cy3B (Figure 6.4.7C). Standard deviation projections of the first 50 frames were generated and shown. The images were all contrasted the same. In the presence of the 101B-anchor at TOM-20, even with just 50 frames processed, subtle lines of mitochondrial network could be noticed in the cell body (white light image for reference). The projection showed several bright puncta

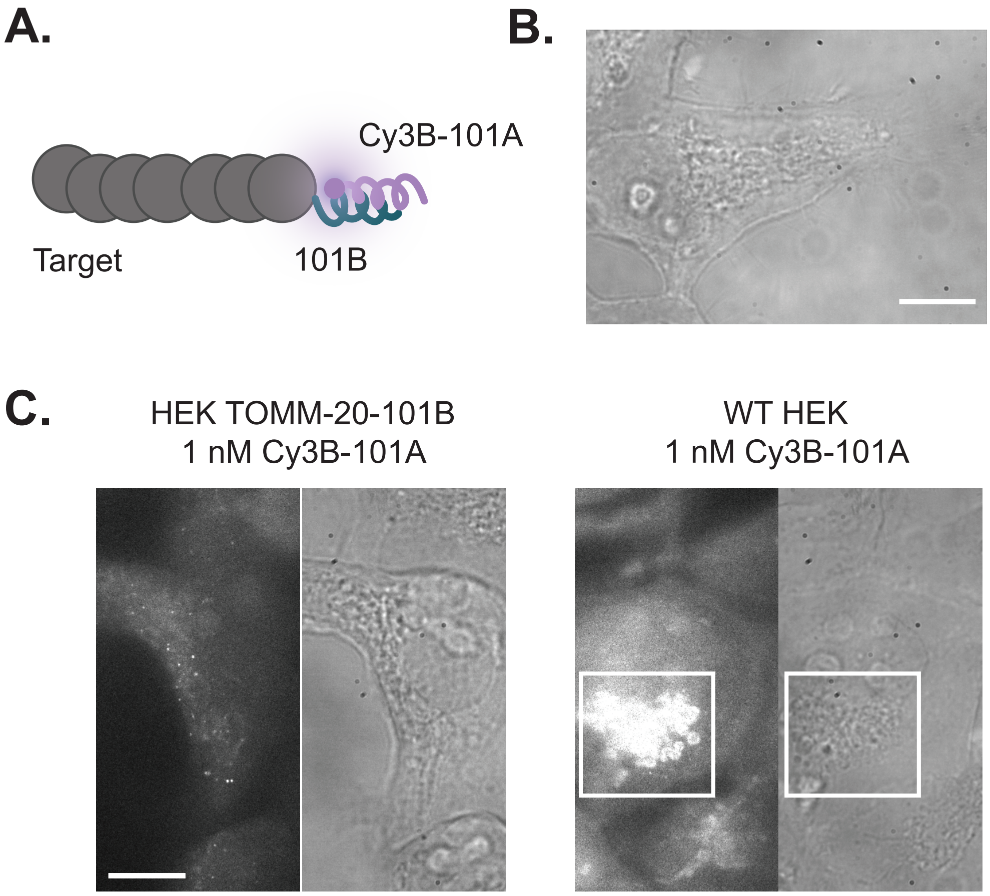

Figure 6.4.7: HEK 101B-TOMM20 cells with 101A imager. A. Cartoon representation of the binding events. B. Representative white light image of cells with the shortened fixation and staining protocol. C. Standard deviation based z-projection from the first 50 frames of HEK 101B-TOMM20 cells in absence (0 nM 101A) and presence (Cy3B-101A and SeNBD-101A) imager peptide. Scale bar is 10 μm.

since distinct blinks were captured on the camera. Whilst the WT HEK cells appeared generally bright, no blinking was observed during data collection. Thus no puncta were present on the projection. The fluorescence signal was generally spread across the cell body, with the brightest region highlighted by a white box. The higher level of general fluorescence in the cell body was not unexpected due to the presence of Cy3B-101A. The brightest region corresponded to a textured protrusion in the WL image of the cell. This was also unsurprising, as the Cy3B dye could partake in non-specific interactions.

Satisfied that the expression of the 101B anchor peptide directly at the targeted protein has resolved the anchor localisation issues, super-resolution imaging with Cy3B-101A was further attempted on the 101B-TOM-20 HEK cell line. The cells were fixed, permeabilised and blocked before staining. Three concentrations of the imager strand: 20, 10, 1 nM were first tested. 10,000 frames were acquired and super-resolution images reconstructed. In all cases, the observed structures corresponded to what would be expected of TOM-20 mitochondrial networks.[317,318] At 20 nM imager, the mitochondria could be identified immediately due to a high amount of signal. However, upon bleaching down some of the peptide fluorescence, distinct blinking has been observed and the super-resolution images revealed a branched mitochondrial network. 10 nM and 1 nM Cy3B-101A also resulted in super-resolution images of the branched structures (6.4.8).

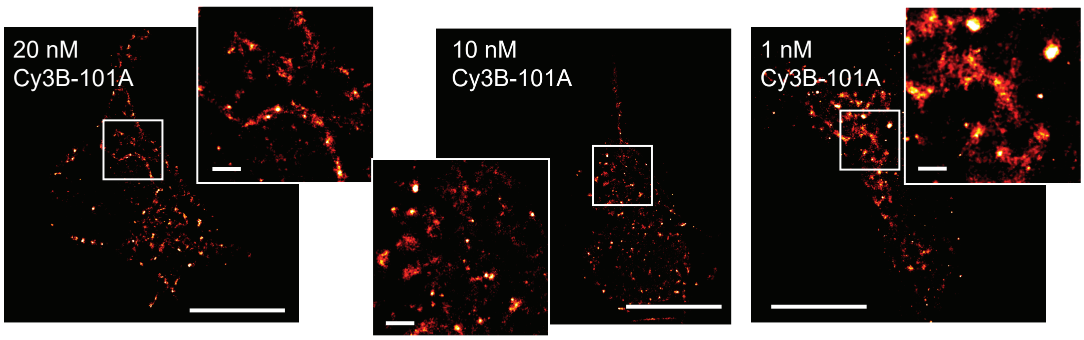

Figure 6.4.8: HEK 101B-TOM-20 cells stained with Cy3B-101A. Three different concentrations of imager strand allow sufficient localisations to super-resolved the branched mitochondrial network. Scale bar is 10 μm on large images, and 1 μm on close-ups.

Higher concentrations of the imager peptide resulted in the need for photobleaching to observe blinking, and even then off-target localisations across the cell body were observed. Lower peptide concentrations did not generate comparable number of localisations (within the 10,000 frames) and led to a more punctate pattern missing localisations along the branches. The optimal concentration for imaging was dye dependent. SeNBD-101A required a higher concentration regime to observe blinking and produce super-resolution images of TOM-20. Concentrations lower than 50 nM did not produce sufficient signal, 50 nM was sufficient to observe mitochondria across the cell (Figure 6.4.9). Higher concentrations were only used to generate diffraction-limited images due to similar issues as observed in case of the Cy3B-analogue. Whilst it was shown that using SeNBD-101A is possible here, further work might be require to make its performance as compelling as that of Cy3B. Despite being able to use a higher concentration of the imager strand, the switch-on properties were not fully exploited here. The aa sequence is long enough to tolerate a larger dye, with a higher quantum yield. Possibly a different position of the dye within the sequence would allow for a stronger switch-on effect, brighter blinks, and more precise localisations.

Finally, to confirm the signal was coming from the organelle of interest, a counter-stain was introduced to check for co-localisation of fluorescent signal. 101B-TOM-20 and 101B-LAMP-1 cell lines were fixed, permeabilised, blocked and stained. Overnight incubation with a primary antibody against the target (TOM-20 and LAMP-1 respectively) was followed by a 2h incubation with a secondary antibody against the primary labelled with AF-647. 5nM Cy3B-101A was applied after washes, prior to imaging the cells. A representative ROI, showcasing part of a 101B-TOMM-20 cell, is shown in Figure 6.4.10.

A maximum intensity projection across a 50-frame z-stack was generated from the antibody signal (left hand side). Peptide signal was collected for 10,000 frames to enable super-resolution imaging. The stack was first z-projected to generate a standard deviation based projection image. The co-localisation was compared by creating a composite image (middle) where the antibody signal was

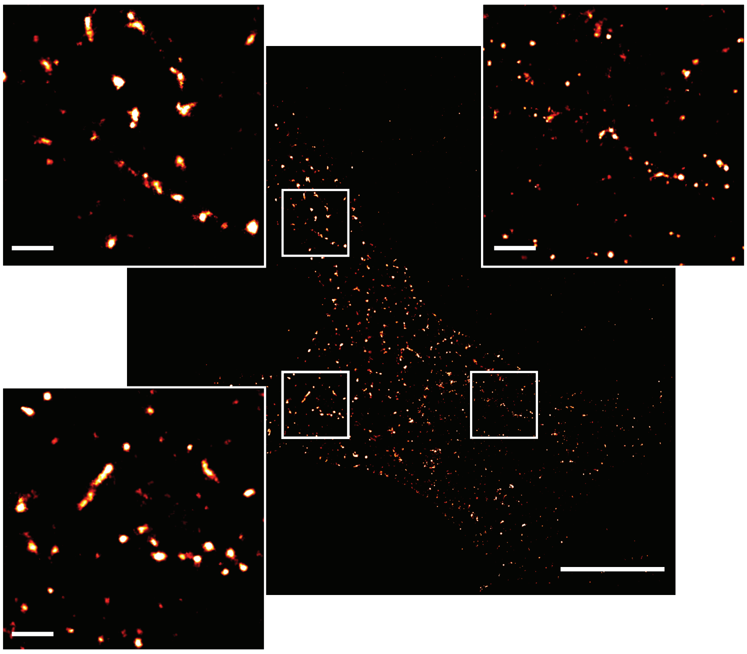

Figure 6.4.9: HEK 101B-TOM-20 cells imaged using 50 nM of SeNBD-101A imager. Three regions of interest are indicated by white boxes and zoom-ins for these presented. Scale bar is 10 μm on large images, and 1 μm on close-ups.

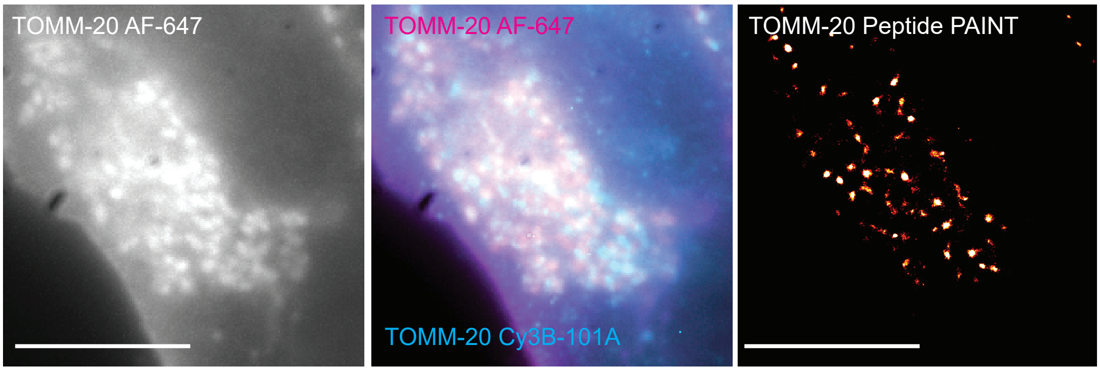

Figure 6.4.10: HEK 101B-TOMM20 cells imaged using 5 nM of Cy3B-101A imager, costained using a TOMM-20 primary antibody and a red-labelled secondary. The three images shown are: maximal intensity projection from the antibody signal; composite between the antibody signal and peptide (standard deviation based z-projection) in magenta and cyan, respectively; super-resolution image from the peptide signal. Scale bar is 10 μm.

presented in magenta, and the peptide singal in cyan. White regions indicated good co-localisation between the signals. The peptide signal was further analysed to generate a super-resolution image of the mitochondrial network.

The same experiment was performed on a HEK cell line stably expressing 101B-LAMP1. Figure 6.4.11A shows the super-resolution image of the lysosomal network - the lysosomes are distributed across the cell and slightly circular in nature. The observed structure is similar to those observed by researchers previously.[319,320] The standard deviation based projection from the peptide signal (cyan) and antibody maximal intensity projection (magenta) were superimposed to create a composite in Figure 6.4.11B. Here, slightly less white can be observed, however there is some noticable colocalisation. This could be partly explained by the fact that the two channels are not perfectly aligned, with magenta dominating the right hand side of the image and cyan - the left. Equally, the cell could have lifted and the two focal planes used in the images could have highlighted different parts of the cell. The close ups of singular lysosomes of the characteristic circular structure were chosen and compared to the diffraction-based image in Figure 6.4.11C. These highlight the level of detail that can be obtained during super-resolution imaging that is lost when working at the diffraction-limit of light. Whilst some further optimisation for this application would be desired, the results satisfactorily concluded the possibility of imaging multiple cellular targets with a high level of detail.

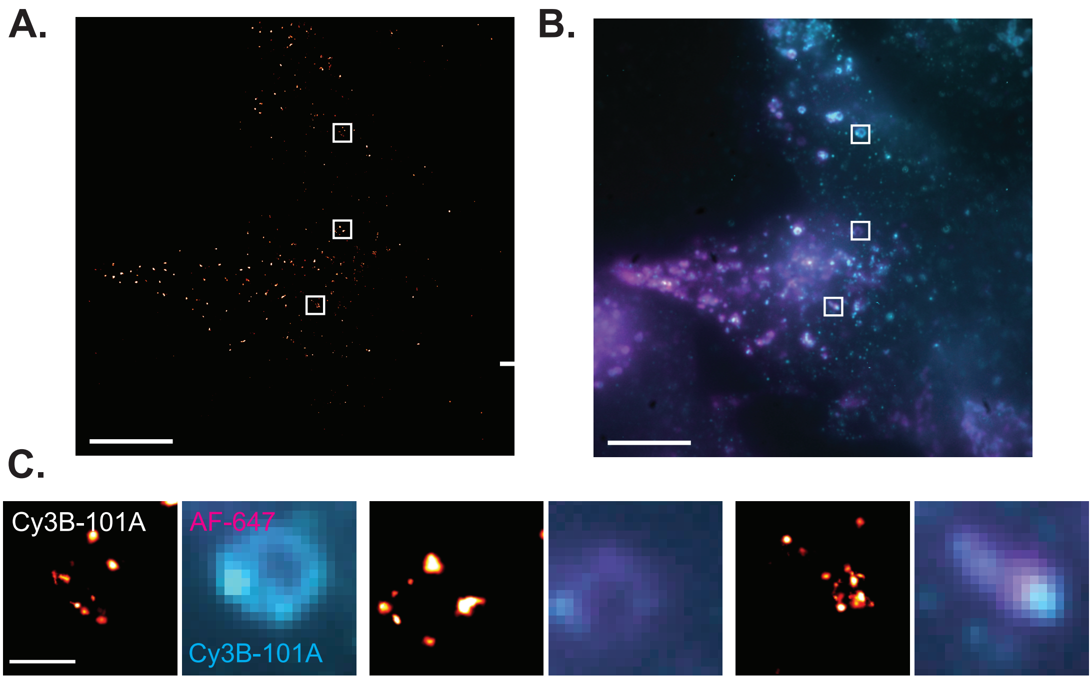

Figure 6.4.11: HEK 101B-LAMP1 cells imaged using 5 nM of Cy3B-101A imager, costained using a LAMP1 primary antibody and a red-labelled secondary. A. super-resolution image of the lysosomal network. B. A composite image showing co-localisation between the antibody signal and peptide (standard deviation based z-projection) in magenta and cyan, respectively. Scale bar is 10 μm.. C. Close-up of three selected regions of interest (white squares on panels A and B), showcasing the circular structure of lysosomes. Scale bar is 1 μm.

6.5 Discussion

Whilst FCS allowed for quick determination of the K_D for the PDZ interactions studied, it proved more tricky for the 101A and 101B peptides. Another approach to quantification of the 101A and 101B pair binding affinity could utilised the 101B-biotin peptide and red-labelled streptavidin. The AF647-labelled streptavidin could be employed to observe co-localisation between red (AF647) and green (SeNBD) fluorescence and determine the number of bound species diffusing through the confocal volume. However, more work would be required to optimise the method first and find the right combination of incubation times, order, and concentration of protein. Despite the more difficult optimisation process, the method is still very reliable and would translate easily across other peptide-protein systems.

The 101A-101B system was used to create a proxy in the absence of a peptide binding directly to a protein of interest. The main challenges in implementing this approach were: overcoming the homo dimerisation of the peptides when stored at high μM concentrations, and the localisation of the anchor peptide at the target protein. The dimerisation process limited the options for conjugation of peptide to antibodies, where low concentrations or heat treatment were required for successful imaging. The protocol for conjugating 101B-DBCO to an azido-labelled antibody concentrated the peptide stocks and the antibody-peptide complex could not be subjected to heat. Biotin-streptavidin labelling strategy introduce a bit more flexibility, and the peptide solutions could be heated prior to use. However, it is likely that despite a few rounds of optimisation of the protocol, the right concentration regime and incubation conditions were not found. A multifactorial analysis experiment taking all factors into consideration could be performed to find optimal conditions (this would be time and reagent-intensive). Fortunately, a big advantage of working with peptides was that they could be genetically encoded and expressed by cells *in vivo*. With the anchor localised at target through co-expression, and subsequent imager peptide delivery, preliminary super-resolution images for two-cellular targets were obtained. With some further optimisation, the 101A-101B pair could show promise across other targets, highlighting the advantages of a genetic modification with a small tag and using synthetic dyes for better resolution.

6.6 Conclusions

The above body of work showcases the development and application of peptides for super-resolution microscopy.

A coiled-coil Peptide-PAINT method was presented as an alternative for imaging targets without known peptide binders. The transient interactions between 101A (imager) and 101B (anchor) peptide were harnessed. When prepared synthetically (as opposed to expressed *in cellulo*), the peptides showed a propensity to form homo dimeric coils as suggested by CD and peptide mobility data. Heating of the solutions was enough to disrupt the homo dimers and enabled the observation of the interaction between the imager and anchor *in vitro*. Despite the difficulty in chemically conjugating the anchor peptide to target of interest, it was possible to genetically modify the target to express the peptide at the desired location (here: TOM-20 and LAMP-1). The cellular structures were resolved with a good level of detail, and the peptide signal co-localised to that from conventional antibody staining. The system developed here is a good model for studying the effect of disease states on cellular structures and shows good potential to be translated to other organelles or proteins of interest.

6.7 Future perspectives

The 101A and 101B system was developed as a universal Peptide-PAINT pair and could enable super-resolution imaging of various organelles and proteins of interest. The anchor peptide is small in comparison to most proteins and as such unlikely to cause issues with protein folding, function, or localisation when genetically encoded and expressed *in vivo*. Delivering the 101A imager externally, as opposed to co-expressing the 101A with a fluorescent protein,[299] allows for a larger arsenal of dyes to be used. At low imager peptide concentrations, where the blinking dynamics are conserved, bright dyes with high quantum yields can be used to ensure high signal to noise and high localisation precision. At high concentrations, different dyes including environment-sensing ones, could also be used for complementary imaging such as FLIM, or FS-FLIM. Considering the impact the positioning of a fluorescent amino acid such as SeNBD can have on the brightness of the fluorophore, 101A analogues where SeNBD substitutes a position within the peptide chain rather than decorates the N-terminal, could also be designed and tested. The imager peptide could be further modified, introducing "staples" and restricting the degrees of freedom of the peptide, to test whether it could be transported across the membrane and potentially allow for delivery to live cells further down the line.

6.8 Contributions

The fluorescent dyes (SeNBD and SNBD) used in this chapter were synthesised by Dr Fabio de Moliner. The peptide probes were synthesised and purified by the author.

The CD measurements were performed at the University of Glasgow, thanks to Dr Andrew Jamieson's hospitality, and with the expert guidance of Dr Danielle Morgan.

Dr Rebecca Saleeb was the Peptide-PAINT pioneer: she modified and conjugated the antibody and performed the first Peptide-PAINT experiments using the DBCO-101B peptide. Further experimental work was designed and conducted by the author. Dr Zoë Gidden generated stable cell lines expressing 101B-TOMM-20 and 101B-LAMP-1, and cultured and plated live cells for fixation and imaging. Noelia Pelegrina-Hidalgo supplied live SH-SY5Y cells and Haresh Bhaskar supplied live WT HEKs. Later on, Agustina Salis Torres and Haresh Bhaksar took over the 101B-HEK cell line day-to-day maintenance and plating prior to experiments. Fixation, staining and imaging of the cells was performed by the author. All imaging experiments were designed and performed by the author, as was the

image processing and data analysis.

The TIRF microscope used in this chapter is a home-built instruments. It was built by Dr Craig Leighton, Dr Alexandre Chappard, Dr Owen Kantelberg, Dr Katie Morris and Dr Zoë Gidden with guidance from Prof. Mathew Horrocks.

Chapter 7

Concluding remarks and future directions

7.1 Overview

In this thesis, a novel instrument, FS-FLIM, was applied to tissue imaging. This approach aimed at increasing the amount of information that could be extracted from a fluorescent image and provide means at distinguishing α-syn aggregates *in situ*. The chosen tissue sample preparation and fluorescent probe made it difficult to distinguish α-syn above the autofluorescence background. It was suggested the FS-FLIM could be used to distinguish the autofluorescence from the fluorescence of a probe, however further work is necessary to make the approach feasible and provide a robust analysis pipeline.

In addition, the thesis explored fluorescent peptides and specifically fluorogenic internally-labelled peptides as a new imaging modality. This new approach relied on incorporation of SeNBD amino acid into short peptide scaffolds. The small size of the dye enabled fluorescent labeling of short peptides (up to 7 aa) without the introduction of linker chains. This design ensured the dye was placed directly at the target-of-interest during imaging, allowing for localisation and image reconstruction of nano-structures with high precision. The work aimed to illustrate the versatile applications of peptide probes across several fluorescence-based techniques including super-resolution microscopy.

7.2 Summary of conclusions

The FS-FLIM instrument was successfully constructed and its performance characterised. The advantages of accessing fluorescence intensity, wavelength and lifetime data were showcased in several applications of the instrument described by collaborators and in this body of work. The application of the instrument ranged from cancerous cell line detection,[165] through long-lifetime bacterial dye imaging of *E.Coli*,[321] to brain tissue imaging. The instrument was used in a pilot experiment and enabled visualisation of brain tissue derived from PD patients, including pathological α-syn inclusions.

The NBD-derived dye family was successfully characterised and the switch-on and lifetime-sensing properties of the Fmoc-SeNBD-OH amino acid were presented herein. The stability of the dye to SSPS methods and its small size was exploited to its full potential through labelling sequences of several lengths (40 aa, 22 aa, and even 6 aa). Internally-labelled sequences, where the dye replaced a native amino acid in the sequence, were also prepared and showed retention of binding to target. This approach did not require additional purification steps, maximising yield when working at a μM scale. Peptides for both super-resolution and FLIM applications were developed.

In the context of neurodegeneration, the PSMα sequence was derivatised and used in a series of experiments to visualise α-syn *in vitro* and *in situ*. Whilst further work is needed, this indicated the sequence seems to tolerate fluorescent labels and could be used to follow aggregation dynamics and pathological inclusions across their lifespan.

Looking beyond α-syn, the applications of peptides in super-resolution imaging were investigated. Short peptides sequences, known to transiently bind to PDZ, were fluorescently labelled and used to super-resolve PSD-95 nanoclusters in a synaptosome preparation. The small peptide size enabled the localisation of the fluorophore at the target-of-interest, minimising the linkage error when compared to other, standard, approaches. Furthermore, the feasibility of a more universal approach, employing peptide-peptide rather than peptide-protein interactions, was considered. Despite the initial issues with localising the anchor counterpart (101B) to target, incorporation of the 101B sequence into the cell genome enabled successful localisation of the 101B peptide at the protein of interest in HEK cells. Subsequent fixation, permeabilisation and staining with fluorescent-101A peptide enabled super-resolution of TOM-20 and LAMP-1 in cells.

Overall, it is hoped the methods developed in this thesis could be further translated to characterise protein aggregates characteristic of PD and allow for sensitive visualisation of any biomarker.

7.3 Future directions

Whilst the thesis covered method development, further applications and experimentation could showcase the potential of the tools presented.

7.3.1 FS-FLIM: imaging tissue in neurodegeneration

Whilst an application of FS-FLIM in tissue imaging was presented here, there is a lot more that can achieved using FS-FLIM.

As hinted in Chapter 4, autofluorescence signal from tissue introduces a significant level of difficulty in imaging patient-derived samples. The autofluorescence signal can be reduced with the use of quenchers during tissue staining steps. The compatibility of quencher with the imaging modality used needs to be confirmed, and usually only bright dyes (with high quantum yields) can be used as some loss of fluorescence is expected. The removal of autofluorescence in post-processing is made difficult by the broad emission of lipofuscin pigment. Whilst in some applications, the signal can be easily distinguished from features of interest, the appearance of pathological protein aggreagates is remarkably similar to lipofuscin inclusions. Thus, a two-pronged approach where both the emission spectrum and the decays from each pixel are considered, could provide a new method of classification of signal. Automated approaches that could classify even small differences would be most appropriate for this type of analysis. Methods such as principal component analysis or artificial intelligence for image analysis, that could further elucidate differences that might be difficult to spot otherwise, should be considered for this purpose.

Moreover, FS-FLIM could enable spectral multiplexing as well as lifetime multiplexing. The "filterless" emission enables detection of fluorophores across 250 nm, where at least three dyes could be imaged simultaneously. The acquired intensity data could be then split to generate "channels" or colour-code features depending on the emission wavelength. Co-localisation between signal could be therefore easily investigated. This type of experiment could provide further insight into which species are detected by PSMα peptide *in situ*. Two different antibodies for α-syn could be tested against the peptide in one experiment, and both the co-localisation (intensity) confirmed as well as the lifetime compared.

Finally, FS-FLIM could introduce an additional level of contrast that could distinguish features that appear identical in intensity-only imaging methods. ThT, the gold standard amyloid dye, has been shown to exhibit slight lifetime changes depending on the amyloid protein used in bulk experiments. Lindberg *et. al.* previously reported a change in the observed average ThT lifetime between protein constructs of different length: Aβ(1-40) and Aβ(1-42).[322] Examining the lifetime and emission spectrum of ThT, alongside other non-specific amyloid dyes, could reveal subtle differences between the different pathological amyloid proteins and potentially even between the same protein isoforms associated with different diseases.

7.3.2 Fluorescence imaging applications of PSMα

The test IHC staining conducted with the PSMα sequence is a promising step towards peptide validation. Since IHC is the standard method used by pathologists to view and describe tissue, it would enable a direct comparison of the peptide performance with the gold-standard probes used in the field. IHC could be attempted in high-throughput and allow for meaningful statistical comparison in structures visualised between PD patients and age-matched controls. Further efforts to quench autofluorescence and modify the existing protocol for tissue staining would be needed, before fluorescence imaging of tissue and any attempts at super-resolution imaging *in situ* are made.

An exciting next step for the PSMα, not attempted here, would involve using the peptide with a cellular model of PD. Cells such as SH-SY5Ys can be genetically modified to express α-syn under a promoter (such as doxycycline). Thus, the concentration of protein in the cell can be controlled during cell growth. Additionally, mutations in the α-syn gene could be further introduced to mimic familial cases of the disease. Alternatively, an induced pluripotent stem cell (iPSC) model of PD, where patient derived cells are be differentiated into neuronal cells, could be used for imaging. The aggregation kinetics of α-syn could be monitored though employing one of the PSMα sequences. The model could be validated using both the TIRFM and the FS-FLIM set-up and the dependence of fluorescent signal on α-syn concentration observed. TIRFM could potentially be used with low concentrations of the red-labelled PSMα to try to super-resolve the early aggregation species. This could prove difficult, depending on the exact K_D of the labelled peptide. The point at which the inclusions become visible to a diffraction-limited system (such as the FS-FLIM) could be established, and further lifetime analysis of mature aggregates would be possible. Equally, the response of the model cells to seeding or introduction of therapeutic agents could be monitored. A potential difficulty with this approach is the permeability of the peptide sequence. PSMα is unlikely to be able to cross cellular membranes, so prior permeabilisation of cells might be necessary. Alternatively, "stapling" of the sequence could be considered. In this approach, chemical modifications are introduced between amino acids in the sequence to stabilise the secondary structure of the peptide,[323] Introduction of staples would constrain the degrees of freedom of the peptide, and the α-helical shape could facilitate interactions with the cellular membrane.[324,325] Given a choice of a membrane permeable fluorophore, this could further enable live cell imaging.

7.3.3 Expanding the 101A dye toolbox: super-resolution and beyond

The proxy-peptide-PAINT method, using the 101A and 101B interaction pair, could be used as an alternative approach to PSMα detection of α-syn. Where the PSMα peptide could have a therapeutic effect and reverse or modify the aggregate species, the 101B-α-syn construct could provide means to monitor the *status quo* and super-resolve aggregation species in the aggregation reaction. It would be interesting to compare the two methods, both in terms of resolution and performance, but also the biological information that could be accessed using the two.

Further work could focus on increasing the potential resolution achievable using peptide-PAINT. The next exciting step would be developing a PALM-Peptide-PAINT approach. Conjugation of a photoactivable fluorophore to the 101A peptide could further reduce signal-to-background ratio, through activating a subset of 101As at any given point in the experiment. Alternatively, it could be possible to work at higher (μM) concentrations, where 101A-101B binding sites are suturated, whilst still obtaining super-resolution images (using PALM). This could be advantageous for any low-concentration target where the 101A concentration might be significantly higher than the 101B concentration present in the cell.

The cell models described herein could enable super-resolution imaging of structures in pathology and cellular stress models, but could also potentially be used for FLIM and FS-FLIM applications. The N-terminus of 101A can be conjugated with any reporter dye molecule, including SeNBD. Whilst N-terminal incorporation of SeNBD leads to relatively low signal from the dye, its incorporation within the peptide scaffold could ensure there is an increase in fluorescence upon 101A-101B interaction. To see how the fluorogenic properties of SeNBD can be better harnessed, a range of rational substitutions of amino acids in the 101A sequence with SeNBD could be attempted. The compatibility of SeNBD with SSPS methods would ensure relative ease of preparation and purification of numerous analogues in a 101A library. The secondary structure of the different versions of 101A should first be checked using CD. α-helical peptides could then be further screened for the largest fluorescence increase upon binding to 101B. The library could be tested in an *in vitro* experiment comparing the brightness of signal between 101A analogues and surface-immobilised 101B. Additionally, the substitution of the native amino acid with SeNBD could further change the binding affinity and dynamics of the 101A-101B interactions. An *in vitro* screen could further allow to observe these under the microscope and choose a 101A-analogue with the best properties for imaging. A SeNBD-labelled 101A chosen in this way could find applications in super-resolution microscopy and potentially enable FS-FLIM studies at higher peptide concentration.

Bibliography

(1) M. Prince, A. Wimo, M. Guerchet, M. G.-C. Ali, Y.-T. Wu, M. Prina, K. Y. Chan and Z. Xia, *World Alzheimer Report 2015. The Global Impact of Dementia. An An Analysis of Prevalence, Incidence, Cost and Trends.* Alzheimer's Disease International, 2015.

(2) A. Burns and J. O'Brien, *J. Psychopharmacol.*, 2006, **20**, 732–755.

(3) V. M. Dembitsky, L. Dzhemileva, T. Gloriozova and V. D'yakonov, *Biochem.*, 2020, **524**, 772–783.

(4) G. R. Horowitz, *"Clin.*, 1988, **4**, 163–180.

(5) R. A. Murden, *The Diagnosis of Alzheimer's Disease*, ed. R. J. Z. Taher and Ham, Springer US, 1990, pp. 59–64.

(6) K. A. Jellinger, *J. Cell. Mol. Med.*, 2001, **5**, 1–17.

(7) M. G. Tansey and M. S. Goldberg, *Neurobiol. Dis.*, 2010, **37**, 510–518.

(8) K. Franze, P. A. Janmey and J. Guck, *Annu. Rev. Biomed. Eng.*, 2013, **15**, 227–251.

(9) P. Damier, E. C. Hirsch, Y. Agid and A. M. Graybiel, *Brain*, 1999, **122**, 1437–1448.

(10) E. Hill, R. Gowers, M. J. E. Richardson and M. J. Wall, *Eneuro*, 2021, **8**, ENEURO.0330–20.2020.

(11) G. B. Irvine, O. M. El-Agnaf, G. M. Shankar and D. M. Walsh, *Mol. Med.*, 2008, **14**, 451–464.

(12) C. A. Ross and M. A. Poirier, *Nat. Med.*, 2004, **10**, S10.

(13) W. R. Gibb and A. J. Lees, *J. Neurol. Neurosurg. Psychiatry*, 1988, **51**, 745–752.

(14) M. G. Spillantini, M. L. Schmidt, V. M.-Y. Lee, J. Q. Trojanowski, R. Jakes and M. Goedert, *Nat.*, 1997, **388**, 839–840.

(15) L. Maroteaux, J. T. Campanelli and R. H. Scheller, *J. Neurosci*, 1988, **8**, 2804–2815.

(16) F. N. Emamzadeh, *J. Res. Med. Sci.*, 2016, **21**, DOI: `10.4103/1735-1995.181989`.

(17) O. Marques and T. F. Outeiro, *Cell Death Dis*, 2012, **3**, e350–e350.

(18) H. Braak, D. Sandmann-Keil, W. Gai and E. Braak, *Neurosci*, 1998, 67–69.

(19) M. Y. Ryu, D. W. Kim, K. Arima, M. M. Mouradian, S. U. Kim and G. Lee, *J. Neurol. Sci.*, 2008, 9–12.

(20) M. G. Spillantini, R. A. Crowther, R. Jakes, M. Hasegawa and M. Goedert, *PNAS*, 1998, **95**, 6469–6437.

(21) T. Kanazawa, E. Adachi, S. Orimo, A. Nakamura, H. Mizusawa and T. Uchihara, *Brain Pathol.*, 2012, **22**, 67–78.

(22) K. Wakabayashi, K. Tanji, F. Mori and H. Takahashi, *Neuropathol.*, 2007, **27**, 494–506.

(23) S. Chartier and C. Duyckaerts, *Cell Tissue Res.*, 2018, **373**, 1–12.

(24) S. H. Shahmoradian, A. J. Lewis, C. Genoud, J. Hench, T. E. Moors, P. P. Navarro, D. Castaño-Díez, G. Schweighauser, A. Graff-Meyer, K. N. Goldie, R. Sütterlin, E. Huisman, A. Ingrassia, Y. de Gier, A. J. Rozemuller, J. Wang, A. D. Paepe, J. Erny, A. Staempfli, J. Hoernschemeyer, F. Großerüschkamp, D. Niedieker, S. F. El-Mashtoly, M. Quadri, W. F. V. IJcken, V. Bonifati, K. Gerwert, B. Bohrmann, S. Frank, M. Britschgi, H. Stahlberg, W. D. V. de Berg and M. E. Lauer, *Nat. Neurosci.*, 2019, **22**, 1099–1109.

(25) S. Greffard, M. Verny, A.-M. Bonnet, D. Seilhean, J.-J. Hauw and C. Duyckaerts, *Neurobiol. Aging*, 2010, **31**, 99–103.

(26) H. Payami, K. Larsen, S. Bernard and J. Nutt, *Ann. Neurol.*, 1994, **36**, 659–661.

(27) M. H. Polymeropoulos, C. Lavedan, E. Leroy, S. E. Ide, A. Dehejia, A. Dutra, B. Pike, H. Root, J. Rubenstein, R. Boyer, E. S. Stenroos, S. Chandrasekharappa, A. Athanassiadou, T. Papapetropoulos, W. G. Johnson, A. M. Lazzarini, R. C. Duvoisin, G. D. Iorio, L. I. Golbe and R. L. Nussbaum, *Science*, 1997, **276**, 2045–2047.

(28) C. B. Anfinsen, *Science*, 1973, **181**, 223–230.

(29) P. E. Leopold, M. Montal and J. N. Onuchic, *Proc. Natl. Acad. Sci.*, 1992, **89**, 8721–8725.

(30) S. E. Radford and C. M. Dobson, *Cell*, 1999, **97**, 291–298.

(31) R. C. Rivers, J. R. Kumita, G. G. Tartaglia, M. M. Dedmon, A. Pawar, M. Vendruscolo, C. M. Dobson and J. Christodoulou, *Prot. Sci.*, 2008, **17**, 887–898.

(32) R. Trivedi and H. A. Nagarajaram, *Int. J. Mol. Sci.*, 2022, **23**, 14050.

(33) N. Bisi, L. Feni, K. Peqini, H. Pérez-Peña, S. Ongeri, S. Pieraccini and S. Pellegrino, *Front. Chem.*, 2021, **9**, DOI: 10.3389/fchem.2021.666585.

(34) J. Brown and M. H. Horrocks, *Semin. Cell Dev. Biol.*, 2020, **99**, 65–77.

(35) P. J. Thomas, B.-H. Qu and P. L. Pedersen, *Trends Biochem. Sci.*, 1995, **20**, 456–459.

(36) J. Klucken, A. M. Poehler, D. Ebrahimi-Fakhari, J. Schneider, S. Nuber, E. Rockenstein, U. Schlötzer-Schrehardt, B. T. Hyman, P. J. McLean, E. Masliah and J. Winkler, *Autophagy*, 2012, **8**, 754–766.

(37) S. Nath, L. Agholme, F. R. Kurudenkandy, B. Granseth, J. Marcusson and M. Hallbeck, *J. Neurosci.*, 2012, **32**, 8767–8777.

(38) T. J. Betthauser, *Prog. Mol. Biol. Transl. Sci.*, 2019, **165**, 107–138.

(39) R. Watson, A. M. Blamire and J. T. O'brien, *Dement Geriatr Cogn Disord*, 2009, **28**, 493–506.

(40) S. De, D. C. Wirthensohn, S. F. Lee, C. Ø. Vincke, S. Muyldermans, T. P. uomas J Knowles, S. Gandhi, C. M. Dobson and D. Klenerman, *Angew. Chem. Int. Ed.*, 2017, **56**, 7750–7754.

(41) N. Cremades, S. I. Cohen, E. Deas, A. Y. Abramov, A. Y. Chen, A. Orte, M. Sandal, R. W. Clarke, P. Dunne, F. A. Aprile, C. W. Bertoncini, N. W. Wood, T. P. Knowles, C. M. Dobson and D. Klenerman, *Cell*, 2012, **149**, 1048–1059.

(42) J. Parkinson, *J. Neuropsych. Clinic. Neurosci.*, 2002, **14**, 223–236.

(43) A. J. M. Wollman, R. Nudd, E. G. Hedlund and M. C. Leake, *Open Biol.*, 2015, **5**, 150019.

(44) C. A. Noble, A. P. Biesemier, S. F. McClees, A. M. Alhussain, S. E. Helms and R. T. Brodell, *Semin. Diagn. Pathol.*, 2024, DOI: `10.1053/j.semdp.2024.01.002`.

(45) A. L. Berge, *Perspect. Sci.*, 1999, **7**, 111–142.

(46) O. Liczbik, S. Goertz, J. Wiśniewski, P. Kurlandt, W. Libionka, S. Adamski and W. Kloc, *Pol. J. Pathol.*, 2019, **70**, 14–20.

(47) J. G. van den Tweel and C. R. Taylor, *Virchows Archiv.*, 2010, **457**, 3–10.

(48) D. Ribatti, *Exp. Cell Res.*, 2018, **364**, 1–4.

(49) J. D. Sipe and A. S. Cohen, *J. Struct. Biol.*, 2000, **130**, 88–98.

(50) A. J. Lees, M. Selikhova, L. A. Andrade and C. Duyckaerts, *Mov. Disord.*, 2008, **23**, 777–783.

(51) C. Trétiakoff, *Theses de Paris*, 1919.

(52) L. Fritz, *Dtsch. Z. Nervenheilk*, 1913, **50**, 50–55.

(53) J. K. Chan, *Int. J. Surg. Pathol.*, 2014, **22**, 12–32.

(54) M. Goedert, M. G. Spillantini, K. D. Tredici and H. Braak, *Nat. Revs. Neurol.*, 2013, **9**, 13–24.

(55) T. Uchihara, A. E. Ayako, N. Ae, Y. Mochizuki, M. Hayashi, A. E. Satoshi, O. Ae, E. Isozaki and T. Mizutani, *Acta Neuropathol.*, 2005, **110**, 255–260.

(56) K. Koenig and I. Riemann, *J. Biomed. Opt.*, 2003, **8**, 432.

(57) D. Sandmann-Keil, H. Braak, M. Okochi, C. Haass and E. Braak, *Acta Neuropathol.*, 1999, **98**, 461–464.

(58) N. S. Ryan, M. N. Rossor and N. C. Fox, *Brain*, 2015, **138**, 3816–3821.

(59) T. Uchihara, *Acta Neuropathol.*, 2007, **113**, 483–499.

(60) C. O. Hidalgo, in ed. L. D. Valle, Springer US, 2022, vol. 2422, pp. 17–31.

(61) J. R. Marrack, *Int. Arch. Allergy Immunol.*, 1954, **5**, 192–197.

(62) J. E. García-Sánchez, E. García and M. L. Merino, *Enferm. Infecc. Microbiol. Clín.*, 2010, **28**, 521–533.

(63) M. Nurjayadi, D. Apriyani, U. Hasan, I. Santoso, F. Kurniadewi, I. R. Kartika, K. Agustini, F. Puspasari, D. Natalia and W. Mangunwardoyo, *Procedia Chem.*, 2016, **18**, 237–245.

(64) H. Braak, K. D. Tredici, U. Rüb, R. A. de Vos, E. N. J. Steur and E. Braak, *Neurobiol. Aging*, 2003, **24**, 197–211.

(65) B. H. Falkenburger, T. Saridaki and E. Dinter, *J. Neurochem.*, 2016, **139**, 121–130.

(66) M. F. Beal, *Nat. Revs. Neurosci.*, 2001, **2**, 325–332.

(67) J. Lama, Y. Buhidma, E. J. Fletcher and S. Duty, *Neuronal Signal.*, 2021, **5**, DOI: `10.1042/NS20210026`.

(68) M. Kasha, *Discuss. Faraday Soc.*, 1950, **9**, 14–19.

(69) Q. Zheng, S. Jockusch, Z. Zhou and S. C. Blanchard, *Photochem. Photobiol.*, 2014, **90**, 448–454.

(70) Y. Wang, Y. Lin, S. He, S. Wu and C. Yang, *J. Hazard. Mats.*, 2024, **461**, 132538.

(71) T. J. Lambert, *Nat. Methods*, 2019, **16**, 277–278.

(72) G. B. Cserép, A. Herner and P. Kele, *Methods Appl. Fluoresc.*, 2015, **3**, 042001.

(73) K. M. Dean and A. E. Palmer, *Nat. Chem. Biol.*, 2014, **10**, 512–523.

(74) O. Shimomura, F. H. Johnson and Y. Saiga, *J. Cell. Comp. Physiol.*, 1962, **59**, 223–239.

(75) M. V. Matz, A. F. Fradkov, Y. A. Labas, A. P. Savitsky, A. G. Zaraisky, M. L. Markelov and S. A. Lukyanov, *Nat. Biotech.*, 1999, **17**, 969–973.

(76) D. Shcherbo, C. S. Murphy, G. V. Ermakova, E. A. Solovieva, T. V. Chepurnykh, A. S. Shcheglov, V. V. Verkhusha, V. Z. Pletnev, K. L. Hazelwood, P. M. Roche et al., *Biochem. J.*, 2009, **418**, 567–574.

(77) N. C. Shaner, M. Z. Lin, M. R. McKeown, P. A. Steinbach, K. L. Hazelwood, M. W. Davidson and R. Y. Tsien, *Nat. Methods*, 2008, **5**, 545–551.

(78) N. C. Shaner, R. E. Campbell, P. A. Steinbach, B. N. Giepmans, A. E. Palmer and R. Y. Tsien, *Nat. Biotech.*, 2004, **22**, 1567–1572.

(79) G.-J. Kremers, S. G. Gilbert, P. J. Cranfill, M. W. Davidson and D. W. Piston, *J. Cell Sci.*, 2011, **124**, 157–160.

(80) G. H. Patterson, S. M. Knobel, W. D. Sharif, S. R. Kain and D. W. Piston, *Biophys. J.*, 1997, **73**, 2782–2790.

(81) N. Pandey, R. E. Schmidt and J. E. Galvin, *Exp. Neurol.*, 2006, **197**, 515–520.

(82) J. R. v. Wagner, *A Handbook of Chemical Technology*, J. & A. Churchill, 1872.

(83) A. Baeyer, *Ber. Dtsch. Chem. Ges.*, 1871, **4**, 555–558.

(84) M. S. T. Gonçalves, *Chem. Rev.*, 2009, **109**, 190–212.

(85) A. Loudet and K. Burgess, *Chem. Rev.*, 2007, **107**, 4891–4932.

(86) J. Frangioni, *Cur. Opin. Chem. Biol.*, 2003, **7**, 626–634.

(87) P. Somerharju, *Chem. Phys. Lipids*, 2002, **116**, 57–74.

(88) T. Terai and T. Nagano, *Curr. Opin. Chem. Biol.*, 2008, **12**, 515–521.

(89) J. B. Grimm, B. P. English, H. Choi, A. K. Muthusamy, B. P. Mehl, P. Dong, T. A. Brown, J. Lippincott-Schwartz, Z. Liu, T. Lionnet and L. D. Lavis, *Nat. Methods*, 2016, **13**, 985–988.

(90) M. Cooper, A. Ebner, M. Briggs, M. Burrows, N. Gardner, R. Richardson and R. West, *J. Fluoresc.*, 2004, **14**, 145–150.

(91) S. Abou-Hatab, V. A. Spata and S. Matsika, *J. Phys. Chem. A*, 2017, **121**, 1213–1222.

(92) E. Birtalan, B. Rudat, D. K. Kölmel, D. Fritz, S. B. L. Vollrath, U. Schepers and S. Bräse, *Pep. Sci.*, 2011, **96**, 694–701.

(93) P. Greenspan, E. P. Mayer and S. D. Fowler, *J. Cell Biol.*, 1985, **100**, 965–973.

(94) S. K. Mallela, D. M. Patel, G. M. Ducasa, S. Merscher, A. Fornoni and H. Al-Ali, *Methods Mol. Biol.*, 2019, **1996**, 199–206.

(95) G. V. Los, L. P. Encell, M. G. McDougall, D. D. Hartzell, N. Karassina, C. Zimprich, M. G. Wood, R. Learish, R. F. Ohana, M. Urh, D. Simpson, J. Mendez, K. Zimmerman, P. Otto, G. Vidugiris, J. Zhu, A. Darzins, D. H. Klaubert, R. F. Bulleit and K. V. Wood, *ACS Chem. Bio.*, 2008, **3**, 373–382.

(96) A. Juillerat, T. Gronemeyer, A. Keppler, S. Gendreizig, H. Pick, H. Vogel and K. Johnsson, *Chem. Biol.*, 2003, **10**, 313–317.

(97) V. I. Stsiapura, A. A. Maskevich, V. A. Kuzmitsky, V. N. Uversky, I. M. Kuznetsova and K. K. Turoverov, *J. Phys. Chem. B*, 2008, **112**, 15893–15902.

(98) M. Biancalana and S. Koide, *Biochim. Biophys. Acta (BBA) - Prots. Proteoms.*, 2010, **1804**, 1405–1412.

(99) R. Nelson, M. R. Sawaya, M. Balbirnie, A. Madsen, C. Riekel, R. Grothe and D. Eisenberg, *Nature*, 2005, **435**, 773–778.

(100) N. P. Rodina, M. I. Sulatsky, A. I. Sulatskaya, I. M. Kuznetsova, V. N. Uversky and K. K. Turoverov, *J. Spectrosc.*, 2017, **2017**, DOI: 10.1155/2017/2365746.

(101) S. Freire, M. H. D. Araujo, W. Al-Soufi and M. Novo, *Dyes Pigments*, 2014, **110**, 97–105.

(102) M. H. Horrocks, S. F. Lee, S. Gandhi, N. K. Magdalinou, S. W. Chen, M. J. Devine, L. Tosatto, M. Kjaergaard, J. S. Beckwith, H. Zetterberg, M. Iljina, N. Cremades, C. M. Dobson, N. W. Wood and D. Klenerman, *ACS Chem. Neurosci.*, 2016, **7**, 399–406.

(103) S. Campagna, F. Puntoriero, F. Nastasi, G. Bergamini and V. Balzani, *Photochemistry and Photophysics of Coordination Compounds I;* ed. V. Balzani and S. Campagna, Springer-Verlag, 2007, vol. 280.

(104) B. B. Hueholt, W. Xu, M. Sabat, B. A. DeGraff and J. N. Demas, *J. Fluoresc.*, 2007, **17**, 522–527.

(105) L. Flamigni, A. Barbieri, C. Sabatini, B. Ventura and F. Barigelletti, *Photochemistry and Photophysics of Coordination Compounds II*, Springer-Verlag, 2007, vol. 281.

(106) N. P. Cook, K. Kilpatrick, L. Segatori and A. A. Martí, *JACS*, 2012, **134**, 20776–20782.

(107) I. ASHIKAWA, Y. NISHIMURA, M. TSUBOI, K. WATANABE and K. ISO, *J. Biochem.*, 1982, **91**, 2047–2055.

(108) K. König, *J. Biophotonics*, 2008, **1**, 13–23.

(109) B. Seefeldt, R. Kasper, T. Seidel, P. Tinnefeld, K.-J. Dietz, M. Heilemann and M. Sauer, *J. Biophotonics*, 2008, **1**, 74–82.

(110) Y. Povrozin and E. Terpetschnig, *luorescence Lifetime Measurements of BODIPY and Alexa Dyes on ChronosFD and K2*, ISS Inc., 2009.

(111) V. Buschmann, K. D. Weston and M. Sauer, *Bioconjug. Chem.*, 2003, **14**, 195–204.

(112) E. Sciuto, M. Santangelo, G. Villaggio, F. Sinatra, C. Bongiorno, G. Nicotra and S. Libertino, *Sens. Bio-Sens. Res.*, 2015, **6**, 67–71.

(113) J. W. Dobrucki and U. Kubitscheck, in *Fluorescence Microscopy*, John Wiley & Sons, Ltd, 2017, ch. 3, pp. 85–132.

(114) T. A. Klar, E. Engel and S. W. Hell, *Phys. Rev. E*, 2001, **64**, 066613.

(115) S. W. Hell and J. Wichmann, *Opt. lett.*, 1994, **19**, 780–782.

(116) M. G. L. Gustafsson, *J. Microsc.*, 2000, **198**, 82–87.

(117) F. Chen, P. W. Tillberg and E. S. Boyden, *Science*, 2015, **347**, 543–548.

(118) B. Huang, M. Bates and X. Zhuang, *Ann. Rev. Biochem.*, 2009, **78**, 993–1016.

(119) J. Valli, A. Garcia-Burgos, L. M. Rooney, B. V. de Melo e Oliveira, R. R. Duncan and C. Rickman, *J. Biol. Chem.*, 2021, **297**, 100791.

(120) M. Lelek, M. T. Gyparaki, G. Beliu, F. Schueder, J. Griffié, S. Manley, R. Jungmann, M. Sauer, M. Lakadamyali and C. Zimmer, *Nat. Revs. Methods Primers*, 2021, **1**, 39.

(121) M. N. Bongiovanni, J. Godet, M. H. Horrocks, L. Tosatto, A. R. Carr, D. C. Wirthensohn, R. T. Ranasinghe, J.-E. Lee, A. Ponjavic, J. V. Fritz, C. M. Dobson, D. Klenerman and S. F. Lee, *Nat. Commun.*, 2016, **7**, 13544.

(122) J.-E. Lee, J. C. Sang, M. Rodrigues, A. R. Carr, M. H. Horrocks, S. De, M. N. Bongiovanni, P. Flagmeier, C. M. Dobson, D. J. Wales, S. F. Lee and D. Klenerman, *Nano Letters*, 2018, **18**, 7494–7501.

(123) W. Becker, *J. Microsc.*, 2012, **247**, 119–136.

(124) W. Jahr, B. Schmid, C. Schmied, F. O. Fahrbach and J. Huisken, *Nat. Commun.*, 2015, **6**, 1–7.

(125) C. Stringari, A. Cinquin, O. Cinquin, M. A. Digman, P. J. Donovan and E. Gratton, *Proc. Natl. Aca. Sci.*, 2011, **108**, 13582–13587.

(126) Q. Yu and A. A. Heikal, *J. Photochem. Photobiol. B: Biol.*, 2009, **95**, 46–57.

(127) N. Plotegher, C. Stringari, S. Jahid, M. Veronesi, S. Girotto, E. Gratton and L. Bubacco, *The FASEB Journal*, 2015, **29**, 2484–2494.

(128) A. Esteves, D. Arduino, D. Silva, C. Oliveira and S. Cardoso, *Parkinson's dis.*, 2011, **2011**, 693761.

(129) D. Freeman, R. Cedillos, S. Choyke, Z. Lukic, K. McGuire, S. Marvin, A. M. Burrage, S. Sudholt, A. Rana, C. O'Connor et al., *PloS one*, 2013, **8**, e62143.

(130) M. POKUSA and A. K. TRANČÍKOVÁ, *Physiol. Res.*, 2018, S673–S683.

(131) R. F. Laine, T. Sinnige, K. Y. Ma, A. J. Haack, C. Poudel, P. Gaida, N. Curry, M. Perni, E. A. Nollen, C. M. Dobson, M. Vendruscolo, G. S. K. Schierle and C. F. Kaminski, *ACS Chem. Biol.*, 2019, **14**, 1628–1636.

(132) J. Klucken, T. F. Outeiro, P. Nguyen, P. J. McLean and B. T. Hyman, *The FASEB Journal*, 2006, **20**, 2050–2057.

(133) T. Klingstedt, B. Ghetti, J. L. Holton, H. Ling, K. P. R. Nilsson and M. Goedert, *Acta Neuropathol. Commun.*, 2019, **7**, 193.

(134) J. M. Mason, *Future Med. Chem.*, 2010, **2**, 1813–1822.

(135) D. J. Craik, D. P. Fairlie, S. Liras and D. Price, *Chem. Biol. Drug Des.*, 2013, **81**, 136–147.

(136) M. Muttenthaler, G. F. King, D. J. Adams and P. F. Alewood, *Nat. Rev. Drug Discovery*, 2021, **20**, 309–325.

(137) Z. Feng and B. Xu, *Biomol. Concepts*, 2016, **7**, 179–187.

(138) M. Moiola, M. G. Memeo and P. Quadrelli, *Molecules*, 2019, **24**, 3654.

(139) M. L. Merz, S. Habeshian, B. Li, J.-A. G. L. David, A. L. Nielsen, X. Ji, K. I. Khwildy, M. M. D. Benitez, P. Phothirath and C. Heinis, *Nat. Chem. Biol.*, 2024, **20**, 624–633.

(140) S. G. Allen, R. M. Meade, L. L. W. Stenner and J. M. Mason, *Mol. Neurodegeneration*, 2023, **18**, 80.

(141) B. Popova, D. Wang, A. Rajavel, K. Dhamotharan, D. F. Lázaro, J. Gerke, J. F. Uhrig, M. Hoppert, T. F. Outeiro and G. H. Braus, *Front. Mol. Neurosci.*, 2021, **14**, DOI: `10.3389/fnmol.2021.659926`.

(142) M. Chemerovski-Glikman, E. Rozentur-Shkop, M. Richman, A. Grupi, A. Getler, H. Y. Cohen, H. Shaked, C. Wallin, S. K. T. S. Wärmländer, E. Haas, A. Gräslund, J. H. Chill and S. Rahimipour, *Chem. Eur. J.*, 2016, **22**, 14236–14246.

(143) Y. H. Tan, M. Liu, B. Nolting, J. G. Go, J. Gervay-Hague and G.-y. Liu, *ACS Nano*, 2008, **2**, 2374–2384.

(144) F. de Moliner, Z. Konieczna, L. Mendive-Tapia, R. S. Saleeb, K. Morris, J. A. Gonzalez-Vera, T. Kaizuka, S. G. N. Grant, M. H. Horrocks and M. Vendrell, *Angew. Chem. Int. Ed.*, 2023, **62**, DOI: `10.1002/anie.202216231`.

(145) A. Chappard, C. Leighton, R. S. Saleeb, K. Jeacock, S. R. Ball, K. Morris, O. Kantelberg, J.-E. Lee, E. Zacco, A. Pastore, M. Sunde, D. J. Clarke, P. Downey, T. Kunath and M. H. Horrocks, *Angew. Chem. Int. Ed.*, 2023, **62**, DOI: `10.1002/anie.202216771`.

(146) G. O. S. Williams, E. Williams, N. Finlayson, A. T. Erdogan, Q. Wang, S. Fernandes, A. R. Akram, K. Dhaliwal, R. K. Henderson, J. M. Girkin and M. Bradley, *Nat. Commun.*, 2021, **12**, 6616.

(147) M. Y. Berezin and S. Achilefu, *Chem. Rev.*, 2010, **110**, 2641–2684.

(148) E. Becquerel, *Ann. Chimie Phys.*, 1895, **3**.

(149) P. Radvanyi and J. Villain, *Comptes Rendus. Physique*, 2017, **18**, 544–550.

(150) T. O'Haver and J. Windefordner, *Anal. Chem.*, 1966, **38**.

(151) E. Gaviola, *Ann. Phys.*, 1926, **386**, 681–710.

(152) R. Datta, T. M. Heaster, J. T. Sharick, A. A. Gillette and M. C. Skala, *J. Biomed. Opt.*, 2020, **25**, 1.

(153) M. M. Lukina, L. E. Shimolina, N. M. Kiselev, V. E. Zagainov, D. V. Komarov, E. V. Zagaynova and M. V. Shirmanova, *Methods Appl. Fluoresc.*, 2019, **8**, 014002.

(154) D. Maji, J. Lu, P. Sarder, A. H. Schmieder, G. Cui, X. Yang, D. Pan, S. Achilefu and G. M. Lanza, *Prnano*, 2018, **1**, 128–145.

(155) M. Popleteeva, K. Haas, D. Stoppa, L. Pancheri, L. Gasparini, C. F. Kaminski, L. D. Cassidy, A. R. Venkitaraman and A. Esposito, *Opt. Express*, 2015, **23**, 23511.

(156) X. Liu, D. Lin, W. Becker, J. Niu, B. Yu, L. Liu and J. Qu, *J. Innov. Opt. Health Sci.*, 2019, **12**, 12.

(157) A. T. Erdogan, R. Walker, N. Finlayson, N. Krstajic, G. Williams, J. Girkin and R. Henderson, *IEEE J. Solid-State Circuits*, 2019, **54**, 1705–1719.

(158) N. Bertone, R. Biasi and B. Dion, ed. M. J. Cohen and E. L. Dereniak, 2005, p. 153.

(159) M. Straume, S. G. Frasier-Cadoret and M. L. Johnson, in Kluwer Academic Publishers, 2002, pp. 177–240.

(160) M. Maus, M. Cotlet, J. Hofkens, T. Gensch, F. C. D. Schryver, J. Schaffer and C. A. M. Seidel, *Anal. Chem.*, 2001, **73**, 2078–2086.

(161) X.-F. Zhang, J. Zhang and L. Liu, *J. Fluoresc.*, 2014, **24**, 819–826.

(162) F. M. Zehentbauer, C. Moretto, R. Stephen, T. Thevar, J. R. Gilchrist, D. Pokrajac, K. L. Richard and J. Kiefer, *Spectrochim. Acta A: Mol. Biomol. Spectrosc.*, 2014, **121**, 147–151.

(163) I.-Y. S. Lee and H. Suzuki, *J. Phys. Chem. B.*, 2008, **112**, 4561–4570.

(164) K. A. Selanger, J. Falnes and T. Sikkeland, *J. Phys. Chem.*, 1997, **81**.

(165) J. G. Hughes, Ph.D. Thesis, University of Durham, 2024.

(166) A. Bryce, MA thesis, University of Edinburgh, School of Chemistry, 2021, pp. 31–39.

(167) D. Dong, J. Xie and J. Wang, *Neurosci. Bulletin*, 2019, **35**, 1085–1096.

(168) D. Aksoy, V. Solmaz, T. Çavuşoğlu, A. Meral, U. Ateş and O. Erbaş, *Am. J. Med. Sci.*, 2017, **354**, 319–324.

(169) G. A. Badawi, M. A. A. E. Fattah, H. F. Zaki and M. I. E. Sayed, *Inflammopharmacol.*, 2017, **25**, 369–382.

(170) I. Aviles-Olmos, J. Dickson, Z. Kefalopoulou, A. Djamshidian, P. Ell, T. Soderlund, P. Whitton, R. Wyse, T. Isaacs, A. Lees, P. Limousin and T. Foltynie, *J. Clin. Investig.*, 2013, **123**, 2730–2736.

(171) I. Aviles-Olmos, J. Dickson, Z. Kefalopoulou, A. Djamshidian, J. Kahan, P. Ell, P. Whitton, R. Wyse, T. Isaacs, A. Lees, P. Limousin and T. Foltynie, *J. Parkinson's Dis.*, 2014, **4**, 337–344.

(172) D. Athauda and T. Foltynie, *Drug Disc. Today*, 2016, **21**, 802–818.

(173) M. Watson, H. Nobuta, C. Abad, S. Lee, N. Bala, C. Zhu, F. Richter, M.-F. Chesselet and J. Waschek, *Neuroscience*, 2013, **240**, 277–286.

(174) H. Jiang, L.-J. Li, J. Wang and J.-X. Xie, *Experimental Neurology*, 2008, **212**, 532–537.

(175) M. M. Unger, J. C. Möller, K. Mankel, K. M. Eggert, K. Bohne, M. Bodden, K. Stiasny-Kolster, P. H. Kann, G. Mayer, J. J. Tebbe and W. H. Oertel, *Journal of Neurology*, 2011, **258**, 982–990.

(176) T. S. Ulmer, A. Bax, N. B. Cole and R. L. Nussbaum, *J. Biol. Chem.*, 2005, **280**, 9595–9603.

(177) J. A. Rodriguez, M. I. Ivanova, M. R. Sawaya, D. Cascio, F. E. Reyes, D. Shi, S. Sangwan, E. L. Guenther, L. M. Johnson, M. Zhang, L. Jiang, M. A. Arbing, B. L. Nannenga, J. Hattne, J. Whitelegge, A. S. Brewster, M. Messerschmidt, S. Boutet, N. K. Sauter, T. Gonen and D. S. Eisenberg, *Nature*, 2015, **525**, 486–490.

(178) H. Fujiwara, M. Hasegawa, N. Dohmae, A. Kawashima, E. Masliah, M. S. Goldberg, J. Shen, K. Takio and T. Iwatsubo, *Nat. Cell Bio.*, 2002, **4**, 160–164.

(179) R. M. Meade, S. G. Allen, C. Williams, T. S. Tang, M. P. Crump and J. M. Mason, *Cell Rep. Phys. Sci.*, 2023, **4**, 101563.

(180) C. E. Bavinton, R. Sternke-Hoffmann, T. Yamashita, P. C. Knipe, A. D. Hamilton, J. Luo and S. Thompson, *Chem. Commun.*, 2022, **58**, 5132–5135.

(181) J. R. Horsley, B. Jovcevski, T. L. Pukala and A. D. Abell, *Biochim. Biophys. Acta (BBA) - Prots. Proteoms.*, 2022, **1870**, 140826.

(182) H. Cheruvara, V. L. Allen-Baume, N. M. Kad and J. M. Mason, *J. Biol. Chem.*, 2015, **290**, 7426–7435.

(183) H.-J. Koo, M. Y. Choi and H. Im, *Biochem. Biophys. Res. Commun.*, 2009, **386**, 165–169.

(184) S. Sangwan, S. Sahay, K. A. Murray, S. Morgan, E. L. Guenther, L. Jiang, C. K. Williams, H. V. Vinters, M. Goedert and D. S. Eisenberg, *eLife*, 2020, **9**, DOI: `10.7554/eLife.46775`.

(185) S. Nim, D. M. O'Hara, C. Corbi-Verge, A. Perez-Riba, K. Fujisawa, M. Kapadia, H. Chau, F. Albanese, G. Pawar, M. L. D. Snoo, S. G. Ngana, J. Kim, O. M. A. El-Agnaf, E. Rennella, L. E. Kay, S. K. Kalia, L. V. Kalia and P. M. Kim, *Nat. Commun.*, 2023, **14**, 2150.

(186) J. W. Jin, X. Fan, E. del Cid-Pellitero, X.-X. Liu, L. Zhou, C. Dai, E. Gibbs, W. He, H. Li, X. Wu, A. Hill, B. R. Leavitt, N. Cashman, L. Liu, J. Lu, T. M. Durcan, Z. Dong, E. A. Fon and Y. T. Wang, *Communications Biology*, 2021, **4**, 232.

(187) M. Pirhaghi, S. A. Frank, P. Alam, J. Nielsen, V. Sereikaite, A. Gupta, K. Strømgaard, M. Andreasen, D. Sharma, A. A. Saboury and D. E. Otzen, *J. Biol. Chem.*, 2022, **298**, 102688.

(188) J. Santos, P. Gracia, S. Navarro, S. Peña-Díaz, J. Pujols, N. Cremades, I. Pallarès and S. Ventura, *Nat. Commun.*, 2021, **12**, 3752.

(189) R. M. Meade, K. J. Morris, K. J. Watt, R. J. Williams and J. M. Mason, *J. Mol. Biol.*, 2020, **432**, 166706.

(190) J. H. Torpey, R. M. Meade, R. Mistry, J. M. Mason and J. Madine, *Front. Neurosci.*, 2020, **14**, DOI: 10.3389/fnins.2020.561462.

(191) H.-S. Joo, G. Y. Cheung and M. Otto, *J. Biol. Chem.*, 2011, **286**, 8933–8940.

(192) J. Santos, I. Pallarès and S. Ventura, *Trends Biochem. Sci.*, 2022, **47**, 641–644.

(193) J. Santos, I. Pallarès and S. Ventura, *BioFactors*, 2024, **50**, 439–449.

(194) C. Pintado-Grima, O. Bárcenas, V. Iglesias, J. Santos, Z. Manglano-Artuñedo, I. Pallarès, M. Burdukiewicz and S. Ventura, *Database*, 2023, **2023**, DOI: 10.1093/database/baad084.

(195) J. Santos, J. Cuellar, I. Pallarès, E. J. Byrd, A. Lends, F. Moro, M. B. Abdul-Shukkoor, J. Pujols, L. Velasco-Carneros, F. Sobott, D. E. Otzen, A. N. Calabrese, A. Muga, J. S. Pedersen, A. Loquet, J. M. Valpuesta, S. E. Radford and S. Ventura, *JACS*, 2024, **146**, 12702–12711.

(196) N. Dadina, J. Tyson, S. Zheng, L. Lesiak and A. Schepartz, *Curr. Op. Chem. Biol.*, 2021, **65**, 154–162.

(197) J. Tyson, K. Hu, S. Zheng, P. Kidd, N. Dadina, L. Chu, D. Toomre, J. Bewersdorf and A. Schepartz, *ACS Central Sci.*, 2021, **7**, 1419–1426.

(198) P. Delcanale, D. Porciani, S. Pujals, A. Jurkevich, A. Chetrusca, K. D. Tawiah, D. H. Burke and L. Albertazzi, *Angew. Chem. Int. Ed.*, 2020, **59**, 18546–18555.

(199) E. Fuentes, K. Boháčová, A. M. Fuentes-Caparrós, R. Schweins, E. R. Draper, D. J. Adams, S. Pujals and L. Albertazzi, *Chem. Eur. J.*, 2020, **26**, 9869–9873.

(200) P. Eiring, R. McLaughlin, S. S. Matikonda, Z. Han, L. Grabenhorst, D. A. Helmerich, M. Meub, G. Beliu, M. Luciano, V. Bandi, N. Zijlstra, Z.-D. Shi, S. G. Tarasov, R. Swenson, P. Tinnefeld, V. Glembockyte, T. Cordes, M. Sauer and M. J. Schnermann, *Angew. Chem. Int. Ed.*, 2021, **60**, 26685–26693.

(201) K. Uno, N. Sugimoto and Y. Sato, *Nat. Commun.*, 2021, **12**, 2650.

(202) S. S. Matikonda, R. Götz, R. McLaughlin, M. Sauer and M. J. Schnermann, in ed. D. M. Chenoweth, Academic Press, 2020, vol. 641, pp. 225–244.

(203) D.-P. Klötzner, K. Klehs, M. Heilemann and A. Heckel, *Chem. Commun.*, 2017, **53**, 9874–9877.

(204) N. R. Conley, J. S. Biteen and W. E. Moerner, *J. Phys. Chem. B*, 2008, **112**, 11878–11880.

(205) J. B. Grimm, B. P. English, H. Choi, A. K. Muthusamy, B. P. Mehl, P. Dong, T. A. Brown, J. Lippincott-Schwartz, Z. Liu, T. Lionnet and L. D. Lavis, *Nat. Methods*, 2016, **13**, 985–988.

(206) J. B. Grimm, T. Klein, B. G. Kopek, G. Shtengel, H. F. Hess, M. Sauer and L. D. Lavis, *Angew. Chem. Int. Ed.*, 2016, **55**, 1723–1727.

(207) G. Lukinavičius, K. Umezawa, N. Olivier, A. Honigmann, G. Yang, T. Plass, V. Mueller, L. Reymond, I. R. C. Jr, Z.-G. Luo, C. Schultz, E. A. Lemke, P. Heppenstall, C. Eggeling, S. Manley and K. Johnsson, *Nat. Chem.*, 2013, **5**, 132–139.

(208) D. Hara, S.-n. Uno, T. Motoki, Y. Kazuta, Y. Norimine, M. Suganuma, S. Fujiyama, Y. Shimaoka, K. Yamashita, M. Okada, Y. Nishikawa, H. Amino and S. Iwanaga, *J. Phys. Chem. B*, 2021, **125**, 8703–8711.

(209) R. S. Erdmann, D. Toomre and A. Schepartz, in ed. H. Erfle, Springer New York, 2017, pp. 65–78.

(210) Y. Han, Z. Zhang, W. Liu, Y. Yao, Y. Xu, X. Liu, C. Kuang and X. Hao, *Front. Chem.*, 2021, **8**, DOI: `10.3389/fchem.2020.601436`.

(211) S. A. Meyer, B. N. Ozbay, M. Potcoava, E. Salcedo, D. Restrepo and E. A. Gibson, *J. Biomed. Opt.*, 2016, **21**, 066017.

(212) A. Löschberger, T. Niehörster and M. Sauer, *Biotech. J.*, 2014, **9**, 693–697.

(213) S. I. Suarez, C. C. Warner, H. Brown-Harding, A. M. Thooft, B. VanVeller and J. C. Lukesh, *Org. Biomol. Chem.*, 2020, **18**, 495–499.

(214) B. A. D. Neto, J. R. Correa and J. Spencer, *Chem. Eur. J.*, 2022, **28**, DOI: 10.1002/chem.202103262.

(215) S. Benson, A. Fernandez, N. D. Barth, F. de Moliner, M. H. Horrocks, C. S. Herrington, J. L. Abad, A. Delgado, L. Kelly, Z. Chang, Y. Feng, M. Nishiura, Y. Hori, K. Kikuchi and M. Vendrell, *Angew. Chem. Int. Ed.*, 2019, **58**, 6911–6915.

(216) R. S. Saleeb, C. Leighton, J.-E. Lee, J. O'Shaughnessy, K. Jeacock, A. Chappard, R. Cumberland, T. Zhao, S. R. Ball, M. Sunde, D. J. Clarke, K. Piché, J. A. McPhail, A. Louwrier, R. Angers, S. Gandhi, P. Downey, T. Kunath and M. H. Horrocks, *Sci. Adv.*, 2023, **9**, DOI: 10.1126/sciadv.adi7359.

(217) N. Kaplaneris, J. Son, L. Mendive-Tapia, A. Kopp, N. D. Barth, I. Maksso, M. Vendrell and L. Ackermann, *Nat. Commun.*, 2021, **12**, 3389.

(218) R. Cascella, S. W. Chen, A. Bigi, J. D. Camino, C. K. Xu, C. M. Dobson, F. Chiti, N. Cremades and C. Cecchi, *Nat. Commun.*, 2021, **12**, 1814.

(219) B. Li, P. Ge, K. A. Murray, P. Sheth, M. Zhang, G. Nair, M. R. Sawaya, W. S. Shin, D. R. Boyer, S. Ye, D. S. Eisenberg, Z. H. Zhou and L. Jiang, *Nat. Commun.*, 2018, **9**, 3609.

(220) A. Oueslati, *J. Parkinson's Dis.*, 2016, **6**, 39–51.

(221) D. A. Gray and J. Woulfe, *Sci. Aging Knowl. Environ.*, 2005, **2005**, DOI: 10.1126/sageke.2005.5.re1.

(222) V. Sadashivaiah, M. Tippani, S. C. Page, S. H. Kwon, S. V. Bach, R. A. Bharadwaj, T. M. Hyde, J. E. Kleinman, A. E. Jaffe and K. R. Maynard, *BMC Neurosci.*, 2023, **24**, 6.

(223) R. Sim, J. Lee, J. Chieng, K. H. Tan, G. Lim, A. Foo, S. H. Wong, K. L. Lim and K. Liang, *Fluorescent Peptide-based Probe for the Detection of Alpha-synuclein Aggregates in the Gut*, 2023.

(224) N. K. Polinski, *J. Parkinson's Dis.*, 2021, **11**, 1555–1567.

(225) A. Terman and U. T. Brunk, *APMIS*, 1998, **106**, 265–276.

(226) O.-D. Ilie, A. Ciobica, S. Riga, N. Dhunna, J. McKenna, I. Mavroudis, B. Doroftei, A.-M. Ciobanu and D. Riga, *Medicina*, 2020, **56**, 626.

(227) M. Katz, A. Groome and W. Robison, *J. Nutri.*, 1985, **115**, 1355–65.

(228) J. F. Giarola, J. Santos, M.-C. Estevez, S. Ventura, I. Pallarès and L. M. Lechuga, *Anal. Chim. Acta*, 2024, **1304**, 342559.

(229) J. Valli, A. Garcia-Burgos, L. M. Rooney, B. V. de Melo e Oliveira, R. R. Duncan and C. Rickman, *J. Biol. Chem.*, 2021, **297**, 100791.

(230) B. Turkowyd, D. Virant and U. Endesfelder, *Anal. Bioanal. Chem.*, 2016, **408**, 6885–6911.

(231) F. M. Raymo, *J. Phys. Chem. Lett.*, 2012, **3**, 2379–2385.

(232) G. T. Dempsey, J. C. Vaughan, K. H. Chen, M. Bates and X. Zhuang, *Nat. Methods*, 2011, **8**, 1027–1036.

(233) J. Schnitzbauer, M. T. Strauss, T. Schlichthaerle, F. Schueder and R. Jungmann, *Nat. Protoc.*, 2017, **12**, 1198–1228.

(234) M. Dai, R. Jungmann and P. Yin, *Nat. Nanotechnol.*, 2016, **11**, 798–807.

(235) R. Jungmann, C. Steinhauer, M. Scheible, A. Kuzyk, P. Tinnefeld and F. C. Simmel, *Nano Letters*, 2010, **10**, 4756–4761.

(236) S. S. Agasti, Y. Wang, F. Schueder, A. Sukumar, R. Jungmann and P. Yin, *Chem. Sci.*, 2017, **8**, 3080–3091.

(237) S. Sograte-Idrissi, T. Schlichthaerle, C. J. Duque-Afonso, M. Alevra, S. Strauss, T. Moser, R. Jungmann, S. O. Rizzoli and F. Opazo, *Nanoscale*, 2020, **12**, 10226–10239.

(238) A. Banerjee, M. Anand and M. Ganji, *Nanoscale*, 2023, **15**, 6563–6580.

(239) S. Strauss, P. C. Nickels, M. T. Strauss, V. J. Sabinina, J. Ellenberg, J. D. Carter, S. Gupta, N. Janjic and R. Jungmann, *Nat. Methods*, 2018, **15**, 685–688.

(240) L. S. Fischer, T. Schlichthaerle, A. Chrostek-Grashoff and C. Grashoff, *ChemBioChem*, 2021, **22**, 2872–2879.

(241) H. Bhaskar, D.-J. Kleinjan, C. Oi, Z. Gidden, S. J. Rosser, M. H. Horrocks and L. Regan, *Protein Sci.*, 2023, **32**, DOI: `10.1002/pro.4558`.

(242) R. P. Tas, L. Albertazzi and I. K. Voets, *Nano Lett.*, 2021, **21**, 9509–9516.

(243) L. C. Zanetti-Domingues, C. J. Tynan, D. J. Rolfe, D. T. Clarke and M. Martin-Fernandez, *PLoS ONE*, 2013, **8**, e74200.

(244) L. Funke, S. Dakoji and D. S. Bredt, *Ann. Rev. Biochem.*, 2005, **74**, 219–245.

(245) S. R. Gilman, I. Iossifov, D. Levy, M. Ronemus, M. Wigler and D. Vitkup, *Neuron*, 2011, **70**, 898–907.

(246) H.-C. Kornau, L. T. Schenker, M. B. Kennedy and P. H. Seeburg, *Science*, 1995, **269**, 1737–1740.

(247) L. Chen, D. M. Chetkovich, R. S. Petralia, N. T. Sweeney, Y. Kawasaki, R. J. Wenthold, D. S. Bredt and R. A. Nicoll, *Nature*, 2000, **408**, 936–943.

(248) H. D. MacGillavry, Y. Song, S. Raghavachari and T. A. Blanpied, *Neuron*, 2013, **78**, 615–622.

(249) D. Nair, E. Hosy, J. D. Petersen, A. Constals, G. Giannone, D. Choquet and J.-B. Sibarita, *J. Neurosci.*, 2013, **33**, 13204–13224.

(250) Y. Fukata, A. Dimitrov, G. Boncompain, O. Vielemeyer, F. Perez and M. Fukata, *J. Cell Biol.*, 2013, **202**, 145–161.

(251) M. J. Broadhead, M. H. Horrocks, F. Zhu, L. Muresan, R. Benavides-Piccione, J. DeFelipe, D. Fricker, M. V. Kopanitsa, R. R. Duncan, D. Klenerman, N. H. Komiyama, S. F. Lee and S. G. N. Grant, *Sci. Rep.*, 2016, **6**, 24626.

(252) J. Zhang, S. M. Lewis, B. Kuhlman and A. L. Lee, *Structure*, 2013, **21**, 402–413.

(253) G. A. Tavares, E. H. Panepucci and A. T. Brunger, *Mol. Cell*, 2001, **8**, 1313–1325.

(254) A. Cámara-Artigas, J. Murciano-Calles, J. A. Gavira, E. S. Cobos and J. C. Martínez, *J. Struct. Biol.*, 2010, **170**, 565–569.

(255) J.-F. Long, H. Tochio, P. Wang, J.-S. Fan, C. Sala, M. Niethammer, M. Sheng and M. Zhang, *J. Mol. Biol.*, 2003, **327**, 203–214.

(256) E. Kim and M. Sheng, *Nat. Revs. Neurosci.*, 2004, **5**, 771–781.

(257) D. A. Doyle, A. Lee, J. Lewis, E. Kim, M. Sheng and R. MacKinnon, *Cell*, 1996, **85**, 1067–1076.

(258) D. L. Daniels, A. R. Cohen, J. M. Anderson and A. T. Brünger, *Nat. Struct. Biol.*, 1998, **5**, 317–325.

(259) M. Zhang, H. Tochio, Q. Zhang, P. Mandal and M. Li, *Nature Struct. Biol.*, 1999, **6**, 417–421.

(260) E. Kim, M. Niethammer, A. Rothschild, Y. N. Jan and M. Sheng, *Nature*, 1995, **378**, 85–88.

(261) H.-C. Kornau, L. T. Schenker, M. B. Kennedy and P. H. Seeburg, *Science*, 1995, **269**, 1737–1740.

(262) M. Niethammer, E. Kim and M. Sheng, *J. Neurosci.*, 1996, **16**, 2157–2163.

(263) M. Niethammer, J. G. Valtschanoff, T. M. Kapoor, D. W. Allison, R. J. Weinberg, A. M. Craig and M. Sheng, *Neuron*, 1998, **20**, 693–707.

(264) C. Nourry, S. G. N. Grant and J.-P. Borg, *Science's STKE*, 2003, **2003**, DOI: `10.1126/stke.2003.179.re7`.

(265) W. G. Walkup and M. B. Kennedy, *Curr. Protoc. Protein Sci.*, 2015, **80**, DOI: `10.1002/0471140864.ps0910s80`.

(266) R. K. Carlin, D. J. Grab, R. S. Cohen and P. Siekevitz, *J. Cell Biol.*, 1980, **86**, 831–845.

(267) E. Bulovaite, Z. Qiu, M. Kratschke, A. Zgraj, D. G. Fricker, E. J. Tuck, R. Gokhale, B. Koniaris, S. A. Jami, P. Merino-Serrais, E. Husi, L. Mendive-Tapia, M. Vendrell, T. J. O'Dell, J. DeFelipe, N. H. Komiyama, A. Holtmaat, E. Fransén and S. G. Grant, *Neuron*, 2022, **110**, 4057–4073.e8.

(268) J. Sander, M. Ester, H.-P. Kriegel and X. Xu, *Data Min. Knowl. Discov.*, 1998, **2**, 169–194.

(269) T. J. Gould, V. V. Verkhusha and S. T. Hess, *Nat. Protoc.*, 2009, **4**, 291–308.

(270) B. Z. Harris, B. J. Hillier and W. A. Lim, *Biochem.*, 2001, **40**, 5921–5930.

(271) I. A. Lim, D. D. Hall and J. W. Hell, *J. Biol. Chem.*, 2002, **277**, 21697–21711.

(272) I. A. Lim, M. A. Merrill, Y. Chen and J. W. Hell, *Neuropharmacol.*, 2003, **45**, 738–754.

(273) S. M. Marfatia, J. H. M. Cabral, L. Lin, C. Hough, P. J. Bryant, L. Stolz and A. H. Chishti, *J. Cell Biol.*, 1996, **135**, 753–766.

(274) B. M. Müller, U. Kistner, S. Kindler, W. J. Chung, S. Kuhlendahl, S. D. Fenster, L.-F. Lau, R. W. Veh, R. L. Huganir, E. D. Gundelfinger and C. C. Garner, *Neuron*, 1996, **17**, 255–265.

(275) Z. Songyang, A. S. Fanning, C. Fu, J. Xu, S. M. Marfatia, A. H. Chishti, A. Crompton, A. C. Chan, J. M. Anderson and L. C. Cantley, *Science*, 1997, **275**, 73–77.

(276) L. Wang, A. Piserchio and D. F. Mierke, *J. Biol. Chem.*, 2005, **280**, 26992–26996.

(277) S. M. Tieze, S. S. Chandra and D. J. Vidyadhara, *J. Visual. Exp.*, 2022, DOI: `10.3791/64574`.

(278) E. Bulovaite, Z. Qiu, M. Kratschke, A. Zgraj, D. G. Fricker, E. J. Tuck, R. Gokhale, B. Koniaris, S. A. Jami, P. Merino-Serrais, E. Husi, L. Mendive-Tapia, M. Vendrell, T. J. O'Dell, J. DeFelipe, N. H. Komiyama, A. Holtmaat, E. Fransén and S. G. Grant, *Neuron*, 2022, **110**, 4057–4073.e8.

(279) J.-M. Masch, H. Steffens, J. Fischer, J. Engelhardt, J. Hubrich, J. Keller-Findeisen, E. D'Este, N. T. Urban, S. G. N. Grant, S. J. Sahl, D. Kamin and S. W. Hell, *Proc. Natl. Acad. Sci.*, 2018, **115**, DOI: `10.1073/pnas.1807104115`.

(280) N. Banterle, K. H. Bui, E. A. Lemke and M. Beck, *J. Struct. Biol.*, 2013, **183**, 363–367.

(281) F. de Moliner, Z. Konieczna, L. Mendive-Tapia, R. S. Saleeb, K. Morris, J. A. Gonzalez-Vera, T. Kaizuka, S. G. N. Grant, M. H. Horrocks and M. Vendrell, *Angew. Chem. Int. Ed.*, 2023, **62**, DOI: `10.1002/anie.202216231`.

(282) P. Burkhard, J. Stetefeld and S. V. Strelkov, *Trends Cell Biol.*, 2001, **11**, 82–88.

(283) A. Lupas, *Trends Biochem. Sci.*, 1996, **21**, 375–382.

(284) F. H. C. Crick, *Acta Crystallograp.*, 1953, **6**, 689–697.

(285) J. K. Doh, J. D. White, H. K. Zane, Y. H. Chang, C. S. López, C. A. Enns and K. E. Beatty, *Proc. Natl. Acad. Sci.*, 2018, **115**, 12961–12966.

(286) R. Chen, H. S. Rishi, V. Potapov, M. R. Yamada, V. J. Yeh, T. Chow, C. L. Cheung, A. T. Jones, T. D. Johnson, A. E. Keating, W. C. DeLoache and J. E. Dueber, *ACS Synth. Biol.*, 2015, **4**, 1205–1216.

(287) H. Chao, D. L. Bautista, J. Litowski, R. T. Irvin and R. S. Hodges, *J. Chromatograph. B: Biome. Sci. Appl.*, 1998, **715**, 307–329.

(288) U. Reinhardt, J. Lotze, K. Mörl, A. G. Beck-Sickinger and O. Seitz, *Bioconjug. Chem.*, 2015, **26**, 2106–2117.

(289) J. Lotze, P. Wolf, U. Reinhardt, O. Seitz, K. Mörl and A. G. Beck-Sickinger, *ACS Chem. Biol.*, 2018, **13**, 618–627.

(290) Y. Yano, A. Yano, S. Oishi, Y. Sugimoto, G. Tsujimoto, N. Fujii and K. Matsuzaki, *ACS Chem. Biol.*, 2008, **3**, 341–345.

(291) H. Chao, S. Grothe, C. M. Kay, M. O'Connor-McCourt, R. T. Irvin and R. S. Hodges, *Biochem.*, 1996, **35**, 12175–12185.

(292) J. R. Litowski and R. S. Hodges, *J. Biol. Chem.*, 2002, **277**, 37272–37279.

(293) K. Gröger, G. Gavins and O. Seitz, *Angew. Chem. Int. Ed.*, 2017, **56**, 14217–14221.

(294) A. S. Eklund, M. Ganji, G. Gavins, O. Seitz and R. Jungmann, *Nano Letters*, 2020, **20**, 6732–6737.

(295) B. K. Maity, D. Nall, Y. Lee and P. R. Selvin, *Small Methods*, 2023, **7**, DOI: 10.1002/smtd.202201181.

(296) A. S. Eklund and R. Jungmann, *Small*, 2023, **19**, DOI: 10.1002/smll.202206347.

(297) C. Oi, Z. Gidden, L. Holyoake, O. Kantelberg, S. Mochrie, M. H. Horrocks and L. Regan, *Commun. Biol.*, 2020, **3**, 458.

(298) Z. Gidden, C. Oi, E. J. Johnston, Z. Konieczna, H. Bhaskar, L. Mendive-Tapia, F. de Moliner, S. J. Rosser, S. G. J. Mochrie, M. Vendrell, M. H. Horrocks and L. Regan, *Nano Letters*, 2023, **23**, 10633–10641.

(299) Z. Gidden, 2023, 143–176.

(300) M. Muttenthaler, G. F. King, D. J. Adams and P. F. Alewood, *Nat. Revs. Drug Disc.*, 2021, **20**, 309–325.

(301) J. R. Kintzing and J. R. Cochran, *Curr. Op. Chem. Biol.*, 2016, **34**, 143–150.

(302) I. Vetter, J. L. Davis, L. D. Rash, R. Anangi, M. Mobli, P. F. Alewood, R. J. Lewis and G. F. King, *Amino Acids*, 2011, **40**, 15–28.

(303) J. K. Klint, S. Senff, N. J. Saez, R. Seshadri, H. Y. Lau, N. S. Bende, E. A. B. Undheim, L. D. Rash, M. Mobli and G. F. King, *PLoS ONE*, 2013, **8**, e63865.

(304) G. P. Smith, *Science*, 1985, **228**, 1315–1317.

(305) A. M. Davis, A. T. Plowright and E. Valeur, *Nat. Revs. Drug Disc.*, 2017, **16**, 681–698.

(306) F. A. Aprile, P. Sormanni, M. Perni, P. Arosio, S. Linse, T. P. J. Knowles, C. M. Dobson and M. Vendruscolo, *Sci. Adv.*, 2017, **3**, DOI: 10.1126/sciadv.1700488.

(307) Y. Goto and H. Suga, *Acc. Chem. Res.*, 2021, **54**, 3604–3617.

(308) J. B. Kaplan, A. W. Reinke and A. E. Keating, *Prot. Sci.*, 2014, **23**, 940–953.

(309) A. W. Reinke, R. A. Grant and A. E. Keating, *JACS*, 2010, **132**, 6025–6031.

(310) A. N. Lupas, J. Bassler and S. Dunin-Horkawicz, *The Structure and Topology of -Helical Coiled Coils*, ed. D. A. D. Parry and J. M. Squire, Springer, 2017, pp. 95–129.

(311) B. Hua, K. Y. Han, R. Zhou, H. Kim, X. Shi, S. C. Abeysirigunawardena, A. Jain, D. Singh, V. Aggarwal, S. A. Woodson and T. Ha, *Nat. Methods*, 2014, **11**, 1233–1236.

(312) A. Wurzer, C. Seidl, A. Morgenstern, F. Bruchertseifer, M. Schwaiger, H.-J. Wester and J. Notni, *Chem. Eur. J.*, 2018, **24**, 547–550.

(313) Y. Krishanan, A. T. Veetil and M. S. Jani, *Method and composition for measurement of nitric oxide*, 2021.

(314) L. A. Linhares and C. H. I. Ramos, *Appl. Biosci.*, 2023, **2**, 639–655.

(315) T. Rao, G. Ruiz-Gómez, T. A. Hill, H. N. Hoang, D. P. Fairlie and J. M. Mason, *PLoS ONE*, 2013, **8**, e59415.

(316) V. Kamat and A. Rafique, *Anal. Biochem.*, 2017, **536**, 16–31.

(317) C. S. Palmer, J. Lou, B. Kouskousis, E. Pandzic, A. J. Anderson, Y. Kang, E. Hinde and D. Stojanovski, *J. Cell Sci.*, 2021, **134**, DOI: `10.1242/jcs.252197`.

(318) S. S. Agasti, Y. Wang, F. Schueder, A. Sukumar, R. Jungmann and P. Yin, *Chem. Sci.*, 2017, **8**, 3080–3091.

(319) C. S. Abeywickrama, K. J. Wijesinghe, R. V. Stahelin and Y. Pang, *Bioorg. Chem.*, 2019, **91**, 103144.

(320) J. Ecard, Y.-L. Lian, S. Divoux, Z. Gouveia, E. Vigne, F. Perez and G. Boncompain, *Mol. Biol. Cell*, 2024, **35**, DOI: `10.1091/mbc.E23-06-0251`.

(321) A. Baibek, Z. Konieczna, M. Üçüncü, Z. S. Alghamdi, R. Sharma, M. H. Horrocks and M. Bradley, *ChemRxiv (pre-print)*, 2024.

(322) D. J. Lindberg, M. S. Wranne, M. Gilbert Gatty, F. Westerlund and E. K. Esbjörner, *Biochem. Biophys. Res. Commun.*, 2015, **458**, 418–423.

(323) Y. Li, M. Wu, Y. Fu, J. Xue, F. Yuan, T. Qu, A. N. Rissanou, Y. Wang, X. Li and H. Hu, *Pharmacol. Res.*, 2024, **203**, 107137.

(324) D.-H. Kim and S.-M. Kang, *Biomimet.*, 2024, **9**, DOI: `10.3390/biomimetics9090537`.

(325) P. G. Dougherty, J. Wen, X. Pan, A. Koley, J.-G. Ren, A. Sahni, R. Basu, H. Salim, G. Appiah Kubi, Z. Qian and D. Pei, *J. Med. Chem.*, 2019, **62**, PMID: 31657556, 10098–10107.